Experimental and Numerical Investigation of Reverse-Micro-EDM Fabricated Arrayed Micro Protrusions

Doctoral Thesis

by

HREETABH KISHORE

2017MEZ0007

DEPARTMENT OF MECHANICAL ENGINEERING

INDIAN INSTITUTE OF TECHNOLOGY ROPAR

MAY, 2023

Experimental and Numerical Investigation of Reverse-Micro-EDM Fabricated Arrayed Micro Protrusions

A Thesis Submitted

In Partial Fulfilment of the Requirements

for the Degree of

DOCTOR OF PHILOSOPHY

by

HREETABH KISHORE

2017MEZ0007

DEPARTMENT OF MECHANICAL ENGINEERING

INDIAN INSTITUTE OF TECHNOLOGY ROPAR

MAY, 2023

Hreetabh Kishore: *EXPERIMENTAL AND NUMERICAL INVESTIGATION OF REVERSE-MICRO-EDM FABRICATED ARRAYED MICRO PROTRUSIONS*

Copyright © 2023, Indian Institute of Technology Ropar
All Rights Reserved

DEDICATED

TO

KISHORE AND SHRIVASTAVA FAMILIES

Declaration of Originality

I hereby declare that the work which is being presented in the thesis entitled **"Experimental and Numerical Investigation of Reverse-Micro-EDM Fabricated Arrayed Micro Protrusions"** has been solely authored by me. It presents the result of my own independent investigation/research conducted during the time period from **August 2017** to **September 2022** under the supervision of **Dr. Chandrakant Kumar Nirala**, Assistant Professor and **Dr. Anupam Agrawal**, Associate Professor in the Department of Mechanical Engineering, Indian Institute of Technology Ropar. To the best of my knowledge, it is an original work, both in terms of research content and narrative, and has not been submitted or accepted elsewhere, in part or in full, for the award of any degree, diploma, fellowship, associateship, or similar title of any university or institution. Further, due credit has been attributed to the relevant state-of-the-art collaborations (if any) with appropriate citations and acknowledgments, in line with established ethical norms and practices. I also declare that any idea/data/fact/source stated in my thesis has not been fabricated/ falsified/ misrepresented. All the principles of academic honesty and integrity have been followed. I fully understand that if the thesis is found to be unoriginal, fabricated, or plagiarized, the Institute reserves the right to withdraw the thesis from its archive and revoke the associated Degree conferred. Additionally, the Institute also reserves the right to appraise all concerned sections of society of the matter for their information and necessary action (if any). If accepted, I hereby consent for my thesis to be available online in the Institute's Open Access repository, inter-library loan, and for the title & abstract to be made available to outside organizations.

Hreetabh
Kishore

Signature

Name: Hreetabh Kishore
Entry Number: 2017MEZ0007
Program: Ph.D.
Department: Mechanical Engineering
Indian Institute of Technology Ropar
Rupnagar, Punjab 140001

Date: 26th May 2023

ACKNOWLEDGEMENTS

As another phase of life is ready to dawn with the submission of my PhD thesis, there have been numerous helping hands and genuine advice behind the successful completion of my work. First and foremost, I express my sincere gratitude and respect to my thesis supervisor(s) **Dr. Chandrakant Kumar Nirala,** Assistant Professor and **Dr. Anupam Agrawal**, Associate Professor, Department of Mechanical Engineering, IIT Ropar, for his valuable guidance, constant encouragement throughout this study and untiring help, without which this research would not have attained its shape. Words would not be enough to describe the ocean of knowledge he has, and I feel divinely blessed to have worked under his guidance and command. I would also like to thank them for the brotherly support and the parent-like emotional care that not only helped me evolve myself as a researcher but also develop me as a better individual.

I extend my gratefulness to **Prof. Sarit Kumar Das**, former director IIT Ropar and **Prof. Rajiv Ahuja**, Director, IIT Ropar for their excellent and strategic administration and research-friendly environment provided to me during my stay at IIT Ropar.

I feel fortunate to have witnessed the tenures of **Prof. Navin Kumar** followed by **Dr. Ekta Singla** as the head of the department, Mechanical Engineering and **Dr. Prabhat Kumar Agnihotri** as the current head of the department. Also, I am highly thankful to **Prof. Navin Kumar**, Dean (Research and Development) and the Chairman of my DC Committee, IIT Ropar, for his highly appreciative expert comments during research discussions which helped me a lot to improve the standards of this research work.

I would like to express my heartiest gratitude to **Prof. Ravindra Kumar Saxena,** Professor, in the Department of Mechanical Engineering and Head Training and Placement Cell also to **Prof. Shankar Singh,** Professor, in the Department of Mechanical Engineering at **SLIET, Longowal**, for their unrelenting nature to transfer their expertise and the way they trained me, has made the whole period of my technical education starting from **Certificate, Diploma, B.E., M.Tech., Ph.D.** a great learning experience.

It would be unfair if I proceed without thanking my DC committee members, **Prof. C.C. Reddy**, Professor, Department of Electrical Engineering, **Dr. Ranjan Das**, Associate Professor, Department of Mechanical Engineering, and **Dr. RaviKant** Assistant Professor, Department of Mechanical Engineering, IIT Ropar for his concern for me and efficient and timely advice on research activities that helped me to complete my research with ease and well in time.

I hereby mention special heartfelt thanks to **Dr. Girish Pramodrao Kathane,** Hindi Translator at IIT Ropar (**Rajbhasha Hindi cell**), for his profound guidance on teamwork and in publishing quarterly Institute Hindi magazine "**Sangam Patrika**" also for being my inspiration always and for his continuous support and encouragement.

I sincerely thank all the staff members of the Mechanical Engineering Department, IIT Ropar- **Mr. Kaushal Kishor Jha, Mr. Jagmail Singh, Mr. Ram Kumar, Mr. Sukhwinder Singh, Mr. Hemant, and Mr. Rupinder Singh** for helping me out in my office and field-related work whenever I was stuck with problems. I express my special regards to **Mr. Varinder Kumar**, (Technical Assistant, Micromanuafcturing Lab), Department of Mechanical Engineering, IIT Ropar for being my constant field companion, a reliable friend and an excellent teacher on the field, from whom I learned a lot of concepts. I also thank him for his elder brother like encouragement, advice and sharing his expertise which I shall carry throughout my professional life.

Words will not be enough to express my gratitude for all the staff members of Central Workshop at IIT Ropar: **Mr. Rambir Singh, Mr. Rajiv Kumar, Mr. Randhir, Mr. Girdhari, Mr. Yograj, Mr. Bhupinder, Mr. Jaskaran, Mr. Jaswinder** for carrying and supporting me in all my experimental setup fabrication and for being my strength toughest of times.

Friends make our life loom or gloom. I am lucky to have my friends as my B.E. (Mechanical Engineering) juniors/seniors/colleagues at SLIET, Longowal and IIT Ropar– **Dr. Santosh Kumar, Mr. Abhishek Kumar, Mr. Arjun Singh, Ms. Priyanka Sinha** along with my Ph.D. colleagues- **Mr. Chandra Shekhar, Dr. Akshar Tripathi** and **Ms. Papiya Bhowmik** from the various Departments, whose cheerful presence always gave me the energy to face all obstacles I had and to complete this research successfully.

I am highly obliged and thankful to my seniors, colleagues, well-wishers and friends- **Dr. Harish Kumar Nirala, Dr. Narinder Kumar, Dr. Shuja Ahmed, Dr. Kamal Prakash, Dr. Malkeet Singh, Mr. Rakesh Kumar, Mr. Mainak Pal, Mr. Shoaib Raza, Mr. Jay Airao, Mr. Rahul Nadda, Mr. Saurabh Rai, Mr. Yash Desai, Mr. Peeyush Mahajan, Mr. Mainak Banerjee, Mr. Vikrant Sharma, Mr. Raushan Kumar, Mr. Sahil Rana** whom I might not have made a special mention of here, but they always stay with a special mention in my life.

I feel lucky to have the encouraging and cheering support of my grandfather (Maternal) **Late Er. Bimal Narayan Shrivastava**, retired Assistant Engineer (PWD, Civil department), from Bihar Government Services (BSBCCL). I thank him for giving me the positive energy to go ahead with my life and this research, and for being my strongest support and a true well-wisher at all times.

Yet importantly, I extend my salutations to my beloved parents: **Sh. Peeyusa Kishora** and **Smt. Lily Shrivastava** for their everlasting encouragement and support. I would like to dedicate this thesis to my highly respected parents whose unwavering support was the backbone for completing this thesis work. I am incredibly grateful to my elder brother, sister-in-law and their son **Mr. Hrishabh Kishore, Mrs. Jyoti Kumari** and **Tanush** for their continuous moral support.

Last but not least, I wish to record my gratitude, with utmost reverence and gracious faithfulness to the **almighty God** for his indomitable lead and guidance throughout my life.

Thank You all!

May of 2023 **Hreetabh Kishore**

CANDIDATE’S DECLARATION

I hereby certify that the work which is being presented in this thesis entitled **“Experimental and Numerical Investigation of Reverse-Micro-EDM Fabricated Arrayed Micro Protrusions”** in partial fulfilment of the requirements for the award of the Degree of Doctor of Philosophy and submitted in the Department of Mechanical Engineering of the Indian Institute of Technology Ropar, Rupnagar, is an authentic record of my work carried out during the period from August 2017 to September 2022, under the supervision of Dr. Chandrakant Kumar Nirala, Assistant Professor, and Dr. Anupam Agrawal, Associate Professor, Department of Mechanical Engineering, Indian Institute of Technology Ropar, Rupnagar (Punjab), India.

The matter presented in the thesis has not been submitted by me for the award of any other degree of this or any other Institute.

Hreetabh
Kishore

HREETABH KISHORE

This is to certify that the above statement made by the candidate is correct to the best of my knowledge.

Date: 26th May 2023

Chandrakant Km Nirala

Anupam Agrawal

Dr. CHANDRAKANT K NIRALA **Dr. ANUPAM AGRAWAL**

ABSTRACT

Among micromachining processes, μEDM and its variants have revolutionized the surface texturing phenomenon on conductive materials irrespective of hardness values. A potential application of surface texturing could be in the thermal management of high heat flux devices when used as arrayed protrusions (or micro pin-fins) heat sinks. Reverse-micro-electric-discharge machining (RμEDM) as one of the μEDM variants has evolved as a method for the fabrication of single/arrayed micro protrusions. These protrusions find applications in many technological fields, including optics, surface energetics, lubrication, bioengineering, component assembly and thermal management of high-performance microelectronics etc.

For fabricating these protrusions by RμEDM, the tool used in the form of a plate consisting of micro holes is one of the key components. These holes are generally required with high accuracy and precision arranged in the form of an array of similar shapes and sizes of the arrayed protrusions. Tool plate fabrication technologies such as mechanical and EDM micro drilling are extensively used. Though, having certain limitations such as longer machining time for an array of micro holes, overcut etc. Laser beam micromachining (LBμM) is identified as an alternative for the fabrication of tool plate for RμEDM due to enhanced machining speed and dimensional accuracy.

In this regard, a comprehensive feasibility study has been done on the fabrication of arrayed protrusions by RμEDM using LBμM fabricated tool plates. This combined process is termed as 'integrated RμEDM-LBμM technology'. To establish the developed integrated process for the mentioned purpose, issues such as burr formation in the LBμM fabricated micro holes and hence, its replication as damages at the edges of RμEDM fabricated micro protrusions, need to be taken care of. Comprehensive studies have been performed for finding optimum process parameters using GA for both processes to ensure minimum errors in the arrayed micro holes, thereby in the micro protrusions. The different machining responses associated with both processes have been critically analyzed in these regards.

Improvement in the responses, such as MRR and surface characteristics through parametric optimization in RμEDM can be achieved up to a limit only. Due to the stochastic behavior of debris in the tiny discharge gap, the removal of that debris is cumbersome, especially in the case of an array fabrication. This has led to a difference in the process stability due to the heavy occurrence of abnormal discharges in the tiny gap affecting the material removal efficiency and life of the tool plate. Therefore, a suction-based high-pressure dielectric flushing mechanism is proposed for effective debris removal. This technology ensures a reduction in total machining time, which is highly desirable in machining high aspect ratio arrayed micro protrusions.

Numerical and experimental thermal performance evaluations of densely arrayed protrusions (to act as pin-fin heat exchangers) in both inline and staggered arrangements is another key contribution of the thesis. A geometrical design-based optimization study using the Particle swarm multi-objective optimization (PSO) algorithm has been performed to quantify the optimal geometrical design of the cross-section of micro pin-fins (MPFs) in an array. It is followed by the thermal performance evaluation of different arrayed MPFs cross-sectional profiles and arrangements through numerical simulation and experimental approach. A thermal performance index (*TPI*) parameter is defined in a laminar flow regime under constant heat loading conditions for evaluation. An in-house testing facility has been designed and developed for evaluating the overall thermal performance of optimized arrayed MPFs experimentally.

The thesis will lay the ground for the quality fabrication of arrayed protrusions (as MPFs) by enhancing the processes' stability through geometrical design optimization, thermal performance analysis, and experimental validation. This work is significantly important for the early mitigation and evaluation of fabricated micro protrusions for various applications.

Keywords - RμEDM, Arrayed micro protrusions, LBμM, optimization, suction-based dielectric flushing, MPFs, numerical simulation, thermal performance evaluation.

LIST OF PUBLICATIONS/PATENT

RESEARCH PAPERS IN REFERRED JOURNALS

1. **Kishore, H.**, Nirala, C. K., Agrawal, A. (2020). Feasibility Demonstration of µEDM for Fabrication of Arrayed Micro Pin-fins of Complex Cross-sections, *Manufacturing Letters*, 23, pp.14-18. https://doi.org/10.1016/j.mfglet.2019.11.005

2. **Kishore, H.**, Nirala, C. K., Agrawal, A. (2021). Assessment of process parameters and performance enhancement through a novel suction flushing technology in RµEDM. *Materials and Manufacturing Processes*, 36(13), 1476-1488. https://doi.org/10.1080/10426914.2021.1948051

3. **Kishore, H.**, Nirala, C. K., Agrawal, A. (2022). Laser Micromachining in Fabrication of Reverse-µEDM Tools for Producing Arrayed Protrusions. *Micromachines,* 13(2):306, 1-17. https://doi.org/10.3390/mi13020306

4. **Kishore, H.**, Nirala, C. K., Agrawal, A. (2022). Exploring AZ31B Magnesium Alloy for Innovative Micro Products by Reverse µEDM. *Materials Letters*, 328, 133109 (1-4). https://doi.org/10.1016/j.matlet.2022.133109

5. Raza, S., **Kishore, H.**, Nirala, C. K., Rajurkar, K.P. (2023). Multiphysics Modeling and High-Speed Imaging-based Validation of Discharge Plasma in Micro-EDM. *CIRP Journal of Manufacturing Science and Technology*, 43, 15-29. https://doi.org/10.1016/j.cirpj.2023.02.006

6. **Kishore, H.**, Nirala, C. K., Agrawal, A. (2023). Thermal Performance Index Based Characterization and Experimentation Validation for Heat Dissipation by Unconventional Arrayed Pin-fins. *Thermal Science Engineering Progress* (Minor revision submitted).

7. **Kishore, H.**, Pal, M., Nirala, C. K., Agrawal, A. (2023). Thermal Design Based Dimensional Optimization and Fabrication Feasibility of Unconventional Micro Pin-fin Heat Exchangers. *International Journal of Precision Engineering and Manufacturing* (Accepted).

PAPERS IN CONFERENCE/SYMPOSIA/BOOK CHAPTER

1. **Kishore, H.**, Nirala, C. K., Agrawal, A. (2018). Development of a New Technology for Fabrication of Complex Shaped Arrayed Micro-pin-fins. Presented in *Research Conclave* at *IIT Ropar* on April 23rd 2018.

2. **Kishore, H.**, Nirala, C. K., Agrawal, A. (2019). Modelling and Simulation Based Surface Characterization of Reverse-µEDM Fabricated Micro Pin-fins. *Proced. CIRP*. 81: 1230-1235. https://doi.org/10.1016/j.procir.2019.03.299.

3. **Kishore, H.**, Nirala, C. K., Agrawal, A. (2019). Characterization of LBM Fabricated Tool-plate for RµEDM. *7th International conference on Advancements and*

Futuristic Trends in Mechanical and Materials Engineering (Proceedings of AFTMME 2019), IIT Ropar, 5-7th December 2019.

4. **Kishore, H.**, Nirala, C. K., Agrawal, A. (2019). Unconventional Shaped Micro Pin-fins for Electronic Cooling: A New Fabrication Approach. *22nd International Conference on Advances in Materials and Processing Technology (AMPT- 2019)*, Oct. 20-24, 2019, Taipei, Taiwan.

5. **Kishore, H.**, Nirala, C. K., Agrawal, A. (2019). A New Approach for Fabrication of Complex-Shaped Arrayed Micro Electrodes. In: Shunmugam M., Kanthababu M. (eds) *Advances in Micro and Nano Manufacturing and Surface Engineering*. *Lecture Notes on Multidisciplinary Industrial Engineering*. Springer, Singapore. https://doi.org/10.1007/978-981-32-9425-7_3.

6. **Kishore, H.**, Raza, S., Nirala, C. K., Agrawal, A. (2019). Poster-I Hybrid μEDM-LASER Technology for Fabrication of Complex Shaped Arrayed Micro-structures" Poster II-"Process Development in μEDM using Hybrid Ultrasonic Vibration and Suction Technology" Participated and presented Poster at *IESS-2019*, Chennai Trade Center, Chennai, Tamilnadu, 14-16 March, 2019.

7. **Kishore, H.**, Nirala, C. K., Agrawal, A. (2019). A New Technology for Fabrication of Arrayed Micro-pin-fins. Presented Poster by (Dr. Chandrakant K Nirala) on March 17th 2018 at *Titan Technology Tune-In*, Hosur Titan watches factory:- Address, No.3 SIPCOT Industrial Complex, Hosur, Banglore city, Registration ID- 20143818.

8. **Kishore, H.**, Nirala, C. K., Agrawal, A. (2021). Integrated Micromachining Processes and its Applications. Two Day National Level Inter-Departmental 3rd Research Talk Series (METRIX-3.0). IIT Ropar. 21-22nd October 2021. (First Prize for Best Presentation Award)

9. **Kishore, H.**, Sharma, V., Airao J., Nirala, C., K., Agrawal A. (2021). Introduction of a New Suction-based Dielectric Flushing in Reverse-μEDM. *4th World Congress on Micro & Nano Manufacturing (Proceedings of WCMNM-21)*, Paper ID-35, IIT Bombay.1-6. (Achieved student Award with fee exemption)

10. Nirala H. K., **Kishore, H.**, Agrawal, A. (2022). Effect of Nd- YAG LBμM process parameters on the surface characterization of fabricated micro components. 20th ISME (Advancement in Mechanical Engineering) conference held at IIT Ropar, 19th -21st May, 2022.

RESEARCH PAPERS IN REFERRED JOURNALS (outside Ph.D. work)

1. Airao, J., **Kishore, H.**, Nirala, C. K. (2022). Tool Wear Behavior in μ-turning of Nimonic 90 Under Vegetable Oil-Based Cutting Fluid. *Micro and Nano-Manufacturing*. 9(4): 041003 (10 pages). https://doi.org/10.1115/1.4053315.

2. Airao, J., **Kishore, H.**, Nirala, C. K. (2023). Measurement and analysis of tool wear and surface characteristics in micro turning of SLM Ti6Al4V and wrought Ti6Al4V. *Measurement*. 206: 112281 (14 pages). https://doi.org/10.1016/j.measurement.2022.112281.

3. Airao, J., **Kishore, H.**, Nirala, C. K. (2023). Comparative analysis of tool wear in micro-milling of wrought and selective laser melted Ti6Al4V, *Wear*. 523: 204788. https://doi.org/10.1016/j.wear.2023.204788.

PAPERS IN CONFERENCE/SYMPOSIA/BOOK CHAPTER (outside Ph.D. work)

1. Rai, S., **Kishore, H.**, Nirala, K. H., Agrawal, A. (2020). Finite Element Analysis of Sheet Thickness and Force Variation in AA6063 During Single Point Incremental Forming. In: Shunmugam M., Kanthababu M. (eds) *Advances in Simulation, Product Design and Development. Lecture Notes on Multidisciplinary Industrial Engineering*. Springer, Singapore. https://doi.org/10.1007/978-981-32-9487-5_13

2. Pal, M., Mahajan, P., Athikkai, N., Rai, S., **Kishore, H.,** Kumar, R., Agrawal, A. (2019). Development of GUI and Comparison of Tool path Strategies for Incremental Forming of Polycarbonate Sheet. *11th International Conference on Precision, Meso, Micro & Nano Engineering (COPEN-2019)*, IIT, Indore, December 12-14, 2019.

3. **Kishore, H.**, Banerjee, M., Rai S., Kumar, R., Agrawal, A. (2020). Experimental and Numerical Investigation on Micro Friction Stir Welding of Dissimilar Metal Joints. *Proceedings of the ASME 2020 15th International Manufacturing Science and Engineering Conference, (MSEC-2020)*. Paper ID- MSEC2020-8525, June, 2020.

4. Pal, M., **Kishore, H.**, Agrawal, A., Nirala, C. K. (2022). Fabrication of Precise Hemispherical End Tool for Micro Incremental Sheet Forming using Reverse-µEDM. *55th CIRP Conference on Manufacturing Systems-2022. Procedia CIRP*. 107, 1600-1605. https://doi.org/10.1016/j.procir.2022.06.001

5. Ahmed, S., Singh, A. **Kishore, H.**, Quamar, M. D., Tiwari, R., Nirala, C. K. Singh, H. (2021). Fabrication of shoulder features on tungsten carbide FSP tool through EDM process - A feasibility study. *9th International conference on Advancements and Futuristic Trends in Mechanical and Materials Engineering (Proceedings of AFTMME 2021)*, IIT Ropar, 9-11th December 2021.

6. Raza, S., **Kishore, H.**, Nirala, C. K., (2022). Simulation of crater formation during µEDM using the ALE method" 5th World congress on micro and nano manufacturing, *Proceedings of WCMNM-22*, Paper ID-56, KU LEUVEN, Belgium, (19th-22th September, 2022).

PATENT

Application No: 202211036538
Date of filing: 25/06/2022
Title: 'A dielectric flushing system for Reverse-micro-electric discharge machining and method of flushing thereof'
Applicant: Indian Institute of Technology Ropar
Inventors: Hreetabh Kishore, Chandrakant K Nirala, & Anupam Agrawal
Status: Under review

TABLE OF CONTENTS

DECLARATION OF ORIGINALITY **i**
ACKNOWLEDGEMENT **iii-v**
CANDIDATE DECLARATION **vii**
ABSTRACT **ix-x**
LIST OF PUBLICATIONS **xii-xiv**
TABLE OF CONTENTS **xvi-xix**
LIST OF FIGURES **xxi-xxiv**
LIST OF TABLES **xxvi-xxvii**
LIST OF ABBREVIATIONS **xxix**
NOTATIONS **xxxi-xxxiii**

CHAPTER 1: INTRODUCTION **1**
1.1 Background and Motivation **1**
1.2 Introduction to the Research Problem **4**
1.3 Organization of the thesis **6**
1.4 Research plan **9**

CHAPTER 2: LITERATURE REVIEW **11**
2.1 Introduction **11**
2.2 Surface texturing by microfabrication technologies **11**
2.3 RμEDM for micro protrusions fabrication **17**

2.3.1. Issues associated with fabricated micro protrusions 20
2.3.2. Quality enhancement of RμEDM fabricated micro protrusions 21

2.4 Fabrication methods of tool plate for RμEDM **24**
2.5 Heat transfer augmentation through arrayed micro protrusions **31**
2.6 Scope of the research **37**
2.7 Research objectives **38**
2.8 Methodology **39**

CHAPTER 3: FEASIBILITY STUDY OF RμEDM **43**
3.1 Introduction **43**
3.2 RμEDM: An Overview **43**

3.2.1. Material removal mechanism in RμEDM 45

3.3 Fabrication feasibility study of RμEDM **50**

3.3.1. Technology details and experimentation 51
3.3.2. Outcomes of the feasibility study 52
3.3.3. Issues and possible solutions associated with fabricated micro protrusions 55

3.4 Capability enhancement through parametric study of RµEDM 58

3.4.1. Experimentation 58
3.4.2. Experimental outcomes 61

3.4.2.1. Geometrical and surface characterization 61
3.4.2.2. Analysis of MRR 63
3.4.2.3. Micro protrusions taper root angle evaluation 65
3.4.2.4. Surface roughness measurement 67

3.5 Identification of optimal RµEDM process parameters 69
3.6 Chapter conclusion 72

CHAPTER 4: LBµM FOR FABRICATION OF RµEDM TOOL PLATE 74

4.1 Introduction 74
4.2 Fiber laser generation process 74

4.2.1. Mechanism of material removal in LBµM 75

4.3 Experimentation 75
4.4 Results and discussion 80

4.4.1. LBµM experiments 80
4.4.2. EDS analysis of tool plate 81
4.4.3. Recast layer and MRR estimation of micro holes 82
4.4.4. Taper measurement of micro holes 84
4.4.5. Avg. surface roughness measurement 85
4.4.6. Micro-hardness measurement of micro holes HAZ 85

4.5 Process parametric optimization study 86

4.5.1. Parametric optimization results 89

4.6 RµEDM using optimally fabricated tool plate 89

4.6.1. Optimal tool plate for arrayed protrusions fabrication 90

4.7 Chapter conclusion 94

CHAPTER 5: SUCTION-BASED DIELECTRIC FLUSHING IN RμEDM 96

5.1 Introduction 96
5.2 Issues of debris accumulation in RμEDM 96
5.3 Suction-based high-pressure dielectric flushing in RμEDM 98

5.3.1. Key aspects of the new flushing technology 99

5.4 Design consideration for new flushing technology 100

5.4.1. Development of numerical model 101

5.5 Experimental setup of new flushing technology 107

5.5.1. Working of the new flushing technology 109

5.6 Outcomes of the new flushing technology 112
5.7 Chapter conclusion 116

CHAPTER 6: NUMERICAL EVALUATION OF THERMAL PERFORMANCE……………………………………………………………..…….118

6.1 Introduction 118
6.2 Mathematical model for thermal performance optimization 118

6.2.1. Numerical modeling using PSO 118
6.2.2. Boundary conditions 120
6.2.3. Assumptions in the present study 120
6.2.4. Mathematical formulation of main PSO algorithm 121
6.2.5. Developed PSO mathematical model 125

6.3 Numerical simulation for thermal performance evaluation 127

6.3.1. Governing equations 128
6.3.2. Validation of the model 130

6.4 Thermal performance results 132
6.5 Chapter conclusion 137

CHAPTER 7: EXPERIMENTAL EVALUATION OF THERMAL PERFORMANCE………………………………………………………………...140

7.1 Introduction 140
7.2 Test rig design 140

7.2.1. Thermal Performance experimental design 144

7.2.2. Material selection 145

7.3 Thermal performance using the developed test rig 146
7.4 Thermal performance index 148
7.5 Experimental results and uncertainty analysis 150

7.5.1. Experimental results 150
7.5.2. Uncertainty analysis 151

7.6 Results and discussion 152

7.6.1. Thermal resistance evaluation 152
7.6.2. Average heat transfer coefficient 153
7.6.3. Average Nusselt number 154
7.6.4. Pressure drop 155
7.6.5. Thermal performance index 156

7.7 Validation study 157
7.8 Chapter conclusion 159

CHAPTER 8: CONCLUSIONS AND FUTURE SCOPE 161

8.1 Overview 161
8.2 Conclusions 162
8.3 Scope for future work 163

Appendix-A 166-173

REFERENCES 175-198

BIODATA 200-201

LIST OF FIGURES

Figure No.	Title	Page No.
1.1	Rectangular pin-fins heat sink installed on computer motherboard	**2**
1.2	(a) High aspect ratio micro rods fabricated by RμEDM showing the tool plate used (b) before, and (c) after RμEDM	**3**
1.3	Schematic of (a) conventional EDM-drilling, and (b) RμEDM	**5**
1.4	Schematic of Nd-YAG pulsed fiber LBμM setup	**5**
1.5	Schematic representation of the LBμM-RμEDM integrated technology for fabrication of arrayed micro protrusions	**6**
1.6	The problem structure with the research plan	**9**
2.1	(a) Number of papers published on tribological surface texturing since 1996 (b) contributions of different countries/regions, and (c) main application areas of these papers (Source: Web of Science topic search)	**12**
3.1	Schematic of RμEDM process for the fabrication of micro protrusion	**44**
3.2	SEM images of machined arrayed micro protrusions using RμEDM, (a) circular micro protrusions, (b) U-shaped micro protrsuion, and the corresponding tool plate (each hole fabricated by μEDM)	**45**
3.3	Material removal principle in μEDM (a) single discharge description and (b) discharge gap phenomenon	**46**
3.4	SEM images of typical crater geometries at different discharge energies in RμEDM	**47**
3.5	Real-time representation of single discharge circuit and RμEDM setup	**47**
3.6	Secondary and higher-order discharging phenomena during RμEDM	**48**
3.7	(a) Primary discharge and (b) second and higher order discharges in RμEDM	**49**
3.8	Heat source equivalent radius and crater radius	**49**
3.9	*Ra* measurement by depth of overlapping craters in (a) numerical model, and (b) SEM image of the machined surface	**50**
3.10	Illustration of (a) μEDM drilling, (b) RμEDM by reversing the polarity of (a), (c) pre-drilled tool plate for RμEDM and (d) LBμM used for pre-drilled tool plate	**51**
3.11	SEM images of actual fabricated (a) piranha, (b) aerofoil, (c) diamond and (d) droplet cross-sections of arrayed protrusions	**53**
3.12	3D ANSYS model of fabricated micro protrusions for MRR estimation	**54**
3.13	Burrs present at the tip of pre-drilled micro holes	**56**

3.14 SEM images of fabricated arrayed micro protrusions (a) elliptical, (b) aerofoil profiles, and (c) EDS plots **57**

3.15 Schematic of (a) µEDM drilling, (b) RµEDM by reversing the polarity of (a), (c) pre-drilled tool plate for RµEDM, and (d) LBµM used for fabrication of pre-drilled tool plate **59**

3.16 SEM pictograph of fabricated diamond cross-section micro protrusions at different discharge energy segments as lower, moderated, moderately high and higher **62**

3.17 Spectrum on diamond cross-section pre-drilled tool plate (enlarged view of surface in inset), and (b) elemental analysis of the pre-drilled tool plate surface **63**

3.18 MRR estimation (a) 3D solid model of workpiece electrode before machining, and (b) single diamond cross-section profile micro protrusion after machining **64**

3.19 (a) MRR at the different discharge energy segments, and (b) the plot of avg. MRR values vs avg. discharge energy (Avg. Q) **64**

3.20 Schematic of an ideal micro protrusion, and (b) actual micro protrusion having some taper root angle **66**

3.21 (a) (θ) variation of the fabricated micro protrusion at different discharge energy segments, and (b) the plot of avg. (θ) values vs avg. discharge energy (Avg. Q) **67**

3.22 (a) Ra of each fabricated micro protrusion at different discharge energy segments, and (b) Ra vs avg. discharge energy segments (Avg. Q) **68**

3.23 SEM images (a,b) and its corresponding and 3D surface profiles (c,d) on the machined surfaces at (i) V = 110 V, C = 10 nF, F = 10 µm/sec, and (ii) V = 120 V, C = 100 nF, F = 20 µm/sec **68**

3.24 Comparison of the fittest objective functions with the number of generations using an in-house developed GA algorithm **70**

4.1 Typical image of (a) LBµM setup, (b) ongoing LBµM for fabrication of micro holes, (c) trepanning scanning pattern, and (d) Gaussian beam profile distribution **77**

4.2 (i) Fabricated tool plate, illustration for estimating (ii) taper, (iii) Ra_T, (iv) and micro-hardness of tool plate **79**

4.3 Image of cut kerf of micro holes at different parametric combinations (indicated by corresponding duty cycle values) **81**

4.4 SEM images of holes' cut-section depicting striation marks at different duty cycles **81**

4.5 EDS plots on tool plate (i) base metal, (ii) cut edge of micro hole, and (b) enlarge view of the cut edge **82**

4.6 Variation of (a) recast layer heights (b) MRR_T with duty cycle **83**

4.7 Variation of taper with duty cycle **85**

4.8 Variation of (a) Ra_T, and (b) HAZ micro-hardness with duty cycle at the current percentage of 20% **85**

4.9 SEM image of single elliptical protrusion produced using micro hole (shown in the inset) **90**

4.10 Illustration for (i) MRR, (ii) TWR estimation, and (iii) location for Ra_P measurement **91**
4.11 SEM images of fabricated elliptical arrayed protrusions with (a) non-optimal and (b) optimal LBμM parametric combinations **92**
4.12 SEM images of fabricated droplet arrayed protrusions with (a) non-optimal and (b) optimal LBμM parametric combinations **93**
4.13 Energy spectrum on (a) tool plate after RμEDM, and (b) corresponding EDS plot **94**
5.1 Schematic illustration of the machining zone in RμEDM **96**
5.2 Illustration of debris accumulation in (a) μEDM and (b) RμEDM process at 3600fps **97**
5.3 Typical pictorial view of debris accumulation during RμEDM for the fabrication of arrayed protrusions **98**
5.4 A 2D schematic illustration of suction-based high-pressure dielectric flushing in RμEDM **98**
5.5 Brachistochrone curves for the shortest time path **100**
5.6 2D numerical model of the new suction funnel **101**
5.7 Debris particle trajectory at different time steps (a) injection from workpiece surface towards tool plate surface, (b) ejection of debris out of pre-drilled micro holes into fluid domain, (c) chain-linked cluster formation at the bottom end of tool plate, (d) cluster fragmentation of debris cluster due to applied pressure, (e) subsequent cluster formation and fragmentation due to intermittent debris ejection, and (f) debris outflow towards the suction funnel **107**
5.8 3D geometrical representation of the suction unit **108**
5.9 Fabricated suction cup/funnel using (a) 3D printing machine, and (b) different views of fabricated suction funnel **110**
5.10 (i) Overall suction flushing setup (a) machine setup, (b) RμEDM setup, (c) centrifugal pump with motor (d) suction cup/funnel, and (ii) measuring equipment used **111**
5.11 SEM images of fabricated micro protrusions under (i) normal, and (ii) suction flushing conditions **114**
6.1 Flowchart of a PSO algorithm **120**
6.2 Typical boundary conditions for the developed computational domain **121**
6.3 EGM convergence plots for (a) inline and (b) staggered arrangements of arrayed MPFs heat sinks **126**
6.4 (i) Arrayed MPFs heat sink arrangements (a) inline (b) staggered along with the geometrical representation of different MPFs profiles, and (ii) mesh model of the computational domain **127**
6.5 Representation of circular MPFs: (a) experimental test section, (b) similar CAD model **130**
6.6 (a) Temperature contours of the validation model, and (b) velocity vectors in staggered arrangement of circular MPFs **131**

6.7 Validation results of simulation and experimental runs (a) f, (b) Nu, and (c) ΔP through circular MPFs **132**

6.8 Nu as a function of Re in (a) inline and (b) staggered arrangement of different MPFs cross-sections **133**

6.9 (i) Temperature distribution (a,c) inline, and (b,d) staggered arrangement of different MPFs cross-sections at Re = 319 **134**

6.10 Flow pathlines (a,c) inline, and (b,d) staggered arrangement of different MPFs cross-sections at Re = 319 **135**

6.11 ΔP as a function of Re in (a) inline and (b) staggered arrangement of different cross-sections **136**

6.12 TPI as a function of Re for different MPFs cross-sections in a staggered arrangement **137**

7.1 In-house designed test rig used for experimental analysis **141**

7.2 Numerical model of the heating block **143**

7.3 Schematic illustration of the in-house developed test rig **144**

7.4 Schematic diagrams of MPFs heat sink: (a) staggered, (b) inline arrangements; (c) cross-sections of the three different MPFs heat sink; (i) droplet, (ii) piranha, and (iii) aerofoil **146**

7.5 (a) Pictorial view of thermal performance testing facility setup, and (b) closed view of in-house developed test rig **148**

7.6 Variation of R_{max} in (a) inline, (b) staggered arrangement of different MPFs heat sinks **153**

7.7 Variation of h_{avg} in (a) inline, (b) staggered arrangement of different MPFs heat sinks **154**

7.8 Variation of Nu in (a) inline, (b) staggered arrangement of different MPFs heat sinks **155**

7.9 Variation of ΔP in (a) inline, (b) staggered arrangement of different MPFs heat sinks **156**

7.10 Variation of TPI in (a) inline, (b) staggered arrangement of different MPFs heat sinks **157**

7.11 Comparative experimental and simulation results for ΔP and R_{max} with increasing Re **158**

7.12 Flow streamlines in arrayed Piranha MPFs: (a) inline (b) staggered arrangements (Re -766) **158**

7.13 Temperature distribution in arrayed Piranha MPFs: (a) inline (b) staggered arrangements (Re - 601) **159**

LIST OF TABLES

Table No.	Title	Page No.
2.1	Summary of literature on various aspects of surface texturing	**14-17**
2.2	Summary of literature on single/arrayed micro protrusion/s fabrication by the RμEDM	**19-20**
2.3	Summary of literature studies on the enhancement of process capabilities in μEDM and its variants	**23-24**
2.4	Summary of literature on different fabrication processes suitable for RμEDM tool plate	**29-31**
2.5	Summary of literature heat transfer augmentation through micro protrusions	**34-36**
2.6	Proposed strategies to improve the effectiveness of the RμEDM process	**37-38**
3.1	Comparison between conventional EDM and μEDM	**43**
3.2	Machining conditions	**52**
3.3	Factors and their levels	**59**
3.4	*L16* Orthogonal array experimental design and responses	**60**
3.5	Optimal process parameters and corresponding machining responses	**71**
3.6	Validation results of the predicted GA model and validation experimental run	**71**
4.1	Specifications of the CNC pulsed Nd: YAG laser setup	**76**
4.2	Factors and their levels	**78**
4.3	Experimental runs and the recorded LBμM responses	**78**
4.4	The normalized values of the recorded responses	**87**
4.5	Grey relation coefficient of the recorded responses	**87**
4.6	Grey relation grade and ranking of the recorded responses	**86**
4.7	Average grey relational grade at each level	**89**
4.8	Process conditions of RμEDM and LBμM and measured responses	**91**

5.1	Specification of the suction-based high-pressure flushing technology used in the present study	**112**
5.2	RμEDM and LBμM conditions for the fabrication of arrayed micro protrusions	**113**
6.1	Operating parameters	**125**
6.2	Optimal geometric design parameters of MPFs heat sinks	**127**
6.3	Boundary conditions	**129**
6.4	Detailed geometric dimensions of circular MPFs arrangement	**131**
7.1	Optimal geometric design parameters of MPFs	**140**
7.2	Test rig components materials and its properties	**145**
7.3	Thermal data of experimental runs for different MPFs heat sinks	**151**
7.4	Bulk temperature data of experimental runs for different MPFs heat sinks	**151**
7.5	Interval of confidence for other quantities	**152**

LIST OF ABBREVIATIONS

Abbreviations	Term
C	Capacitance
CAD	Computer Aided Design
CFD	Computational Fluid Dynamics
CNC	Computerized Numerical Control
DLP	Digital light processing
DPM	Discrete Phase Modeling
EDS	Energy Dispersive Spectroscopy
EGM	Entropy Generation Minimization
GA	Genetic Algorithm
GRA	Grey Relational Analysis
HAZ	Heat Affected Zone
Hv	Vicker Hardness
LBµM	Laser Beam Micromachining
LDW	Linear Decreasing Weight
MEMS	Micro Electro Mechanical Systems
MPFs	Micro Pin-fins
MOGA	Multi-objective Genetic algorithm
MRR	Material Removal Rate
Nd: YAG	Neodymium-Doped Yttrium Aluminum Garnet
PSO	Particle Swarm Optimization
Ra	Average surface roughness
RC	Resistance-Capacitance
RµEDM	Reverse-Micro-Electric-Discharge-Machining
RSM	Response surface methodology
SEM	Scanning Electron Microscopy
TPI	Thermal Performance Index
TWR	Tool Wear Rate
V	Gap Voltage
WC	Tungsten carbide
µEDM	Micro-Electric-Discharge-Machining
µECM	Micro-Electrochemical Machining

NOTATIONS

English symbols	Description
A_f	Cross-sectional area of the protrusions in an array
$A_{frontal\ face}$	Frontal surface of workpiece
A_p	Cross-sectional area of a single micro protrusion
a_1, a_2, a_3	Constants for Re
C_D	Drag coefficient
C_f	Frictional coefficient factor
C_p	Specific heat capacity of the fluid
C_1	Perceptional (cognitive) parameter
C_2	Social parameter
D_D	Diagonal distance between two MPFs
d_h	Hydraulic diameter of MPFs heat sink
D_L	Longitudinal distance between two MPFs
D_T	Transverse distance between two MPFs
d_p	Diameter of debris particle
D_1	Axial length at the tip
D_2	Axial length at the root of micro protrusion
d	Distance of nozzle from tool plate
E_{pulse}	Energy of each laser pulse
F_D	Drag force
f	Pulse frequency
f_1, f_2, f_3	Functions in GA
G	Mass flux
$\overrightarrow{g}$	Gravity force
H	Height of MPF
h_{avg}	Average heat transfer coefficient
h_{bp}	Heat transfer coefficient of base plate
h_{fin}	Heat transfer coefficient of fins
i	Experimental run
k	Thermal conductivity of MPFs
L	Taper visible height
L_b	Longitudinal length of base plate
L_f	Characteristic length of MPF
L_i	Current velocity limit of particle
l_i	Initial velocity limit of particle
M^2	Beam propagation ratio
MRR_P	Material removal rate of protrusions

MRR_T	Material removal rate of tool plate
$\dot{m}$	Mass flow rate of debris particles
m	Fin parameter
N	Total number of MPFs in an array
Nu	Nusselt number
Nu_o	Nusselt number without MPF
n	Number of micro protrusions in an array
P	Perimeter of MPF
P_{avg}	Average laser power
p_c	Crossover probability
P_{in}	Pressure at inlet
P_{out}	Pressure at outlet
p_m	Mutation probability
ΔP	Pressure drop
ΔP_o	Pressure drop without MPF
Q	Maximum stored energy in the capacitor
Q_{flow}	Flow rate of the working fluid
$Q_{heat\ flux}$	Effective heat flux at the base of heat sink
$q_{conduction}$	Heat loss by conduction
$q_{convective}$	Heat loss by convection
$q_{electrical}$	Total input power
$q_{radiation}$	Heat loss by radiation
Ra_T	Average surface roughness of micro holes side-wall surface
Ra_P	Average surface roughness of protrusions surface
R_c	Contact resistance
Re	Reynolds number
R_{fins}	Overall resistance of MPFs heat sink
R_{hs}	Heat sink thermal resistance
R_m	Bulk heat sinks material resistance
R_{max}	Maximum thermal resistance
T	Time taken in the fabrication of a complete array of protrusions
T_{amb}	Ambient temperature
T_{base}	Base temperature
t_{bp}	Thickness of base plate
T_h	Heater temperature
T_p	Pulse width
$\vec{u}$	Dielectric fluid velocity
U_{app}	Approach velocity of fluid
$\overrightarrow{u_p}$	Velocity of the debris particle
V	Volume of the workpiece undergoing RμEDM
V_R	Volume of the material removed
v	Volume of one fin

W	Width of base plate
w	Weight factor
α	Impingement angle of dielectric
Γ_ϕ	Diffusion coefficient
γ_i	Grey relation grade
η_f	Fin efficiency
θ	Taper root angle
Λ	Pumping power
μ	Fluid dynamic viscosity
$\xi i(k)]$	Grey relation coefficient
ρ	Fluid density
ϕ	Dependent variable
ϕ & S_ϕ	Source term

Chapter 1

Introduction

1.1. Background and Motivation

Over the last two decades, innovations in microfabrication technologies have satisfied the demands for compact micro-electro-mechanical systems (MEMS) devices and miniaturized components. Advanced and non-traditional microfabrication technologies have the capability to fabricate components of metallic, nonmetallic, and advanced materials with complicated intrinsic micro-features. Arrayed microstructures such as micro-holes and micro protrusions of size ~ 35-100 μm and aspect ratios ~ 20-100 have shown an increasing demand for industrial products [1],[2]. A few of those products include hydro-pneumatic valves, micro-optical products, dozers for drugs, automobile nozzle heads, diesel fuel injectors, printer heads, and micro-heat exchangers.

The targeted application of arrayed micro protrusions is mostly explored in the form of micro pin-fins (MPFs) heat exchangers, as active cooling technologies, for the thermal management of high-performance microelectronics and MEMS devices. However, augmenting heat transfer efficiency is extremely important for such systems, which may require the dissipation of ultra-high heat fluxes exceeding 1 kW/cm^2 [3]. A decrease in size and increase in power consumption in high-performance micro devices inevitably results in overheating and associated thermal stresses, which need to be dissipated effectively. Although, with advancements in high-performance devices in engineering and device packaging, the cost and reliability have improved. But thermal management has received less attention, leaving scope for future research. The heat dissipation capabilities of existing cooling techniques are being undertaken in the following areas [4]:

- Increased card or module total heat dissipation (heat power levels higher than 100 W)
- Increased local heat densities for highly integrated components (heat fluxes; 10 W/cm^2)
- Maximum use of low-cost plastic components even in severe applications.

The dissipation of the heat for a given heat density and the material, remains a primary concern that could either be attempted by 'air or liquid flow through' as active cooling or 'airflow around' as a passive or conventional method. Considering the space constraint in miniature devices, single-phase passive cooling using MPFs heat sinks could be applied for more effective thermal management of the MEMS devices. The idea is generated from the proven capabilities of such MPFs in passive heat management for up to 300 W/cm^2 of heat flux. Arrayed MPFs based thermal management exhibits a high surface-to-volume ratio, dense structure, and superior heat transfer coefficient. Figure 1.1 shows a pictorial view of arrayed pin-fins mounted over a motherboard used to cool high-power transistors, microprocessors etc.

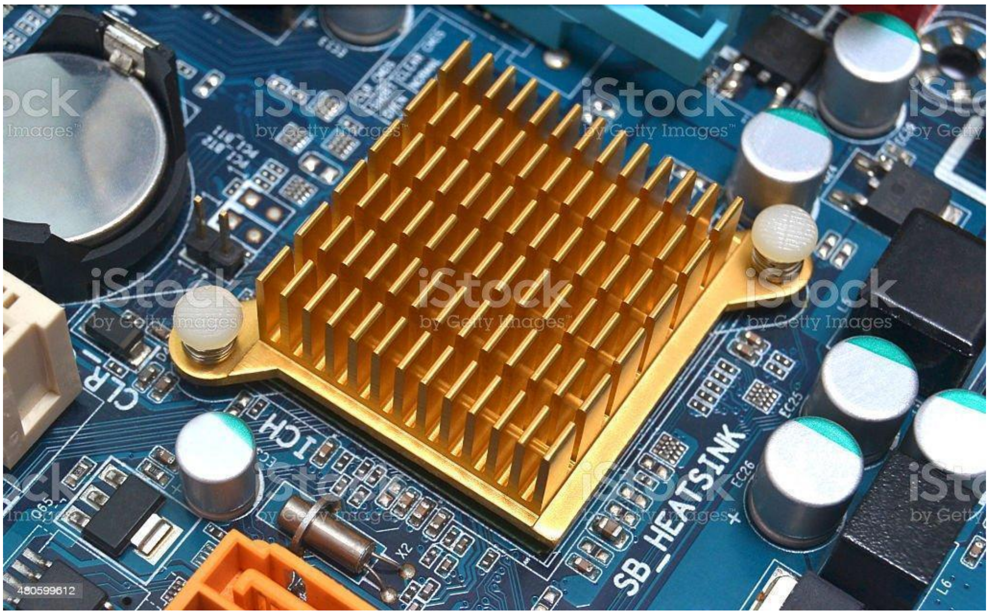

Fig. 1.1 Rectangular pin-fins heat sink installed on computer motherboard [5].

These arrayed protrusions (as MPFs) are very specific to their fabrication technologies including precisely controlled conventional and non-conventional processes. However, batch fabrication of high quality arrayed micro protrusions is the need of different microfabrication industries. Various existing technologies have proven their capabilities for fabricating arrayed protrusions, but their process limitations for precision manufacturing are not addressed well. The process capabilities of existing technologies are still under exploration for low-cost and high-quality fabrication.

Micro-electric-discharge-machining (µEDM) is one such microfabrication technique that has shown tremendous application in machining conductive materials, irrespective of the material's mechanical properties, with excellent precision and dimensional accuracy. The μEDM process has various process variants depending upon the tool-work configuration, axial motion control, and basic electrical setup changes to ensure 2D and 3D products with a wide range aspect ratios and array sizes. Among them, 'Reverse micro-electro-discharge machining' (RμEDM) has shown its excellent capability in the fabrication of high aspect ratio arrayed micro protrusions (or micro-rods) on the surface of metallic materials [6]. Figure 1.2 shows the RμEDM fabricated high aspect ratio micro-rods.

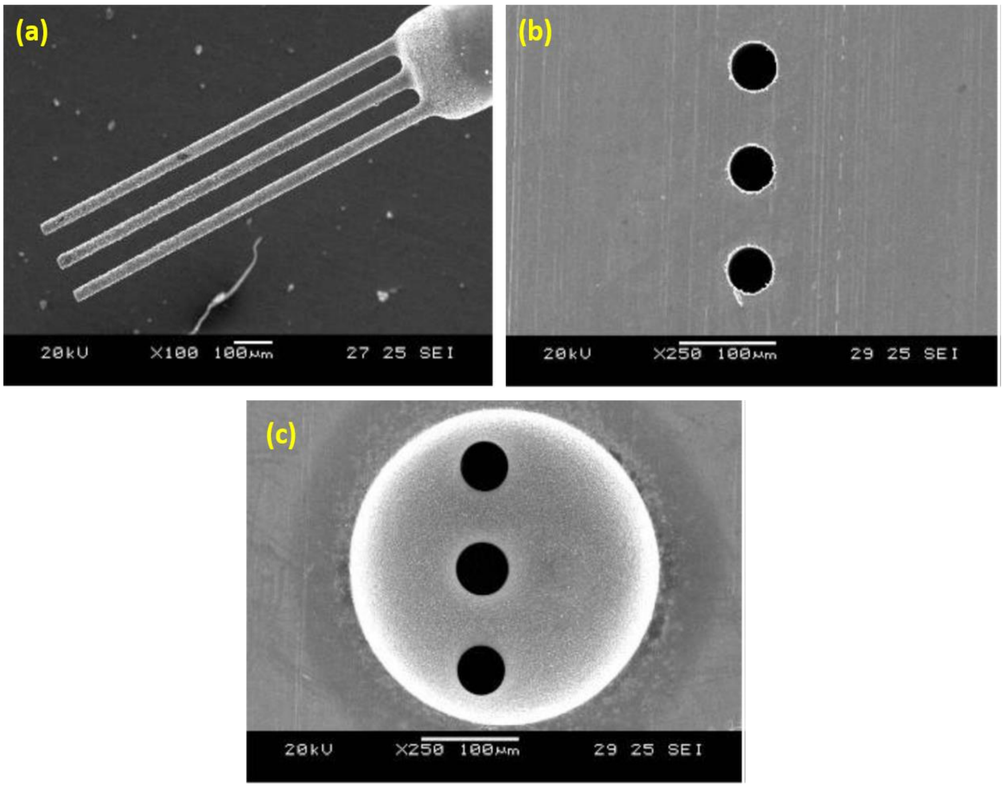
(a)
20kU X100 100μm 27 25 SEI
(b)
20kU X250 100μm 29 25 SEI
(c)
20kU X250 100μm 29 25 SEI

Fig. 1.2 (a) High aspect ratio micro rods fabricated by RμEDM showing the tool plate used (b) before, and (c) after RμEDM [6].

Arrayed micro protrusions as heat exchangers, could be more beneficial if fabricated in different cross-sectional profiles, aspect ratios, and arrangements (in-line or staggered). It may lead to a better life span of the mounting components under high heat flux, if the cross-sectional profiles MPFs are chosen other than the regular ones (e.g., rectangular, square, or circular). Some of the unconventional cross-sectional profiles of the MPFs could be aerofoil, droplet, hydroformed, Piranha, and diamond shapes. In this connection, the numerical modeling and thermal simulation have proven an enhanced heat transfer through those unconventional MPFs. Although thermal scientists have proven the heat dissipation capabilities using non-conventional arrayed MPFs from hot spots, there is still a need for the fabrication and testing of physical MPFs in a real environment. With this motivation, the thesis introduces the research problem as mentioned in section 1.2.

1.2. Introduction to the Research Problem

The importance of the aforementioned cross-sectional profiles of MPFs for active/passive heat dissipation in the heating components has motivated the thesis works to aim at experimental and numerical investigation. Broadly, it includes successful attempts for their fabrication feasibility over different materials, process parameters optimization for faster and quality fabrication, and optimal geometrical cross-sectional design consideration. With a prime focus on producing arrayed protrusions with unconventional cross-sectional profiles, thermal performance evaluations of optimized arrayed micro protrusions (in the form of MPFs) are also kept under the scope. It is achieved by setting up testing facilities using an in-house developed test rig followed by validation in terms of thermal performance index (*TPI*).

As the micro protrusions features mentioned in section 1.1 are very specific to their fabrication technologies, RμEDM is explored here for the fabrication of MPFs in the cross-sectional profiles similar to the ones available with the micro holes of RμEDM tool plate. Figure 1.3(b) shows a schematical representation of the RμEDM process derived from the conventional EDM-drilling shown in Figure 1.3(a). A detail on the working principle of RμEDM is presented separately in chapter 3. Despite several advantages, RμEDM has not achieved widespread acceptance in fabricating arrayed micro protrusions due to the issues like requirement of a tool plate with desired profiles of arrayed micro holes, and a low material removal rate.

The former of the two issues mentioned is more crucial as the profile and the array shape and size of the pre-drilled tool plate replicates arrayed micro protrusions fabricated by RμEDM. Sequential drilling to make arrayed through holes in the tool plate has never been easy using mechanical or EDM drilling as they are time-consuming, and restricted to only circular holes. It is attempted by exploring laser beam micromachining (LBμM) as a feasible solution for the rapid fabrication of pre-drilled micro holes in the desired complex cross-section profiles in the tool plates on a wide range of materials. Figure 1.4 shows the schematic of the LBμM setup used in the fabrication of the tool plate for RμEDM.

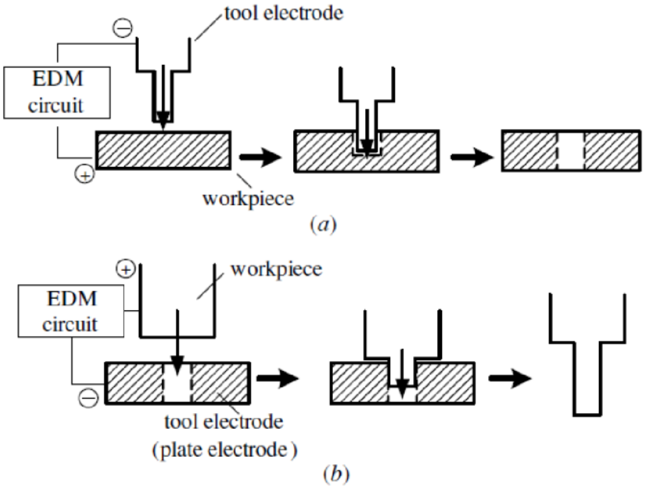
tool electrode
EDM circuit
workpiece
(a)
workpiece
EDM circuit
tool electrode
(plate electrode)
(b)

Fig. 1.3 Schematic of (a) conventional EDM-drilling, and (b) RμEDM [6].

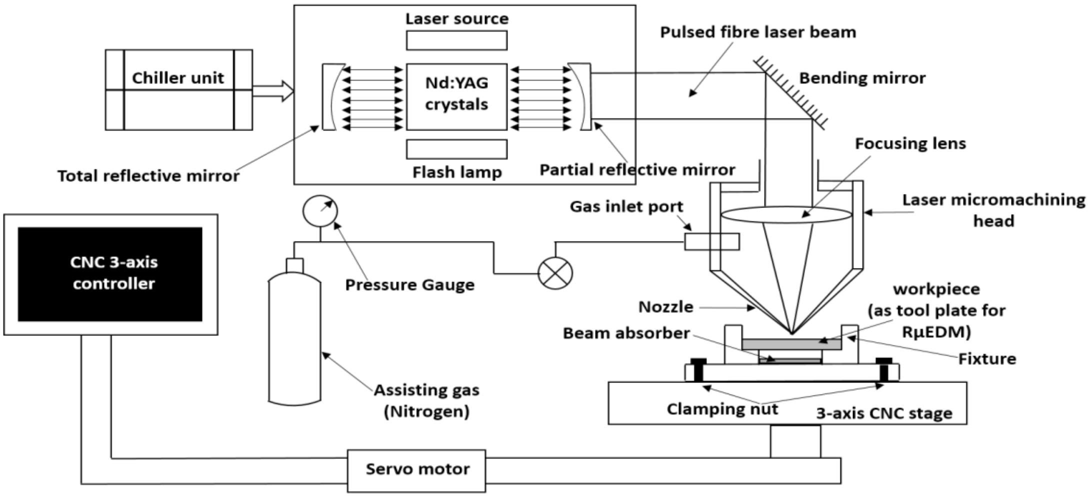
Laser source
Chiller unit
Nd:YAG crystals
Flash lamp
Total reflective mirror
Partial reflective mirror
Pulsed fibre laser beam
Bending mirror
Focusing lens
Laser micromachining head
Gas inlet port
CNC 3-axis controller
Pressure Gauge
Nozzle
Beam absorber
workpiece (as tool plate for RμEDM)
Fixture
Assisting gas (Nitrogen)
Clamping nut
3-axis CNC stage
Servo motor

Fig. 1.4 Schematic of pulsed fiber LBμM setup.

While the use of LBμM enables the fabrication of precise micro holes, improperly selected process parameters may result in low tolerance and distorted walls of the micro holes. These damaged walls may lead to distorted edges of micro protrusions if used as a tool plate for RμEDM in their present form. Therefore, to make these processes fully acceptable for the fabrication of tool plates for RμEDM, multi-objective optimization for LBμM for accurate and precise fabrication of micro holes is performed, which details are discussed in chapter 4. The RμEDM, assisted by LBμM for the fabrication of the desired tool plate, is named LBμM-RμEDM integrated technology for the intended purpose. The integrated technology is represented schematically in Figure 1.5.

Accumulation of debris near the spark zone in any μEDM process is an inherent issue which sometimes becomes critical if not properly dispelled from the discharge gap as it exhibits arcing and short-circuiting. The situation becomes severe during RμEDM of arrayed micro protrusions where the tool-work interface used to be huge as compared to a single protrusion. Tiny debris in the dielectric pool near the machining zone alters the discharge profiles, affecting the machining process destructively. Therefore, a robust technology is required to be designed to effectively remove the debris.

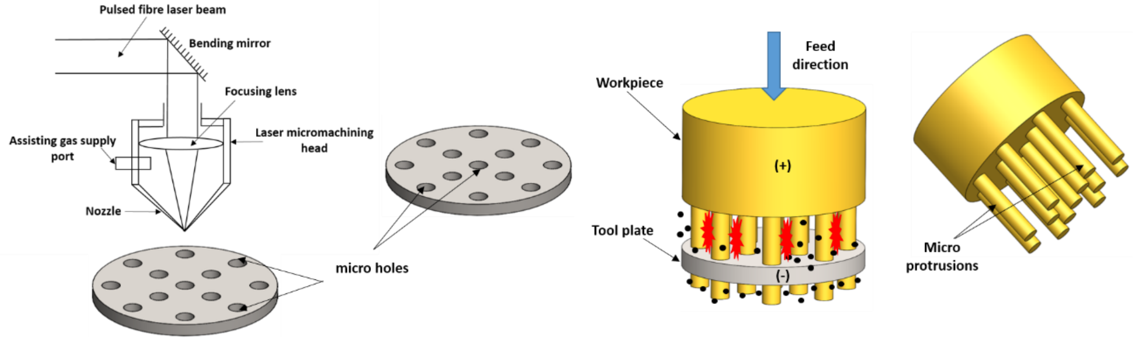

(a) Machining of arrayed micro holes on a thin metal plate by LBμM

(b) The fabricated plate to be used as tool plate in RμEDM

(c) Fabrication of micro protrusions using tool plate by RμEDM

(d) Fabricated micro protrusions

Fig. 1.5 Schematic representation of the LBμM-RμEDM integrated technology for fabrication of arrayed micro protrusions.

In this way, the second issue mentioned above is tackled. In this direction, a new in-house developed suction-based high-pressure dielectric flushing technology is integrated with the existing RμEDM setup for effectively and continuously removing debris from the machining gap and ensuring a high material removal rate (MRR). The detailed study of the functioning and development of flushing technology has been discussed in chapter 5. The developed flushing setup is incorporated into the LBμM-RμEDM integrated technology for the fabrication of arrayed micro protrusions in multiple unconventional cross-sections at the optimized LBμM and RμEDM parameters. The arrayed micro protrusions are tested as MPF heat sinks for which thermal performance is evaluated by setting up an in-house developed testing facility.

1.3. Organization of the thesis/dissertation

The overall Ph.D. work has been presented in the form of chapters as follows:

Chapter 1 of the thesis describes the need for non-conventional micromachining, its recent trends, introduction to μEDM technology and its prominent variant, RμEDM, and assessment of fabricated micro products by RμEDM. Another popular technology, i.e., LBμM used for precision microfabrication, is elaborated by exploring its potential for integration with other similar technologies in the fabrication of micro products (arrayed protrusions). The chapter summarizes the need for proposing the integrated microfabrication technology for the fabrication of micro arrayed protrusions in the thermal management of microelectronics in detail with their respective importance.

Chapter 2 presents literature reviews and explains the previous research works done in the context of micro rod fabrication using micro-milling, μEDM and its variants, Laser micromachining, and a combination of any two of them. The chapter also reviews recent development in RμEDM, starting from the history of the fabrication of single/arrayed micro rods for various engineering applications. It explains the challenges and limitations of poor machining efficiency and tool plate fabrication. Further, the chapter also explains the advent of notable works performed on the existing debris flushing techniques in the μEDM setup. The chapter then presents a comprehensive review of the current research trend pertaining to the thermal management of microelectronics or MEMS devices with the commonly used active cooling technique, i.e., MPFs heat exchangers.

Chapter 3 demonstrates a detailed study of the process capability of RμEDM as a potential microfabrication technology used for the fabrication of arrayed protrusions. It includes a study on the fabrication feasibility, analysis of machining responses at different parametric settings, issues encountered in fabrication and its pertaining solutions, etc. It also describes understanding the material removal mechanism in RμEDM by performing a single discharge analysis followed by average roughness evaluation. An optimization study to find the optimal parametric combination for fabricating arrayed micro protrusions is also performed using a multi-objective optimization tool. Moreover, the capability of RμEDM in the fabrication of useful microstructures used in the biomedical field has been explored and presented through initial experimentation.

Chapter 4 investigates the LBμM process parameters effect on the tool plates fabrication for RμEDM. This chapter presents a systematic study of the various process parameters and their effects on the surface qualities of the fabricated micro holes of different cross-section profiles. A multi-objective optimization approach is used for the selection of optimal process parametric combination and recommended appropriate machining environment. Later on, this chapter shows the applicability of optimal process parameters for the fabrication of pre-drilled arrayed micro holes, subsequently, the arrayed micro protrusions, followed by validation experimentation.

Chapter 5 explains the approach to enhance the process stability by introducing a new suction-based high-pressure flushing technology in RμEDM. A detailed procedure has been presented used in the development of an in-house fabrication of this technology. This chapter enumerates the effect of the integration of the new flushing methodology on improving machining responses. Moreover, a simulation study has been presented to analyze the debris flow in this setup. A feasibility study by fabricating arrayed micro protrusions has been presented as a benchmark solution.

Chapter 6 presents dimensional optimization, thermal modeling, and simulation of different unconventional cross-section of MPFs in different arrangements (in-line and staggered). Multi-objective particle swarm optimization (PSO) code is developed for numerical modeling. The optimal geometrical design consideration is taken for thermal simulation using ANSYS® for a comparative analysis of thermal performances under heat loading conditions and laminar flow regimes.

Chapter 7 demonstrates the fabrication of optimal arrayed protrusions as MPFs in different cross-section profiles by implementing optimal machining parameters and assisted facility. A detailed demonstration has been presented to develop an in-house testing facility for analyzing the thermal performances of fabricated MPFs heat sinks. A highly sensitive test-rig fabrication and testing procedure have been discussed in a simplified manner. Here a comparative experimental study has been conducted to analyze the overall thermal performance viz. thermal performance index.

Chapter 8 summarizes the conclusion of the preceding chapters starting from the fabrication feasibility and process stability enhancement methodology in RμEDM. It is followed by optimal geometrical design consideration of arrayed MPFs heat sinks, viz. modeling, simulation, testing with the datasets used, and future scope of the work. In the discussion part, it is presented how well the objectives are completed with success. It gives an insight into the further expansion of the study in the future, and a major takeaway for future researchers is also presented. Finally, a list of relevant references is presented.

1.4. Research Plan

This thesis is organized into eight chapters which can be understood by the below flow chart diagram:

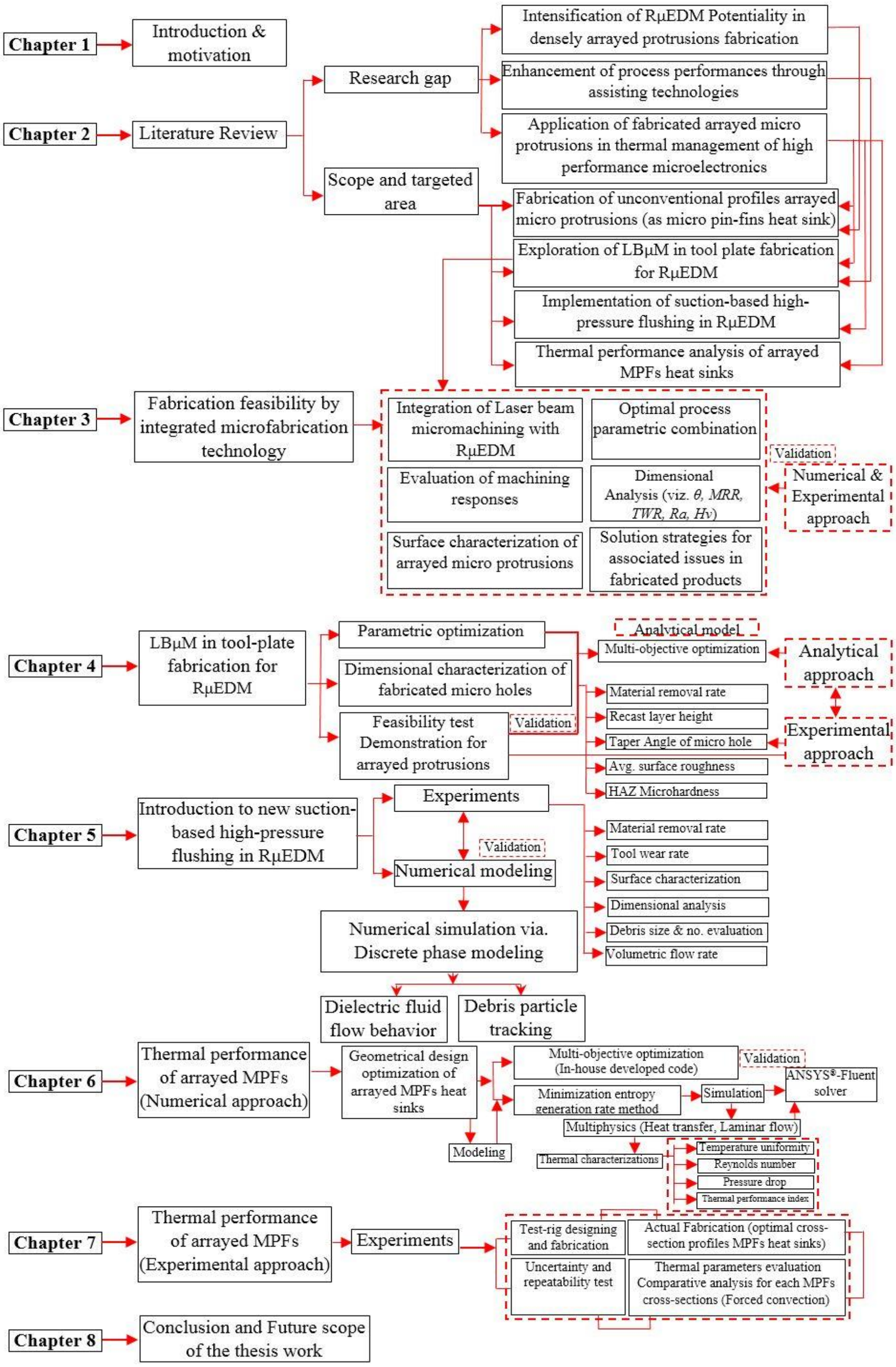
Chapter 1
Introduction & motivation
Chapter 2
Literature Review
Research gap
Scope and targeted area
Intensification of RμEDM Potentiality in densely arrayed protrusions fabrication
Enhancement of process performances through assisting technologies
Application of fabricated arrayed micro protrusions in thermal management of high performance microelectronics
Fabrication of unconventional profiles arrayed micro protrusions (as micro pin-fins heat sink)
Exploration of LBμM in tool plate fabrication for RμEDM
Implementation of suction-based high-pressure flushing in RμEDM
Thermal performance analysis of arrayed MPFs heat sinks
Chapter 3
Fabrication feasibility by integrated microfabrication technology
Integration of Laser beam micromachining with RμEDM
Optimal process parametric combination
Evaluation of machining responses
Dimensional Analysis (viz. θ, MRR, TWR, Ra, Hv)
Surface characterization of arrayed micro protrusions
Solution strategies for associated issues in fabricated products
Validation
Numerical & Experimental approach
Chapter 4
LBμM in tool-plate fabrication for RμEDM
Parametric optimization
Dimensional characterization of fabricated micro holes
Feasibility test Demonstration for arrayed protrusions
Validation
Analytical model
Multi-objective optimization
Material removal rate
Recast layer height
Taper Angle of micro hole
Avg. surface roughness
HAZ Microhardness
Analytical approach
Experimental approach
Chapter 5
Introduction to new suction-based high-pressure flushing in RμEDM
Experiments
Validation
Numerical modeling
Material removal rate
Tool wear rate
Surface characterization
Dimensional analysis
Debris size & no. evaluation
Volumetric flow rate
Numerical simulation via. Discrete phase modeling
Dielectric fluid flow behavior
Debris particle tracking
Chapter 6
Thermal performance of arrayed MPFs (Numerical approach)
Geometrical design optimization of arrayed MPFs heat sinks
Modeling
Multi-objective optimization (In-house developed code)
Validation
Minimization entropy generation rate method
Simulation
ANSYS®-Fluent solver
Multiphysics (Heat transfer, Laminar flow)
Thermal characterizations
Temperature uniformity
Reynolds number
Pressure drop
Thermal performance index
Chapter 7
Thermal performance of arrayed MPFs (Experimental approach)
Experiments
Test-rig designing and fabrication
Actual Fabrication (optimal cross-section profiles MPFs heat sinks)
Uncertainty and repeatability test
Thermal parameters evaluation Comparative analysis for each MPFs cross-sections (Forced convection)
Chapter 8
Conclusion and Future scope of the thesis work

Fig. 1.6 The problem structure with the research plan.

Chapter 2

Literature Review

2.1. Introduction

This chapter covers the various research activities carried out by researchers working in surface textures fabrication in various research fields. A critical state-of-the-art in the recent development in the RμEDM process, starting from the history of the fabrication of arrayed surface textures as single/arrayed micro protrusions for various engineering applications, has been presented. Moreover, it elaborates on previous studies about the challenges and limitations of getting augmented process stabilities. Further, the chapter also explains the advent of notable works performed on the debris flushing methodologies along with surface features generated by μEDM and its variants. A comprehensive study on the current research trend pertaining to the thermal management of high-performance microelectronics or MEMS devices with the commonly used active cooling technique, i.e., arrayed micro protrusions (as MPFs heat exchangers), is critically reviewed. Based on the extensive literature survey, research gap has been identified. It is followed by the scope of this research work along with the objectives and research plan to execute the objectives, which are also presented.

2.2. Surface texturing by microfabrication technologies

Surfaces with nano and micro-scale textures are widely used to augment engineered components' tribological properties. Applicable fields include tribology, avionics, automotive and semiconductor industries, microfluidics, surface wettability, mechanical tooling, biomedical, thermal management of high-performing devices etc. [7],[8]. Moreover, the effect of shape and geometrical accuracy of micro components has a key role in enhancing surface properties required for the specific application.

Almost 99% of the research on the generation of surface textures has been performed in the last two decades, which is driven by the significant modeling results as surveyed by Etsion’s group. The study said that the research on tribological aspects is still capturing attention. Figure 2.1(a) depicts the volume of research done on surface texturing since

1996, and Figure 2.1(b) presents the topmost countries involved in doing research in various sectors shown in Figure 2.1(c) [9].

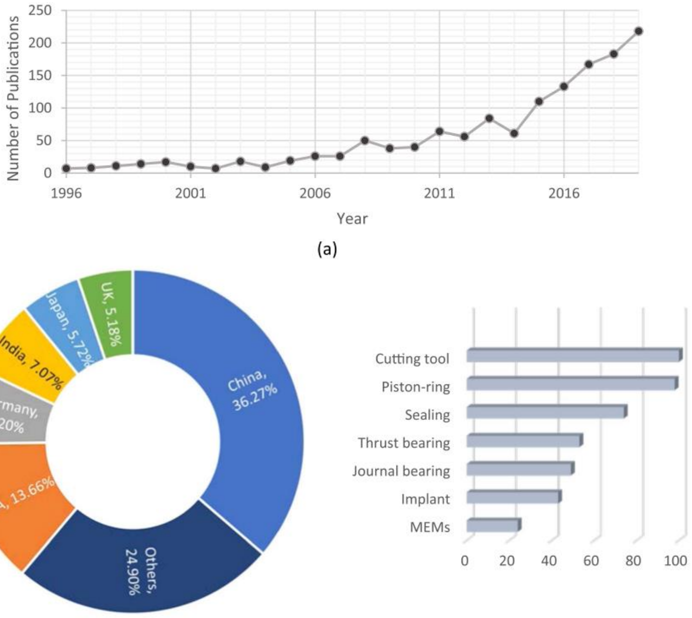

(a)

(b)

(c)

Fig. 2.1 (a) Number of papers published on tribological surface texturing since 1996 (b) contributions of different countries/regions, and (c) main application areas of these papers (Source: Web of Science topic search) [9].

In automotive as a specific example, the lubrication requirement at the contact surfaces of engines causes severe scuffing, eventually leading to seizure and failure. To counter these shortcomings, surface texturing at the piston ring-cylinder interfaces is still now an alternative to prevent failure [10]. Imran et al. [11] did a comparative study on the different geometrical shape micro features to reduce the frictional force of which triangular-shaped features produce the lowest value. An experimental study by Segu et al., showed the improvement in reducing frictional performance by engraving multi-dimple textured patterns, viz. circles and triangles, and circles on laser textured steel surfaces compared to untextured surfaces [12]. Zhang et al., [8] proposed an analytical model for predicting the coefficient of friction on a textured tool using Reynolds equations and an elastic FEM model. A drastic reduction in friction coefficient has been observed due to the surface's textured patterns, thereby improving machinability.

The studies above focus on 2.5D micro textures on the substrate surface. Even 3D micro textures in form of arrayed micro protrusions found wide applications in various fields of surface engineering viz. energy conversion devices, solar cells, tribological, micro lenslet arrays, heat transfer applications etc. Yuan et al., [13] presented state-of-the-art fabrication methodologies of arrayed micro lenses used in the next generation of 3D imaging systems. The review work discussed the challenges and opportunities of a manufacturing micro lens array in industries and academic research. Hejazi et al., [14] developed two classical models of Wenzel and Cassie–Baxter to predict the roughness factor and wettability of the rough surfaces with multiscale structures at the interface. An experimental study is also performed to investigate the second-order effects on the wettability of such surfaces.

Surface interaction with the fluid depends on the size, geometrical shape, and frequency of different cross-section protrusions and depressions. Microchannels with triangular cross-section micro protrusions (as micro pin-fins) are resulted in enhanced heat transfer coefficient at high fluid flow velocities compared to circular and square cross-sections protrusions or microchannels without protrusions [15]. Shape effects of micro protrusions on the PDMS surface affect the interaction of fluid flowing on the surface. A comparative study on the contact angle has been studied using theoretical and experimental approaches considering different protrusions cross-sections viz. rectangular, circular, triangular, and cross-shaped [16]. A monotonic increase in apparent contact angle has been found to increase with a decreasing surface area at the top of protrusions. Yadav et al. [17] showed the enhanced thermal performance of hemispherical protrusions in rectangular ducts compared to smooth ducts during the turbulent flow of air through them. Li et al. [18] found higher light absorbance by 90% due to the fabricated micro/nano low aspect ratio protrusions on ultrathin GaAs solar cells. Markal et al., [19] performed a comparative flow boiling analysis using three different heat sinks (i) straight parallel channels, (ii) uniformly distributed micro pin-fins, and (iii) decreasing the number of MPFs in the flow direction. Heat transfer coefficient of gradually decreasing MPFs increases up to nearly 501% compared to straight parallel and 365% to uniformly distribute micro pin-fins heat sinks. Therefore, surface texturing design is highly intended for the functionality requirements of specific applications for future industrial design and development [20].

Typically, micro/nano surface texturing is broadly classified into two types: negative textures, cavities on the surface (individual or arrayed dimples, spots or narrow channels), and positive textures protruding from the surface (individual protrusions or arrayed protrusions, asperities). Both negative and positive textures can be fabricated by several conventional and non-conventional micromanufacturing processes. For negative textures (dimples, micro slots etc.), micro-drilling [21–23], µEDM [24–29], µECM [30–32], LBµM [33–35], etc. Whereas for positive textures (arrayed protrusions or pillars etc.) LIGA [36], [37], photolithography [38–40], chemical deposition, layer-by-layer deposition, sol-gel method, etc. are promising technologies. Each microfabrication process has its advantages and disadvantages over others and is limited to different application fields. Of all the processes, µEDM and its variants with assisting facilities, viz. high-frequency vibration, coated tools, and improved flushing, has been widely used for fabricating negative and positive high aspect ratio 2.5D and 3D textured surfaces on metallic material [41], [42]. A summary of the literature discussed above is presented in Table 2.1:

Table 2.1. Summary of literature on various aspects of surface texturing.

Authors	**Context of the study**	**Key findings**
Becker *et al.* [36]	LIGA for fabricating microstructures	Produced PMMA plates for high aspect ratios microstructures and heights of several hundred µm with minimum dimensional deviations of less than 0.1 µm.
Etsion, *et al.* [9]	Mechanical sealants with generated microstructures	Developed a mathematical model to allow performance prediction of all-liquid non-contacting mechanical seals with regular micro-surface structures in the form of hemispherical pores.
Egashira *et al.* [23]	Micro holes in a few tens of microns ranges	Tested the monocrystalline silicon sheet using a µEDG produced cutting tool of 0.5 µm cutting radius with the aim of fabricating 3D and high aspect ratio micro shapes of minimum 6.7 µm diameter using micro-drilling.
Aguilar *et al.* [35]	Femto-second pulsed laser for producing thin films of biodegradable polymers	Demonstrated that both UV and femto-second lasers are excellent tools for micro-patterning biodegradable polymers keeping intact the bulk properties of the base material.
Jahan *et al.* [28]	Pulse generators in µEDM	Investigated the influence of major operating parameters on the performance of µEDM of WC with a focus on obtaining quality micro holes in both transistor and RC-type generators.
Yu *et al.* [42]	Vibration-assisted EDM for pre-drilled	Presented a new method of drilling high aspect ratio micro holes by EDM due to planetary movement of tool electrode assisted with

	holes fabrication	ultrasonic vibration for producing micro holes with an aspect ratio of 29.
Jo *et al.* [31]	µECM for microstructures	Investigated the application of microelectrochemical machining for the micromachining of internal features.
Yeo *et al.* [16]	Substrate hydrophobicity	Designed, fabricate and characterize robust hydrophobic surfaces with four different shapes (rectangle, circle, triangle and cross) of a micropillar array using photolithography.
Byun *et al.* [30]	Micro dimples using µECM	A friction test on the textured specimen is performed and compared with a non-textured specimen.
Qin *et al.,* [39]	Soft lithography for different industrial applications	Provided an introduction to soft lithography-a collection of techniques based on printing, molding, and embossing with an elastomeric stamp.
Wang *et al.* [15]	Photolithography	Fabricated Microchannel embedded with different cross-sections micro protrusions Experimented the range 100 <= Re <= 5600.
Segu *et al.* [12]	Laser surface texturing for multi-dimples on steel surfaces	Investigated the effect of multi-dimple steel surfaces on tribological properties under non-conforming contact.
Li *et al.* [18]	Textured surfaces for solar-based applications	Introduced low aspect ratio nano/micro-hemisphere surface texturing for improving light management in ultrathin GaAs solar cells.
Yadav *et al.* [17]	Textured surface with protrusions for an enhanced heat transfer rate	Studied the effect of heat transfer and friction characteristics of turbulent flow of air passing through circular protrusions arranged in an angular arc fashion.
Hejazi *et al.* [14]	Wettability on patterned surfaces	Measured water contact angles on pairs of metallic surfaces with nominally the same Wenzel roughness obtained by abrasion and by chemical etching.
Yadav *et al.* [25]	Hybrid micromachining technology for machining aerospace material	Attempted to use altogether a new hybrid machining process for making the holes in nickel-based superalloy aerospace material and termed it an electro-discharge diamond drilling process.
Zhang *et al.* [8]	Tribological behaviour of textured surface	Developed an analytical numerical model specific for understanding the tribological behavior of textured surfaces in a mixed lubrication regime.
Imran *et al.* [11]	Digital maskless lithography and bio-machining	Presented the development of a digital maskless lithography process and its capabilities for square-shaped micro feature fabrication using DLP projector.

Singh *et al.* [26]	Patterned holes fabrication using vibration-assisted µEDM	Developed a new ultrasonic-assisted µEDM setup and fitted it to an already available EDM machine.
Correa *et al.,* [33]	Femto-second laser machining for optical and photonics devices	Presented a survey of results on polymer fs-laser processing, resulting in 3D waveguides, electroluminescent structures, and active hybrid-microstructures for luminescence or biological microenvironments.
Romoli *et al.* [7]	Nano-second pulsed laser ablation on the adhesive strength	Studied the influence of surface laser texturing on the adhesive strength of bonded joints in aluminium alloys.
Umer *et al.* [34]	Nd: YAG laser micro-milling of Alumina ceramic	Considered the analysis and multi-response optimization of machining parameters during Nd: YAG laser micro-milling of Alumina ceramic using MOGA-II.
Rühe J. [40]	Topographic patterns by maskless photolithography technologies	Discussed the prospects of maskless photolithography technologies with a focus on two-photon lithography and scanning-probe-based photochemical processes based on scanning near-field optical microscopy or beam pen lithography
Yuan *et al.* [13]	Arrayed microlens for 3D imaging systems	Reviewed the fabrication of microlens array and its application.
Kim *et al.* [10]	Hatch pattern in automobile cylinder lining by plateau honing	Developed a plateau honing technology on the cylinder liners of large ship engines and automotive engines.
Arumugaprabu *et al.* [20]	Cutting tool life enhancement for machining applications	Presented a detailed review about the need for surface texturing in materials, its importance, and its role in tool life enhancement had been discussed and reported.
Kumar *et al.* [24]	µEDM-drilling on carbon fiber reinforced polymer matrix composites	Analyzed the variance using Taguchi design of experiments, and an optimized set of parameters has been reported for maximum material removal rate and minimum tool wear rate.
Roy *et al.* [42]	RµEDM for various industrial applications	Generated numerical model and experimentally investigated the variation in surface roughness on the 3D hemispherical convex micro-feature by incorporating a multi-physics simulation approach.

Liu *et al.* [32]	μECM for hollow electrodes	Studied the effect of electrolyte pressure through hollow electrodes on shape accuracy by both numerical simulations and experimental tests.
Markal *et al.* [19]	Different heat sinks configuration	Experimentally investigated the effect of gradually expanding flow passages on saturated flow boiling characteristics of MPFs heat sinks.

2.3. RμEDM for micro protrusions fabrication

RμEDM is one of the promising variants of μEDM used for producing medium to high aspect ratio positive microstructures as single/arrayed protrusions [43]. In this process, a thin metallic sheet with single/multiple pre-drilled holes acts as the cathode. Whereas the anode is in the form of a solid metallic rod that is traversed toward the tool plate. The material removal occurs mostly from the anode due to frequent electrical discharges between the anode and cathode, adhering to the shape of cathode features in the form of single/arrayed protrusions. The aspect ratio of fabricated micro protrusions depends on the traverse length of the anode through the cathode.

Using the RμEDM process, Yamazaki et al. [44] fabricated a single metallic protrusion to fabricate micro holes and micro slits on the foil electrode. These fabricated micro holes and slits have been used further to fabricate micro protrusion with a minimum diameter of 4 μm. This study tailored the advantages of RμEDM over conventional micromachining, including the use of micro holes as a tool, micro protrusions can be fabricated without chucking, and the positioning of the tool for complicated shapes generation. Furthermore, Kim et al. [6] fabricated arrayed micro protrusions with diameters of 35 μm and 1.5 mm in length using RμEDM. Using fabricated protrusions, arrayed micro holes are fabricated with an average diameter of 45 μm. Apart from the RμEDM capability, the effect of machining parameters viz. V and C on the process stability have been studied well. Yi et al. [45] successfully fabricated 3×3 and 4×4 arrays of Cu micro protrusions using a 100 μm thick AISI 304 stainless steel tool plate. The holes on the tool plate have been fabricated by μEDM-drilling with a single electrode having 80×80 μm square cross-section. These arrayed micro protrusions are further used to fabricate 6×6 and 16×16 micro cavity patterns on metal foils (for applications in organic thin-film transistors) by batch mode μEDM-drilling. It has also been revealed that by using batch mode μEDM-drilling, the productivity was improved to four times that of single micro protrusion. Further improvement in RμEDM has been presented by Zeng et al. [46], who added ultrasonic vibration to the RμEDM tool plate.

The outcomes of the applied ultrasonic are analyzed through theoretical and experimental observation. They reported that RμEDM when performed with and without ultrasonic vibration, single discharging energy decreases by half, discharge frequency improves by four times, and machining efficiency increases by two times with better surface quality. An array of 3×3 micro protrusions (diameter less than 30 μm and height-to-width aspect ratio are more than 10) are fabricated, and subsequently, micro holes using these protrusions. This work is further carried out by incorporating four machining parameters, including V, C, ultrasonic amplitude, and inter holes spacing in RμEDM. It has been observed that the machining efficiency reduces with increasing V, and C in an already developed ultrasonic vibration-assisted RμEDM process [47]. Later on, Hwang et al., [48] utilized the capability of RμEDM in the fabrication of arrayed micro protrusions in an array of 40×40. The diameter of the single protrusion is 30 μm, length of 625 μm with an inter-electrode gap of 100 μm is achieved. The aforesaid work is about removing material from the bulk to fabricate micro protrusions. Using another way, Peng et al. [49] fabricated complex micro protrusions of high aspect ratio by clubbing RμEDM and μEDM deposition processes. This selective material removal occurs by sequentially depositing or removing metal material using an identical machining system.

In the recent past, Mujumdar et al. [50] fabricated a high aspect ratio micro protrusion of 60 μm in diameter and a high aspect ratio of 33 using the RμEDM process. The fabricated protrusions at different parametric combinations such as V, C, threshold, and feed rate, are critically analyzed for dimensional accuracy, pin cylindricity, and surface roughness. The gap voltage is found as the single most important factor governing the responses mentioned above of the fabricated micro protrusions. A well-established Taguchi-based RμEDM parametric analysis on the fabrication of micro protrusion of diameter 80 μm and 200 μm and length 1.5 mm on bulk WC rod are carried out by Mastud et al. [51]. This work relied on the effective machining rate due to the reduced thickness of the tool plate in RμEDM and concluded that the tool plate with lower thickness provides better workpiece frontal surface erosion and surface finish of the fabricated micro protrusions. A reduced tool plate thickness from 500 μm to 300 μm showed an improvement in the surface finish by 20% and 11% at the tip of 80 μm and 200 μm protrusion, respectively. In another work, Mastud et al. [52] have also shown the assistive beneficiary of the vibration-assisted RμEDM process in fabricating textured surfaces that exhibit hydrophobicity and hemocompatibility. Arrayed micro protrusions, each with 40-50 μm diameter and inter-electrode-gap of 35 μm on bulk Ti6Al4V micro rod have been fabricated [53] which have shown potential applications in cardiovascular biomedical implants and mimic hierarchical structures generic on lotus leaves. Other systematic application-based studies of arrayed micro protrusions on surface engraving [54], intra-cortically recording of brain activity [55], different electrode materials [56], and neural applications [57] have been performed. A detailed summary of the literature discussed above is presented in Table 2.2:

Table 2.2. Summary of literature on single/arrayed micro protrusion/s fabrication by the RμEDM.

Authors	**Key findings**
Yamazaki *et al.* [44]	Developed a new method of machining electrodes using pre-machined holes.
Kim *et al.* [6]	Micro electrodes of various shapes are fabricated and different machining characteristics are investigated by varying capacitances and applied gap voltages.
Zeng *et al.* [47]	Reverse copying μEDM enhanced with ultrasonic vibration on the plane of the tool electrode is explored as a method for generating a micro electrode array.
Yi *et al.* [45]	An array of 6 × 6 and 16 × 16 micro electrodes are fabricated. Negative electrodes with multiple micro holes (3 × 3 or 4 × 4) are fabricated using a single tool electrode.
Peng *et al.* [49]	Fabricated a micro square column with side length of 0.070 mm, height of 0.750 mm, and a micro cylinder with 0.140 mm in diameter, and height of 1.180 mm.
Mujumdar *et al.* [50]	Their study focuses on fabrication of micro rod arrays of diameter 60 μm and a higher aspect ratio of 33.
Hwang *et al.* [48]	A combined method of mechanical peck-drilling and RμEDM is proposed to fabricate circular cross-section micro protrusions array with high hardness and high density, quickly and efficiently.
Mastud *et al.* [51]	Utilizes the advantages of the lower thickness of tool plate for the fabrication of micro rods, and found notably difference in machining responses by reducing the plate thickness from 500 μm to 300 μm.
Jahan *et al.* [58]	They investigated the feasibility of *in-situ* machining of 2 × 2 micro-punch arrays of varied-shaped microelectrodes diameter of 50 μm.
Mastud *et al.* [53]	Studied the nature of discharge pulse duration responsible for the material erosion during the fabrication of arrayed features on difficult-to-erode materials.

Singh *et al.* [59]	Micro electrodes of diameter 170 µm with a high aspect ratio of 18 has been successfully fabricated for several applications in ink jet nozzles, air bearings, and biomedical devices.
Nirala *et al.* [60]	Discussed a new approach of tool wear compensation based on 'volume removal per discharge' (VRD) for the faster fabrication of single or arrayed micro electrodes.
Roy *et al.* [42]	Attempted numerical and experimental study to understand the process mechanism for fabrication of high aspect ratio single or multiple 2.5D features with different cross-sections like square, circular, triangular etc.
Singh *et al.* [61]	Using the optimal parametric setting of feed rate of 5 µm/s, C of 1000 pF and V of 120 V, an array of 4 × 4, i.e., 16 micro-rods with 58 µm diameter and 830 µm length, has been fabricated on the bulk tungsten rod of 800 µm diameter.
Roy *et al.* [62]	Performed numerically and experimentally to calculate the mechanical properties of the parent material, HAZ and the recast layer on a hemispherical protruded micro protrusion.
Zhang *et al.* [63]	Fabricated tungsten tool electrode used to machine micro hole (<100 µm diameter) array of 3 × 3, 5 × 5 and 10 × 10 using ultrasonic vibration on debris evacuation from the machining gap.
Shah *et al.* [64]	Studied the effect of the discharge gap condition at various performance characteristics while fabricating micro protrusions on an emerging Ti-6Al-7Nb bio-material.

2.3.1. Issues associated with fabricated micro protrusions

Longer normal discharging and higher material removal in RµEDM show process immensity compared to µEDM [2]. The RµEDM capability is profoundly affected at high machining depths due to debris accumulation in the machining gap that leads to abnormal discharging. However, the workpiece electrode rotation is not possible in RµEDM while producing arrayed micro protrusions, causing debris accumulation in the machining gap, resulting in the generation of arcing and short-circuiting. The consequences lie in reduced machining efficiency, including high surface roughness [50], taper formation [65], debris adhesion [48] etc. The removed material in the form of debris plays a significant role in controlling dielectric breakdown strength, discharge transitivity, and inter-electrode gap during discharging [48], [66]. Debris plays a key role in defining the machining output in terms of shape, size, and surface finish of the fabricated micro protrusions. Mastud et al., [52] showed that numerous debris clusters have formed at the machining gap due to the influence of the electric field, it acts as a low resistance path for subsequent discharges in RµEDM. Hence, it resulted in short bridge formation where the debris clusters get bonded to either of the electrodes. On the other hand, the ejected debris promotes arcing between the electrodes leading to barreling at the side walls of the pre-drilled micro holes.

Sometimes the debris sticking to the hole surface becomes beneficial to achieve a smooth surface finish on the fabricated components. Hence, it is clear that flushing debris and controlling debris sticking on machined protrusions is of prime importance in augmenting the process stability and achieving better-machined surfaces [67].

Several effective flushing strategies, such as jet flushing [68], internal flushing [69], and spray flushing [70], vacuum-assisted debris removal system [71], magnetic force [72] rotary workpiece [73], and geometrically modified electrodes proposed earlier, are limited to only conventional straight polarity EDM processes. Additionally, the effect of electrode jump height on the effective removal of the debris and dielectric flow in deep hole EDM-drilling has shown its competency in dispelling debris from the machining gap [63]. A similar conclusion has been drawn with the appropriate electrode jump height and speed, which evacuates much debris from the discharge gap [74].

It is evidenced that the machining gap in RμEDM is of the order of 5-10 μm where the removal of debris clusters formation is difficult for progressive machining. To flush the debris from the machining gap, ultrasonic vibration to the workpiece is supposed to be the most effective methodology for driving out the debris in RμEDM [75] [76]. Mastud et al. [52] performed numerical modeling of the debris motion and its interaction with the dielectric fluid under low-amplitude vibrations generated via a magnetostrictive actuator. The effects of varying ultrasonic frequency and amplitude on the electrode vibration on the motion of debris have been quantified, the higher of which potentially reduces the debris accumulation at the discharge gap. The debris accumulation can also be reduced significantly by adequate dielectric flushing at the machining gap [77], [78], [79]. In this regard, Hwang et al. [48] introduced new dielectric flushing techniques to enhance the machining efficiency. Makenzi et al., [80] reviewed various flushing technologies used in EDM. The influence of flushing as a sole requirement in enhancing machining efficiency and stability is also discussed well.

2.3.2. Quality enhancement of RμEDM fabricated micro protrusions

Determination of the extent of surface finish is essential, especially in RμEDM fabricated arrayed micro protrusions. In RμEDM, primary discharges constitute material removal, and the degree of high-order discharges increases with increasing depth of arrayed protrusions. Higher-order discharges result in uneven material removal at random places, leading to poor surface roughness, particularly in localized areas where severe debris accumulation is [75]. Kiran and Joshi [67] developed a surface roughness model in µEDM by considering pure dielectric mixed with debris. The developed model indicates that the dielectric consideration in surface roughness prediction shows better results than those without dielectric conditions. Salonitis et al., [81] developed a thermal surface roughness model by incorporating various input parameters of die-sinking EDM. Multiple overlapping craters in the model are considered for predicting the average surface roughness of the machined surface. Furthermore, an electro-thermal model is developed based on the crater geometry of the µEDM process to predict surface roughness. In this model, the effects of overlapping of craters, pockmarks, micro cracks, and reattachment of debris have been considered for the same [82]. Tong et al. [83] showed that the accumulated cluster debris at the tip of the protrusions could be removed by oil dielectric during machining. Abbasi et al. [84] utilized regression analysis to predict the surface roughness of HSLA steel machined by wire-EDM. The study's outcomes showed that the interaction of process parameters (pulse-on time, pulse ratio, power, wire speed, and discharge gap) is accountable for analyzing the surface roughness from individual machining parameters. The effect of discharge energy on surface roughness in EDM has been investigated using different tool electrode diameters [85]. The discharge energy has shown detrimental effects on the surface roughness of the machined surface in addition to the effect of present debris. In the recent past, Roy et al., [42] developed a numerical model using a multi-physics simulation approach for predicting the surface roughness of 3D hemispherical convex micro features fabricated by RµEDM. A validation experiment with a maximum error of 13% in surface roughness value is reported compared to simulation results. In another study, the same authors have determined the extent of the formed recast layer, heat affected zone (HAZ), and mechanical properties viz. hardness, elastic modulus, and residual stress of the fabricated 3D hemispherical protrusion by RµEDM. The results showed that HAZ has higher hardness and elastic modulus than the parent metal. Moreover, the hard recast layer generated on the machined surface has shown compressive residual stresses, while the soft layer has tensile residual stresses [62].

The amount of ejected debris also depends on the selected machining parameters and the aspect ratio of the fabricated micro protrusions. A group of researchers tried to understand the mechanics of RµEDM technology and also did a parametric study on the quality of fabricated micro protrusions [48], [49], [50]. Singh et al. [86] have performed RµEDM to fabricate micro protrusions with an average diameter of 182 µm using a copper sheet as a tool plate from a bulk tungsten rod diameter of 800 µm. For these fabrications, feed rate, C, and V are taken as input parameters, whereas machining responses such as machining time, erosion rate, and dimensional variation have been analyzed for different process parametric combinations. It has been revealed that the RµEDM process can be operated at higher C and V levels without any significant increase in arcing. RµEDM yields a higher material erosion rate for identical machining conditions than µEDM-drilling.

In another work by the same research group, the process mechanism has been understood by detailed experimental investigation using Taguchi's orthogonal array design of experiments. To find the optimal parametric combination, machining time, deviation in length, deviation in average diameter, standard deviation (SD) in diameter, and surface roughness of the fabricated micro protrusion have been quantified. As a result, the normal discharge duration, which is responsible for the material erosion, is increased, and fabrication of arrayed features on difficult-to-erode materials and the creation of arrayed micro protrusions over the large frontal surface area of workpiece became feasible [59]. Talla et al. [87] have used reverse polarity EDM to fabricate arrayed micro protrusions on mild steel. Response surface methodology (RSM) is used for designing the experimental run to select optimal parametric conditions. A confirmatory test has been performed using grey relational analysis (GRA). Using an optimal parametric combination, micro protrusions and micro cavities in an array of 3×3 are fabricated using RµEDM and followed by WEDG for trimming protrusions end. A detailed summary of the literature discussed above is presented in Table 2.3:

Table 2.3. Summary of literature studies on the enhancement of process capabilities in µEDM and its variants.

Authors	**Key findings**
Takahata *et al.* [88]	Investigated the variation of hole diameter along a 20 × 20 hole array due to debris accumulation resulting in higher-order discharges. Proposed ultrasonic vibration effect provided to the tool electrode.
Yu *et al.* [89]	Utilized planetary movement and ultrasonic vibration in µEDM-drilling for fabricating micro holes with an aspect ratio of 29.
Cetin *et al.* [74]	Utilized the CFD approach for understanding the wall concavity phenomenon of the holes due to the dielectric fluid flow and the debris distribution in the machining gap.
Kunieda *et al.* [90]	Elaborated discharge gap phenomena and accumulation of conductive debris, affect the insulation strength of the discharge gap.

Hung *et al.* [91]	Performed machining by combining ultrasonic vibration with a helical micro tool electrode fabricated by WEDG to drill and finish micro holes.
Yu *et al.* [92]	Proposed a new approach to reduce the debris concentration and improve precision using the planetary movement of the electrode.
Ferraris *et al.* [93]	Presented an innovative method for the µEDM of ultra-high aspect ratio (AR > 30) micro holes. An insulated tool electrode is used for machining to promote the process stability of µEDM deep hole drilling.
Wang *et al.* [94]	Proposed a 3D flow field modeling from a machining gap to investigate the debris and bubble movement in EDM and found that the bubble is the main cause of expelling the debris.
Mastud *et al.* [52]	Implemented a vibration-assisted mechanism to analyze the effect of electrode vibration on debris movement during micro electrode fabrication by RµEDM process.
Pattabhiraman *et al.* [70]	Investigated debris flushing of EDM during the Spray-EDM process and found that the dielectric film plays an important role in the evacuation of debris from the machining gap.
Tanjilul *et al.* [71]	Presented an instantaneous flushing strategy using vacuum-assisted flushing. A numerical model is developed to track the debris flow behavior in the machining gap.
Shabgard *et al.* [76]	Analyzed the machining gap directly using high-speed camera and found that tool vibration caused the increase in discharge dispersion, periodic discharge, and discharge frequency.
Kliuev *et al.* [95]	Conducted CFD simulations to study the variation in pressure drop and dielectric flow pattern during µEDM by employing the tool electrode's single-channel and multi-channel configurations.
Kumar *et al.* [96]	Analyzed the process performance of µEDM-drilling using featured electrodes with inclined through holes (pathways) that eliminate the need for flushing and act as a self-flushing electrode.
Feng *et al.* [97]	Developed a model to investigate the effects of variable tool electrode rotational speed in debris evacuation during side nozzle flushing.
Li *et al.* [78]	Studied gradual deteriorating inter-electrode environment in µEDM from tool wear, bubbles, and debris.
Shah *et al.* [53]	Attempted to enhance the RµEDM process stability under different vibrations and no vibration conditions and analyzed real-time debris evacuation using high-speed camera and image processing technique while machining Ti-6Al-7Nb, an emerging bio- material.

2.4. Fabrication methods of tool plate for RµEDM

Although RµEDM has found potential application areas in the recent past, the process's full potential depends upon the quality of the fabricated micro holes in the tool plate. The poor fabricated tool plate hindered the quality of fabricated protrusions due to uneven tool plate wear. This wear of the tool plate leads to the following issues: (i) restriction on the fabrication of micro protrusions having high aspect ratio and (ii) impossible to achieve dimensionally accurate micro protrusions. To understand the tool plate fabrication for the RμEDM process, researchers have used several existing fabrication methodologies intended for such purposes. Takahata et al. [88] fabricated 20×20 arrayed copper micro protrusions of diameter 20 μm and length 300 μm using LIGA technology. Further, the μEDM process successfully fabricated the arrayed micro holes on a 50 μm thick stainless steel sheet. Amorim et al. [2] used tool electrodes of copper plate in μEDM because it possesses desirable properties like relatively low wear rate and ease to machine, which is essential for process stability [99]. Later on, Amit et al., [61] fabricated micro pre-drilled holes of diameter 212 μm in circular cross-sections on a thin copper plate of thickness 293 μm. The block electrical discharging grinding process is used to fabricate a single protrusion of aspect ratio 62, which is further used to fabricate multiple micro holes in the tool plate [59]. Li et al., [100] have used a novel active supplying wire electric discharge grinding device for high quality and large aspect ratio micro protrusion, which is used further to fabricate arrayed micro holes (2×128) on a 50 μm tool plate of stainless steel for inkjet nozzles of industrial printers. Zilong et al., [101] strategically used μEDM-drilling and μEDM-milling for the fabrication of micro holes with 80 μm in diameter of brass and steel sheets. Masaki et al., [102] proposed a repeated transcript μEDM method for fabricating arrayed holes. Using this methodology, more than one micro hole could be fabricated simultaneously, and subsequently, the arrayed micro protrusions of complex shape geometry.

The machining parameters of μEDM utilized in the fabrication of micro holes have an important impact on the geometrical accuracies such as diameter, overcut, and taper rate. D'Urso et al., [103] reflected that the peak current is an important parameter affecting the taper rate of the fabricated micro hole because increasing current value eventually results in rapid tool wear and produces larger taper at the tip front of the micro hole. Siva et al., [104] found that second-order discharges result in a larger overcut in the micro hole due to higher gap voltage. This research has been carried out further by D'Urso et al., [105] conducted experiments by the combined effect of machining parameters and electrode size on different machining responses such as overcut and taper rate of micro hole. It has been found that the tool electrode diameter is reduced significantly less due to the influence of machining parameters during micro hole fabrication. Besides, Jahan et al., [28] marked that an RC-type pulse generator is one such suitable μEDM circuit type for machining micro holes where the geometrical accuracy and surface finish are of prime importance due to its capability of supplying very small discharge energy.

Furthermore, Natarajan et al., [106] found that the accuracy of the fabricated micro hole is worsened due to adhered re-solidified debris at higher discharge energy.

For fabricating arrayed micro holes, it would be crucial to ensure the machining quality and geometrical accuracy of every micro hole, ultimately, it will determine the consistency of the replication of micro hole geometry into arrayed protrusions fabrication. From the perspective of conventional and non-conventional micro-drilling processes, harvesting the fabrication of arrayed micro holes is tedious due to lower efficiency in one processing cycle. Additionally, the fabrication of micro holes through this process is time-consuming and complex concerning tooling cost [107]. Thus, the machining efficiency would not be fruitful if the required amount of micro holes in the tool plate is considered. On the other hand, in RμEDM, the workpiece rotation is not allowed during the fabrication of arrayed protrusions. As a result, the debris becomes difficult to be expelled from the narrow machining gap. Thus, the machining stability and consistency accuracy of pre-drilled arrayed micro holes are difficult to be assured. Therefore, the technology used for the fabrication of micro holes in the tool plate is significantly important for the good quality of the micro holes.

One such promising technology, i.e., LBμM has shown its competency in micro holes fabrication due to its ability and flexibility in fabricating accurate size micro cavities. It can fabricate micro cavities on a wide range of materials, such as ceramics [108],[109], polymers [110],[111], and metals [112–115]. The non-contact nature of operation in LBμM avoids the need for special tooling, jigs, and fixtures for workpiece holding. Also, there is minimal material waste in LBμM. The intense laser beam directly vaporizes the molten metal because of highly localized heat input, allowing sufficient time for a thermal wave to propagate into the material [116]. The molten material is then partially ejected from the micro cavity due to the vapor and plasma pressure. But still, a portion of it remains near the micro cavity wall surface in the form of burrs and recast layer resulting in dimensional inaccuracy and poor surface quality of fabricated micro cavities [117],[118]. In general, the material removal in LBμM is affected by the laser beam characteristics and the way the laser beam and workpiece material interact. Several works on the hole quality as a function of laser characteristics and machining parameters have been studied to improve knowledge in such fabrication [119], [120]. Whitehead et al [119] observed in laser ablation that the reflectivity decreases with increasing pulses in nano-second laser. Moreover, the laser beam's polarization during micro-drilling affects the morphology and shape of the fabricated micro holes.

Banks et al., [120] defined the *s, p* polarization effect on the roughness of holes due to deep craters formation. Nolte et al., [123] further examined that the trepanning polarization in LBμM has significantly improved micro holes' circularity. About the main machining parameters, the wavelength [121], [122], laser power [123], and pulse duration [124-127] affect the machining characteristics but cannot be significantly modified without changing the laser type. Bandhopadhyay et al., [128] performed detailed experimentation on IN718 and Ti-6Al-4V alloy using Nd: YAG laser source. Focal position, pulsating energy, and pulse duration are the most significant parameters that influence the quality of the holes. Particularly, the lower values gave the best outcomes regarding the taper of the drilled micro holes.

Tunna *et al.* [129] analyzed the effect of varying wavelengths (355, 532, and 1064 nm) along with the laser intensity (0.5–57.9 GWm^{-2}) in nano-second pulsed LBμM over the copper foil. It has been observed that the wavelength of 1064 nm gave the minimum etching rate due to the higher reflectivity of copper. Yilbas [130], in similar research work, compared the quality of fabricated micro holes of titanium, nickel, and stainless steel. Out of these three materials, titanium showed the poorest geometrical results due to the low thermal conductivity and density that reduces the amount of heat loss by conduction creating hindrance in the ejection of melted material from the cut kerf. Biffi et al., [131] showed preliminary experimental results on drilling micro holes in titanium sheets using a high-quality fiber laser beam in the nano-second regime. It has been observed that a large amount of spatter and melted material at the entrance and exit of the micro holes are present, which cannot be avoided.

Pulse duration is another crucial process parameter affecting precision in machined micro holes' batch production [40]. Leitz *et al.* [133] conducted a detailed comparative study of pulse durations in micro, nano, pico, and femto-second LBμM. This work was followed by Liu *et al.* [134], who reported that ultra-short laser pulses result in comparatively better precision in micromachining to minimize the deviation in the dimensional accuracy of fabricated holes. It has been reported that pico and femto-second lasers offer sound surface quality compared to micro and nano-second lasers in such fabrication [135]. However, the *MRR* in micro and nano-second lasers is found to be higher than that of femto-second and pico-second lasers, enabling a higher machining rate.

The extensive application of lightweight yet desired-strength materials in various fields has attracted researchers to investigate their machinability [136]. Cicala *et al.* [137] used an Nd: YAG pulsed laser to machine aluminum alloy, stainless steel, and titanium materials to investigate the effects of laser intensity, frequency, scanning speed, and line spacing on the *MRR* and surface roughness. They revealed that the variation in *MRR* and surface roughness depends mainly on the laser pulse frequency and scanning speeds. Demir *et al.* [138] investigated the effect of laser micromachining and its processing conditions on TiN coatings in the nano-second pulsed regime. A pulse range between 12 ns and 200 ns was taken as one of the process variables to study laser irradiation's influence on coated workpieces.

It has been seen that randomly selected parameters would not be feasible for fabricating good quality micro holes by LBµM [139]. Dubey et al., [140] utilized a hybrid experimentation approach of Taguchi and central composite designs to find the effects of gas pressure, pulse width, pulse frequency, and cutting speed on *MRR* and kerf width of the fabricated hole. It has been found that pulse width and cutting speed are the most significant factors affecting both responses, respectively. Later, Dhupal et al. [141] performed LBµM experiments using three approaches, including RSM-ANN-GA, to find the optimal parametric combination. The lamp current, gas pressure, pulse width, pulse frequency, and cutting speed are optimized for the micro grooving of Al_2O_3 and show the dominance of the ANN-GA approach compared to RSM-GA.

Another study by Rao et al., [142] used Taguchi orthogonal array design approach to find the effect of gas pressure, pulse width, pulse frequency, and cutting speed on kerf dimensional accuracy in LBµM of Inconel 718. The GRA is associated with experimental data to obtain optimal processing parameters for fabricating straight and curved grooves. Sharma et al., [143] proposed Taguchi and RSM approach to analyze the performance measures during the machining of Al alloy and reported the optimal selection of assisting gas pressure in minimum deviation of taper while piercing a micro hole using Nd: YAG LBµM. A detailed summary of the literature discussed above is presented in Table 2.4:

Table 2.4. Summary of literature on different fabrication processes suitable for RμEDM tool plate.

Authors	**Microfabrication technology used**	**Key findings**
Banks *et al.* [120]	Ultra-short Laser-drilling	Showed the capability of ultra-short laser-drilling pulses for producing micro holes of excellent quality depending upon fluence, the number of shots, and polarization.
Masaki *et al.* [102]	μEDM	Proposed a repeated transcript μEDM method for fabricating arrayed holes of more than one micro hole in complex shape geometry.
Hallgren *et al.* [144]	LBμM	They investigated complex cross-section implant fabrication by LBμM.
Wiele *et al.* [107]	Ultraviolet femto-second pulse laser	Demonstrated ultraviolet femto-second pulse laser ablation on versatile sub-micron structures on various materials at 100 nm.
Bandhopadhyay *et al.* [128]	Nd: YAG Laser-drilling	Analyzed parametric effect of pulsed Nd: YAG laser on 4 mm thick IN718 and Ti-6A-l4V samples.
Heinemann *et al.* [136]	Micro-drilling	Investigated the performance of small diameter HSS twist drills in drilling micro holes ten times deeper into carbon steel AISI 1045.
Amorim *et al.* [98]	EDM	Experimentally investigated EDM of AISI P20 tool steel using graphite and copper as tool electrodes in the fabrication of holes.
Rahman *et al.* [145]	μEDM & μturning	They used hybrid technology clubbing μEDM and μturning to fabricate micro components (micro rods for drilling purposes) with high precision.
Dubey *et al.* [140]	LBμM	Presented a hybrid Taguchi method and response surface method (RSM) for the multi-response optimization of process parameters for evaluating micro holes quality.
Jahan *et al.* [28]	μEDM-drilling	Studied the influence of major operating parameters on the performance of WC for quality fabrication of micro holes in both transistor and RC-type pulse generators.
Zilong *et al.* [101]	μEDM-drilling	Fabricated micro holes with a diameter of 80 μm in the radial direction of the deposited micro-steel cylinder.
Rahman *et al.* [146]	μEDM, μEDG, Micro-turning	Introduced compound micromachining combining conventional and non-conventional micromachining processes for the fabrication of high aspect ratio microstructures.
Leitz *et al.* [126]	nano, pico and femto-second laser pulses	Presented a comparative study of the ablation of metallic samples with micro, nano, pico and femto-second laser pulses.

Hanon *et al.* [108]	Nd: YAG laser	Determined the effect of the various laser parameters on the dimensions and microsturcture of the micro holes on drilling of the alumina ceramics for different thicknesses (5 and 10.5 mm).
Sharma *et al.* [143]	pulsed Nd: YAG LBμM	Used hybrid approach of RSM and GRA for modeling and multi-objective optimization of process parameters on thin Al-alloy sheet for straight profile and fabricated micro holes.
Liu *et al.* [134]	Ultra-short laser pulses	Reported that ultra-short laser pulses result in comparatively better precision in micromachining to minimize the deviation in dimensional accuracy of fabricated micro holes.
Siva *et al.* [104]	μEDM-drilling	Performed μEDM experiments to fabricate micro holes on D2 steel using brass tool electrodes.
Natrajan *et al.* [106]	μEDM-drilling	Fabricated micro hole on SS 304. The machinability is evaluated for different machining responses of the machined micro holes due to the thermal properties of the work materials.
Behra *et al.* [114]	Q-switched Nd: YAG laser	Performed experiment on underwater-LBμM using a Q-switched Nd: YAG laser for fabricating microchannels on 304 stainless steel.
Rashid *et al.* [147]	LBμM and μEDM	Explored the feasibility of combining LBμM and μEDM to maximize the benefits and eliminate the shortcomings of both processes.
Liu *et al.* [148]	Ultrasound-assisted water-confined LBμM	Performed machining on copper, bronze, stainless steel, and titanium workpieces, where ultrasonic waves are applied through a horn placed near the laser ablation location on the workpiece front surface for micromachining.
Singh *et al.* [124]	LBμM	Presented a systematic experimental investigation into the influence of laser beam conditioning on the quality of a microchannel fabricated on SS316L.
Li *et al.* [100]	μEDM	Focused on the precision machining of the arrayed micro hole with a diameter less than 50 μm by μEDM. An array of micro holes 50 μm thick stainless steel, an array of (2 × 128) is machined with a diameter less than 50 μm.
Farasati *et al.* [135]	LBμM	Carried out experiments to understand the effect of LBμM parameters i.e., laser power, pulse frequency, gas pressure, pulse interval time, and pulse width, on material removal rate dimensional accuracy of biomedical alloy Ti–6Al–4V.

Martan *et al.* [116]	LBμM	Measurement systems based on IR radiometry using a fast liquid nitrogen-cooled IR detector and two paraboloid mirrors are used for surface temperature measurement to optimize process parameters, and monitoring for controlled industrial production.
Sahu *et al.* [149]	Hybrid LBμM	Thoroughly reviewed the laser-based hybrid process mechanism based on theoretical and experimental studies.

2.5. Heat transfer augmentation through arrayed micro protrusions

Advancements in MEMS (Micro Electro Mechanical Systems) technology have generated applications and futuristic research directions in the areas of thermal management of electronic circuits [150] and microbiological systems [151]. One of the most important challenges in MEMS technology is augmented heat dissipation from miniaturized components with lesser power consumption in driving out accumulated heat flux. According to the year 2004 International Electronics Manufacturing Initiative (iNEMI) technology roadmap, the maximum power dissipation from a high-performance microprocessor/chip can reach up to 360 W for a heat flux of up to 190 W/cm^2, by the year 2020 [152]. A pioneer research group of Karayiannis et al., [153] reported that, by the end of 2026, heat dissipation from microprocessor chips would exceed 800 W, which earlier was 270 W in 2015. Mudhafar et al. [154] assumed that in desktop and high-performance computers, the heat flux at the hot spot will account for as high as 27 – 45 MW/m^2 and 12 – 20 MW/m^2 by 2026. It has been reported that high-temperature issues in dense ICs often damage electronic components due to the accumulation of heat energy [155]. Few of these high-end electronics may require the dissipation of ultra-high heat fluxes exceeding 1 kW/cm^2 [156]. In high-performance electronics, there are other applications, such as various cutting tool-based machining operations, where the issue of high heat fluxes affecting the tool life has been experienced. Although, with the advancement in high-performance devices in engineering and device packaging, the cost and reliability have been improved, unfortunately, the thermal management has not been at the same swiftness, leaving scope for future research.

The dissipation of the heat for a given heat density and the material remains a primary concern that could either be attempted by ‘air or liquid flow through’ as active cooling or ‘airflow around’ as conventional, which may be an active or a passive method [157]. Since 1980s, plentiful active and passive cooling technologies have been developed and studied thoroughly in natural and forced convection heat transfer configurations [158], [159], [160], [161]. Several research groups conducted ample research on high heat dissipation technology using microchannel heat sinks [162] microchannels embedded with pin-fins heat sinks [163], arrayed pin-fins [164], phase change materials [165], and liquid cooling [166] etc. Conventional techniques like liquid and spray cooling [167] integrated with microchannel were state-of-the-art solutions for heat dissipation in microelectronics devices. As reported by a research group, the dissipation of heat flux using these techniques was of the order of 790 W/cm^2 while the surface temperatures were maintained at a level of less than 71°C for a very-large-scale integrated VLSI circuit [158]. Another similar approach was attempted to investigate the liquid flow and heat transfer characteristics in rectangular [159] and trapezoidal [160] cross-sectioned microchannel structures of width less than 400 µm. The latter was found to be more significant in thermal performance than the former due to the shape factor of microchannel. Looking at the space constraint and the requirement of light weight systems, passive cooling remains the go-to solution for most compact micro-systems. Such a technique is the pin-fin heat sinks designed to meet modern microelectronics requirements, which is very generic in ICs and MEMS [164]. Chiu et al. [168] investigated the liquid cooling efficiency and thermal performance using fluid flow through fabricated circular MPFs heat sinks of aluminum having a diameter ranging from 0.45-0.66 mm. It has also been reported that the overall performance of MPFs depends on different parameters and fluid flow conditions. It includes dimensions of the base plate [69], MPFs density [70], longitudinal and transverse spacing [171], pin-fins material [172], fluid flow velocity (in case of forced convection) [173], cross-sectional shapes [174], MPFs arrangement and fabrication methodology [164], [175]. Owing to the structural integrity, recent works contrasted heat transfer, and pressure drop effect of perforated MPFs heat sinks over solid MPFs [176] [177]. Their studies are limited to simulation results only.

The above studies have demonstrated enhanced cooling performance using regular-shaped MPFs limited to a lower aspect ratio. But optimizing the cross-sectional profile of MPFs heat sink is still a trending research aspect. During the last decade, several optimization studies focused mainly on the optimal selection of microchannel geometry embedded with pin-fins in the channel width [178], [179], pressure drop [180] across the micro/mini channel, and overall thermal resistance of the plate-finned heat sinks [181]. D. Lorenzini-Gutierrez et al., [182] evaluated 13 different MPFs heat sink designs for the variable fin density configuration, including offset strip fins. They found nine flow channels with embedded MPFs height of 100μm as the best performing thermal management option for dissipating heat input of 200W within a surface area of 1cm^2. Moreover, non-uniform, densely arranged arrayed MPFs attracted augmented thermal management by dissipating a high heat flux of 500W/cm^2 [183] and high surface temperature downstream [184] from hot spots. Their numerical results showed reduced non-uniformity in temperature and pressure drop through variable pin-fins density configurations than the uniformly arrayed pin-fins arrangement. The optimization of pin-fin geometry for controlling such a high heat flux is further demonstrated by Sakanova et al. [185] using complex convex profiles such as circular, cone, and hydrofoil pin-fins in turbulent flow conditions. Furthermore, Ismayilov et al. [186] performed a validation study using a multi-objective optimization Genetic algorithm (MOGA) and a CFD numerical model to analyze the thermal performances of hydrofoil-shaped pin-fins heat sinks. Additionally, they proposed a new bird pin-fins design that showed an enhanced average heat transfer coefficient dominating the pressure drop increase at higher Re than hydrofoil-shaped pin-fins. Bejan et al. [187] performed a pioneering work in thermal management based on EGM principles conceptualized from the second thermodynamics law. Several researchers later on utilized the EGM method to perform the optimization of plate-fin heat exchangers having a low-density array [188], [189], [190], [191]. However, the EGM minimization study on the densely arrayed MPFs heat sink design is not found.

PSO algorithm is a widely used trajectory-based evolutionary search optimization with certain advantages, in terms of storage space, convergence speed, process speed, and operating parameters, over other evolutionary optimization techniques [192]. A substantial number of comparative studies have been performed for PSO [193], GA [194], and ANN [195] on the effective thermal management of plate-fin heat exchangers. The information for thermal performance through unconventional MPFs cross-sections is rare and limited to only simulation studies. Since the cross-sections with different profiles play a significant role in the single-phase heat transfer analysis. Moreover, with the development of micromachining technology, structural improvement has become an effective way to enhance the heat transfer performance of MPFs heat sinks. By changing the cross-section profile of the MPFs, such as circular [196], Piranha [197], droplet [198], aerofoil [199], and hydrofoil [200], etc., reductions in the maximum thermal resistance and enhancement of thermal performance index are assumed [201]. Therefore, it is critical to perform these studies to fulfil the gap for the high heat-flux applications, which builds the aim of this study.

The obtained results from this study showed the enhanced thermal performance of fabricated unconventional arrayed MPFs cross-sections. It has been done through (i) numerical modeling and simulation (for design optimization), and (ii) experimental thermal performance testing. Thermal simulations have been performed of each optimal geometrical design MPFs (obtained by PSO) for the single-phase cooling (in air media) in the laminar flow regime. Arrayed piranha MPFs in a staggered arrangement, height - 931 μm, number of MPFs in an array - 115, inter-electrode-gap - 945 μm proven as best MPFs profile for effective heat transfer for different heat loading conditions. Earlier attempts in this regard are limited to the investigation of flow boiling experiments performed to characterize system level performance of the MECH-X heat sink at different mass fluxes [3]. Till now, very few research works have shown the performance evaluation of arrayed MPFs in terms of *TPI,* especially not for the unconventional MPFs profiles [154],[196],[197]. Therefore, the overall thermal performance of optimized arrayed MPFs has been evaluated experimentally by designing and developing testing facility. Arrayed piranha MPFs have shown an increasing trend of TPI ranging from 2.11-3.7, followed by droplets 1.78-2.96 and aerofoil 1.72-2.94 in a staggered arrangement. Whereas the pressure drop of all MPFs profiles in the staggered arrangement is lower than inline are observed at different *Re* values. A detailed summary of the literature discussed above is presented in Table 2.5:

Table 2.5. Summary of literature heat transfer augmentation through micro protrusions.

Authors	**Key findings**
Tuckerman *et al.* [158]	The dissipation of heat flux using these techniques is of the order of 790 W/cm^2 while the surface temperatures are maintained at less than 71°C for a very-large-scale integrated VLSI circuit.
Peng *et al.* [159]	Attempted to investigate the liquid flow and heat transfer characteristics in rectangular.
Bejan *et al.* [187]	Performed pioneering work in thermal management based on EGM principles conceptualized from the second thermodynamics law.
Jalil *et al.* [157]	Numerically studied impact of MPFs on heat transfer performance. Navier-Stokes equations are solved by steady-state three dimensions turbulent forced convection. A number of MPFs in an inline and staggered configuration are explored.
Mohammadi *et al.* [195]	Developed tool for non-linear multivariable modeling is the Artificial Neural Network.

Zhang *et al.* [202]	Demonstrated heat transfer enhancement in various applications and reviewed the pertinent literature.
Koo *et al.* [150]	The study enables 3D circuits to include greater active levels while exposing external surface area for functional signal transmission.
Koşar *et al.* [201]	Conducted the study of heat transfer and pressure drop associated with the forced flow of deionized water over five micro pin fin heat sinks of different spacing, arrangements, and shapes.
Kleinstreuer *et al.* [151]	Microfluidics offers a promising strategy for making N drug delivery devices due to its capability to precisely control the properties of the drug.
Mishra *et al.* [191]	Developed a genetic algorithm-based optimization technique for cross-flow plate-fin heat exchangers using offset-strip fins.
Ndao *et al.* [178]	Presented a multi-objective thermal design optimization and comparative study of electronics cooling technologies.
Bello-Ochende *et al.* [179]	Studied the geometric optimization of a silicon-based microchannel heat sink using a combined numerical optimization and constructal theory.
Chamoli *et al.* [203]	Investigated the heat transfer and friction loss characteristics in a horizontal rectangular channel with attachments of circular profile fins over one of its heated surfaces.
Zhou *et al.* [198]	Presented a 3D conjugated heat transfer model for Nano-Encapsulated Phase Change Materials (NEPCMs) cooled MPFs Heat Sink.
Tullius *et al.* [170]	Demonstrating the effects of MPFs in a minichannel is essential to maximizing the performance in small-scale cooling apparatuses to keep up with future electronic advancements.
Bar-Cohen *et al.* [156]	Described the physical phenomena underpinning the most promising on-chip thermal management approaches for hot spot remediation, along with basic modeling equations and typical.
Hamadneh *et al.* [193]	Particle swarm optimization (PSO) was employed to investigate the overall performance of a pin-fin.
Lorenzini-Gutierrez *et al.* [182]	Evaluated 13 different MPFs heat sink designs for the variable fin density configuration, including offset strip fins.
Normah *et al.* [180]	Reported the outcome of optimization of the hydraulic diameter and wall width to channel width ratio of square and circular microchannel heat sink for the simultaneous minimization of the two objections.
Zhao *et al.* [169]	Proposed to enhance the cooling performance of the micro square pin-fin heat sink, a geometry optimizing method changing pin-fin porosity and pin-fin located angle.
Yu *et al.* [197]	Presented an experimental and numerical study on a Piranha Pin-fin (*PPF*) microscale heat sink.
Micheli *et al.* [172]	Analyzed the heat transfer from MPFs and compared the thermal performance of plate micro-fin and MPFs arrays under natural convection conditions in the air.
Murshed *et al.* [152]	Provided a critical review of traditional and emerging cooling methods as well as coolants for electronics. In addition to summarizing traditional coolants, heat transfer properties and

	performances of potential new coolants such as nanofluids are also reviewed and analyzed.
Karayiannis *et al.* [153]	Discussed the possible applications of flow boiling in microchannels to highlight the challenges in thermal management for each application.
Chiu *et al.* [168]	Investigated the liquid cooling efficiency and thermal performance using fluid flow through fabricated circular MPFs heat sinks of aluminum having a diameter ranging from 0.45-0.66 mm.
Wan *et al.* [173]	Studied the single-phase thermal/fluid characteristics of micro gaps of aspect ratio of 0.02, incorporating staggered pin-fin arrays.
Reddy *et al.* [183]	Presented fully three-dimensional conjugate heat transfer analysis and multi-objective, constrained optimization to find sizes of pin-fins, inlet water pressure, and average speed for arrays.
Vilarrubí *et al.* [184]	Demonstrated experimentally and numerically the potential of MPFs heat sinks as an effective alternative to microchannel heat sinks for dissipating high heat fluxes from small areas.
Sakanova *et al.* [185]	The optimization of pin-fin geometry for controlling such a high heat flux was demonstrated.
Gao *et al.* [166]	Spray cooling was reviewed from the entire spray (spray level) and droplets (droplet level). The spray level discussion focuses on spray cooling performance as a function of fluid properties, flow conditions, surface conditions, and nozzle positioning.
Qin *et al.* [175]	Micro-Particle Image Velocimetry (Micro-PIV) system used to visualize the flow properties of deionized water flowing across circular, ellipse, and diamond MPFs arrays with Re situated between 100 and 400.
Tan *et al.* [181]	Investigated the demand for the ever-increasing heat flux of electronic chips and the influence of the topology structure of microchannels on its heat transfer performance in chip cooling.
Babar *et al.* [199]	Analyzed the hydrothermal performance of airfoil-shaped pin-fin heat sink employing nanofluids of ferric oxide (Fe_2O_3) and titania (TiO_2), also compared the results with base fluid (distilled water).
Qiu *et al.* [167]	Described an experimental study of the cooling capabilities of microchannel and MPFs-based on-chip cooling systems.
Gupta *et al.* [176]	Investigated the hydrodynamic and thermal characteristics of perforated MPFs heat sink with different shapes and numbers of perforations under a low range (100–1000) of Re and constant base wall heat flux thermal boundary condition with air as the working fluid.
Ismayilov *et al.* [186]	Performed a validation study using a multi-objective optimization Genetic algorithm (MOGA) and a CFD numerical model to analyze thermal performances of hydrofoil-shaped pin-fins heat sinks.
Daewoong *et al.* [196]	Investigated the thermal and hydrodynamic characteristics of various MPFs arrays.
Khalil *et al.* [177]	Studied the benefits of reducing entropy production and improving hydrothermal performance with varied thermal air characteristics through different perforated heat sinks.

Niranjan *et al.* [171]	Studied the heat transfer enhancement of heat sinks using square MPFs is investigated under forced convection.
Ye *et al.* [155]	The rectangular microchannel heat sink with an aspect ratio of 2 is built with a combined construction of fan-shaped cavities and oval pin fins.
Mudhafar *et al.* [154]	Focused on the enhancement of flow boiling heat transfer and improvement of flow instability due to the porous surface modification and channel section expansion, a hot research issue.

2.6. Scope of the Research

Based on the extensive literature review, specific gap areas in the field of arrayed micro protrusions and their intended application have been identified. The present study aims to produce unconventional cross-sectional profiles arrayed micro protrusions (as MPFs heat exchangers) for enhanced heat dissipation from MEMS devices. It has the potential to provide solutions for the high heat flux generated at the hot spot of high-performance microelectronics or similar MEMS devices. The idea is generated from the proven capabilities of such a pin-fin in both active and passive heat management for up to 300 W/cm^2. The capabilities have been assessed through modeling and thermal simulations of arrayed protrusions, heat sinks, different arrangements, and optimal geometrical design considerations. Moreover, comparative heat takeaway capacity through the different cross-section arrayed protrusions can be assessed through the thermal performance evaluation using an in-house developed testing facility, which is one of the contributions of the present work. An extensive literature review indicates that such products are highly relevant for applications such as:

- In thermal management of high-performance microelectronics and;
- Complex structure metallic implants in biomedical applications, etc.

The present study focuses on the development of the potentiality of RμEDM for complex geometrical micro products' (arrayed unconventional shaped micro protrusions) fabrication. Various novel strategies have been developed to achieve these aspects and are presented in Table 2.6.

Table 2.6. Proposed strategies to improve the effectiveness of the RμEDM process.

Strategies	**Outcomes**
1) Feasibility study for fabricating densely arrayed micro protrusions by LBμM-RμEDM integrated technology	● 3D arrayed micro protrusions with different complex cross-sections. ● Analysis of various machining responses. ● Critical review and solution strategies

	for the issues encountered in the fabricated micro protrusions.
2) RµEDM process parametric optimization 3) Optimization of LBµM process parameters for tool plate fabrication for RµEDM	● Optimization of process parameters using GA for the fabrication of high-quality arrayed protrusions. ● Optimization of process parameters using GRA for the fabrication of RµEDM tool plate.
4) New flushing strategy in RµEDM	● Implementation of “Brahistochrone curve” based design and development of suction cup/funnel for high-pressure flushing. Funnel is expected to be valid for a wide range of array and workable parameters with quality of easy to integrate.

Future works could be to upgrade the revealed technology to meet the requirements of arrayed micro protrusions for a wide range of materials, regardless of the geometrical parameters and applications. Moreover, the need for enhanced heat dissipation rate is essentially not only for flat surfaces but also for curvilinear surfaces or in piping systems for multiple applications.

2.7. Research Objectives

Based on the above discussions, the following have been laid down as the objectives of the present work. The main aim of the work is to recognize the proposed LBµM-RµEDM integrated technology as an effective method for the fabrication of various arrayed 3D protrusions for thermal management applications. To achieve this goal, the following set of objectives are attempted:

1. To check the potentiality of RµEDM for fabricating arrayed micro-protrusions of unconventional cross-sectional profiles.
2. To explore the LBµM as a potential process for fabricating the RµEDM tool plate which is used to generate the arrayed micro-protrusions.
3. To enhance RµEDM process capability by introducing pressure-assisted dielectric flushing.
4. To establish a numerical approach for thermal performance evaluation and profile optimization of fabricated micro-protrusions.
5. To validate the thermal performance of the optimized micro-protrusions through an in-house designed and developed test rig facility.

2.8. Methodology

With the main focus on recognizing the LBµM-RµEDM integrated technology as an effective method for the fabrication of various arrayed 3D protrusions, the work is executed by performing some trial experiments. After performing certain development for performance enhancement and identifying the LBµM-RµEDM integrated technology as a potential process for such fabrications, the similar arrayed protrusions are simulated numerically. Based on the results from the numerical simulation for thermal performance and optimized profile of the MPFs are re-fabricated and experimentally tested and verified. This section describes the methodology adapted to carry out the present research work to attain the objectives:

- *Configuration of LBµM-RµEDM for arrayed micro protrusions or MPFs:*

Motivated by the RµEDM proven capabilities in the past for fabrication of single or multiple metallic micro rods, the idea of achieving arrayed micro protrusions by the process for an intended application as arrayed MPFs is generated. The µEDM discharge pulses are stochastic, having very high probabilities of being non-isoenergetic, and hence generating non-uniform material removal by each of them. An initial study on exploring the discharge phenomenon and material removal characteristics by single and multiple discharges in the RµEDM for a wide range of process parameters is performed. Looking at the requirements for generating arrayed MPFs effectively, the following two challenges are experienced.

1. Availability of the dimensional accurate tool plate for RµEDM having arrayed micro holes in the pattern, shape and size as desired for the arrayed MPFs.
2. A less-effective material removal, especially in the case of fabrication of a large array of micro protrusions, due to a poor evacuation of debris from the discharge gap of RµEDM (especially at the central location in an array).

The first is attempted by discovering LBµM (a facility inbuilt in the same machine tool which is used for RµEDM) as a process to be used for fabrication of the tool plate of RµEDM, and the other is through developing a suction-based high-pressure flushing system for RµEDM. Details of these attempts and presented through the next two points of the description of the research work.

The first challenge mentioned above due to poor surface equality of micro holes in the tool plate, can be encountered by an in-depth study of LBµM process parameters for good quality tool plate fabrication is necessary. For the second challenge, due to the severe accumulation of ejected debris at the central location in an array due to insufficient flushing. An innovative dielectric flushing methodology should be integrated which can completely evacuate the ejected debris from the minimal discharge gap in RμEDM.

- *Assessment of LBμM process parameters for the desired tool plate for RμEDM*:

The tool plate used in RμEDM is fabricated by LBμM process whose parametric effects are evaluated for the surface characteristics of fabricated micro holes. The process parameters, including pulse width, frequency, and lamp current percentage, are considered the most influencing parameters affecting the surface qualities such as recast layer, burr formation, taper, and microhardness of fabricated holes. A well-known multi-objective optimization approach namely, GRA, is used to determine the optimal parametric combination for fabricating arrayed micro holes on the tool plate. A validation run is also performed to analyze the percentage deviation in the experiment results.

- *Design and development of 'suction-based high-pressure flushing technology' for RμEDM*:

Owing to the second challenge mentioned above regarding severe debris accumulation and its poor evacuation from the minimal discharge gap. A novel high-pressure suction-based dielectric flushing is introduced and integrated with the existing RμEDM setup for effective debris removal. The developed flushing technology setup performed several tasks, such as removing the ejected debris from the discharge gap, and ensuring the presence of adequate fresh dielectric at the machining zone. A new suction funnel has been designed based on the 'Brachistochrone curve' or the curve of fastest descent for faster debris flow. Therefore, the issue of damaged or distorted tips of a few micro protrusions at the central location in an array has come up with a novel strategy of suction-based high-pressure flushing technology in RμEDM.

- *Numerical modeling, simulation and design optimization of arrayed MPFs:*

The fabricated MPFs are targeted for the application of high heat flux dissipation from the dense ICs of MEMS. The geometrical design optimization of different MPFs cross-sectional profiles subject to variable heat loading conditions is of great concern. Therefore, a design-based optimization study has been performed to identify the optimal geometrical parameters of different MPFs profiles. A numerical modeling approach based on the minimum "Entropy generation rate" is adapted for the intended purpose. A generic code of Particle swarm optimization is written and used to find the best possible solution for optimal geometrical design in knowingly inline and staggered arrangements of MPFs. This study is followed by a thermal simulation of the optimal design of different MPFs profiles for analyzing thermal performances through it. ANSYS$^{®}$ fluent software is used to analyze the different thermal parameters at a constant heat loading condition expected from high-performance microelectronics. Moreover, the comparative assessment and validation of recorded results have been verified experimentally, providing the basis of the present study.

- *Fabrication of optimized profile of arrayed MPFs and their testing:*

The fabrication of the optimal design of each MPFs cross-section profile is mandatory for the validation of the numerical study. Considering this, the different MPFs have been fabricated using the above-discussed assisted microfabrication technology. The fabricated MPFs heat sinks are tested to analyze their thermal performances. A test rig setup has been designed and developed for testing purposes which is equipped with different measurement devices and sensors for capturing the thermal data. Different thermal characteristics using the established correlations are evaluated and compared. The capability of each MPFs heat sink profile is tested for maximum heat transfer coefficient subjected to high heat flux in the laminar flow regime.

Chapter 3

Feasibility Study of RμEDM

3.1. Introduction

This chapter introduces the RμEDM process and describes its material removal mechanism through single discharge analysis. Fabrication feasibility study of arrayed micro protrusions over a wide range of materials (including biocompatible material) is performed using the integration of LBμM and RμEDM processes. An optimization study for RμEDM is performed using a multi-objective optimization tool to find the optimal parametric combination for fabricating arrayed micro protrusions for enhanced material removal rate (MRR), reduced taper root angle (θ) and surface roughness (Ra). Analysis of machining responses at different parametric settings, issues encountered in fabrication and its pertaining solutions are well discussed.

3.2. RμEDM: An overview

The μEDM process is achieved from the conventional EDM by downscaling the parametric conditions which are given in Table 3.1.

Table 3.1. Comparison between conventional EDM and μEDM.

Sr No.	**Parameters**	**Conventional EDM**	**μEDM**
1.	Size of the tool and the fabricated feature[68], [204]	>999 μm	1-500 μm
2.	Discharge gap[205],[9]	Tens of μm	1-10 μm
3.	Discharge energy[206], [207]	Few μJ to 10 J	10^{-6} -10^{-7} J
4.	Pulse frequency[208]	20-40 Hz	Up to 9 μm/sec
5.	Feed rate[209], [210]	Up to 10 mm/min	Up to 9 μm/sec
6.	Types of pulse generator[211]	Transistor type	RC type

The RμEDM, which is a prominent variant of the μEDM process, is achieved by polarity interchange in a basic μEDM circuit for the fabrication of single/arrayed micro protrusions. The RμEDM is a non-conventional micromachining process wherein material removal takes place from the targeted location on the workpiece electrode under high thermal energy generated as a result of serial electrical discharges occurring between the workpiece and tool plate electrodes (assigned as anode and cathode), when submerged in a dielectric medium [43]. The cathode is in the form of a metallic tool plate with a through hole generated by a suitable micromachining process and is clamped on the work table. A solid metallic rod (anode), held in the vertical machine spindle, is traversed through the tool plate with a pre-defined feed rate (Figure 3.1).

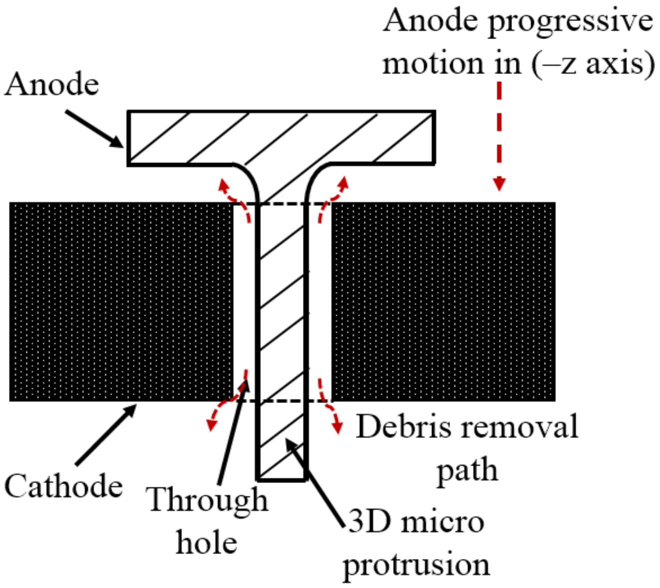

Fig. 3.1 Schematic of RμEDM process for the fabrication of micro protrusion.

The shape of generated micro protrusions is conformal to the cross-section of the micro holes, and therefore 3D micro protrusions are produced by the RμEDM process. Hence, it can produce moderate to high aspect ratio single/arrayed micro protrusions. These arrayed protrusions find applications in fabricating metallic dies for lens let arrays, micro tools, solar cells, heat exchangers, super-hydrophobic surfaces etc. One of the application areas of RμEDM in fabricating micro tools for machining micro parts and components is shown in Figure 3.2. An array of micro protrusions of diameter 35 µm with a height of 1.5 mm is fabricated by RμEDM on the bulk WC rod of 200 µm. An inter-electrode gap of 120 µm is kept uniformly between each protrusion.

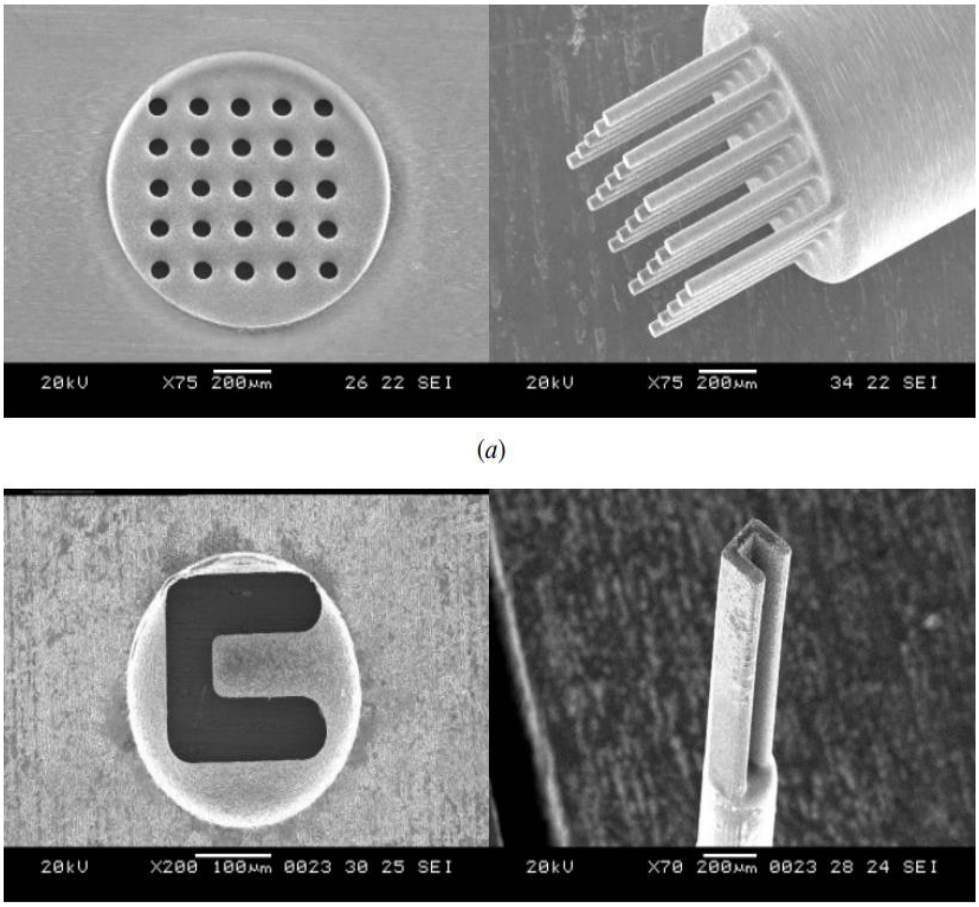
20kU X75 200µm 26 22 SEI
20kU X75 200µm 34 22 SEI
20kU X200 100µm 0023 30 25 SEI
20kU X70 200µm 0023 28 24 SEI

(*a*)

(*b*)

Fig. 3.2 SEM images of machined arrayed micro protrusions using RµEDM, (a) circular micro protrusions, (b) U-shaped micro protrusion, and the corresponding tool plate (each hole fabricated by µEDM) [6].

3.2.1. Material removal mechanism in RµEDM

The material removal mechanism in a typical µEDM process can be understood by the presented diagram (Figure 3.3) [90]. A schematic of the single discharge description in µEDM is shown in Figure 3.3(a), whereas the dielectric breakdown and discharge gap phenomenon are shown in Figure 3.3(b). In µEDM, the thermal effect of the discharge pulses induced by an electrical discharge generator between the terminals of the electrodes (tool and workpiece) resulted in the material removal from the workpiece surface. The mechanical counterpart of the energy which is induced by the dielectric medium is utilized to remove the micron amount of material.

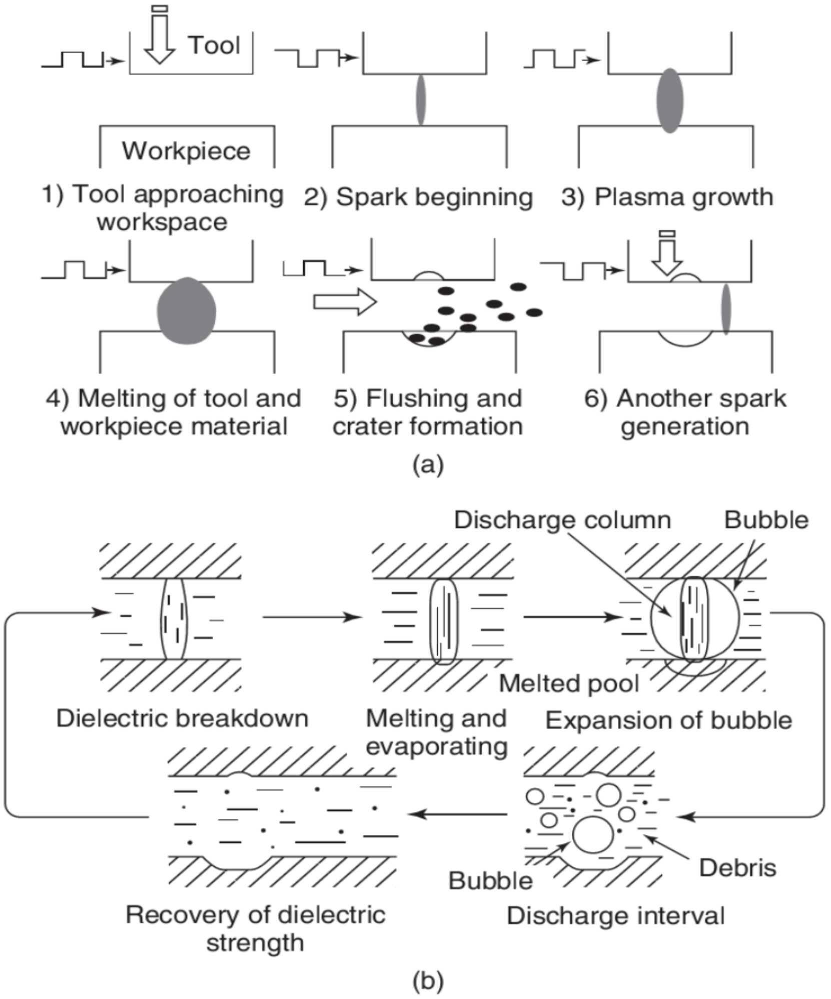
Tool
Workpiece
1) Tool approaching workspace
2) Spark beginning
3) Plasma growth
4) Melting of tool and workpiece material
5) Flushing and crater formation
6) Another spark generation
(a)
Discharge column
Bubble
Dielectric breakdown
Melting and evaporating
Melted pool
Expansion of bubble
Recovery of dielectric strength
Bubble
Debris
Discharge interval
(b)

Fig. 3.3 Material removal principle in µEDM (a) single discharge description and (b) discharge gap phenomenon [90].

The material removal in RµEDM takes place in the same fashion as µEDM due to dielectric breakdown resulting in more than positive ions and electrons accelerated towards the anode (workpiece) and cathode (tool plate consisting of micro holes'). The repetitive electrical discharges occurring between the cathode and the anode, material removal occurs from both the anode and cathode at particular locations, closely approximated to each other. The amount of material removed from the anode is more than the cathode. The remaining material keeps intact and does not face the micro pre-drilled hole areas'. This phenomenon can produce single or arrayed protrusions depending upon the number of pre-drilled micro holes in the cathode (tool plate). The material removed in a single discharge during RµEDM generates similar crater geometry as in µEDM. SEM images of single carter formed at different discharge energy settings in RµEDM are presented in Figure 3.4.

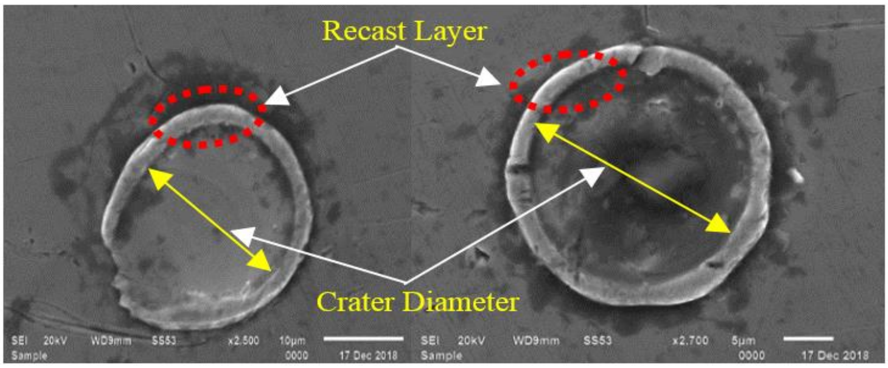
Recast Layer
Crater Diameter
SEI 20kV WD9mm SS53 x2,500 10μm 0000 17 Dec 2018 Sample
SEI 20kV WD9mm SS53 x2,700 5μm 0000 17 Dec 2018 Sample

Fig. 3.4 SEM images of typical crater geometries at different discharge energies in RμEDM.

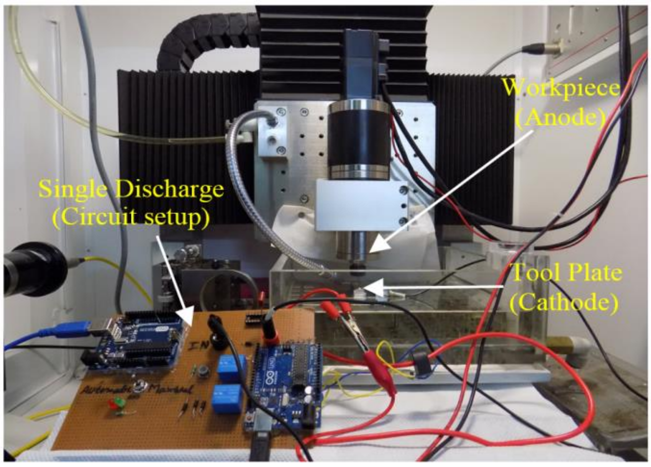
Workpiece
(Anode)
Single Discharge
(Circuit setup)
Tool Plate
(Cathode)

Fig. 3.5 Real-time representation of single discharge circuit and RμEDM setup.

Figure 3.5 presents the in-house developed single circuit setup used for performing single discharge in the RμEDM process. The circuit cuts the power supply after every single discharge for the estimation of the crater geometry formed due to spark discharge. The frontal surface of the workpiece surrounds the pre-drilled micro holes at the interface and plays a significant role in removing the excess material from the anode (Figure 3.6). As the front surface eroded more during the sparking phenomenon. The physics behind that is the front surface faces spark for a long duration after when the anode proceeds towards the pre-drilled holes up to the required length of protrusions. The front surface removes the outer surface of the anode except for the inner surface of the workpiece which does not face sparks during the continuous machining. The front erosion is vulnerable to higher *C* values in comparison to the lower one. It is because the higher *C* involves higher energy which results in the higher removal rate of material from the front surface in contrast to the lower value of *C*.

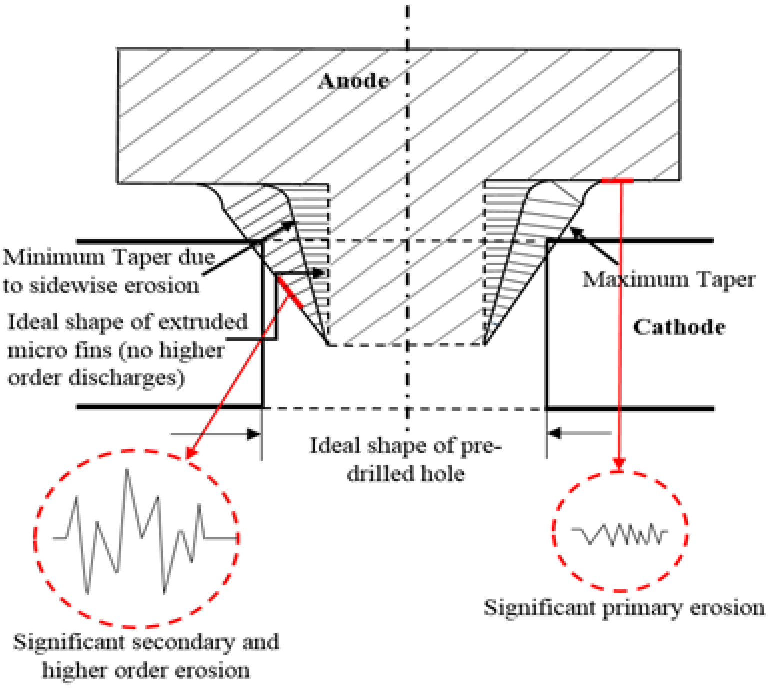
Anode
Minimum Taper due to sidewise erosion
Ideal shape of extruded micro fins (no higher order discharges)
Maximum Taper
Cathode
Ideal shape of pre-drilled hole
Significant secondary and higher order erosion
Significant primary erosion

Fig. 3.6 Secondary and higher-order discharging phenomena during RμEDM.

Rather the deepness of the material removed from the front surface is precisely compensated with the desired length of the machined protrusions [212]. In RμEDM, a series of repetitive discharge pulses leads to material removal at different locations on the (workpiece) anode. Also, the amount of material removed during each spark will vary due to the nature of frequently occurring discharges (such as, primary, secondary and higher-order discharges). The prime requirement of healthier machining is to promote primary discharges that occur at the minimum inter-electrode gap (IEG) between the walls of the workpiece and micro holes in the tool plate (cathode) in Figure 3.7(a). Secondary discharges occur between walls of either the anode or cathode and debris that adheres to either wall of the cathode/anode, respectively, thereby reducing local IEG at specific areas as shown in Figure 3.7(b). The higher-order discharges occur between floating debris in the IEG or attached to walls of the cathode and anode as shown in Figure 3.7(b). It is evidenced that the primary discharge is the main phenomenon for material removal in RμEDM, whereas the amount of secondary and higher-order discharges increases with increasing depth of micro protrusions. Moreover, secondary and higher-order discharging phenomena result in higher surface roughness at the particular areas at which the accumulation of debris is severe [213].

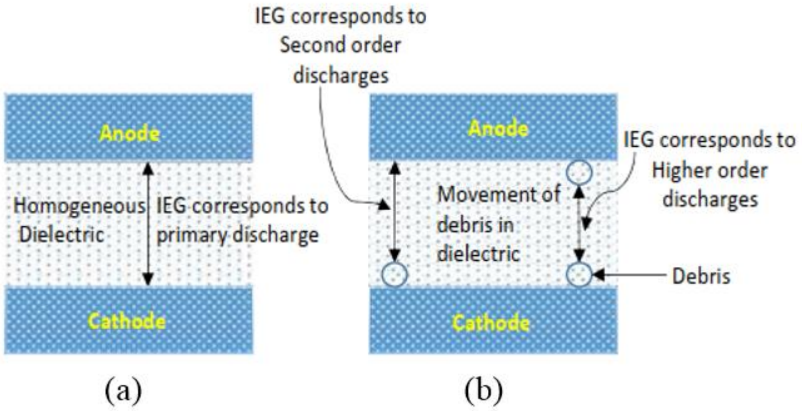
IEG corresponds to Second order discharges
Anode
Homogeneous Dielectric
IEG corresponds to primary discharge
Cathode
(a)
Anode
Movement of debris in dielectric
IEG corresponds to Higher order discharges
Debris
Cathode
(b)

Fig. 3.7 (a) Primary discharge and (b) second and higher order discharges in RμEDM.

The intended surface roughness of fabricated protrusions for specific applications could be estimated before actual experimentation beneficial in reducing the experimental runs. A simple numerical model of RμEDM process is developed using necessary boundary conditions for the determination of the surface roughness of fabricated protrusions (the detail of the model formulation is provided in Appendix A). The results of this developed numerical model (elaborated in Appendix-A) are further utilized to determine the crater’s volume to find the *Ra* values. The possible shape of the crater is hemispherical and is obtained by primary erosion as well as higher-order erosion as shown in Figure 3.8.

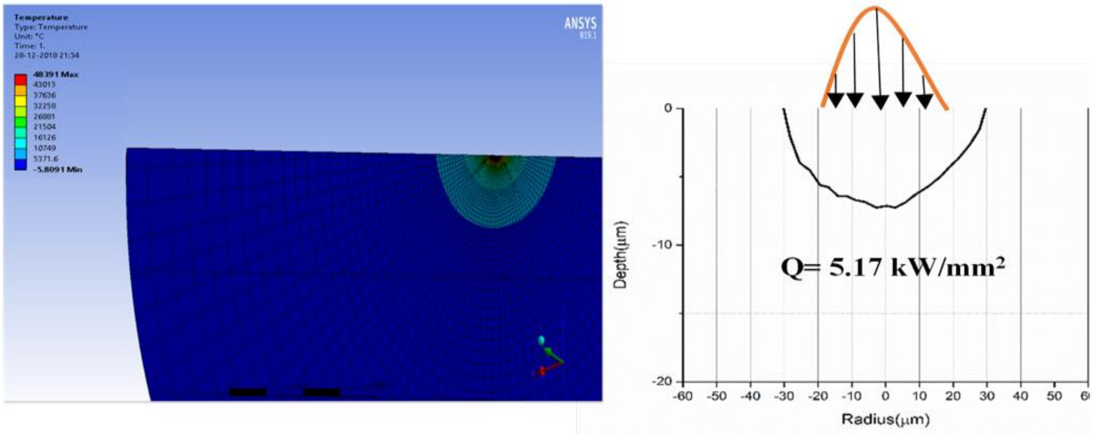

Fig. 3.8 Heat source equivalent radius and crater radius.

The material removal due to higher-order discharges and subsequent surface roughness has been predicted using theoretical correlations and elementary assumptions reported in the existing literature. The maximum surface roughness is assumed to equal the crater's depth formed during an individual spark discharge. The outcome of the numerical results and the typical SEM image of overlapped craters on a machined surface are shown in Figure 3.9(a,b). The maximum non-conformities of the workpiece surface are equal to

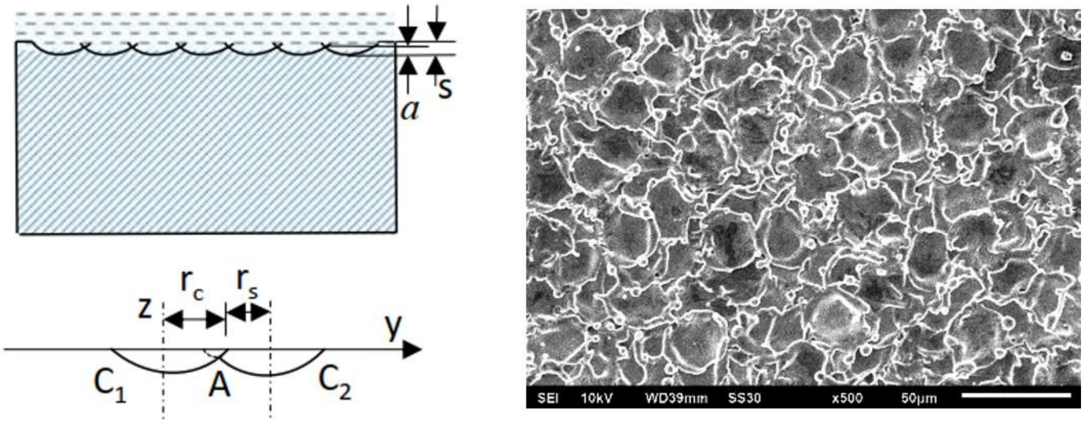

(a) (b)

Fig. 3.9 *Ra* measurement by depth of overlapping craters in (a) numerical model, and (b) SEM image of the machined surface.

the depth a, which corresponds to Ra. The generated surface roughness in RμEDM is quietly different from the other μEDM variants due to the workpiece-tool plate configuration, dielectric flushing and discharge energy settings. It may also be due to process parameters like the V, the current, the spark duration, the crater geometry etc. The RμEDM experiments are performed to fabricate different cross-sectioned arrayed protrusions. Later on, Ra values on the surface of the fabricated arrayed protrusions are measured.

3.3. Fabrication feasibility study of RμEDM

Recent developments in ongoing research on the RμEDM process are more emphasized the fabrication of dimensionally accurate and high surface finished arrayed micro protrusions in different cross-sections profiles. However, the fabrication of single/arrayed micro protrusions through the RμEDM process is highly dependent on the geometrical shape and size, and the quality of micro holes fabricated in the tool plate is evidenced. Since the RμEDM tool plate fabrication is one of the challenging tasks when the required micro holes are of a few tens of microns and in complex cross-sections. To cater to this need, a companion microfabrication process, LBμM is utilized to fabricate any geometrical cross-section profile and aspect ratio micro holes in the tool plate. Integrating both processes sequentially can be termed as '*Integrated microfabrication technology*', the advantages offered by individual processes have been investigated in detail in the following sections.

3.3.1. Technology details and experimentation

The necessary tool-work configuration and polarity retrieval of µEDM to achieve RµEDM is well depicted in Figure 3.10(a) and Figure 3.10(b). As shown in the inset (Figure 3.10(c)), the fabricated pre-drilled micro holes in the tool plate is the key component for the fabrication of the arrayed protrusions. The cross-sectional profile of the fabricated protrusions is just a duplicate copy of the micro holes fabricated in the tool plate. The metallic surface between micro holes only allows erosion to happen wherever it is superimposed on the workpiece surface. As the inter-electrode gap would cross the minimum limit obstruction as it all depends upon the available geometrical array of pre-drilled micro holes. These pre-drilled micro holes can be fabricated of any aspect ratio, and geometrical cross-sections with minimum inter-hole gaps, as shown in Figure 3.10(c). The quality of the fabricated holes can be controlled by proper selection of a parametric combination of LBµM during the processing as shown in Figure 3.10(d). The high-intensity laser irradiation produced in LBµM is of class IV LASER which has fabrication capabilities in the micrometer range less than 100 µm fabricate tool plate for RµEDM. The detailed parametric study of LBµM is also performed of which details are provided in chapter 4. Sequentially, both machining processes have been performed on the multi-process hybrid micromachining tool (make: MIKROTOOLS, model: DT110i) equipped with LASER head for the minimum possible travel on the work table with high accuracy and resolution of 0.1 µm. Noteworthy to mention here that, it would not be completely possible to fabricate pre-drilled micro holes of complex cross-sections in a

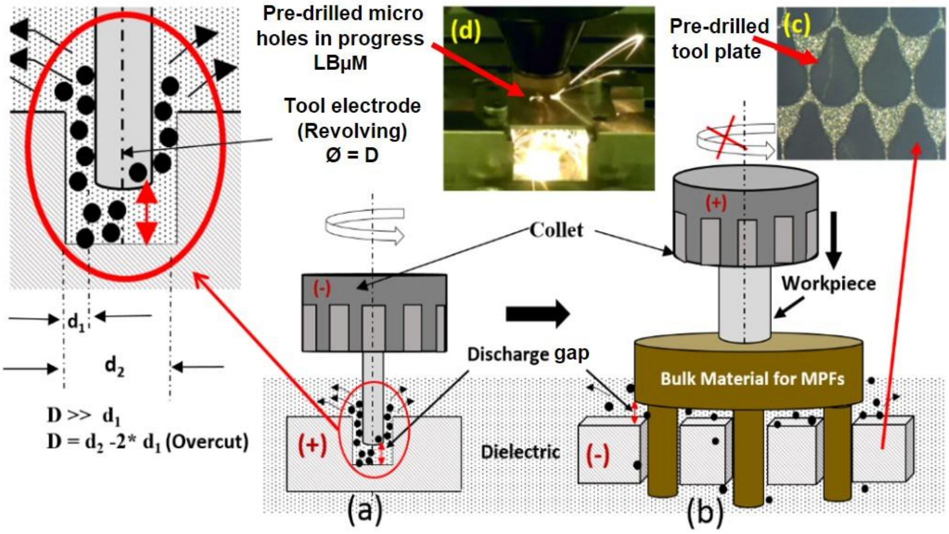

Fig. 3.10 Illustration of (a) µEDM drilling, (b) RµEDM by reversing the polarity of (a), (c) pre-drilled tool plate for RµEDM and (d) LBµM used for pre-drilled tool plate.

large array size using any mechanical micromachining. It is due to high tooling cost and wear of tool teeth when machining harder-to-cut materials. The machining conditions for both processes are presented in Table 3.2. Moreover, a dedicated fixture is fabricated by CNC milling that firmly holds the fabricated tool plate during RμEDM. The workpiece-tool plate configuration has been dipped inside the dielectric tank filled with hydrocarbon-based dielectric oil (Make: Nickunj Eximp Entp P Ltd, Model: NICUT LL21 E EDM oil) and undergoes filtration and continuous supply.

Table 3.2. Machining conditions.

RμEDM process parameters		**LBμM parameters**	
Setup	RC based	LASER type	Nd-YAG YLR-150/1500-QCW-MM-AC-Y11
Resolution (X, Y, Z)	0.1 μm	Wavelength	1070 nm
Tool-plate	SS (grade AISI 304)	Power	150 W
Workpiece	Cu_3Zn_2 (yellow brass)	Frequency	50 Hz
Gap Voltage	125 V	Pulse width	0.5 ms
Capacitance	100 nF	Spot dia.	50 μm
Electrode feed rate	3-5 μm/s	Feed	100 mm/min

Cross-sectional profiles	**Measured Responses**				
	Approximate Machining Time (hrs)	**Height of MPFs (mm)**	**Surface Roughness, R_a (μm)**	**MRR (mm^3/min.)**	**Array size**
Piranha	10	0.65	2.50	0.19	7 x 9
Aerofoil	12	1	2.47	0.17	7 x 21
Diamond	16	1.2	2.42	0.15	9 x 14
Droplet	8	0.6	2.46	0.18	7 x 10

3.3.2. Outcomes of the feasibility study

The discussed microfabrication technology is evidenced through the successful fabrication of several arrayed micro protrusions as shown in Figure 3.11. The fabricated protrusions are in the cross-sections of Piranha (Figure 3.11(a)), aerofoil (Figure 3.11(b)), diamond (Figure 3.11(c)) and droplet cross-sections (Figure 3.11(d)).

The prime requirement of this experimentation is to present the feasibility of fabricating the unconventional cross-section profiles arrayed protrusions in different aspect ratios. The minimum gap was achieved at 40 μm, whereas, the desired aspect ratio of the cross-sections is not the prime focus of the work. The height of fabricated arrayed protrusions

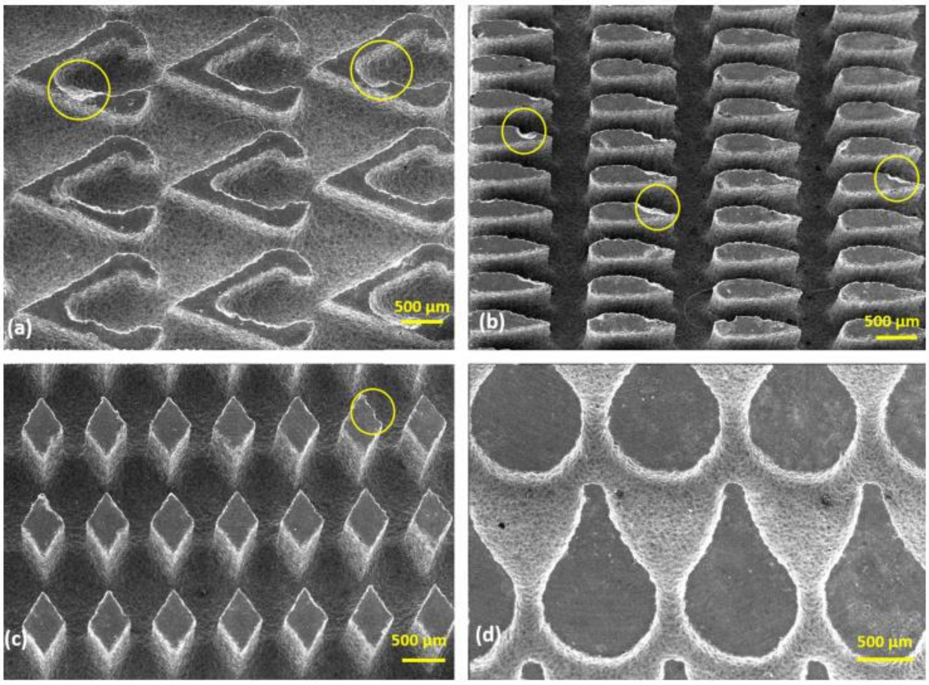

Fig. 3.11 SEM images of actual fabricated (a) Piranha, (b) aerofoil, (c) diamond and (d) droplet cross-sections of arrayed protrusions.

is verified to range from 600 µm to 1.2 mm. The diamond and aerofoil protrusions achieved a height of 1.2 mm, whereas the other two (Piranha and droplet) are having 700 µm. In order to check the characteristics feature of the fabricated arrayed protrusions, the Ra of the protrusions is one of the important features that affect the heat transfer rate due to fluid interaction with the protrusions body [214]. However, direct measurement of surface roughness on the fabricated protrusions is not so easy, due to the curvilinear surface which does not facilitate effective movement of the stylus to move over it. Therefore, an indirect method of measuring surface roughness is performed using Surfcom 130A profiler (make: ZEISS Industrial Metrology) which has a span length of 5 mm and a scanning speed of 0.3 mm/s. Since the input parameters of RµEDM are kept constant for all micro protrusions cross-sections, the Ra values of the machined surfaces subjected to intense pulsating discharges are a maximum of 2.50 µm throughout the length of the single protruded structure. MRR is one of the most important machining responses in µEDM or variant processes. The low values are significantly undesirable from the micromachining point of view. Figure 3.12 provides the illustration of the MRR estimation and the methodology adopted to find it is as follows:

MRR estimation is formulated as given in Eqs. (3.1) and (3.2).

$$MRR = \frac{V_R}{T} = \frac{[V - nv]}{T} \tag{3.1}$$

$$v = A_f H \tag{3.2}$$

V_R = Volume of the material removed

T = Time taken in the fabrication of a complete array of protrusions for different cross-sections (Table 3.2)

V = Volume of the workpiece undergoing RµEDM (represented as a transparent closed box in Figure 3.12)

v = Volume of one fin

n = Number of micro protrusions in an array

A_f = Cross-sectional area of the protrusions in the respective array

H = Height of one protrusion of the respective array

It is assumed that the volume of a protrusion in an array is uniform.

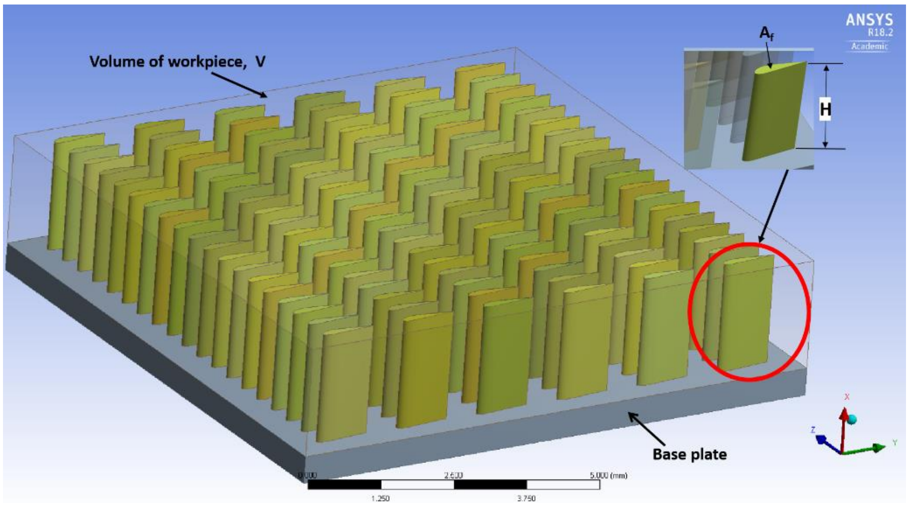

Fig. 3.12 3D ANSYS model of fabricated micro protrusions for MRR estimation.

It is revealed that the aerofoil and diamond cross-sections of micro protrusions have resulted in a low value of MRR (Table 3.2). This can be because of the poor dielectric flushing during machining leading to a non-linear increasing trend of machining time while going deep through the entire length of the micro protrusions. This condition is more significant in µEDM technology than a conventional EDM due to the minimal discharge gap, which generally falls in the range of 5-10 µm at lower discharge energy settings [23].

Another companion machining response called taper of the fabricated protrusions is found prominent in RμEDM, discussed by Nirala et al. [43], [60]. They basically measure the taper root angle of the fabricated micro rod starting from the top edge to the bottom root. The maximum angle was recorded to be up to 2.1^o for a single circular cross-section micro rod fabricated using a brass material tool plate. It is due to the taper formation in the machined micro holes' wall in the tool plate due to the series of high-frequency discharge pulses in RμEDM. However, the present study reports no significant taper in the fabricated arrayed micro protrusions except a round-shaped fillet formation at the bottom root of fabricated arrayed micro protrusions. This fillet formation is due to the use of the tool plate of SS 304, which is a significantly harder material results in very less wear at the micro hole's wall during machining. But noteworthy to say that the top edge of the pre-drilled micro holes in the tool plate faces sparking, for longer machining time and the entire length of the micro protrusions, gets worn out resulting in fillet formation on the chosen input parameters of RμEDM.

3.3.3. Issues and possible solutions associated with fabricated micro protrusions

Rigorous surface characterization of the fabricated micro protrusions revealed the two major issues that can be recalled are (1) total machining time taken in the fabrication of one complete array of micro protrusions, and (2) damage to the top edge of a few protrusions (especially at the center of the array) as encircled in Figure 3.11(a), Figure 3.11(b) and Figure 3.11(c). The reason for the evidence of the above-said issues could be the poor flushing during the whole machining time. The protrusions in the central zone in an array fabricated by RμEDM get severely affected due to the poor evacuation of debris ejected during machining. A factual situation of frequently occurring abnormal discharges, as a result, prevents the ongoing progressive RμEDM until the servo motor retracts in the positive z-axis providing the gap for the removal of accumulated debris. Subsequently, in maintaining the desired discharge gap back between the tool plate and work-electrode at the chosen parameters, the time consumed is longer. The implementation of a retrofittable ultrasonic vibration-assisted spindle for holding the workpiece could be synchronized with the servo-controlled mechanism for faster machining. It can even be made more effective by an optimum synchronization of vibration frequency with the discharge pulse frequency of RμEDM. This ultrasonic vibration incorporation may reduce 'arcing' and 'short-circuiting', resulting due to higher-order discharges during machining [215]. The solution can be anticipated with the developed flushing methodology that accelerated the cleansing action of debris from the discharge gap during the machining of arrayed micro protrusions, hence, lesser machining time.

Owing to the second issue of the damaged edge profile of a few micro protrusions, caused due to the presence of inherent burr formation and the non-uniform wall surface of the fabricated micro holes by LBμM, which has been explained in the next chapter in detail. The parametric selection of LBμM is adopted intentionally to fabricate a set of arrayed micro holes in moderately lesser time (2-4 minutes for each profile).

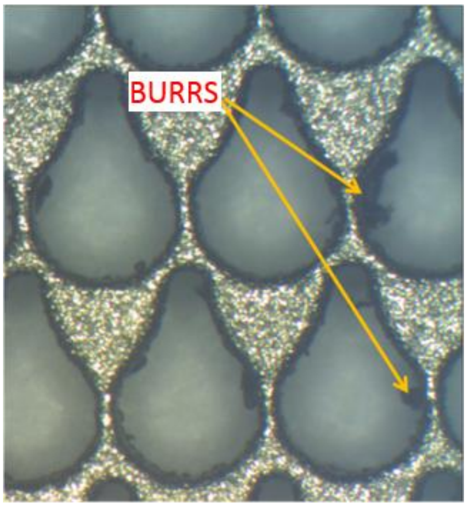

Fig. 3.13 Burrs present at the tip of pre-drilled micro holes.

The inherently formed and attached burrs to the side walls of the fabricated micro holes can be seen in Figure 3.13, where an array of fabricated pre-drilled micro holes in droplet cross-sections are shown. The top edges of the fabricated micro protrusions are the part that is machined at the very beginning of the RμEDM process, where the present burrs affect the progressive machining is highest. These burrs keep on damaging the top edges of the micro protrusions until it gets completely detached from the side walls of the micro holes during machining. It gets worn out by 1/3rd of the theoretical discharge energy in RμEDM dissipated on the tool plate [90].

A detailed parametric study in the direction of finding the optimal parametric combination leading to burr-free profiles on tool plates is included as one of the objectives and is discussed in chapter 4. However, the lower MRR, higher *TWR*, cylindricity of single micro protruded structure and concerning the *Ra* of the fabricated arrayed protrusions. A comprehensive study on finding the suitable parametric combination for quality fabrication of arrayed micro protrusions is discussed in the subsequent section.

The results of comprehensive RμEDM experiments have also been evidenced by fabricating arrayed micro protrusions on a widely used biocompatible material. The SEM analysis of the fabricated micro protrusions in elliptical cross-section profiles at different discharge energy settings has been presented in Figure 3.14(a). Arrayed micro protrusions in elliptical cross-sections having the major and minor axis of 700 μm and 500 μm μm, and a height of 150 μm are successfully fabricated. Moreover, an aerofoil cross-sectional profile arrayed protrusions have also been shown in Figure 3.14(b) in order to check the feasibility of fabricating an unconventional cross-sectional profile on that material. Energy-dispersive X-ray spectroscopy (EDS) analysis of the as-received material and machined surface is shown in Figure 3.14(c) for understanding the chemical alteration (if any) during machining. It is found that the peak of carbon (7.66%) and oxygen (4.55%) is favored on the machined surface rather than the basic composition of AZ31B Mg alloy which is due to the carbon deposition from hydrocarbon-based dielectric oil used in machining, and surface oxidation, respectively.

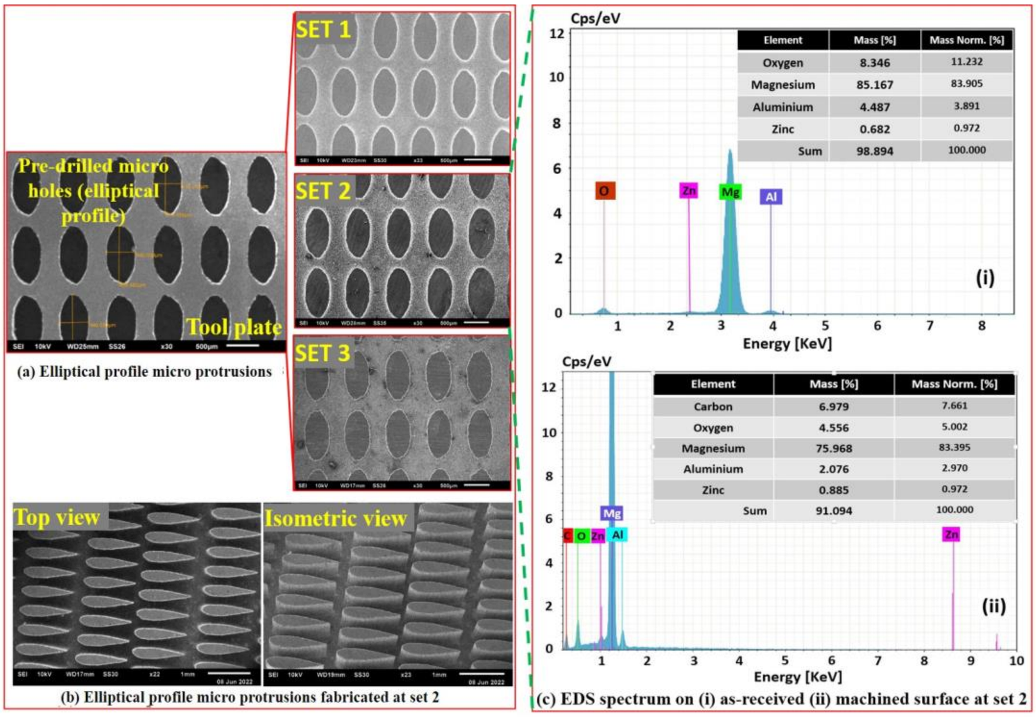

Element	Mass [%]	Mass Norm. [%]
Oxygen	8.346	11.232
Magnesium	85.167	83.905
Aluminium	4.487	3.891
Zinc	0.682	0.972
Sum	98.894	100.000

Element	Mass [%]	Mass Norm. [%]
Carbon	6.979	7.661
Oxygen	4.556	5.002
Magnesium	75.968	83.395
Aluminium	2.076	2.970
Zinc	0.885	0.972
Sum	91.094	100.000

(a) Elliptical profile micro protrusions

(b) Elliptical profile micro protrusions fabricated at set 2

(c) EDS spectrum on (i) as-received (ii) machined surface at set 2

Fig. 3.14 SEM images of fabricated arrayed micro protrusions (a) elliptical, (b) aerofoil profiles, and (c) EDS plots.

3.4. Capability enhancement through parametric study of RµEDM

After the detailed feasibility study towards the fabrication of unconventional cross-section arrayed micro protrusions, process capability in terms of improved machining time and surface qualities is one of the aspects of the present study. Owing to this, faster and more quality fabrication of arrayed micro protrusions, a detailed parametric experimental study has been performed to analyze the influence of machining parameters in that fabrication.

3.4.1. Experimentation

RµEDM experiments are performed for the fabrication of a single diamond-shaped micro protrusion using the discussed hybrid microfabrication technology (shown in Figure 3.15). All the experiments have been performed on the same machine tool mentioned in section 3.3.1., which is based on an RC circuit. Owing to the dependence on the frequently occurring discharge pulses including charging and discharging time, an RC-formulated pulse generator provides a low amplitude of discharge current at a high pulse frequency [43], [60]. The theoretical discharge energy in a single discharge pulse is calculated by using Eq. (3.3):

$$Q = \frac{1}{2} CV^2 \tag{3.3}$$

Where Q is the maximum stored energy in the capacitor, C is the capacitance, and V is the discharge gap voltage. The total discharge energy calculated using Eq. (3.3) has been considered as the basis of performance evaluation by combining the effects of C and V. The pre-drilled tool plate (SS304) consisting of 18 diamond cross-section micro holes fabricated using LBµM which plays an essential role in the fabrication of single micro protrusion as shown in Figure 3.15(d).

The respective diamond cross-section profile micro holes in the tool plate have been fabricated with minimum inter-micro hole gaps at optimal parametric settings. Since the RµEDM process is stochastic and random in realistic nature, it is challenging to predict the output characteristics accurately by mathematical modeling. Hence, Taguchi’s *L16* orthogonal array is utilized for determining the process parameter combinations.

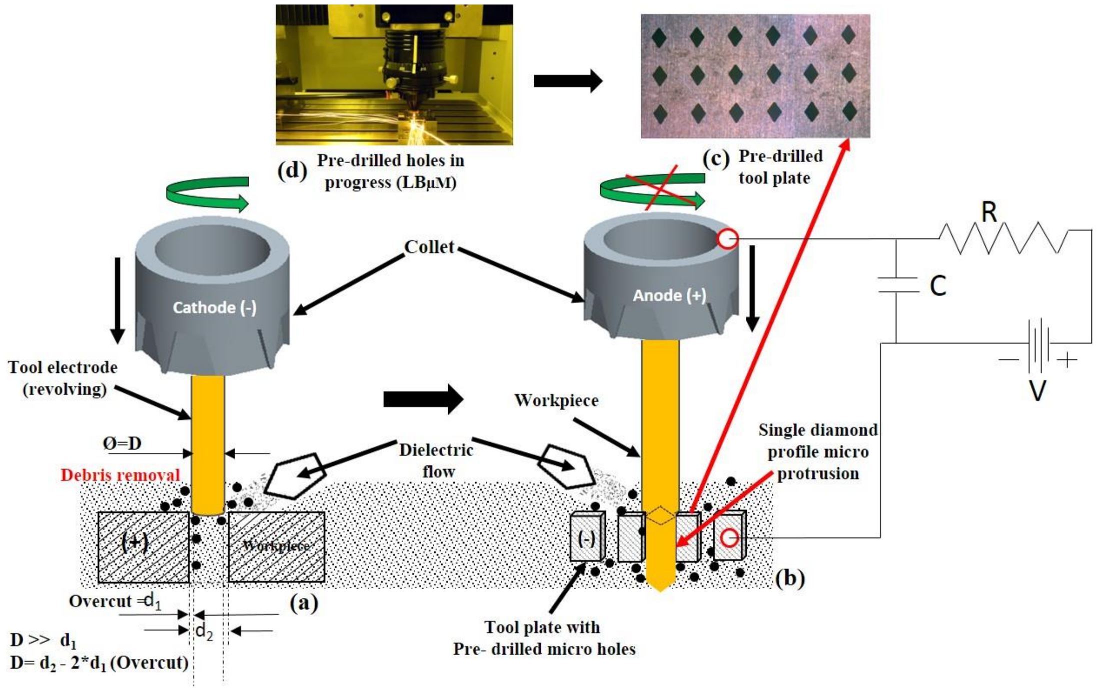
(d) Pre-drilled holes in progress (LBμM)
(c) Pre-drilled tool plate
R
C
V
Collet
Cathode (-)
Anode (+)
Tool electrode (revolving)
Workpiece
Ø=D
Debris removal
Dielectric flow
Single diamond profile micro protrusion
(+)
Workpiece
(-)
(b)
Overcut =d1
(a)
d2
D >> d1
D= d2 - 2*d1 (Overcut)
Tool plate with Pre- drilled micro holes

Fig. 3.15 Schematic of (a) μEDM drilling, (b) RμEDM by reversing the polarity of (a), (c) pre-drilled tool plate for RμEDM, and (d) LBμM used for fabrication of pre-drilled tool plate.

The main reason for using the Taguchi methodology is to select the significant parametric combinations that directly influence the output machining responses in the least number of experimentations [216]. By the design of experiments, a total of 16 experimental runs, three level-four factorials (3^4), have been considered. The discharge voltage (measure across the discharge gap), capacitance, and feed rate have been the experimental work's input parameters, which are considered based on the theoretical perspective of the RμEDM process and the capability of the machine setup. The levels of the discussed input parameters for the experimentation are shown in Table 3.3. All experimental runs have been carried out using a new workpiece and random parametric combination to ensure no error with the machine setup.

Table 3.3. Factors and their levels.

		Levels			
S.No.	**Factors**	**1**	**2**	**3**	**4**
1.	Voltage (v)	100	110	115	120
2.	Capacitance (nF)	1	10	100	400
3.	Feed Rate (μm/sec)	5	10	15	20

The experiment runs are carried out to investigate the effect of the input process parameters on the machining responses like *MRR*, surface roughness, taper root angle of each fabricated micro protrusion. All the micro protrusions are fabricated in a height of 1mm. The RμEDM process parameters combinations including *C* and *V* are arranged in four different segments viz. (i) lower (ii) moderated (iii) moderately higher and (iv) higher, along with the recorded machining responses have been presented in Table 3.4. The fabrication of single diamond micro protrusion at different parametric combinations has been repeated thrice for accurate measurement of machining responses. The repetition has reflected an average error in *MRR* as ±0.0003 mm^3/min, average surface roughness of ±0.018 μm, and taper root angle of ±0.021^0. Table 3.4 presents an average value of the recorded experimental data.

In order to estimate the *MRR*, the weight difference of fabricated micro protrusion before and after machining is adapted. A micro weight balance (Make: RADWAG, Model: MYA 21.4Y) having a readability of 0.1 μg is used for the weight measurement. The obtained values are further divided with the duty factor. The duty factor conveys the actual time utilized in charging (Pulse off-time) and discharging (Pulse-on-time) of the capacitor, neglecting the shorts-circuiting timing and the time consumed in achieving the desired discharge gap by the spindle head.

Table 3.4. *L16* Orthogonal array experimental design and responses.

Input parameters					**Responses**		
Exp. No.	**Voltage (V)**	**Capacitance (nF)**	**Feed Rate (μm/sec)**	**Discharge Energy (μJ)**	**MRR mm^3/min.**	**Avg. surface roughness Ra, (μm)**	**Taper Root Angle (θ)**
01	100	1	5	5	0.0051	1.32	0.03
02	110	1	10	6.05	0.0090	1.34	0.06
03	115	1	15	6.61	0.0109	1.36	0.08
04	120	1	20	7.20	0.0122	1.37	0.09
05	100	10	5	50	0.0239	1.39	0.26
06	110	10	10	60.50	0.0255	1.51	0.35
07	115	10	15	66.12	0.0267	1.59	0.42
08	120	10	20	72	0.0285	1.71	0.56
09	100	100	5	500	0.0587	1.80	0.64
10	110	100	10	605	0.0681	1.87	0.72
11	115	100	15	661.25	0.0767	1.94	0.76
12	120	100	20	720	0.0875	1.99	0.80
13	100	400	5	2000	0.1584	2.07	8.46
14	110	400	10	2420	0.1746	2.17	10.64
15	115	400	15	2645	0.1915	2.22	11.91
16	120	400	20	2880	0.2186	2.31	13.36

The samples have undergone ultrasonic cleaning before the geometrical and surface characterization of each protrusion to confirm that no dangling particles adhered to the fabricated micro protrusions. Subsequently, SEM images of each fabricated micro protrusion have been analyzed for protrusion taper root angle using commercially available Image J software (Figure 3.16). A surface roughness analysis is performed using calibrated Atomic Force Microscopy (AFM) (Make: Bruker Corporation, USA, Model: Bruker multimode 8.0) setup at a force constant of 0.7 N/m. A waviness cut-off length of 0.08 mm for the measurement of filtering form and waviness is considered for recording roughness data. Initially, an area of 100 μm^2 was chosen for scanning the region of interest of 50 μm^2 of each micro protrusion for analyzing the average surface roughness of all the fabricated micro protrusions. Scanning of the micro protrusion's surface has been performed in tapping mode, which ensures no deflection and tilting of the protrusion. The hardware of AFM is controlled by NanoScope 8.10 software (Bruker Corporation, USA).

3.4.2. Experimental outcomes

3.4.2.1. Geometrical and surface characterization

Micro protrusions with a diamond cross-section profile each of height 1mm has been successfully fabricated by the RμEDM process. Besides the successful fabrication, it is essential to evaluate the fabricated micro protrusions health and surface quality at different parametric combinations. The SEM images of the fabricated micro protrusions at different discharge energies have been shown in Figure 3.16. The precisely machined corners of each fabricated micro protrusion show real evidence of the process capability, which augments the outcome of precise machining. Only a fillet or roundness has been observed at the root edges of the few micro protrusions, as shown in Figure 3.16. This may happen due to the simultaneous machining of the pre-drilled tool plate along with the workpiece electrode, which has rarely been observed becoming tapered while machining at the chosen input parameters. Hence, it can be observed that no such occurrence of taper in the shrouding fabricated micro protrusions at lower parametric settings. But at higher discharge energy values the taper in the fabricated micro protrusions can be observed as depicted in Figure 3.16. It is due to the higher tool plate wear that takes place continuously from the frontal surface and at the entry edge of the pre-drilled micro holes in the tool plate. This effect affects the cylindricity of the protrusions in the form of taper as seen from tip to roots of protrusion. During the machining, it has been observed that foreign materials may also get transferred from the liquid dielectric that may be stuck at the minimum gap width inside the pre-drilled micro holes. This might be causing secondary discharges that have resulted in poor surface finish and damaged tips of fabricated micro protrusions. EDS analysis of the tool plate has been performed to observe the elemental changes or chemical alteration if any. The spectrum for elemental analysis has been taken at the upper corner edge of the diamond cross-section pre-drilled tool plate and is shown in Figure 3.17(a). Whereas the EDS plot for the pre-drilled tool plate is presented in Figure 3.17(b), respectively. The elements existing in the tool plate material surface are consistently shown by sharp peaks according to their energy band.

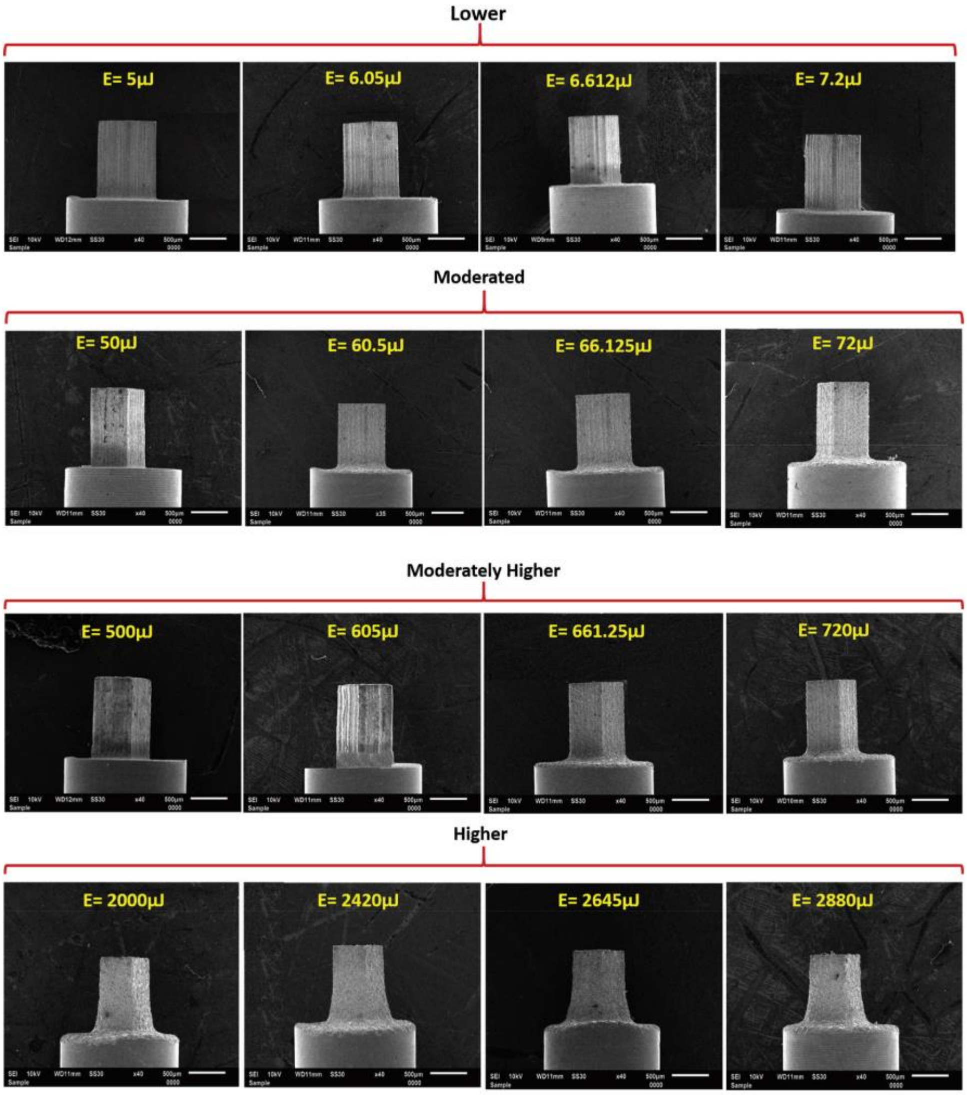
Lower
E= 5μJ
E= 6.05μJ
E= 6.612μJ
E= 7.2μJ
Moderated
E= 50μJ
E= 60.5μJ
E= 66.125μJ
E= 72μJ
Moderately Higher
E= 500μJ
E= 605μJ
E= 661.25μJ
E= 720μJ
Higher
E= 2000μJ
E= 2420μJ
E= 2645μJ
E= 2880μJ

Fig. 3.16 SEM pictograph of fabricated diamond cross-section micro protrusions at different discharge energy segments as lower, moderated, moderately high and higher.

Based on the plot obtained, it is observed that no material transfer takes place in the pre-drilled tool plate (here SS304 is used). For SS304, the observed materials mainly comprise Cr, Mn, Fe, C, Ni, N, Zn, and their weight percentage are 14.4, 1.71, 76.54, 0.18, 9.61, 2.72, and 2.45, respectively. A peak of 2.42% carbon is found in the EDS spectrum after the machining because of the dielectric breakdown over the machined surface of tool plate material and the reduction of debris at the selected discharge energy. It is due to the fact that the tool plate also undergoes sequential melting and evaporation process during the machining. Moreover, a small amount of oxygen (1.8%) may get combined with the pre-drilled tool plate from the atmosphere after the machining that appears in the EDS spectrum. All the additional elements in the EDS spectrum are mainly by the material migration from the sources like workpiece and dielectric at a smaller discharge gap.

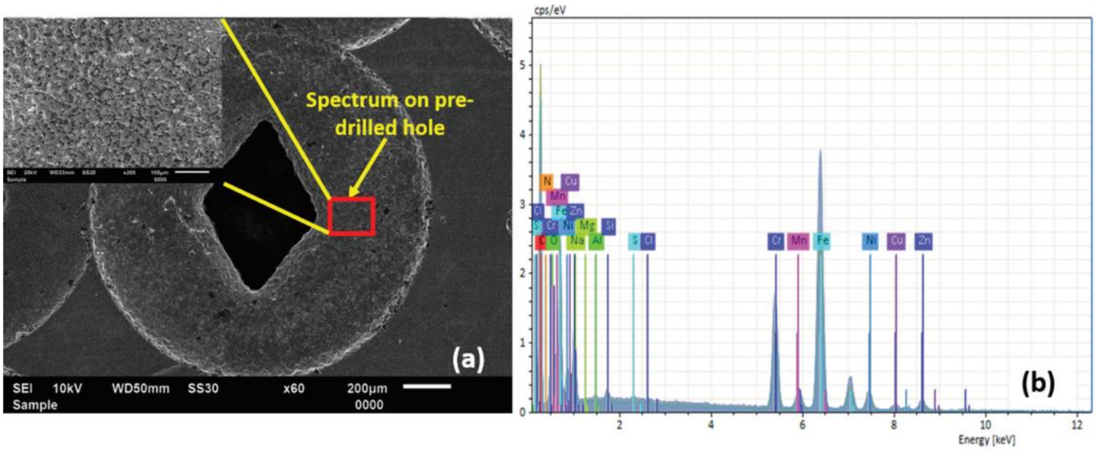

Fig. 3.17 (a) Spectrum on diamond cross-section pre-drilled tool plate (enlarged view of surface in inset), and (b) elemental analysis of the pre-drilled tool plate surface.

Hence, it can be understood that the percentage of different elements present in the pre-drilled tool plate may vary with the changing machining parameters. Similarly, the weight percentage of Cr, Ni, and Fe are comparatively higher than other constituents, which shows the presence of main compositional elements in the tool plate material. However, the presence of copper (Cu) and zinc (Zn) in the EDS spectrum signifies the higher thermal diffusivity of Cu at the low melting regions in the crystal lattices, respectively.

3.4.2.2. Analysis of MRR

The MRR in µEDM is one of the significant machining responses in µEDM due to the reduced discharge gap (mostly less than 10 µm), tool electrode size, and lower pulse discharge energy. The volume of the material removal can be estimated for a single micro protrusion is estimated using the following Eqs. (3.4), and (3.5). It is further elaborated through a pictorial representation in Figure 3.18.

$$MRR = \frac{V_m}{T} = \frac{[V_r - v]}{T} \tag{3.4}$$

$$v = A_p H \tag{3.5}$$

where, V_m = volume of the material removed, T = time taken in the fabrication of a single micro protrusion, V_r = volume of the bulk material (represented by the dotted line in Figure 3.21), v = volume of a micro protrusion, A_p = cross-sectional area of a single micro protrusion, H = height of a micro protrusion.

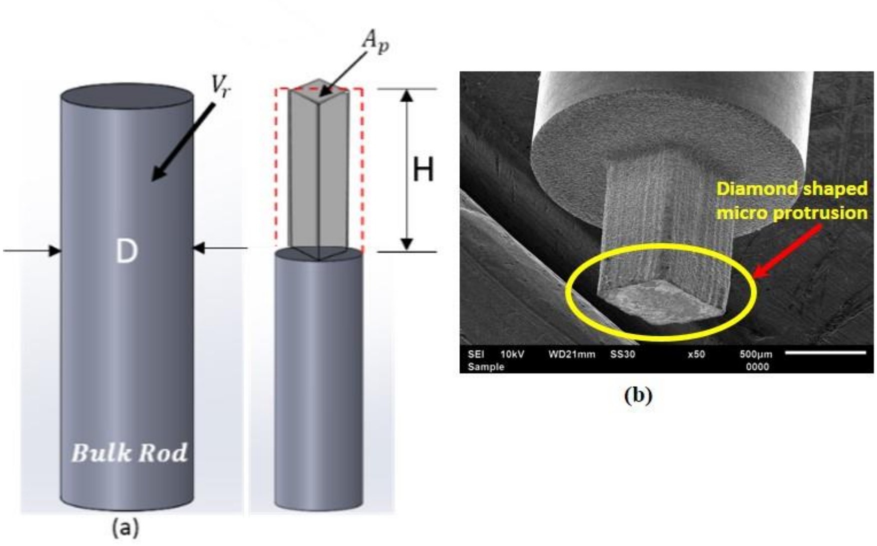
A_p
V_r
H
D
Bulk Rod
(a)
Diamond shaped micro protrusion
SEI 10kV WD21mm SS30 x50 500μm
Sample 0000
(b)

Fig. 3.18 MRR estimation (a) 3D solid model of workpiece electrode before machining, and (b) single diamond cross-section profile micro protrusion after machining.

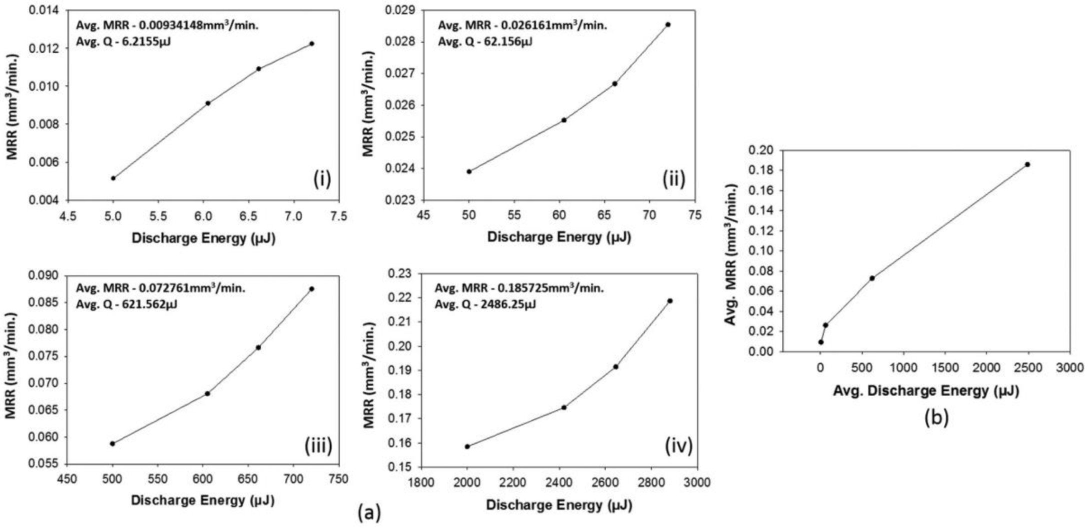

Fig. 3.19 (a) MRR at the different discharge energy segments, and (b) the plot of avg.

MRR values vs avg. discharge energy (Avg. Q).

Figure 3.19(a) shows the variation plot of MRR with the discharge energy. The plots are segmented and presented according to the different discharge energy settings such as, lower, moderated, moderately higher and higher. The increasing trend of MRR in every segment is due to the increasing discharge voltage which results in an increase in discharge energy. A proportional increment in the MRR is observed in the lower segment of discharge energy and is higher than the discharge energy increment. The increasing voltage plays a vital role in giving more clearance to the effective removal of the debris from the machining gap, resulting in the reduction of higher-order non-contributing discharges. Whereas, the proportional increment of the MRR in other segments is showing a significantly decreasing trend compared to increasing discharge energies. These observations may be due to the following two aspects:

1. Reduced frequency of the discharge pulses at higher capacitance due to higher idle time (timing by which workpiece held in spindle approaches to the tool plate for successive discharge).

2. Poor flushing of the ejected debris from a single discharge at higher capacitance and voltage values. For analyzing the combined effect of both the capacitance and voltage average plot of total discharge energies (four segments) against average MRR as presented in Figure 3.19(b).

3.4.2.3. Micro protrusions taper root angle evaluation

The protrusion cylindricity, which is evaluated in terms of the taper root angle of the fabricated micro protrusions, is used for the measurement of deviation in dimensional accuracy. Figure 3.20(a) depicts the ideal geometry of the micro protrusion with zero taper root angle, whereas, Figure 3.20(b) depicts the taper root angle after the mid-length of the actual fabricated single protrusion. The relation used to calculate the taper root angle is given in Eq. (3.6):

$$\theta = tan^{-1} \frac{2L}{D_2 - D_1} \tag{3.6}$$

where, D_1 = axial length at the tip, D_2 = axial length at the root of micro protrusion, L = taper visible height.

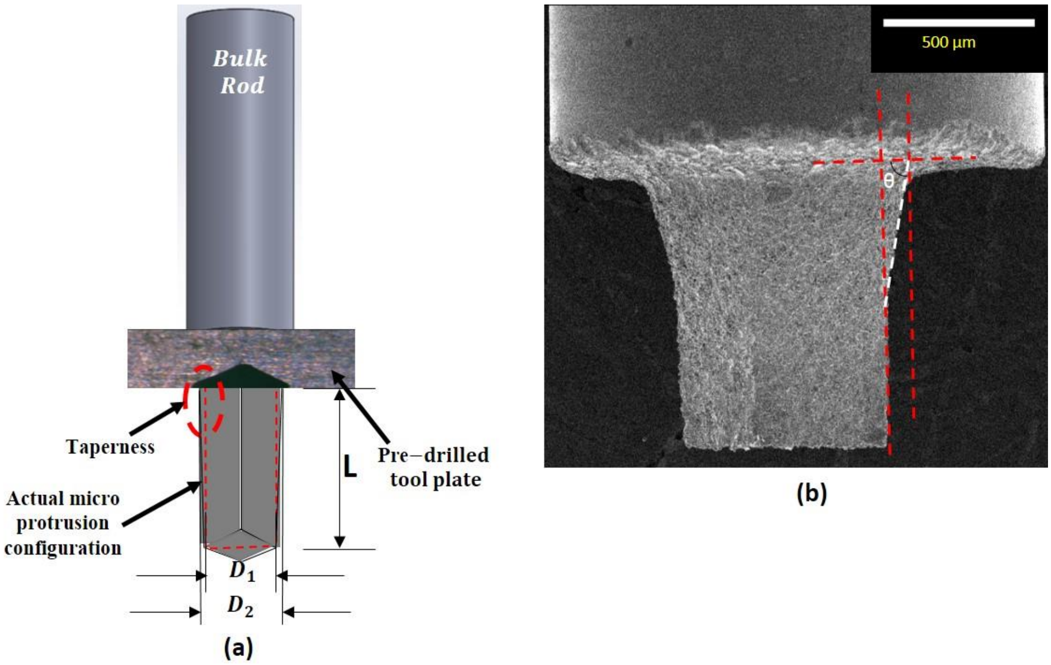

(a)

(b)

Fig. 3.20 (a) Schematic of an ideal micro protrusion, and (b) actual micro protrusion having some taper root angle.

Figure 3.21(a) shows the variation plot of the (θ) increasing discharge energies in different segments. The increased (θ) in each segment is basically due to increasing discharge voltage that resulted in higher discharge energy. A similar result was observed by Nirala et al. [43], where the authors had described that the pre-drilled tool plate has undergone continuous minute sparking for the overall provided length of the fabricated micro protrusion, which causes taper. It is also observed that the proportional increment of (θ), in the lower segment of discharge energy, is higher with increasing discharge energy (Figure 3.21(a)). Comparatively, the (θ) is observed swiftly increasing in other discharge energy segments apart from lower discharge energy. Such variations clearly depict that the discharge voltage constitutes a lower effect than the significantly increasing capacitance values on the taper formation with high angle. Eventually, it can be said that the higher discharge energy due to high capacitance values produces more tool plate wear which in turns generates a reflective image of the micro hole profile in the form of taper to the fabricated micro protrusions. A combined variation plot constituting the effect of voltage and capacitance both are depicted in Figure 3.21(b), showing the trend of average (θ) against average discharge energies of four segments.

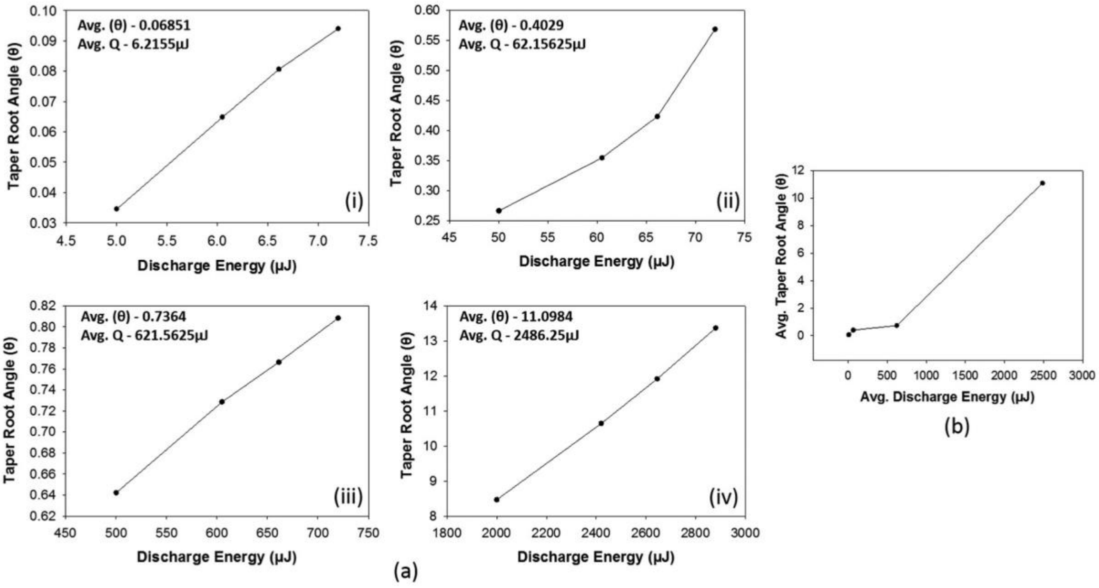

Fig. 3.21 (a) (θ) variation of the fabricated micro protrusion at different discharge energy segments, and (b) the plot of avg. (θ) values vs avg. discharge energy (Avg. Q).

3.4.2.4. Surface roughness measurement

Figure 3.22(a) shows the variation of Ra with increasing discharge energy. The Ra values for each fabricated micro protrusion at different discharge energies segments are in the range of 1.36 µm to 2.3 µm. The increasing values of Ra in each discharge energy segment may be due to increasing discharge voltage that eventually increases the discharge energy. This produces comparatively a larger crater volume in a single discharge pulse. A significant increment of the average Ra value is found in the higher segment of discharge energy which may be due to a large capacitance value providing higher energy responsible for generating a large crater size. A combined variation plot constituting the effect of voltage and capacitance both are depicted in Figure 3.22(b), showing the trend of average Ra against the average discharge energies of four segments.

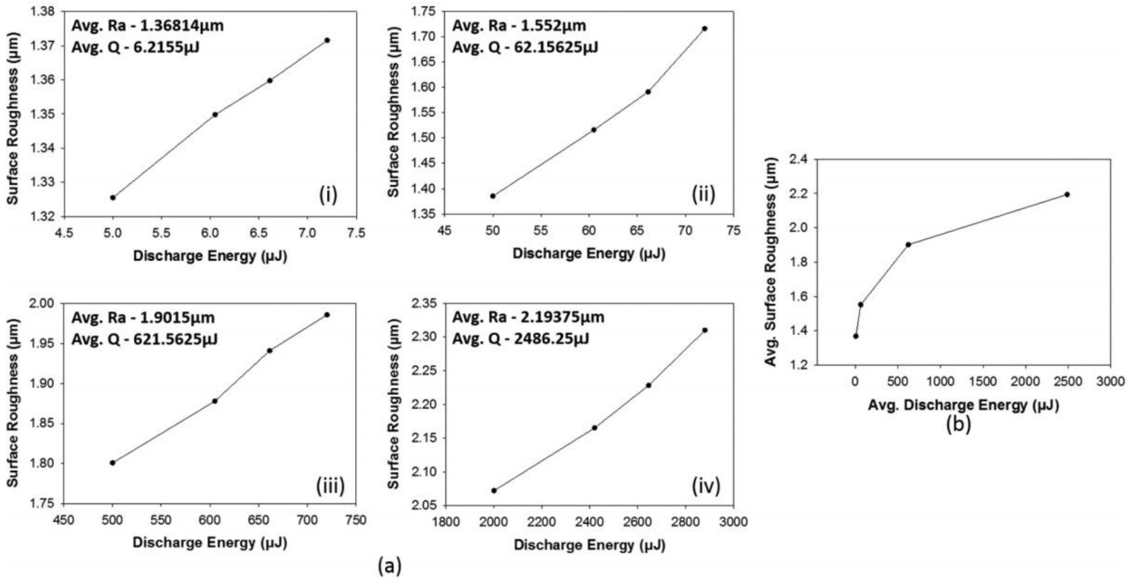

Fig. 3.22 (a) Ra of each fabricated micro protrusion at different discharge energy segments, and (b) Ra vs avg. discharge energy segments (Avg. Q).

A large crater size leading to a rough surface in higher discharge energy segments can be evidenced by SEM images captured at (a) lower and (b) higher discharge energy segments shown in Figure 3.23(a,b). A corresponding comparative 3D profile of the machined surface are shown in Figure 3.23(c,d).

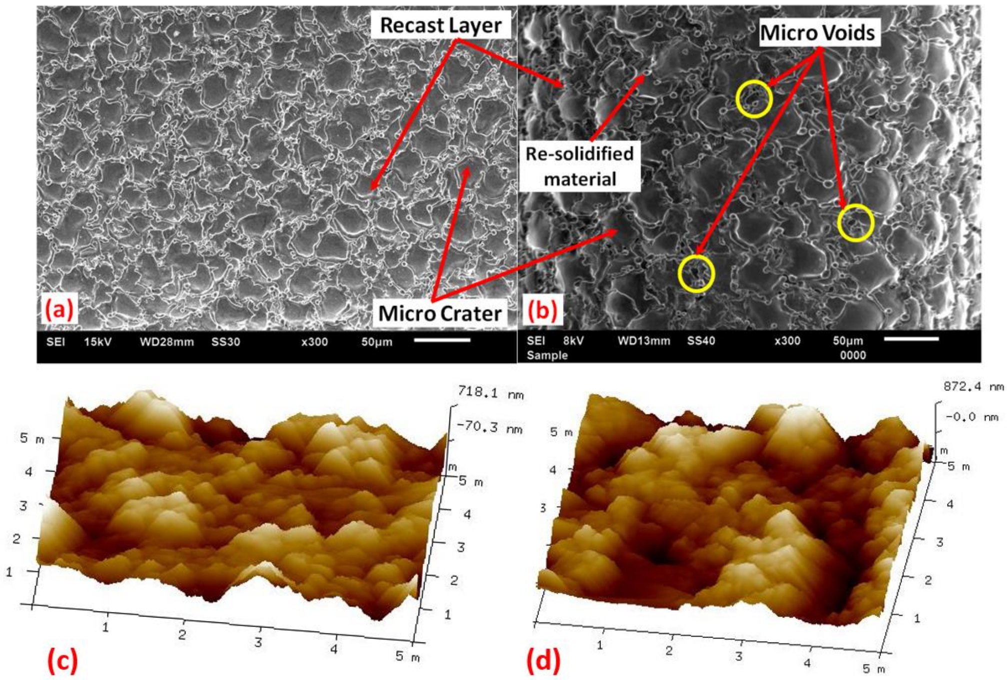
Recast Layer
Micro Voids
Re-solidified material
Micro Crater
(a)
(b)
SEI 15kV WD28mm SS30 x300 50µm
SEI 8kV WD13mm SS40 x300 50µm Sample 0000
718.1 nm
-70.3 nm
872.4 nm
-0.0 nm
(c)
(d)

Fig. 3.23 SEM images (a,b) and its corresponding and 3D surface profiles (c,d) on the machined surfaces at (i) V = 110 V, C = 10 nF, F = 10 µm/sec, and (ii) V = 120 V, C = 100 nF, F = 20 µm/sec.

3.5. Identification of optimal RμEDM process parameters

The intention of this optimization study lies in searching the optimal machining parameters, which are beneficial in fabricating arrayed micro protrusions of higher aspect ratios. It is also believed that machining at optimal parametric setting could improve machining responses in terms of lesser machining time (high MRR), reduced TWR, and good surface finish of the fabricated protrusions.

A well-established Genetic Algorithm (GA) optimization technique is used for finding the optimal parametric setting of the RμEDM process. However, the GA is one such stochastic/evolutionary method in which the solutions by performing an extensive search in the solution space and environment [217]. Its solution quality is mainly dependent on various factors, i.e. effectiveness of the method, robustness, and type of searching methodology, lesser computational time and effort, and the independent estimation of unknowns. In addition to these factors, GA operation is based upon the theory of random numbers and confinement of solution in the local search domain is eliminated.

In this study, the interest of objective function are to maximize the MRR and to minimize Ra and θ. As these objectives are conflicting in nature hence the first objective MRR for minimization, it is suitably modified. The mathematical model correlating the MRR, Ra and θ with the process control parameters as various fitness functions have been generated using the regression model. This model determines the relationship between independent variables and dependent variables using Minitab-19 software. During regression analysis, it is assumed that the variables and the responses are linearly related to each other. The empirical expressions have been developed to evaluate the relationship between input and output variables. The different expressions show the effect of linear order fitness functions and the interaction of the independent process variables and are presented in Eqs. (3.7) and (3.8):

$$Maximize, MRR = Minimize(-MRR) = f_1\ (V, C, F) \tag{3.7}$$

$$Minimize, R_a = f_2\ (V, C, F), and$$

$$Minimize,\ \theta = f_3\ (V, C, F) \tag{3.8}$$

where (V), (C) and (F) are input parameters, respectively. The operational constraints which typically sets the boundaries for the RμEDM machining parameters are presented as follows:

$$100 \leq V \leq 120$$

$$1 \leq C \leq 400$$

$$5 \leq F \leq 20$$

An in-house code for GA algorithm is written in MATLAB®**.** A total of 100 populations is chosen for initializing the algorithm. It is seen that the sufficiently lower value of the objective function remains approximately similar at various operators' values. Hence, two-point crossover and bitwise mutation have been used with a crossover probability, $p_c = 0.9$ and mutation probability, $p_m = 0.03$ as optimal GA parameters. The objective of optimal parametric combination is calculated from the best-fitted pareto multi-objective functions. For achieving better convergence and further deviation (if any), a total of 300 population generations is considered for the final run.

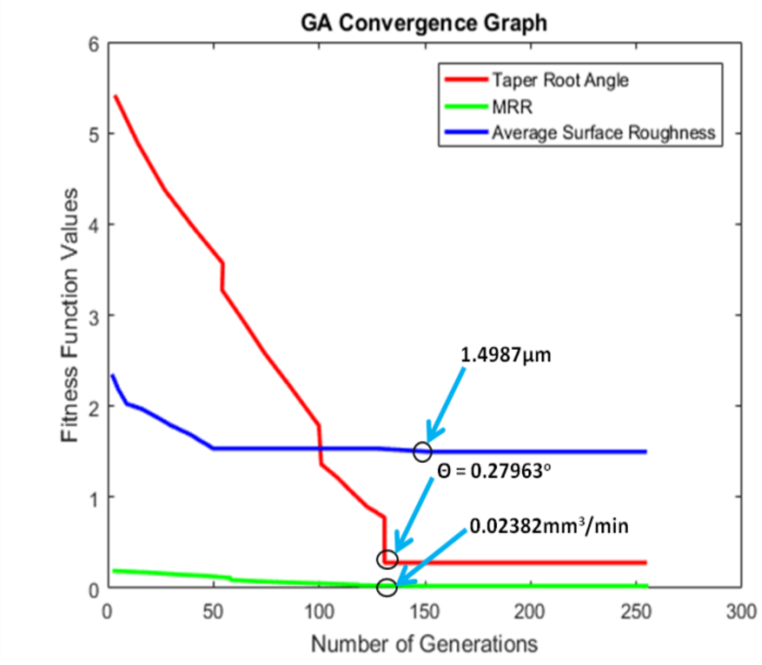

Fig. 3.24 Comparison of the fittest objective functions with the number of generations using an in-house developed GA algorithm.

Figure 3.24 shows the predicted plot of different objectives and the corresponding best fittest values using Pareto multi-optimization functions. These optimum values of machining parameters for which the RµEDM process is expected to offer a high *MRR* and better surface quality and dimensional accuracy. The corresponding values achieved of different objective functions are presented in Table 3.5.

Table 3.5. Optimal process parameters and corresponding machining responses.

Process parameters			**Responses**		
Voltage (V)	Capacitance (nF)	Feed rate (µm/sec)	MRR (mm^3/min)	Ra (µm)	Taper root angle (θ)
110.728	9.859	10.384	0.023	1.42	0.279

The validation of the optimization results with the experimental results is performed in order to confirm the predicted results obtained by GA approach. The optimal RµEDM process parametric setting is used for performing experiments with approximation at a V of 110 V, C of 10 nF, and feed rate of 10 µm/sec. A close relationship between the experimental and predicted results has been achieved. The error percentage in the experimental and predicted GA results is also determined by evaluating the variation in the results obtained, calculated by using Eq. (3.9):

$$Error(\%) = \left(\frac{Experiemental\ values - \ GA\ predicted\ values}{Experimental\ values}\right) \times 100 \tag{3.9}$$

Table 3.6 presents the predicted and validation experimental results for the different machining responses along with the percentage error. The results show that errors of experimental and predicted machining responses are within the acceptable range.

Table 3.6. Validation results of the predicted GA model and validation experimental run.

Responses	**Recorded Values**		
	Predicted (GA Approach)	**Validation experimental Run**	**Error Percentage (%)**
MRR	0.023	0.024	2.05
Ra	1.42	1.49	4.67
θ	0.27	0.30	8.82

Therefore, it has been concluded that the GA modeling approach is suitable for finding the optimal machining parameters. The prediction model results are found to be accurate and precise. The obtained optimal parametric setting is now being used to improve the batch fabrication of arrayed micro protrusions of any cross-sectional profiles with better machining responses. The successful fabrication of arrayed micro protrusions at the optimal parametric combination of RµEDM emphasizes the fabrication feasibility by more downscaling and in different cross-sections, offers many advantages in several applications.

3.6. Chapter conclusion

The present chapter has presented the fabrication feasibility of arrayed micro protrusions of unconventional cross-sections using integrated LBμM and RμEDM processes. The feasibility experiments have been tested over a wide range of materials (including biocompatible material). Additionally, the material removal mechanism in RμEDM is analyzed through single discharge analysis. A detailed RμEDM parametric study has been performed using a multi-objective optimization tool, for finding the optimal parametric combination for enhanced machining responses in those fabrication. Moreover, the quality of fabricated micro protrusions can be improved through and rigorous surface characterization of the fabricated tool plate, which is discussed in the next chapter.

Chapter 4

LBμM for Fabrication of RμEDM Tool Plate

4.1. Introduction

The present chapter investigates the effect of LBμM process parameters on the fabrication of high-quality arrayed micro holes on RμEDM tool plates. A systematic study of the various process parameters and their effects on the surface qualities of the fabricated micro holes of different cross-section profiles is presented in this regard. A multi-objective optimization approach is used for the selection of optimal process parameters. The fabricated arrayed micro holes at the optimized parameters are then used as RμEDM tool plates and the quality of the fabricated protrusions is verified through micrographs.

4.2. Fiber laser generation process

Fiber laser is one of the most accepted solid-state lasers used for micromachining with the beam obtained from suspended ions in a crystal matrix. The name of the laser represents the composition of the crystal grain i.e., Ytterbium. The Ytterbium crystal has excellent thermal, mechanical and optical properties to produce a high-quality coherent laser beam. It is operated at 1070 nm wavelength. Continuous wave and pulsed mode are two types of Ytterbium lasers with the marked difference in output attributes and material machining abilities peak power, pulse repetition rate and pulsed energy affecting the machined speed and ability of pulsed Ytterbium lasers [218]. The efficiency of this laser is comparatively high and laser output can be changed by changing the pump discharge wavefront. Q-switching can regulate the frequency and shape of a laser beam with a shutter shuttling rapidly inside and outside the beam path. In this way, the output beam is broken till the resonator maintains high population inversion energy. The Ytterbium laser’s strongest advantage over other lasers is its ability to produce a continuous beam at room temperature, allowing the laser to be used in typical workplace environments without major modifications. These properties have all contributed to the wide acceptance of the Ytterbium laser in micromachining and other processing applications.

4.2.1. Mechanism of material removal in LBµM

The fundamental means of removing material in LBµM depends on the formation of intense irradiation where high heat flux melts and vaporizes the material at the point where the beam is focused. A lasing medium is needed for generating a laser beam of an appropriate wavelength with a diameter of several millimetres. After that beam is applied on the working surface of the material through the lens. When this beam passes through the lens, the beam converges to a point, with high energy concentration on the surface, where optical energy is converted into heat. The amount of absorption of laser radiation from the workpiece follows primarily on the electrical properties, for example, conductivity, wavelength, and incidence angle of the laser beam, as well as polarization and, finally, directed laser beam intensity. The intense heat of the laser beam melts the material and vaporizes it when the atoms' thermal energy overcomes the binding energy so that the atoms can leave the lattice structure and break down from the surface of the workpiece. Some material vaporizes rapidly to generate a mechanical shock, thereby removing molten material from the cutting area due to the applied assisting gas pressure. It can be concluded that the bulk material removal during LBµM is due to the following factors:

- A high-intensity beam of infrared light generated by a Laser system,
- the beam is directed to a fine spot on the workpiece by a focusing lens,
- focused beam melts the workpiece surface and vaporizes the same, and
- the molten material is ejected out from the melt by assisting gas pressure.

4.3. Experimentation

A fiber Laser head attachment is provided with the machine tool (Hybrid-µEDM DT110i, Mikrotools Pte Ltd.) shown in Figure 4.1(a). The IPG YLM-Q-CW (iPG Photonics, Japan) series Laser is a Class 4 laser product that is designed and tested for safety. The progressive LBµM head is customized to gain an identical positional accuracy. It is a reliable and maintenance-free high-power laser that is developed to meet industrial market demand. Moreover, it is possible to fabricate precise micro holes using LBµM in any profile, which is almost impossible through any other mechanical micromachining. The specification of the laser machining setup is given in Table 4.1.

Table 4.1. Specifications of the CNC pulsed fiber Laser setup.

Specification	**Description**
Type of Laser	Ytterbium fiber laser
Operation mode	Q-switch pulsed
Wavelength (nm)	1070
Laser beam mode	Fundamental mode (TEM$_{00}$)
Q-switch type used	Acoustics optic Q-switched
Mirror reflectivity	Rear mirror 100%, and front mirror 80%
Laser beam spot diameter (µm)	50
Beam Propagation ratio, M^2 (mm)	1
Pulse width (ms)	0-1
Pulse Frequency (Hz)	1-100
Current Percentage (%)	0-100
Assiting gas pressure (bar)	5-20

The experiments are performed on a commercially available pure titanium (ASTM Grade 2) sheet of thickness 0.5 mm. The microsecond pulsed fibre laser is used to fabricate micro holes of desired cross-section profiles. Pulse width, pulse frequency, and laser power expressed as the Percentage of the applied current to the diode lasers are the essential process parameters that can be varied according to the material and sheet thickness. The peak power resulting in material removal is an essential parameter for achieving dimensionally accurate high-quality micro holes calculated by Eqs. (4.1 - 4.3) [219];

$$T_p = Duty\ cycle \,/\, f \tag{4.1}$$

$$P_{peak} = P_{avg} \,/\, f \times T_p \tag{4.2}$$

$$E_{pulse} = P_{peak} \times T_p \tag{4.3}$$

Here 'T_p is pulse width and f is the pulse frequency. It can be observed from Eq. (4.2) that the peak power of the laser is a function of average power P_{avg} developed for a given pulse frequency and pulse width. The present work utilizes a smaller spot size high-intensity laser beam profile, usually based on the fluence profile of the Gaussian distribution function with two thresholds beam diameter, as shown in Figure 4.1(d) [220].

The irradiated laser beam follows the trepanning scanning tool path (Figure 4.2(c)) at beam propagation ratio (M^2=1) in the x-axis on the sheet. An illustration of ongoing LBμM for micro holes fabrication on the sheet is shown in Figure 4.1(b).

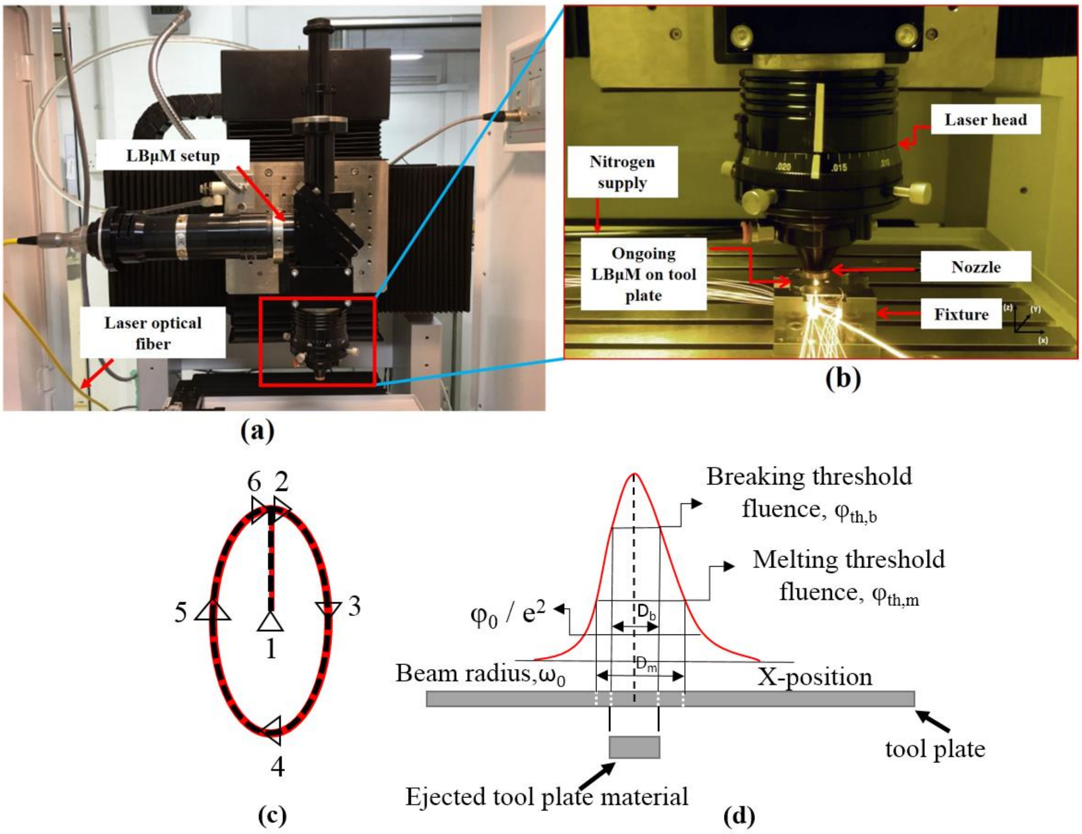
LBμM setup
Laser optical fiber
(a)
Laser head
Nitrogen supply
Ongoing LBμM on tool plate
Nozzle
Fixture
(b)
6
2
5
3
1
4
(c)
Breaking threshold fluence, φth,b
Melting threshold fluence, φth,m
φ0 / e2
Db
Dm
Beam radius,ω0
X-position
tool plate
Ejected tool plate material
(d)

Fig. 4.1 Typical image of (a) LBμM setup, (b) ongoing LBμM for fabrication of micro holes, (c) trepanning scanning pattern, and (d) Gaussian beam profile distribution.

A dedicated fixture is used to hold the workpiece (which is to be used as a pre-drilled tool plate for RμEDM) in such a way that there remains a gap for the free flow of ejected melted material (Figure 4.2(i)). The flow of the molten metal from the cut kerf is assisted by shielding gas (nitrogen) which is coaxially supplied to the laser head. The main LBμM parameters include pulse width, pulse frequency, and average laser power expressed as the percentage of the applied current to the diode lasers. The different LBμM process parameters and their levels considered to perform the experimental runs are summarized in Table 4.2.

Table 4.2. Factors and their levels.

Input factors	Units	Level			
		1	2	3	4
Pulse width	ms	0.25	0.5	0.75	1
Pulse frequency	Hz	95	50	65	80
Current Percentage	DC (%)	20	40	60	80

A design of experiments (DOE) approach based on Taguchi *L16* orthogonal array is applied to identify the best possible parametric combination with minimum experimental runs required, as shown in Table 4.3. The auxiliary parameters viz. stand-off distance, assisting gas pressure, and scanning speed, are kept constant at 300 µm, 9 bar, and 150 mm/min, which has more or less significant in terms of quality fabrication. The quality criterion of LBµM includes the measured machining responses of each micro-hole in terms of minimum recast layer height, Ra_T, taper, and maximum MRR_T, along with HAZ microhardness. All the experimental runs are performed thrice, and the average values of each response are shown in Table 4.3.

Table 4.3. Experimental runs and the recorded LBµM responses.

	Factors				**Responses**				
	A	**B**	**C**	**D** $=A \times B \times 10^{-1}$					
Exp No.	Pulse Width (ms)	Frequency (Hz)	Current (%)	Duty cycle	MRR_T (mm^3/min.)	Height of recast layer (mm)	Ra_T (µm)	Taper (rad)	Hv, *HAZ* (micro holes)
1	**0.25**	**50**	**20**	**1.250**	**0.738**	**0.034**	**1.46**	**0.01**	**123**
2	0.25	65	40	1.625	0.753	0.042	1.78	0.029	128
3	0.25	80	60	2.000	0.782	0.049	1.91	0.043	130
4	0.25	95	80	2.375	0.807	0.056	2.02	0.051	134
5	0.50	50	40	2.500	0.831	0.062	2.14	0.068	139
6	0.50	65	20	3.250	0.878	0.078	2.58	0.077	145
7	0.50	80	80	4.000	0.911	0.083	2.87	0.112	151
8	0.50	95	60	4.750	0.963	0.107	3.17	0.124	162
9	0.75	50	60	3.750	0.876	0.071	2.47	0.094	156
10	0.75	65	80	4.875	0.942	0.093	2.98	0.132	163
11	0.75	80	20	6.000	1.015	0.111	3.58	0.159	171
12	0.75	95	40	7.125	1.062	0.123	3.95	0.181	179
13	1	50	80	5.000	0.952	0.096	3.02	0.146	165
14	1	65	60	6.500	1.029	0.119	3.70	0.168	173
15	1	80	40	8.000	1.094	0.128	4.35	0.211	183
16	1	95	20	9.500	1.108	0.132	4.68	0.237	188

An elliptical cross-sectional profile micro holes have been fabricated at each parametric combination. Each elliptical microhole's major and minor axes are 950 µm and 500 µm.

The machined micro holes at different parametric combinations are evaluated for detailed dimensional analysis, chemical composition, and surface characterization alteration. A 2D Image acquisition of the fabricated holes is conducted using an optical microscope (ZEISS Axio Vert. A1, Carl Zeiss Microscopy GmbH, Germany). It is followed by microstructural and EDS analysis on the micro hole's surface using SEM setup equipped with an XFlash 6130 QUANTAX (Bruker.com) EDS system. Additionally, the inherent burr formation, the height of the recast layer, and striation mark effects have also been evaluated. Besides these, various essential LBµM responses have been evaluated, such as MRR_T (weight difference measurement upon scanning time), Ra_T (using roughness tester, Mitutoyo, 178-923E SJ210 series (Figure 4.2(iii)). The top and bottom kerf width (W_t) and (W_b), and taper (Figure 4.2(ii)) are also evaluated for each micro hole. For the precise calculation of mass loss, an electronic micro-weighing balance (RADWAG Balances and Scales Ltd., MYA 21.4Y) having a repeatability of 0.1 µg is used.

Another response i.e., HAZ micro-hardness, is measured using a Vickers hardness testing machine (Wilson Instruments, 402 MVD) near the cut edge of each micro hole. Each measurement is performed three times, and their average values have been recorded for minimum deviation in the obtained results (Table 4.3). The marked locations near the cut edges and base metal are illustrated in Figure 4.2(iv).

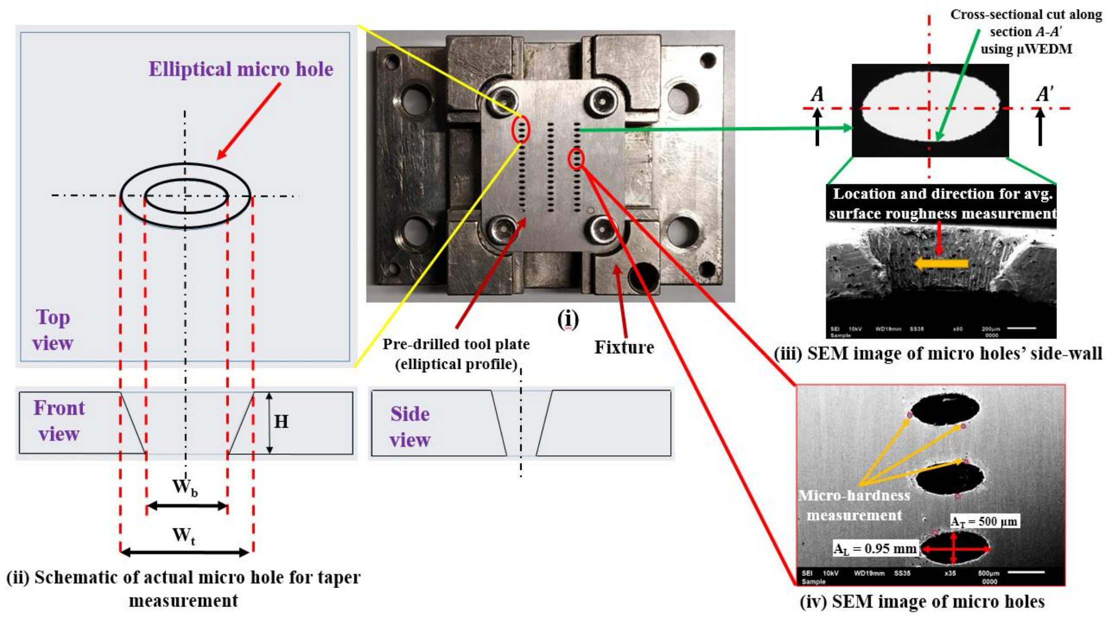
Elliptical micro hole
Top view
Front view
H
W_b
W_t
Side view
Pre-drilled tool plate (elliptical profile)
Fixture
Cross-sectional cut along section A-A′ using µWEDM
A
A′
Location and direction for avg. surface roughness measurement
Micro-hardness measurement
A_T = 500 µm
A_L = 0.95 mm
SEI 10kV WD19mm SS35 x80 200µm 0000 Sample
SEI 10kV WD19mm SS35 x35 500µm 0000 Sample

(i)

(ii) Schematic of actual micro hole for taper measurement

(iii) SEM image of micro holes' side-wall

(iv) SEM image of micro holes

Fig. 4.2 (i) Fabricated tool plate, illustration for estimating (ii) taper, (iii) Ra_T, (iv) and micro-hardness of tool plate.

4.4. Results and Discussion

This section detailed the outcomes of the tool plate fabrication and the recorded responses mentioned in section 4.3 at different LBμM parameters. The multi-objective optimization using Grey relational analysis (GRA) has been performed to find optimal parametric combinations and is also discussed in detail. It is followed by a detailed discussion regarding the dimensional and surface quality evaluations of RμEDM fabricated arrayed protrusions using tool plates fabricated at optimal LBμM parameters.

4.4.1. LBμM experiments

The optical images of all the fabricated micro holes at different duty cycles (combination of pulse width and pulse frequency) are shown in Figure 4.3. The microscopic images are arranged according to the experimental sequence number, as presented in Table 4.3. It is observed that the micro holes fabricated at lower duty cycles have shown good dimensional accuracy with minimal burr formation than the micro holes fabricated at higher duty cycles. It may be due to the required amount of workpiece metal melting and vaporization and better efficiency of molten metal removal from the cut kerf at lower duty cycles. Post-examining of fabricated micro holes reveals the uniform and non-uniform striation patterns on the holes' side-wall at different duty cycles, as shown in Figure 4.4. It is a well-accepted fact in LBμM that the formation of different striation patterns on the holes' side walls depends on the viscosity of molten metal changes due to the purging of assisting gas and laser beam irradiation intensity. The purging gas augments the cooling effect and generates the drag force on the molten metal escaping through the cut kerf, which usually gets stick to the micro holes side-walls. The rate of flow of molten metal (fluid strain) also changes due to the movement of the nozzle head along with the desired holes' profile which alters the amount of molten metal purging outside the cut kerf of micro holes. The increased molten metal's viscosity and surface tension along the tool plate thickness results in the increased viscous shear at the hole's side-wall. This viscous shear force retards the molten metal streamlines to accumulate at the bottom of the micro hole, resulting in better dimensional accuracy and a shallow striation pattern at the lower duty cycles. In comparison, at the higher duty cycles, excessive molten metal is ejected, which is not entirely escaped out through micro hole, resulting in the formation of clogged burrs visible at the bottom of the fabricated micro holes shown in Figure 4.4.

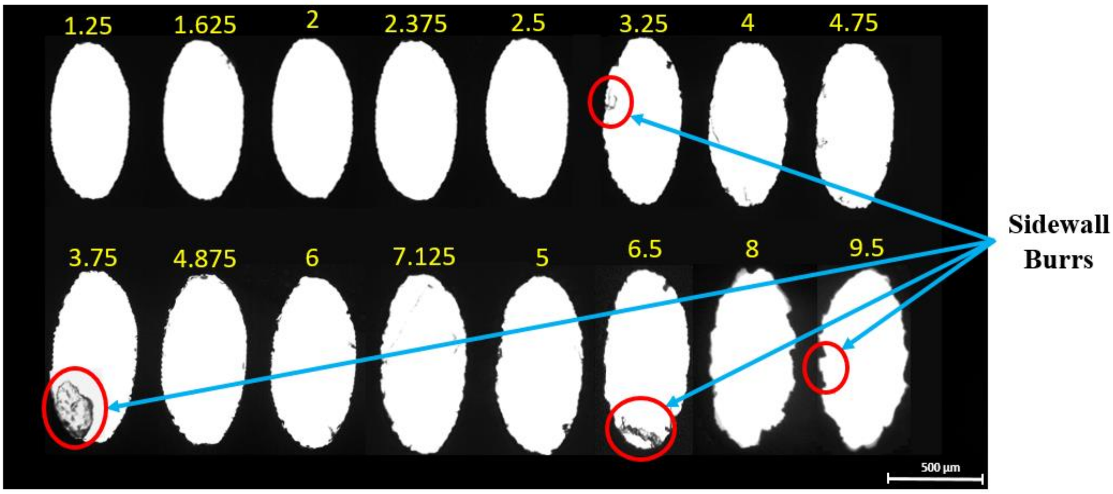
1.25
1.625
2
2.375
2.5
3.25
4
4.75
3.75
4.875
6
7.125
5
6.5
8
9.5
Sidewall Burrs
500 µm

Fig. 4.3 Image of cut kerf of micro holes at different parametric combinations (indicated by corresponding duty cycle values).

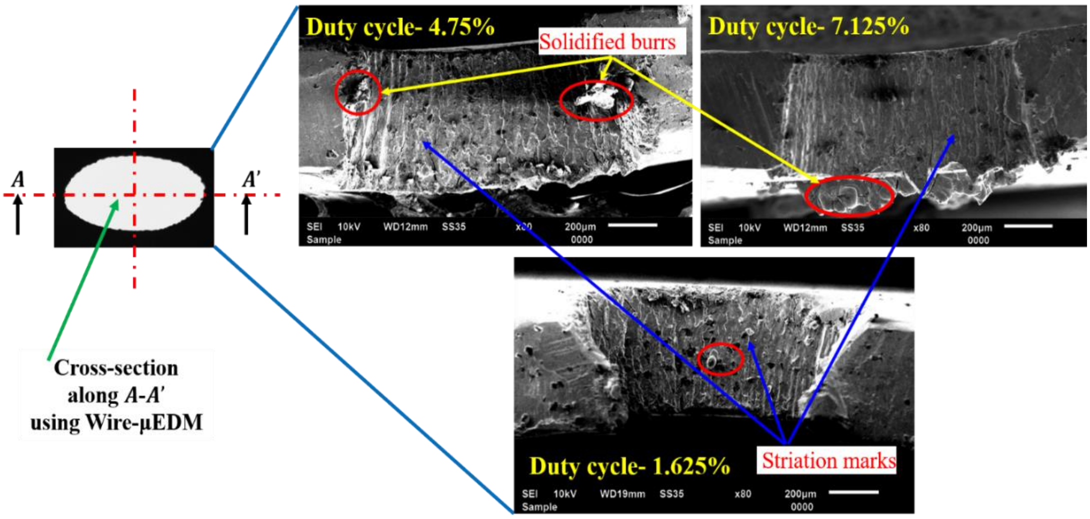
Duty cycle- 4.75%
Solidified burrs
Duty cycle- 7.125%
A
A′
Cross-section along A-A′ using Wire-µEDM
Duty cycle- 1.625%
Striation marks
SEI 10kV WD12mm SS35 x80 200µm 0000 Sample
SEI 10kV WD12mm SS35 x80 200µm 0000 Sample
SEI 10kV WD19mm SS35 x80 200µm 0000 Sample

Fig. 4.4 SEM images of holes’ cut-section depicting striation marks at different duty cycles.

4.4.2. EDS analysis of tool plate

The extent of the alteration in the HAZ region is also analysed through the elemental distribution of the titanium tool plate. Quantitatively, the elemental data has been presented for better comparison between the base metal and the HAZ region of the micro hole are shown in Figure 4.5(a(i,ii)). To illustrate both regions on the tool plate surface, the spectrum is highlighted with a red box in the corresponding SEM image of the micro holes shown in Figure 4.5(a).

It is found from the EDS plot near the cut edge that the smaller percentage of diffused oxygen is approximately 8%, carbon 29%, and the rest is base metal. The presence of smaller oxidation zones and carbide formation may be due to the reaction of the base metal to environmental gases present in the machining chamber during machining or surface oxidation. However, the EDS of the base metal shows only the titanium content. This chemical alteration may affect some base metal properties like strength and micro-hardness around the periphery of the produced micro-hole. Some micro-sized split boundaries, micro pores, and globular solidification impressions are found at the cut edges, as shown in Figure 4.5(b). These features might be occurred due to sudden vaporization and bubble formation in the melted metal layer. A dense recast layer adjacent to the micro holes cut edge is evidenced, and the reasons for the formation are detailed in the next sub-section.

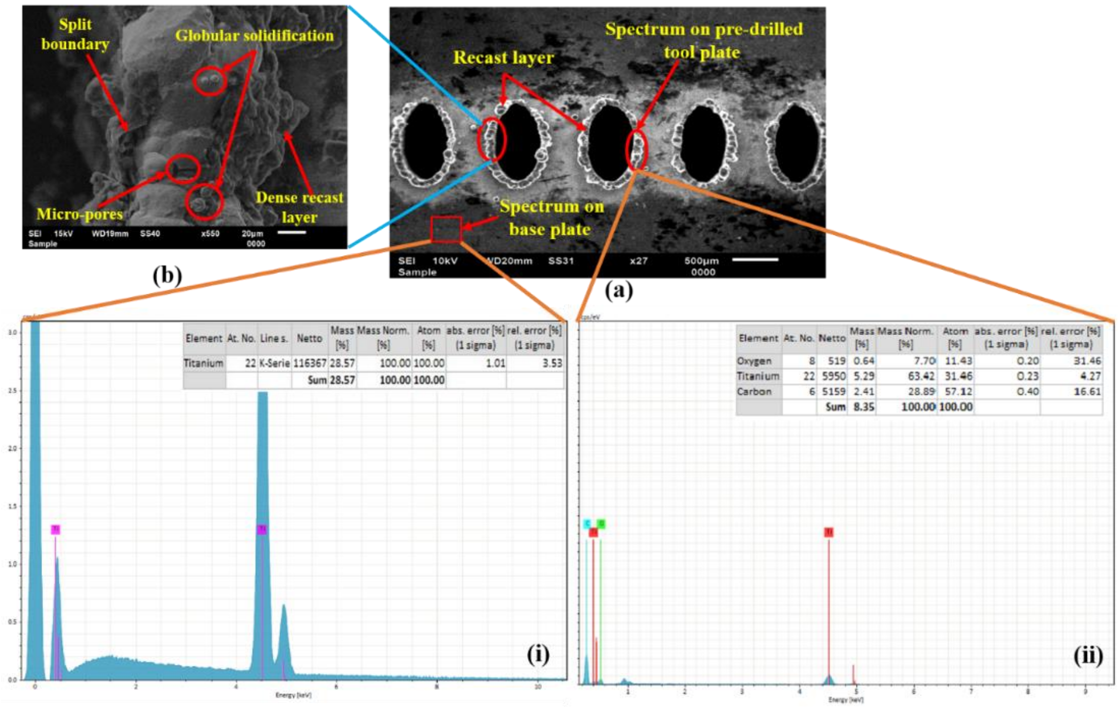

Element	At. No.	Line s.	Netto	Mass [%]	Mass Norm. [%]	Atom [%]	abs. error [%] (1 sigma)	rel. error [%] (1 sigma)
Titanium	22	K-Serie	116367	28.57	100.00	100.00	1.01	3.53
			Sum	28.57	100.00	100.00		

Element	At. No.	Netto	Mass [%]	Mass Norm. [%]	Atom [%]	abs. error [%] (1 sigma)	rel. error [%] (1 sigma)
Oxygen	8	519	0.64	7.70	11.43	0.20	31.46
Titanium	22	5950	5.29	63.42	31.46	0.23	4.27
Carbon	6	5159	2.41	28.89	57.12	0.40	16.61
		Sum	8.35	100.00	100.00		

Fig. 4.5 (a) EDS plots on tool plate (i) base metal, (ii) cut edge of micro hole, and (b) enlarge view of the cut edge.

4.4.3. Recast layer and *MRR* estimation of micro holes

The workpiece top surface is subjected to intense laser beam irradiation resulting in sequential heating, melting, and vaporization, leading to the metal's removal through cut kerf of the respective micro holes. While some portion of the re-solidified molten metal gets interlocked at the cut edge, called as recast layer. The SEM images of micro holes confirm the recast layer formation as shown in Figure 4.5(a,b).

Figure 4.6(a) shows the line graph of the recast layer height against increasing duty cycle at the constant current of 20% (% of peak power) for all micro-holes. It is observed that the trend for recast layer height is growing with the increase in duty cycle lies between 0.034 to 0.132 mm. A similar trend of recast layer heights has been observed with an increasing current percentage from 20 to 80%. It is because of the longer interaction time between the tool plate and the intense laser beam at a particular parametric combination. The increasing laser beam energy per unit area, leads to more melting, causing more recast layer formation at the cut edges. Also, the high vapor pressure on the molten metal surface causes intense shock toward the base metal surface. Thus, the thermal gradient effect from the adjacent base metal generates hot plasma above the tool plate surface at the cut edge. This hot plasma absorbs laser energy coming towards the base metal surface, for which the intensity of the laser beam is somewhat reduced. At the larger duty cycles, high thermal gradients occur between the base metal and cut edge of the tool plate surfaces at a particular assisting gas pressure, resulting in the thicker recast layer height.

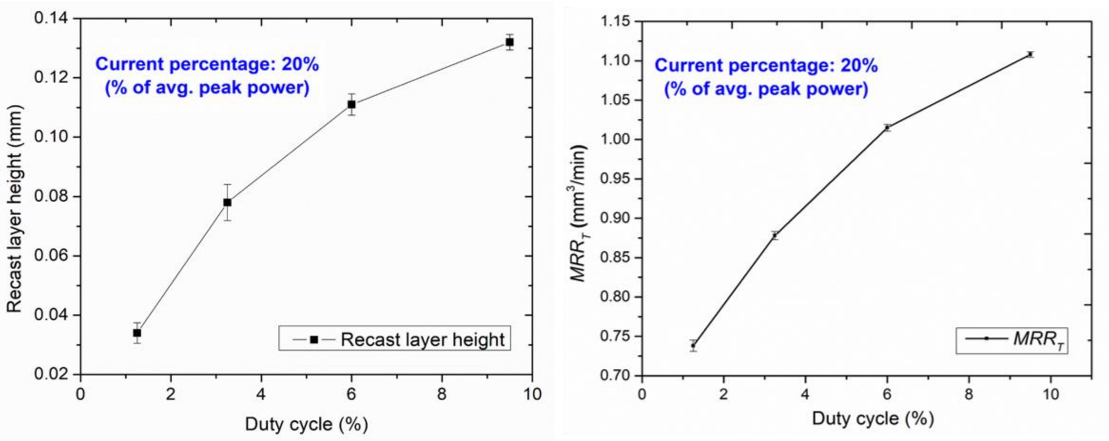

(a) **(b)**

Fig. 4.6 Variation of (a) recast layer heights (b) MRR_T with duty cycle.

The influence of LBμM parameters on MRR_T is also evaluated for the productivity of the micro holes. The corresponding MRR_T data for each experimental run shown in Table 4.3 varies from 0.738 to 1.108 mm^3/min for lower to higher duty cycles. Figure 4.6(b) shows the variation for MRR_T at a constant current of 20%. A similar trend has been observed for the increased MRR_T with an increasing current percentage from 20 to 80%. With the increasing current percentage (at higher duty cycle), the tool plate's top surface is susceptible to intense laser irradiation and faster melting and vaporization, which leads to an improved MRR_T.

4.4.4. Taper measurement of micro holes

The edge and the side-wall of the micro holes get slightly modified, causing the non-identical entrance and exit, producing a taper due to the varying heat input and assisting gas pressure. Figure 4.7 exhibits the effect of increasing the duty cycle at a constant current percentage of 20% on the taper of the micro holes. A similar trend of the increasing taper is observed for every consistent current percentage from 20% to 80%, showing the dominant contribution among other input parameters. As the laser beam's power increases, the incident beams' thermal energy directly transfers to the top surface of the tool plate. As a result, the top surface of the tool plate gets severely melted and vaporized, and the strength of the beam decreases at the bottom edge, causing metal removal through a narrow gap. In addition, assisting gas pressure causes an increment in the taper by simultaneously cooling and ejecting the melted metal from the top surface of the tool plate. Thus, it alters and promotes the settling down of melted metal at the side-walls of the drilled holes at a higher duty cycle.

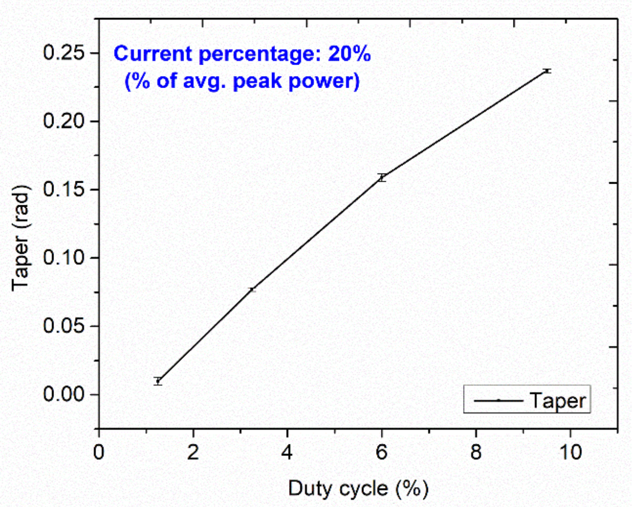

Fig. 4.7 Variation of taper with duty cycle.

4.4.5. Average surface roughness measurement, Ra_T

Increasing laser intensity irradiation on the tool plate surface results in higher amounts of molten metal removal. Also, the drag force generated by assisting gas pressure purging out the molten metal faster causes unevenness on the side-wall surface of micro holes. The effect of LBµM parameters on varying Ra_T of micro holes side-wall can be analyzed through the line plot in Figure 4.8(a). The variation of Ra_T value with duty cycle at different current percentages ranging from 20% to 80% is observed as 1.46 to 4.68 µm (Table 4.3). It is observed that the Ra_T values are minimal at the lower duty cycle in LBµM. A lower duty cycle ensures the availability of great timing for the laser beam to melt and vaporize the molten metal. Also, the melted metal removal from the cut kerf is supported by suitable assisting gas pressure, which drags the molten metal uniformly. However, with an increase in the duty cycle, the Ra_T values show an increasing trend. Excessive melt pool formation caused by partially melting base metal near the cut edge creates non-uniformity on the side-wall's surface as non-uniform striation marks and high Ra_T values.

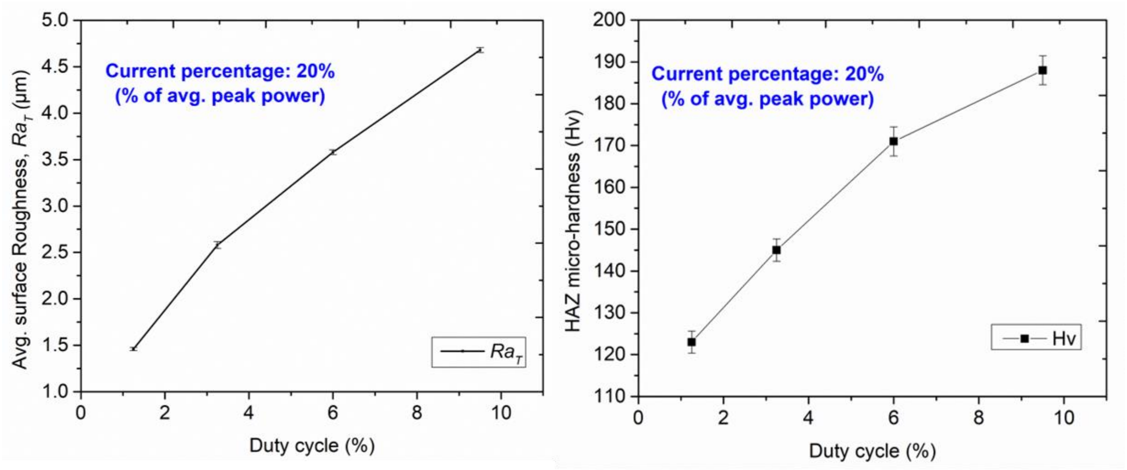

(a) (b)

Fig. 4.8 Variation of (a) Ra_T, and (b) HAZ micro-hardness with duty cycle at the current percentage of 20%.

4.4.6. Micro-hardness measurement of micro holes HAZ

The variation of HAZ micro-hardness with increasing duty cycle at constant current percentage is illustrated in Figure 4.8(b). A similar trend has been observed for increased micro-hardness with an increasing current percentage from 20 to 80%. It is observed that the hardness near the cut edge of each micro hole is significantly higher than the hardness of the base metal. Intense hard and brittle layers of titanium nitrides near the cut edges and varying thermal loading lead to surface modification at the edges. The formation of these layers may be due to chosen assisting gas pressure and grain refinement. The traces of carbide formation at the hole's cut edge are confirmed by EDS analysis shown in Figure 4.5(a(ii)).

4.5. Process parametric optimization study

The present work considers Taguchi *L16* orthogonal array-based Grey relational multi-objective optimization due to the minimization of the variance of the characteristic of interest. The GRA is based on the grey system theory. It is an efficient analysis tool for multi-response analysis for solving complicated inter-relationships of maximizing and minimizing the recorded responses. The first step in GRA is to normalize the results between 0 and 1 using Eq. (4.4) (for maximization) and Eq. (4.5) (for minimization). The normalized values of the measured responses are provided in Table 4.4. The grey relational coefficient is computed from the normalized data in the second step to present a correlation between desired and actual experimental results (Table 4.5). After that, the overall grey relational grade is computed by calculating the mean of the grey relational coefficient corresponding to each performance characteristic. Overall evaluation of the multiple performance characteristics is based on the calculated grey relational grade. This results in the optimization of the complicated multiple performance characteristics converted into the optimization of a single grey relational grade (Table 4.6). A higher grey relational grade of performance characteristic shows the optimum parametric combination of LBμM.

The performance characteristic of recorded responses which is a maximum-the-better is normalized as follows:

$$x_i = \frac{x_i^0(k)-x_i^0(k)}{x_i^0(k)-x_i^0(k)} \tag{4.4}$$

Where (k) =1 to n, i=1-16, n is the performance characteristic, and i is the experimental run.

The performance characteristic of recorded responses which is a minimum-the-better is normalized as follows:

$$x_i = \frac{max\, x_i^0(k)- x_i^0(k)}{x_i^0(k)-x_i^0(k)} \tag{4.5}$$

where x_i is the value after grey relational generation, $x_i^0(k)$ is the smallest value of, $x_i^0(k)$ and is the largest value of x_i.

Table 4.4. The normalized values of the recorded responses.

MRR_T	**Height of recast layer**	**Ra_T**	**Taper**	**HAZ micro-hardness**
0	1	1	1	0
0.04054	0.918367	0.900621	0.931899	0.076923
0.11891	0.846938	0.860248	0.869175	0.107692
0.18648	0.775510	0.826086	0.833333	0.169231
0.25135	0.714285	0.788819	0.757168	0.246154
0.37837	0.551020	0.652173	0.716845	0.338462
0.46756	0.5	0.562111	0.560035	0.430769
0.60810	0.255102	0.468944	0.506272	0.6
0.37297	0.62244	0.686335	0.640681	0.507692
0.55135	0.397959	0.527950	0.470430	0.615385
0.74864	0.214285	0.341614	0.349462	0.738462
0.87567	0.091836	0.226708	0.250896	0.861538
0.57837	0.367346	0.51552	0.407706	0.646154
0.78648	0.132653	0.304347	0.309139	0.769231
0.96216	0.040816	0.102484	0.116487	0.923077
1	0	0	0	1

The grey relational coefficient $[\xi i(k)]$ can be calculated as follows:

$$\xi_i(k) = \frac{\Delta_{min} + \zeta\ \Delta_{min}}{\Delta_{oi}(k) + \zeta\ \Delta_{max}} \qquad (4.6)$$

Note that higher is better when X_i (k) = X_0 (k), i.e., when X = reference.

Table 4.5. Grey relation coefficient of the recorded responses.

MRR_T	**Height of recast layer**	**Ra_T**	**Taper**	**HAZ micro-hardness**
0.33333	1	1	1	0.33333
0.34259	0.85964	0.83419	0.88012	0.35135
0.36203	0.76562	0.78155	0.79261	0.35911
0.38065	0.69014	0.74193	0.75	0.37572
0.40043	0.63636	0.70305	0.67310	0.39877
0.44578	0.52688	0.58974	0.63844	0.43046
0.48429	0.5	0.53311	0.53193	0.46762
0.56060	0.40163	0.48493	0.50315	0.55555
0.44364	0.56976	0.61450	0.58185	0.50387
0.52706	0.45370	0.51437	0.48563	0.56521
0.66546	0.38888	0.43163	0.43457	0.65656
0.80086	0.35507	0.39268	0.40028	0.78313
0.54252	0.44144	0.50788	0.45775	0.58558
0.70075	0.36567	0.41818	0.41986	0.68421
0.92964	0.34265	0.35777	0.36139	0.86666
1	0.33333	0.33333	0.33333	1

Here x_0 (k) denotes the reference sequence, x_j (k) denotes the comparability sequence,

$\zeta \in [0-1]$ is the distinguishing coefficient; 0.5 used for non-linear problems, $\Delta 0i = \|x_0\ (k) - x_i\ (k)\|$ is the difference in absolute value between $x_0\ (k)$ and $x_j\ (k)$, $\Delta_{min} = min_{\nabla j \in i} min_{\nabla j \in k}\ \|x_0\ (k) - x_i\ (k)\|$ is the smallest value of $\Delta 0i$, $\Delta_{max} = max_{\nabla j \in i} max_{\nabla j \in k}\ \|x_0\ (k) - x_i\ (k)\|$ is the largest value of $\Delta 0i$.

After computing grey relational coefficients, the grey relational grade is obtained using the relation as follows:

$$\gamma_i = \frac{1}{n}\sum_{k=1}^{n} \xi_i(k) \tag{4.7}$$

where γ_i is the grey relational grade and *n* is the number of performance characteristics.

Table 4.6. Grey relation grade and ranking of the recorded responses.

Sr. No.	**Grey Relational Grade**	**Ranking**
1	0.733333	1
2	0.653583	2
3	0.612189	3
4	0.587691	5
5	0.562345	7
6	0.526263	10
7	0.503393	15
8	0.501179	16
9	0.54273	9
10	0.509201	13
11	0.515427	12
12	0.546408	8
13	0.507038	14
14	0.517737	11
15	0.57163	6
16	0.6	4

Subsequently, the average grey relation grade for each level of the chosen factor is calculated. The higher the grey relation grade implies the better quality characteristics. The optimum level of each input process parameter is obtained based on the higher grey relation grade. The average grey relational grade and the optimum levels of the factors are listed and highlighted in bold in Table 4.7.

Table 4.7. Average grey relational grade at each level.

Average grey relational grade					
Parameters	**Level 1**	**Level 2**	**Level 3**	**Level 4**	**Max-min**
Pulse width	**0.6466**	0.5232	0.5284	0.5491	0.1234
Pulse frequency	**0.5863**	0.5516	0.5506	0.5588	0.0346
Current (%)	**0.5937**	0.5834	0.5434	0.5268	0.0669

4.5.1. Parametric optimization results

From the Grey relation multi-objective optimization, the parametric combination for the first experimental run (Table 4.3) has shown the best performance for the optimal selection of parametric combination (maximizing MRR_T, HAZ micro-hardness, and minimizing recast layer height, taper, Ra_T. The optimum parametric combination includes pulse width of 0.25 ms, pulse frequency of 50 Hz, and current percentage of 20%. With this optimal parametric combination, an experimental validation run has been performed by fabricating a micro hole. The reproduced machined micro hole fabricated has presented satisfactory machining responses with less than 1% percentage error. It is confirmed through an experimental validation run shown in the inset (Figure 4.9) that has no evidence of side-wall burrs and any significant deviation in the taper. This parametric combination is further utilized in the micromachining of single and arrayed micro-holes for producing arrayed protrusions.

4.6. RμEDM using optimally fabricated tool plate

The machined single micro hole at the optimized LBμM parameters is used to fabricate a single protrusion using RμEDM. The SEM images of the single elliptical protrusion and the fabricated micro hole are shown in Figure 4.9. The fabricated protrusion is almost free from tip damage around its periphery and perpendicular along the orthogonal length, which confirms the better geometrical accuracy when fabricated at an optimal parametric combination.

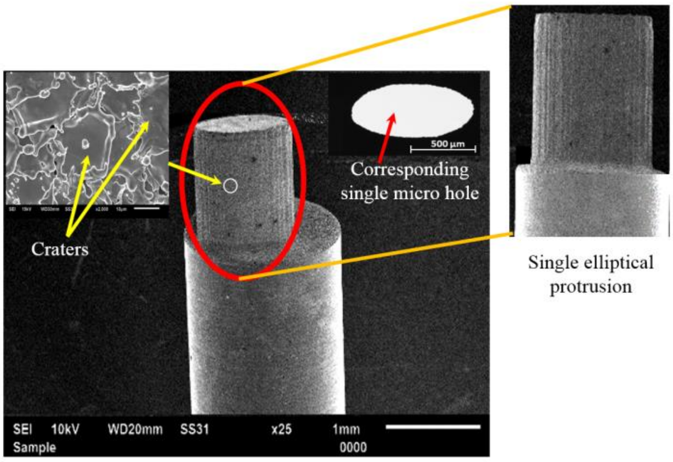
Craters
500 µm
Corresponding single micro hole
Single elliptical protrusion
SEI 10kV WD20mm SS31 x25 1mm
Sample 0000

Fig. 4.9 SEM image of single elliptical protrusion produced using micro hole (shown in the inset).

4.6.1. Optimal tool plate for arrayed protrusions fabrication

The feasibility of the obtained optimal LBμM parametric combination is further checked by fabricating arrayed elliptical and droplet micro holes and subsequent arrayed protrusions. A fabricated tool plate is having a collection of 10 × 15 micro holes is fabricated at two different LBμM parametric settings. (i) a non-optimal combination (includes a pulse width of 0.75 ms, pulse frequency of 75 Hz, and a current of 20%, and (ii) an optimal parametric combination. Whereas, the fabrication methodology is already well-discussed in section 4.3. For the present analysis, the machining conditions for RμEDM and optimal LBμM are given in Table 4.8 of which results are discussed in the next sub-section.

Three essential output responses, i.e., MRR_P, Ra_P, TWR, have been rigorously monitored and recorded as they are significantly affected by the nature of the machining environment. In addition to geometrical analysis, surface characterization, Ra_P and micro-hardness of tool plates have also been evaluated. The locations and measurement approach can be understood through the schematic illustrations shown in Figure 4.10.

Table 4.8. Process conditions of RμEDM and LBμM and measured responses.

RμEDM parameters (based on expertise and availability)		**LBμM parameters (based on GRA optimization)**	
Setup	RC based	LASER type	Nd-YAG YLR-150/1500-QCW-MM-AC-Y11
Resolution (X,Y,Z)	0.1 μm	Wavelength	1070 nm
Tool plate	Titanium	Power	150 W
Workpiece	Brass	Frequency	50 Hz
Gap voltage	110 V	Pulse width	0.25 ms
Capacitance	10 nF	Spot dia	55 μm
Electrode Feed Rate	5 μm/s	current (%)	20
Dielectric oil (type)	NICUT LL21 E		

Measured Responses after RμEDM

RμEDM using tool plate fabricated (Droplet protrusion)	**Approximate Time (hrs)**	***MRR***	***TWR* (mm^3/min.)**	***Ra$_P$* (μm)**	**Micro-hardness of tool plate (Hv) Before M/cing**	**Micro-hardness of tool plate (Hv) After M/cing**
(i) with random parametric set	32	0.119	0.0053	1.63	118	125
(ii) with optimal parametric set	28	0.142	0.0042	1.46	118	129

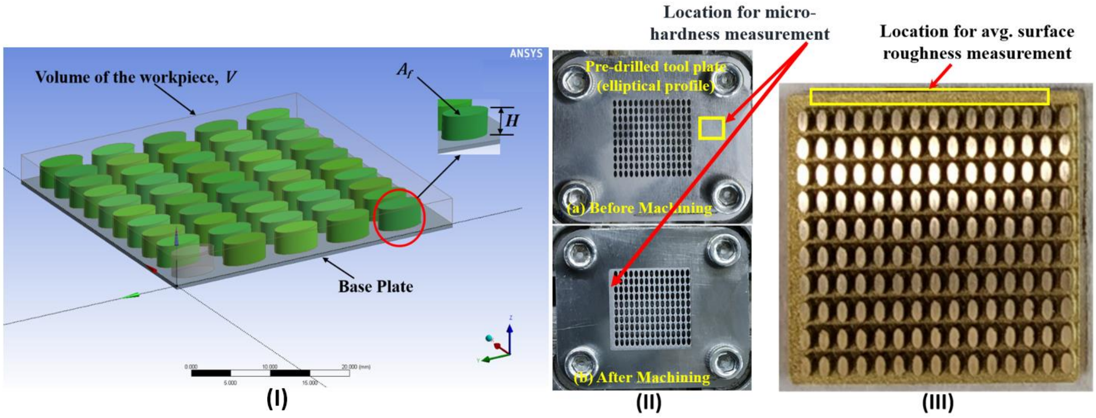
Volume of the workpiece, V
A_f
H
ANSYS
Base Plate
(I)
Location for micro-hardness measurement
Pre-drilled tool plate (elliptical profile)
(a) Before Machining
(b) After Machining
(II)
Location for avg. surface roughness measurement
(III)

$$MRR_P = \frac{V_R}{T} = \frac{[V - nv]}{T}$$

$'V_R'$ = volume of the material removed

$'T'$ = time taken in the fabrication of a complete array

$'V'$ = workpiece volume undergone RμEDM

$'v'$ = volume of a single structure

$'n'$ = number of protrusions in a complete array

$'A_f'$ and $'H'$ = cross-sectional area and height of a single protruded structure

$$TWR = \frac{1000\,(W_0 - W_1)}{D_t T_m}$$

$'W_0'$ =weight of the tool plate before RμEDM

$'W_1'$= weight of the tool plate after RμEDM

$'T_m'$ is total machining time (mins)

Fig. 4.10 Illustration for (i) *MRR*, (ii) *TWR* estimation, and (iii) location for *Ra$_P$* measurement.

The SEM images of fabricated arrayed protrusions at both parametric settings are depicted in Figure 4.11(a,b). The fabricated arrayed protrusions, with the tool plate machined at the non-optimal parametric combination, come up with the issue of damaged edges of a few protrusions, as seen in Figure 4.11(a). The present burrs at the side-walls resulted in longer machining time, due to higher-order discharges. Therefore, the discharging occurs between the edges of the progressive protrusions and the burr material, and continues to erode the workpiece material until it gets removed from the entire micro holes. Comparatively, it is found insignificant while fabricated at optimized LBμM parameters, as shown in Figure 4.11(b). The reason could be well understood by looking back at the micro hole fabricated at the optimized LBμM parameters, as shown in Figure 4.9 (inset). Since it has no apparent cleavage or burrs at the micro holes cut edges, it allows faster machining by restricting high-order discharges and short-circuiting during RμEDM.

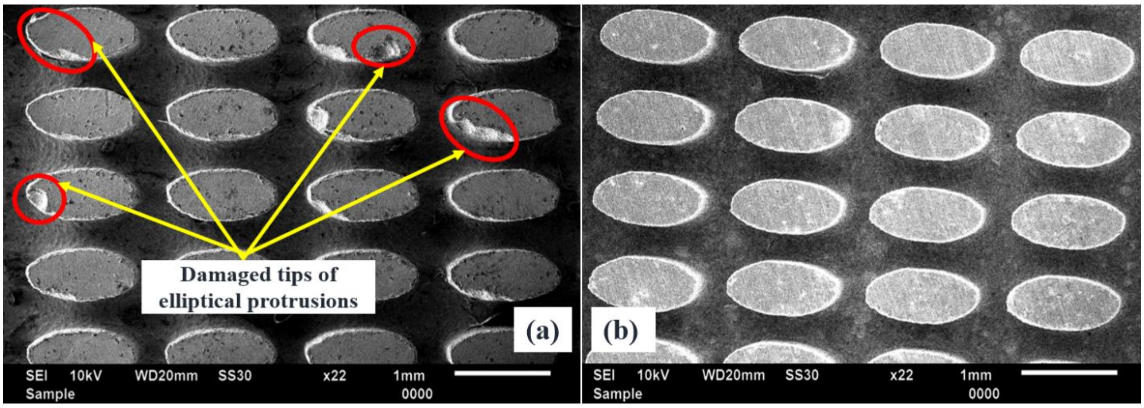
Damaged tips of elliptical protrusions
(a)
(b)
SEI 10kV WD20mm SS30 x22 1mm
Sample 0000
SEI 10kV WD20mm SS30 x22 1mm
Sample 0000

Fig. 4.11 SEM images of fabricated elliptical arrayed protrusions with (a) non-optimal and (b) optimal LBμM parametric combinations.

A more complex cross-section profile has been machined to check the augmented feasibility of optimal LBμM parametric combination. An arrayed droplet cross-section micro holes using LBμM and subsequent protrusions using RμEDM are also fabricated. For which, the minimum inter-electrode gap of 100 μm is taken in a staggered configuration. The partial magnified profile of a few protrusions from an array taken at the center is shown in Figure 4.12(a,b).

The recorded dimensions of each fabricated protrusion are approximately 1 mm in longitudinal and 800 μm in the transverse direction. The height of arrayed protrusions is 1 mm with an almost negligible taper at the walls of protrusions. The reason for high-quality droplet protrusions adheres to a similar explanation reported for elliptical protrusions fabrication.

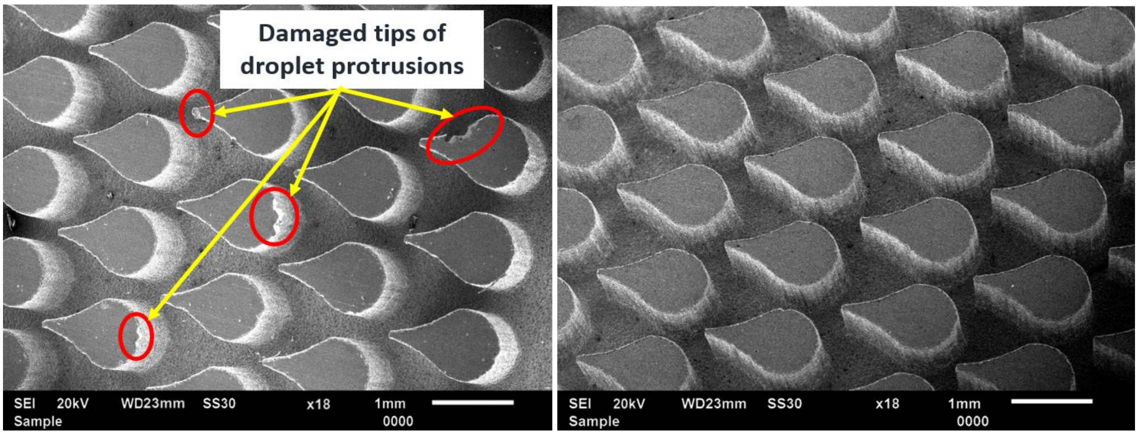
Damaged tips of droplet protrusions
SEI 20kV WD23mm SS30 x18 1mm
Sample 0000
SEI 20kV WD23mm SS30 x18 1mm
Sample 0000

Fig. 4.12 SEM images of fabricated droplet arrayed protrusions with (a) non-optimal and (b) optimal LBµM parametric combinations.

In RµEDM, the workpiece and tool plate, being anode and cathode, are subject to intense sparking to generate a new surface. The alteration in the modified surface of the tool plate is confirmed through elemental analysis captured at the zone where machining takes place after RµEDM. Figure 4.13(a) depicts the spectrum, whereas Figure 4.13(b) shows the elemental plot on the machined tool plate. The composition of the tool plate is observed to be altered compared to before machining conditions. It mainly includes Cu (3.78%), Zn (0.64%), C (26.45%), and the rest of the base metal Ti (69.13%), which shows the migration of workpiece material onto the tool plate. The carbon content is evidenced, mainly due to the vaporization of hydrocarbon-based liquid dielectric during RµEDM.

Responses including MRR_P, TWR and Ra_P recorded improvements of 16%, 20% and 10%, respectively, while using the tool plate fabricated at optimized LBµM parameters. The recorded responses from the RµEDM are presented in Table 4.8. The burr-free tool plate at the optimized LBµM parameter leads to uninterrupted machining, hence, improved MRR_P, TWR, and Ra_P. Also, it leads to the cease of abnormal discharges by proper debris evacuation from the discharge gap. However, abnormal discharges due to debris accumulation significantly increase tool wear in µEDM [60]. As a result, there is less possibility for debris re-solidification, due to its rapid cooling, on the machined tool plate surface in RµEDM. Comparatively, the tool plate fabricated at the optimized LBµM parameters provides scope for rapid cooling during RµEDM. Hence, it leads to slightly better micro-hardness of the pre-drilled tool plate at the cut edge of the micro holes.

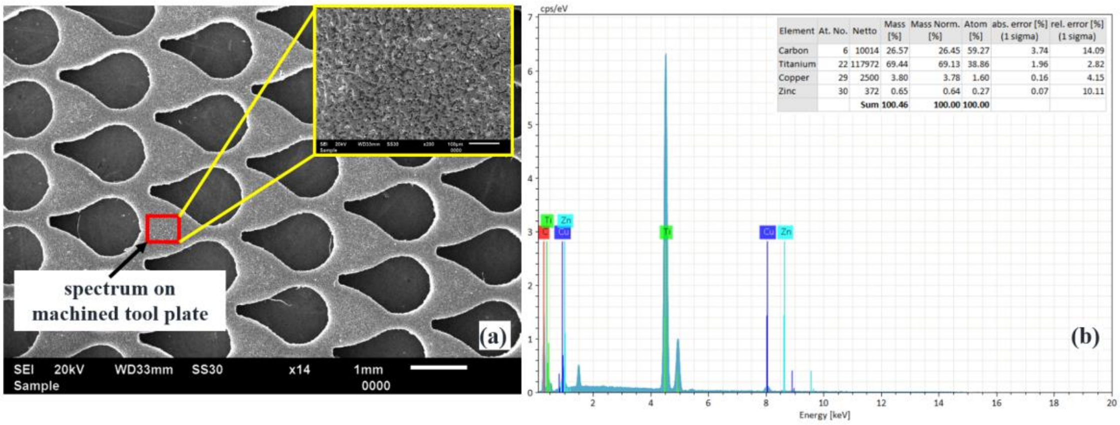

Element	At. No.	Netto	Mass [%]	Mass Norm. [%]	Atom [%]	abs. error [%] (1 sigma)	rel. error [%] (1 sigma)
Carbon	6	10014	26.57	26.45	59.27	3.74	14.09
Titanium	22	117972	69.44	69.13	38.86	1.96	2.82
Copper	29	2500	3.80	3.78	1.60	0.16	4.15
Zinc	30	372	0.65	0.64	0.27	0.07	10.11
		Sum	**100.46**	**100.00**	**100.00**		

Fig. 4.13 Energy spectrum on (a) tool plate after RμEDM, and (b) corresponding EDS plot.

4.7. Chapter conclusion

The present work optimizes fiber laser based LBμM process parameters using the Gray relation analysis technique, for producing good quality arrayed micro holes of unconventional cross-section profiles. The duty cycle which is a combination of pulse width and frequency, and the peak power which is expressed as the percentage of the applied current to the pump system are considered as significant input process parameters for the LBμM affecting the quality of the micro holes. The duty cycle of 1.25% and the current of 20% are optimal settings for the fabrication of burr-free shallow striation micro-holes with a minimal dimensional error. Thereafter, analogous protrusions of high dimensional accuracy and minimum deterioration are produced by RμEDM using the LBμM fabricated tool plates. But still, there is a scope of research in the direction of reducing the total machining time utilized in the fabrication of arrayed protrusions which is discussed in detail in the next chapter.

Chapter 5

Suction-based Dielectric Flushing in RμEDM

5.1. Introduction

This chapter explains the approach to enhance the process stability by introducing a new suction-based high-pressure flushing technology in RμEDM. The procedure used in the development of an in-house fabrication of this technology has been presented in detail. This chapter enumerates the effect of the integration of the new flushing methodology on improving machining responses. Moreover, a simulation study has been presented to analyze the debris flow in this setup. A feasibility study by fabricating arrayed micro protrusions has been presented as a benchmark solution.

5.2. Issues of debris accumulation in RμEDM

The RμEDM and its working principle are explained in chapter 3. Since sparking is the generic phenomenon in any of the μEDM processes' variants, evacuating debris completely from the machining gap is necessary.

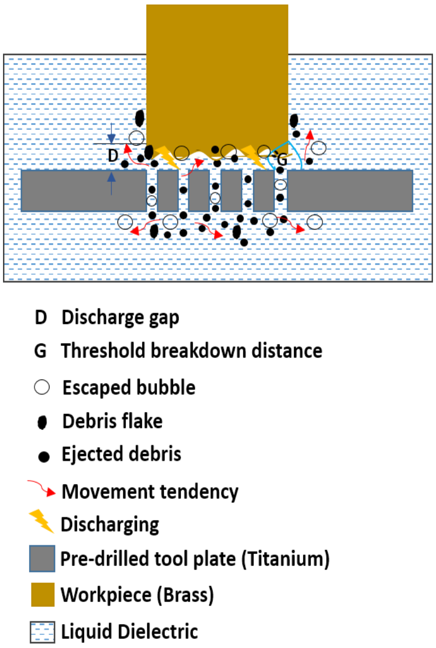
D
G
D Discharge gap
G Threshold breakdown distance
○ Escaped bubble
Debris flake
● Ejected debris
Movement tendency
Discharging
Pre-drilled tool plate (Titanium)
Workpiece (Brass)
Liquid Dielectric

Fig. 5.1 Schematic illustration of the machining zone in RμEDM.

If the removed materials, in the form of tiny debris (in the micro and nano ranges), are not properly dispelled through the machining gap for a longer time frame, short-circuiting and higher-order discharges occur. It also results in the early breakdown of the dielectric, and hence the spark generation becomes challenging. The illustrations in Figure 5.2. (a) and (b) show the debris accumulation in both µEDM and RµEDM captured during the ongoing machining.

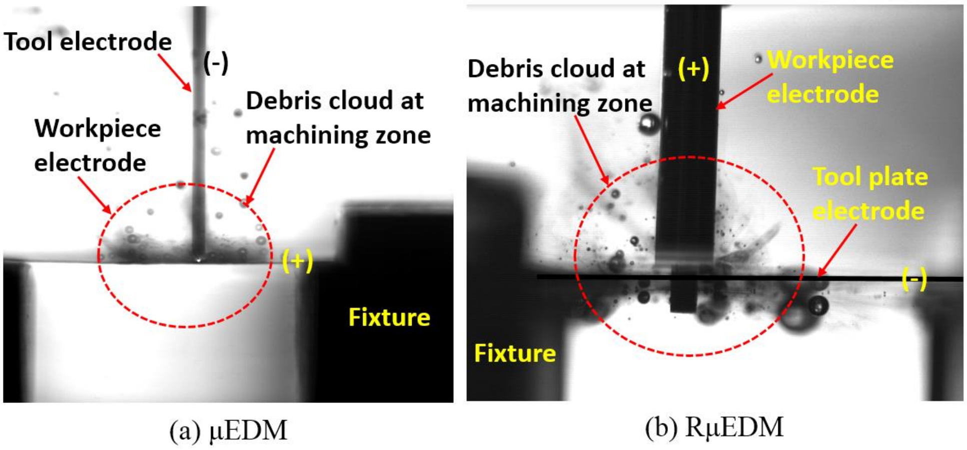

(a) µEDM

(b) RµEDM

Fig. 5.2 Debris accumulation in (a) µEDM and (b) RµEDM process captured using a high-speed camera at 3600fps.

These illustrations show that the ejected debris splashes out and tries to float on the tool plate surface in the µEDM process. In RµEDM, the debris ejects laterally outside in the dielectric pool when subjected to a continuous fresh dielectric supply. Additionally, the tool plate consisting of pre-drilled micro hole(s) somehow proves advantageous in ejecting debris through the multiple gaps due to the gravity drop action. However, it is cumbersome to completely evacuate the debris from the machining gap due to the larger array size of micro protrusions and the complex machining setup, especially from the central zone. The severity of the debris accumulation at the discharge gap can be observed by the real-time machining illustration shown in Figure 5.3. Hence, it has been observed that only an inbuilt machine flushing cannot completely evacuate all the debris from the machining zone due to the unidirectional flow of liquid dielectric.

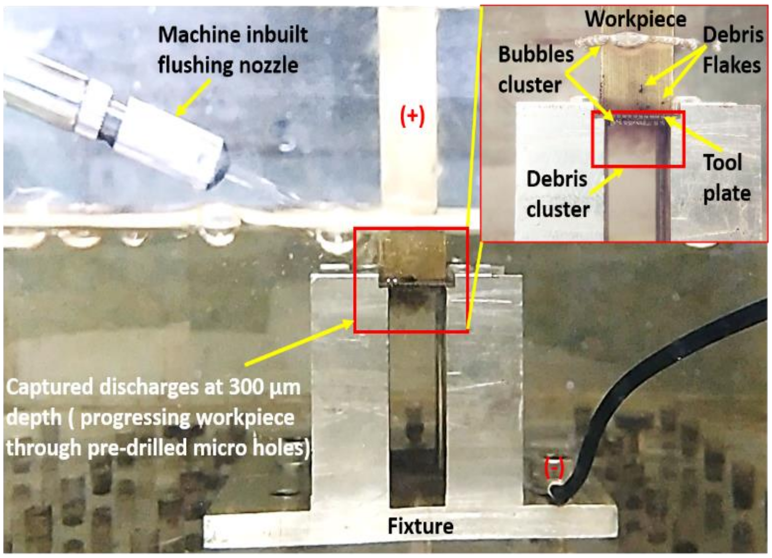
Machine inbuilt flushing nozzle
(+)
Workpiece
Bubbles cluster
Debris Flakes
Debris cluster
Tool plate
Captured discharges at 300 µm depth (progressing workpiece through pre-drilled micro holes)
(-)
Fixture

Fig. 5.3 Typical pictorial view of debris accumulation during RμEDM for the fabrication of arrayed protrusions.

5.3. Suction-based high-pressure dielectric flushing in RμEDM

A new suction-based high-pressure dielectric flushing technology has been developed for complete debris evacuation. The technology comprises a workpiece held in the spindle at one end, a pre-drilled tool plate rigidly mounted on a fixture, a suction unit mounted between pre-drilled tool plate and fixture, and a pump driven by a variable speed motor to generate high pressure suction in the suction unit.

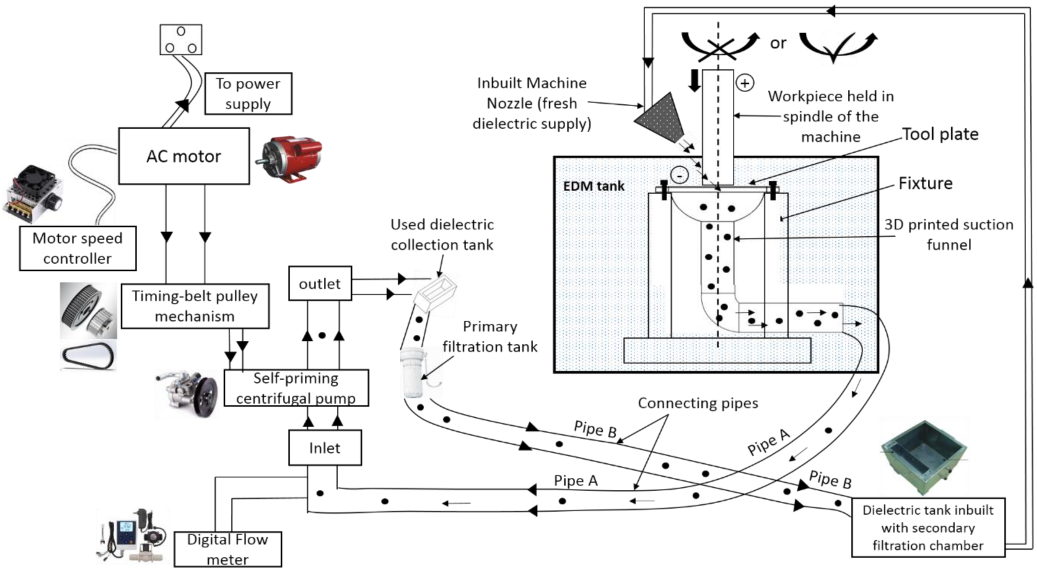
or
Inbuilt Machine Nozzle (fresh dielectric supply)
+
Workpiece held in spindle of the machine
Tool plate
EDM tank
-
Fixture
3D printed suction funnel
To power supply
AC motor
Motor speed controller
Timing-belt pulley mechanism
outlet
Used dielectric collection tank
Primary filtration tank
Self-priming centrifugal pump
Inlet
Connecting pipes
Pipe B
Pipe A
Pipe A
Pipe B
Digital Flow meter
Dielectric tank inbuilt with secondary filtration chamber

Fig. 5.4 A 2D schematic illustration of suction-based high-pressure dielectric flushing in RμEDM.

The suction unit comprises a suction cup/funnel with a flange at one end of a hollow cylindrical section. The suction unit is mounted between the pre-drilled tool plate and the fixture by sandwiching the flange of the suction cup/funnel having mounting holes between the pre-drilled tool plate and the fixture. The dielectric fluid mixed with debris/removed material from the machining zone is sucked by the suction unit due to the high suction pressure generated by the pump. The dielectric fluid mixed with debris from the pump outlet is supplied to a dielectric storage tank after filtration through a used dielectric collection tank facilitated with pre-filter paper and a primary filtration chamber. The filtered dielectric fluid from the dielectric storage tank is supplied to the machining zone through a nozzle for faster machining and maintaining the dielectric level in the EDM tank. The 2D schematic of the new suction flushing technology in RμEDM along with the used components is illustrated in Figure 5.4.

This new suction flushing technology works on the suction pressure applied by the self-centrifuging pump at the desired pressure. The detailed analysis of the developed flushing technology is aimed to enhance the process stability of RμEDM, used in fabricating arrayed micro protrusions, which is less costly and easy to integrate with the machining setup. The design consideration and experimental methodology used in the development of new flushing technology are discussed in the subsequent sections.

5.3.1. Key aspects of the new flushing technology

Upon implementation of the novel technology for debris evacuation, the following issues in the RμEDM can be resolved. The developed suction technology is aimed at resolving the below-mentioned issues in the RμEDM of which details are provided in subsequent sections.

- *Improper debris removal affecting the total machining time*: The consequence of poor debris flushing from the discharge gap can be seen in terms of degraded material removal rate product quality.

- *The degree of the tool plate wear which is an inevitable issue in RμEDM*: The tool plate wear severely affects the dimensional accuracy of the fabricated component.

- *Frequent occurrence of abnormal discharge pulses such as arcing and short-circuiting*: The arcing and shorts in the process is considered as harmful discharge as they exponentially increase the machining time removing almost no materials.

- Poor surface and dimensional accuracy of the fabricated micro products of high aspect ratio.

5.4. Design consideration for new flushing technology

The design consideration of the novel suction cup/funnel is one of the key components of suction flushing technology. The principle of Brachistochrone path or curve of fastest descent (Figure 5.5) is used for selection of the profile of the curved portion of the suction cup/funnel. The Brachistochrone path is helpful to understand the highest possible acceleration of an object in the shortest possible vertical drop; or the quickest way to get between two points. As can be seen in Figure 5.5, cycloid curve path has the highest speed possible in the shortest possible vertical drop or the quickest way to get between two points compared to a line, a parabola, a circle and a six-degree polynomial. Based on the 'Brachistochrone curve' principle, a divergence angle of 20-45 degree for the suction cup/funnel achieves critical volumetric flow rate of liquid dielectric mixed with ejected debris. The cycloidal curve which has shown the fastest descent for effective debris removal is numerically evaluated and opted for fabricating the suction cup/funnel in the present study. The details on the evaluation of the formulated numerical model is elaborated in Appendix-A, section 4.

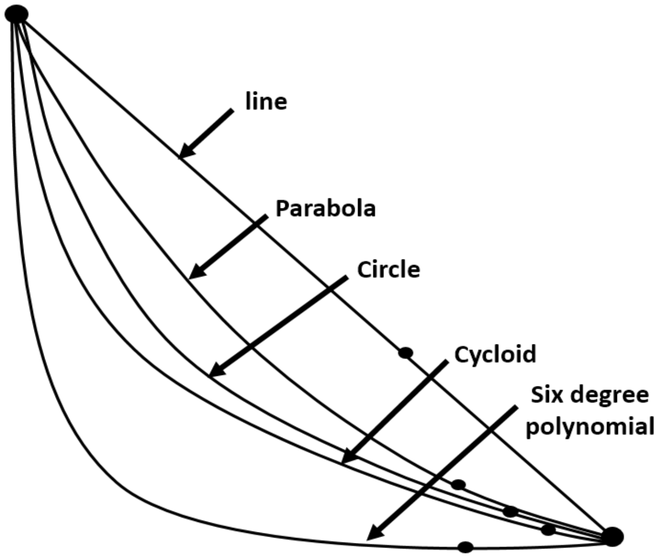

Fig. 5.5 Brachistochrone curves for the shortest time path.

A simulation model is developed in ANSYS® using the essential boundary conditions. The numerical model of the 2D suction funnel along with the RμEDM setup is shown in Figure 5.6. Based on the analysis, the choice is made for a divergence angle of 25 degrees for the critical volumetric flow rate. It meant that the adverse pressure gradient of the cycloidal curve would be lower for hypotenuse or other surfaces.

5.4.1. Development of a numerical model

Analyzing the debris flow pattern is the most important aspect of the developed flushing technology. It is augmented with the aspect of faster machining and complete debris removal of the debris from the machining gap in RμEDM. However, it is cumbersome to analyze the debris flow behavior experimentally. Therefore, a numerical model is formulated, apart from the designing of suction funnel/cup, for analyzing the debris flow behavior in the suction funnel.

During the machining, in a few microseconds, multiple phenomena occur in the discharge gap, ejection of debris due to dielectric pressure, and formation of vapor bubbles and sparks. It is challenging to capture the debris motion during experimentation. As the objective of the newly developed suction flushing technology is smooth removal of debris, it is essential to study the accretion status and trajectory of the debris particles dispelling out of the suction funnel. Thus, the computational fluid dynamics (CFD) based approach is relevant for studying these aspects of debris flushing. The purpose of the numerical study is to determine the divergence angle of the suction cup/funnel for a faster ejection rate and frictionless transfer of ejected debris mixed with liquid dielectric during machining.

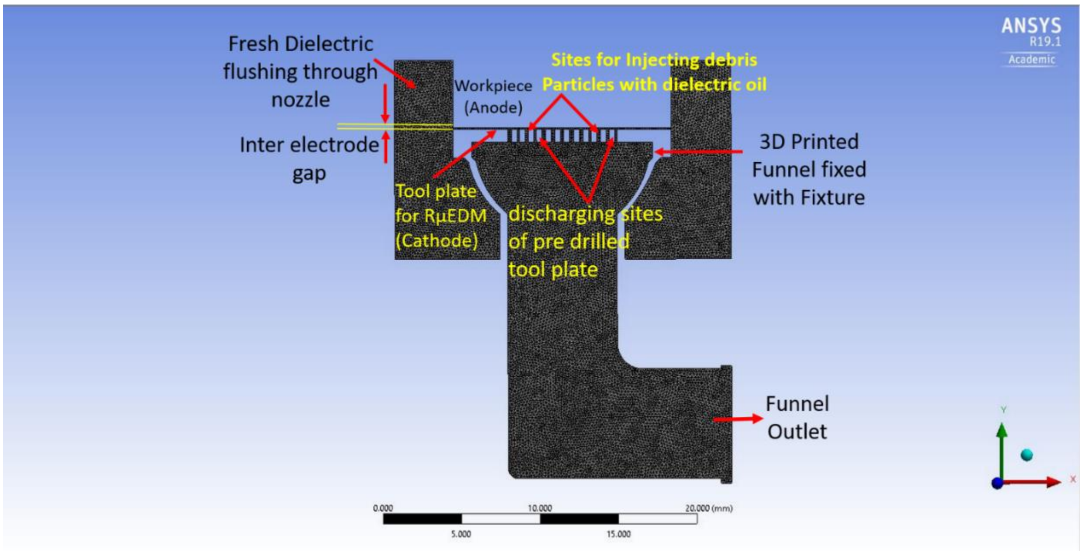
ANSYS
R19.1
Academic
Fresh Dielectric flushing through nozzle
Inter electrode gap
Workpiece (Anode)
Sites for Injecting debris Particles with dielectric oil
3D Printed Funnel fixed with Fixture
Tool plate for RμEDM (Cathode)
discharging sites of pre drilled tool plate
Funnel Outlet
Y
X
0.000
10.000
20.000 (mm)
5.000
15.000

Fig. 5.6 2D numerical model of the new suction funnel.

The simulation for both the dielectric flow and the debris movement at the discharge gap in the RμEDM process is performed using ANSYS® Fluent software. The numerical analysis is done on 2D domain which provides insight into the debris behavior in the suction funnel due to lower computation time and simpler computational domain compared to 3D analysis. A continuous dielectric fluid flow at pressurized flushing conditions has been modeled at the inlet (Figure 5.6). The dielectric oil leaves the machining area through the suction outlet at a high pressure of 0.6 MPa. The pre-drilled tool plate and the corresponding workpiece material is assigned solid titanium and brass material, respectively. Although, this analysis is based on 2D, such that each side of the workpiece electrode is taken 10 mm with 5 μm of initial discharge gap. The debris size is considered spherical in shape due to the surface tension and size ranges between 1 nm or lower and up to 10 μm in the RμEDM process [52]. For the present study, the diameter of the debris is 4 μm, mass 2.87×10^{-13} kg, and density of 8.73 g/cm^3 have been considered for simulation. During the process, debris is injected from the lower end of the workpiece towards the pre-drilled tool plate. Similarly, in the computational domain, debris particles are injected from the workpiece surface with an injection velocity of 125 cm/s and a flow rate of 0.001 g/s. The pressurized dielectric flushing with a velocity of 0.02 m/sec is applied for fresh dielectric supply near the machining area.

The meshed model and the respective boundary conditions are presented in Figure 5.6. A very fine-structured linear quad elemental mesh has been considered for the present study. The grid independency test has been performed with two optimum mesh structures to find the computational model having a higher convergence rate. Therefore, two meshed models have been developed with a maximum of 23,364 nodes to capture the debris motion in the dielectric fluid. A relatively coarse mesh of quad elements is selected for the workpiece, assuming that the amount of debris ejected from the workpiece frontal surface is not affected during the simulation. The maximum number of 18892 nodes is chosen to capture debris particle's behavior in the fluid domain. Eventually, the analysis has been carried out by considering specific references along and across the discharge gap. The total time step utilized to run a simulation is approximately 3 hrs with an incremental step time of $3\text{x}10^{-5}$ sec. The assumptions made in the numerical simulation are as follows:

(i) The addition of debris particles is considered from the workpiece surface on the spindle side.

(ii) A No-slip boundary condition is applied to the workpiece, tool plate, and suction funnel surfaces.

(iii) The effect of the spark and the electrostatic force acting on the tool electrode is neglected.

(iv) The gravity effect (-9.81 m/s^2) is applied for the downward natural movement of debris particles.

(v) As reported, most of the μEDM debris particles are taken as solid, in the nano-size range, with vapor bubbles [52].

(vi) The shape of debris is assumed of spherical in shape, and they do not stick with each other.

(vii) It is assumed that dielectric is a homogenous, isotropic, and incompressible fluid.

(viii) Cathode wear is not considered, i.e., debris is not ejected from the cathode surface.

As mentioned earlier, the meshed model is used for discrete phase modeling in ANSYS-FLUENT® to study the debris particle's behavior. In this module, the primary and secondary phases are considered dielectric fluid (fluid domain), and the tertiary phase is considered injected debris particles. The primary and secondary phases have been solved using Navier Stokes equations, and the discrete (tertiary) phase is solved using the Eulerian-Lagrangian approach. The well-established partial differential equations of fluid flow phenomena are represented by Eq. (5.1) is integrated over each controlled volume in the computational domain. This equation defines the particle trajectory in which a dependent variable (ϕ) is considered and is transported through the fluid hence termed as transportation equation [221]:

$$\frac{\partial}{\partial t}(\rho\phi) + \frac{\partial}{\partial x_i}(\rho u_i \phi) - \frac{\partial}{\partial x_i}\left[\Gamma_\phi \frac{\partial \phi}{\partial x_i}\right] = S_\phi \tag{5.1}$$

where, ρ is the fluid density, ϕ is a dependent variable, Γ_ϕ is a diffusion coefficient for ϕ and S_ϕ is a source term. The following mathematical equations are used to describe the flow of fluids corresponding to continuity and momentum equations, representing mass and momentum conservation, respectively. For the continuity equation, $\phi = 1$ while Γ_ϕ and S_ϕ are zero in Eq. (5.1). For the momentum equation (Eq. 5.1), the variable transported is the velocity (u_i), (Γ_ϕ) is viscosity and (S_ϕ) represents the sum of the forces acting on the fluid [222]:

$$\frac{\partial \rho}{\partial t} + \frac{\partial}{\partial x_i}(\rho u_i) = 0 \tag{5.2}$$

$$\frac{\partial}{\partial t}(\rho u_i) + \frac{\partial}{\partial x_i}\left(\rho u_j u_i\right) = -\frac{\partial P}{\partial x_i} + \frac{\partial}{\partial x_j}\left[\mu\left(\frac{\partial u_i}{\partial x_j} + \frac{\partial u_j}{\partial x_i}\right)\right] \tag{5.3}$$

where, t is the time, u is the fluid flow velocity, the subscript i indicates the Cartesian coordinates and the respective velocity components, x is the coordinate, and μ is the fluid viscosity. The first term on the left-hand side of Eq. (5.3) represents the temporal variation of momentum, while the second term is the fluid's acceleration. The right-hand side forces represent the normal stresses (the pressure gradient force) and the tangential shear stresses (the viscous force). Using a source term, other forces, such as gravity, have been added to the equations.

In this study, the debris particle volume is considered less than 10% of the total fluid phase in the computational domain, and the debris effect on the liquid dielectric is neglected. Therefore, the one-way coupling is correlated with debris particles for getting the debris particle tracking. Hence, integrating the force balance equation coupled with the Eulerian-Lagrangian frame has evaluated debris particles' trajectory along the tertiary phase. This force balance evaluates the particles' inertia and forces acting on the particles in the primary phase. The respective force-balance equation per unit mass of the particle is given by Eq. (5.4) [222]:

$$\frac{du_p}{dt} = F_D\left(\vec{u} - \overrightarrow{u_p}\right) + \frac{\vec{g}\,(\rho_p - \rho)}{\rho_p} + \vec{F} \tag{5.4}$$

where, $(\frac{du_p}{dt})$ is the net inertia of the particle, $(\vec{g})$ is the gravity force, F_D is the drag force and $\vec{F}$ is the additional force as source terms. The drag force equation is given by Eq. (5.5) [222]:

$$F_D = \frac{18\mu C_D R_E}{24\rho_p d_p^2} \tag{5.5}$$

where $(\vec{u})$ is the dielectric fluid velocity, $(\overrightarrow{u_p})$ is the velocity of the debris particle, μ is the dynamic viscosity of the dielectric fluid, ρ is the density of the dielectric fluid, ρ_p is the density of the particle in the dielectric fluid, d_p is the debris particle diameter and Re is the Reynolds number and is given by Eq. (5.6):

$$Re = \frac{\rho d_p \left|\overrightarrow{u_p} - \vec{u}\right|}{\mu} \tag{5.6}$$

In the present work, the debris particles have been considered to be spherical in shape; the drag coefficient for smooth motion of the particles is given in Eq. (5.7):

$$C_D = a_1 + \frac{a_2}{R_E} + \frac{a_3}{R_E^2} \tag{5.7}$$

where, $a_1, a_2, a_3,$ are the constants applied for a specific range of Re. The accretion of the debris particles started from the surface of the workpiece electrode, and the rate of accretion is calculated by material added upon (area multiplied by time) i.e., mass flux (g/mm^{2}s) and is given by Eq. (5.8):

$$R_{accretion} = \sum_{p=1}^{N\,particles} \frac{\dot{m}}{A_{frontal\,face}} \tag{5.8}$$

Here, $A_{frontal\,face}$ is the area of the frontal surface of the workpiece face towards the tool plate (in mm^2) and $\dot{m}$ is considered as the mass flow rate of debris particles (in g/s). By integrating Eq. (5.4) with time yields the velocity of the debris at each point along the trajectory, with the trajectory itself predicted by Eq. (5.9):

$$\frac{dx_p}{dt} = u_p \tag{5.9}$$

Both the Eqs. (5.4) and (5.9) are solved for coordinate direction for predicting debris trajectories in the discrete phase. The debris particles exchange mass, momentum, and energy within the dielectric fluid. The inlet is maintained at the atmospheric condition and the outlet is assigned with negative pressure boundary conditions. Further, the model is subjected to discrete phase modelling (DPM) for studying the debris particle's behavior. The DPM model sequentially constitutes four boundary conditions: ' reflect', 'trap', 'escape', and 'wall jet'. When the debris particle hits the tool plate surface with 'reflect' boundary condition, it rebounds from the surface where the pre-drilled holes are not present by changing its momentum and direction. The debris path is terminated in 'trap' and 'escape' boundary conditions when the particle touches the wall surface. The number of particles trapped at the discharge gap or escaped from the pre-drilled holes is then calculated. The 'wall jet' boundary condition is used for the workpiece surface where 2/3rd of discharge energy is generated. The fresh dielectric spray impinges at the surface with high pressure. Moreover, the suction surface at the outlet has given ‘escape’ boundary conditions to prevent the debris particles' reflection. The remaining walls of the computational domain are considered as ‘reflection’ boundary conditions. The realizable $k-\varepsilon$ model with enhanced wall functions is used to track the debris ejection in this simulation. This model is utilized for capturing localized turbulence or vortex formation at the other end of the pre-drilled tool plate as a function of negative pressure. The Semi-Implicit Method for Pressure Linked Equations (SIMPLE) algorithm is considered for the discretization of pressure-velocity coupling equations. The movement of the debris is solved using transient-based DPM along with the spherical drag law used for capturing the particle tracking behavior in the fluid domain. For studying the debris flow trajectory, particles are injected from the frontal surface of the workpiece electrode in the fluid domain.

During the suction flushing, the debris experiences several flow behaviors while going downside in the liquid dielectric, such as (i) accretion on the workpiece and tool plate surface, (ii) formation of a chain-like cluster of debris, (iii) vortex formation along the sidewall towards the back-end of the tool plate (iv) particle ejection trajectory at the funnel outlet. The debris movements at different positions and time steps are recorded, as shown in Figure 5.7(a-f). From Figure 5.7, it is observed that most of the ejected debris gets flushed away through pre-drilled holes due to plasma implosion and high suction pressure. The debris trajectory is computed through the fluid domain over many steps when it passes through the tool plate. A change in the trajectory length of the debris is observed in the fluid domain. This is attributed to larger fluid velocity and pressure variation across the discharge gap towards the tool plate. The overall trajectory of the debris flow has been determined by computing the force balance acting on it and the debris transport assumptions in the flow field domain. Moreover, the dynamic nature of debris movement reduces debris concentration at the localized zone. In summary, it is observed that at a suction pressure of 0.6 MPa and with machine flushing, the debris particles have been found to be considerably flushed out from the discharge gap.

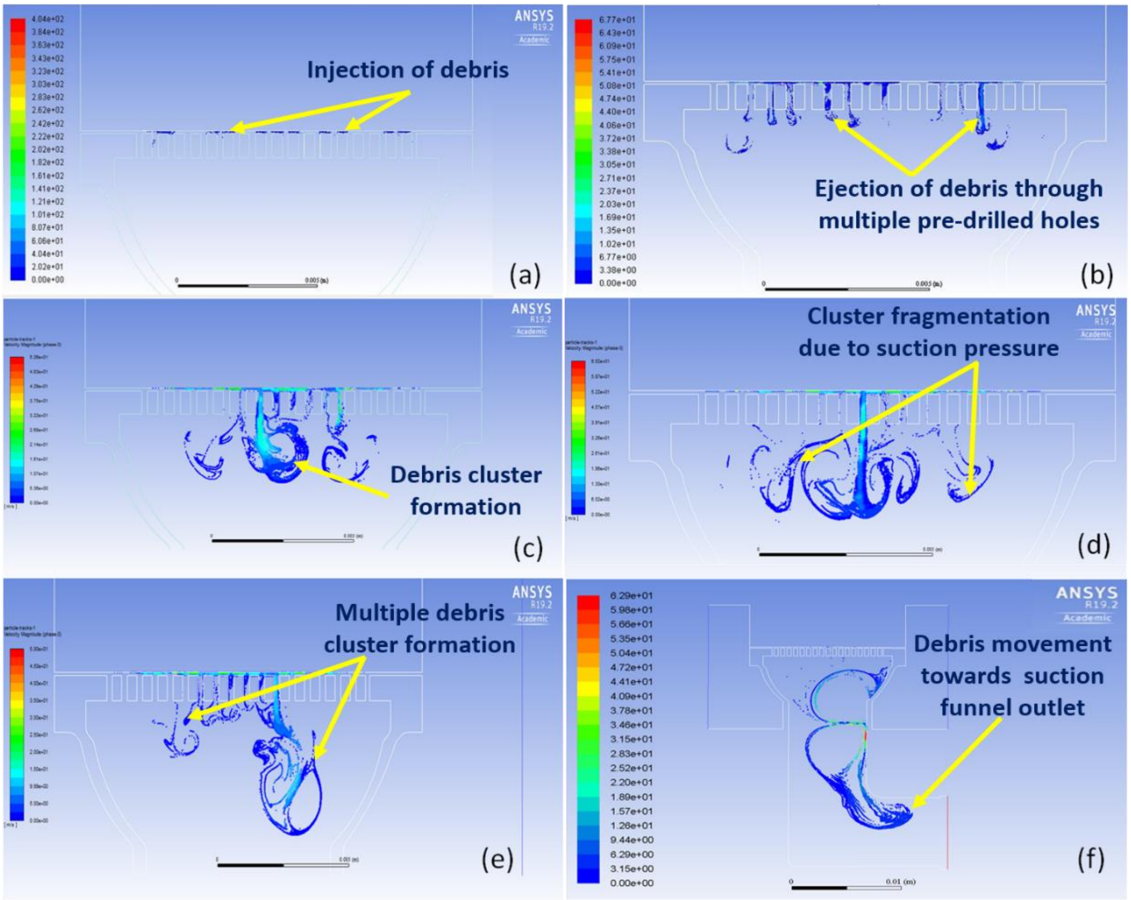
ANSYS
R19.2
Academic
4.04e+02
3.84e+02
3.63e+02
3.43e+02
3.23e+02
3.03e+02
2.83e+02
2.62e+02
2.42e+02
2.22e+02
2.02e+02
1.82e+02
1.61e+02
1.41e+02
1.21e+02
1.01e+02
8.07e+01
6.06e+01
4.04e+01
2.02e+01
0.00e+00
Injection of debris
(a)
6.77e+01
6.43e+01
6.09e+01
5.75e+01
5.41e+01
5.08e+01
4.74e+01
4.40e+01
4.06e+01
3.72e+01
3.38e+01
3.05e+01
2.71e+01
2.37e+01
2.03e+01
1.69e+01
1.35e+01
1.02e+01
6.77e+00
3.38e+00
0.00e+00
Ejection of debris through multiple pre-drilled holes
(b)
Debris cluster formation
(c)
Cluster fragmentation due to suction pressure
(d)
Multiple debris cluster formation
(e)
6.29e+01
5.98e+01
5.66e+01
5.35e+01
5.04e+01
4.72e+01
4.41e+01
4.09e+01
3.78e+01
3.46e+01
3.15e+01
2.83e+01
2.52e+01
2.20e+01
1.89e+01
1.57e+01
1.26e+01
9.44e+00
6.29e+00
3.15e+00
0.00e+00
Debris movement towards suction funnel outlet
0.01 (m)
(f)

Fig. 5.7 Debris particle trajectory at different time steps (a) injection from workpiece surface towards tool plate surface, (b) ejection of debris out of pre-drilled micro holes into the fluid domain, (c) chain-linked cluster formation at the bottom end of tool plate, (d) cluster fragmentation of debris cluster due to applied pressure, (e) subsequent cluster formation and fragmentation due to intermittent debris ejection, and (f) debris outflow towards the suction funnel.

5.5. Experimental setup for new flushing technology

The suction unit of the developed flushing technology comprises a suction cup/funnel whose one end is a hollow cylindrical section as shown in Figure 5.8. Figure 5.8(a-d) shows isometric, side, front and top views of the arrangement of the workpiece electrode, pre-drilled tool plate and suction unit. A flange with holes is formed at the suction cup/funnel for bolting the suction cup/funnel on the fixture along with the RμEDM tool plate.

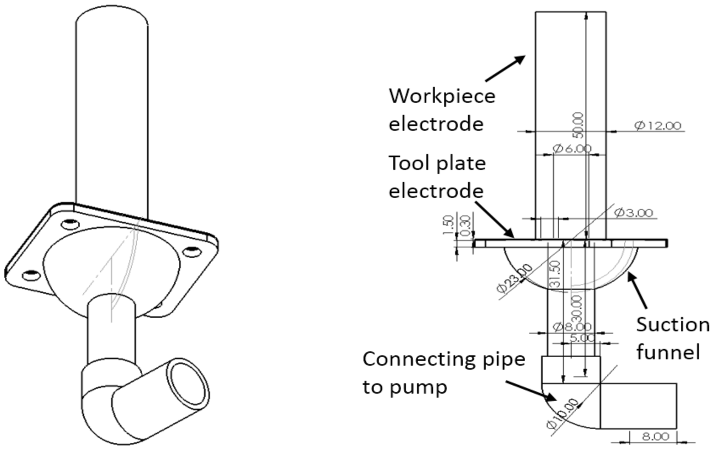
Workpiece electrode
Ø12.00
50.00
Ø6.00
Tool plate electrode
1.50
0.30
Ø3.00
Ø23.00
31.50
30.00
Ø8.00
5.00
Suction funnel
Connecting pipe to pump
Ø10.00
8.00

(a) Isometric view (b) Side view

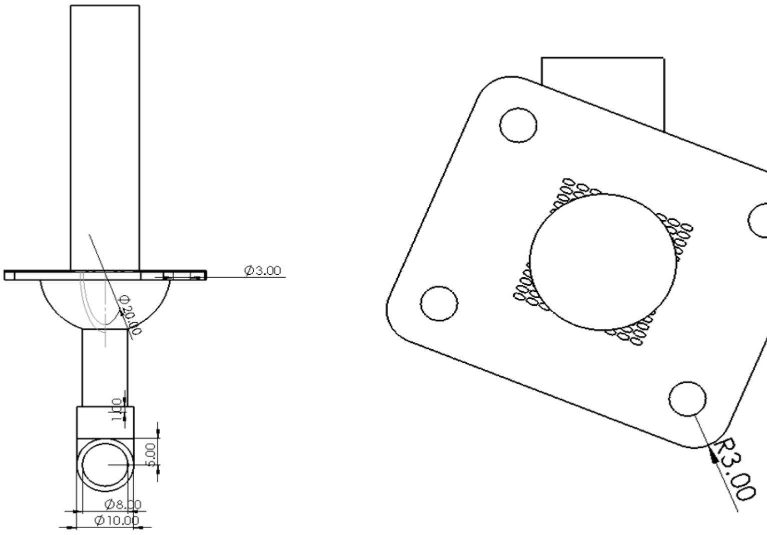
Ø3.00
Ø20.00
1.00
5.00
Ø8.00
Ø10.00
R3.00

(c) Front view (d) Top view

Fig. 5.8 3D geometrical representation of the suction unit.

Based on the selection of optimal divergence angle and dimensions of the suction cup/funnel obtained through numerical simulation, the fabrication part is more challenging and interesting. The 3D printing technology has been chosen to fulfill the fabrication feasibility of the suction funnel. Figure 5.9 shows the (a) machine setup used to fabricate the suction funnel, and (b) the different views of the fabricated suction funnel in (i) top, (ii) side, and (iii) front views. The fabrication of the funnel has done on the FABX 3D printer machine (Make: 3Ding Reddx Technologies Pvt Ltd.; Model: FABX XL, E3D V6), in which the printing material ABSPlus P430 is used. The ABS

(Acrylonitrile Butadiene Styrene) material is known for its good printing ability used in personal or household 3D printing, primarily using the FDM (fused deposition modeling) process. This material is also useful where aesthetics are essential. Due to its lower printing temperature it is easier to print with and, therefore, better suited for parts with fine details. The suction funnel was initially designed in the SOLIDWORKS®. The .stl format CAD model is integrated with the machine software used to print the funnel with the required amount of material. After fabrication, it was kept in the water-based solution in the circulation tank that uses heat and ultrasonic waves to create scrubbing bubbles, which gently clean printed parts.

After post-cleaning, the fabricated suction cup/funnel is mounted between the pre-drilled tool plate and the fixture with the help of bolts, ensuring no dielectric leakage from the peripheral surface. The dimensions of the suction cup/funnel is considered based on the dimensions of the desired micro protrusions on the workpiece electrode to accommodate the length of the micro protruded structures.

5.5.1. Working of new flushing technology

In RμEDM, a workpiece (anode) with a flat face is held in the vertical spindle, aligned towards the tool plate (cathode), consisting of arrayed micro-holes in a pattern similar to the required micro protrusions. The freshly LBμM fabricated tool plate is bolted in the dedicated fixture and submerged inside the EDM tank's dielectric pool. The workpiece and tool plate material are commercial brass and a titanium grade II sheet of thickness 0.4mm, respectively. Once the machining starts by providing CNC code in the machine GUI, the z-axis of the machine spindle is set for a negative value to progress in the direction of the pre-drilled tool plate. Due to the electrical discharges between the tool plate and workpiece, the material removal in the RμEDM takes place in the form of tiny debris.The ejected debris from both the workpiece and tool plate surface floats near the discharge gap. Since erosion occurs at the bottom surface of the workpiece, the ejected debris tries to settle down onto the tool plate surface due to gravitational pull (Figure 5.3). This is evidenced before the suction unit starts. A practical demonstration of new suction-based high-pressure flushing technology integrated with RμEDM setup and measuring facilities are shown in Figure 5.10(i,ii). The depicted schematic in the

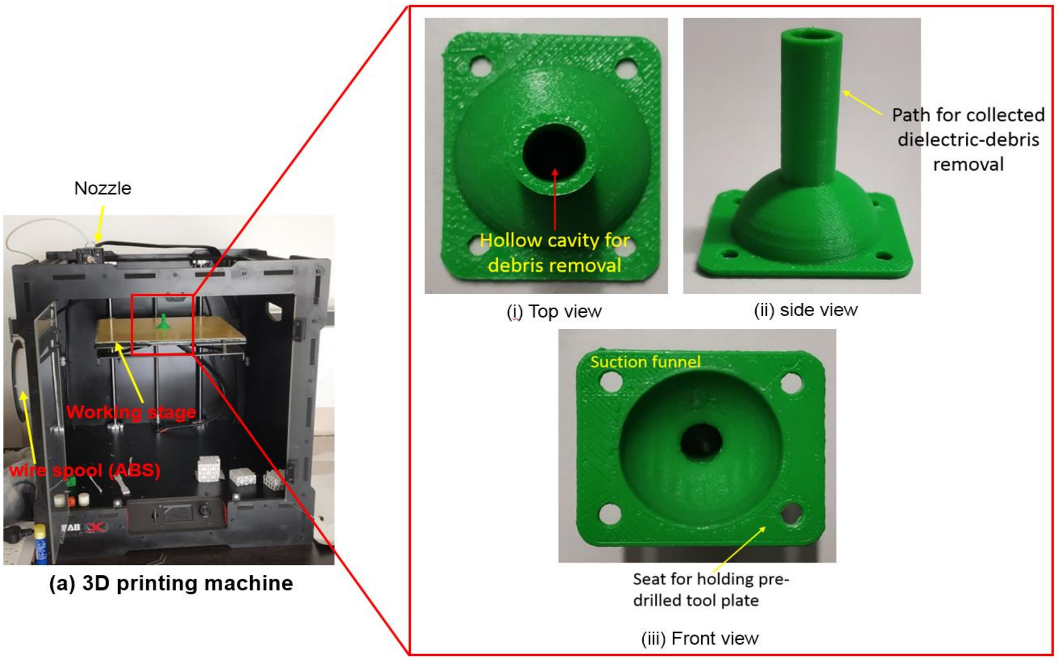
Nozzle
Working stage
wire spool (ABS)
Hollow cavity for debris removal
(i) Top view
Path for collected dielectric-debris removal
(ii) side view
Suction funnel
Seat for holding pre-drilled tool plate
(iii) Front view

(a) 3D printing machine

(b) 3D printed suction funnel

Fig. 5.9 Fabricated suction cup/funnel using (a) 3D printing machine, and (b) different views of fabricated suction funnel.

inset (right side of Figure 5.10(i)) shows the 3D representation of suction unit in RμEDM. The following are the details of inset schematic: 1. Inbuilt machine flushing nozzle, 2. Dielectric, 3. Workpiece electrode, 4. Pre-drilled tool plate, 5. 3D printed funnel for high-pressure suction, 6. Dielectric spray impingement point, ‘L’ represents any moderated distance of the nozzle from the discharge gap, ‘d’ is any moderated distance of the nozzle from the tool plate and ‘α’ is any moderated angle of impingement for the spray in XY plane.

After the machining starts, the power supply is given to the self-priming centrifugal pump (Make: Mahindra & Mahindra Ltd.; Model: 2007-20). The maximum flow rate is measured using a digital flow meter (Make: ShenZhen Huimai technology co., Ltd.; Model: DIGITEN DFC15) and a maximum of up to 7 L/min can be achieved. A single-phase AC motor (Make: Godrej Lawkim motors group; Model: LK1374H) linked with timing belt and pulley motion system with a maximum power rating-1 HP 0.75 kW and 1400 rpm is used to run the pump. The timing belt pulley mechanism is in-house fabricated based on the pump and motor shaft diameter. A motor speed controller (auto-transformer) is used and connected in parallel with the AC motor to control the motor's rpm. Eventually, the pressure generated by the pump can be varied and is measured

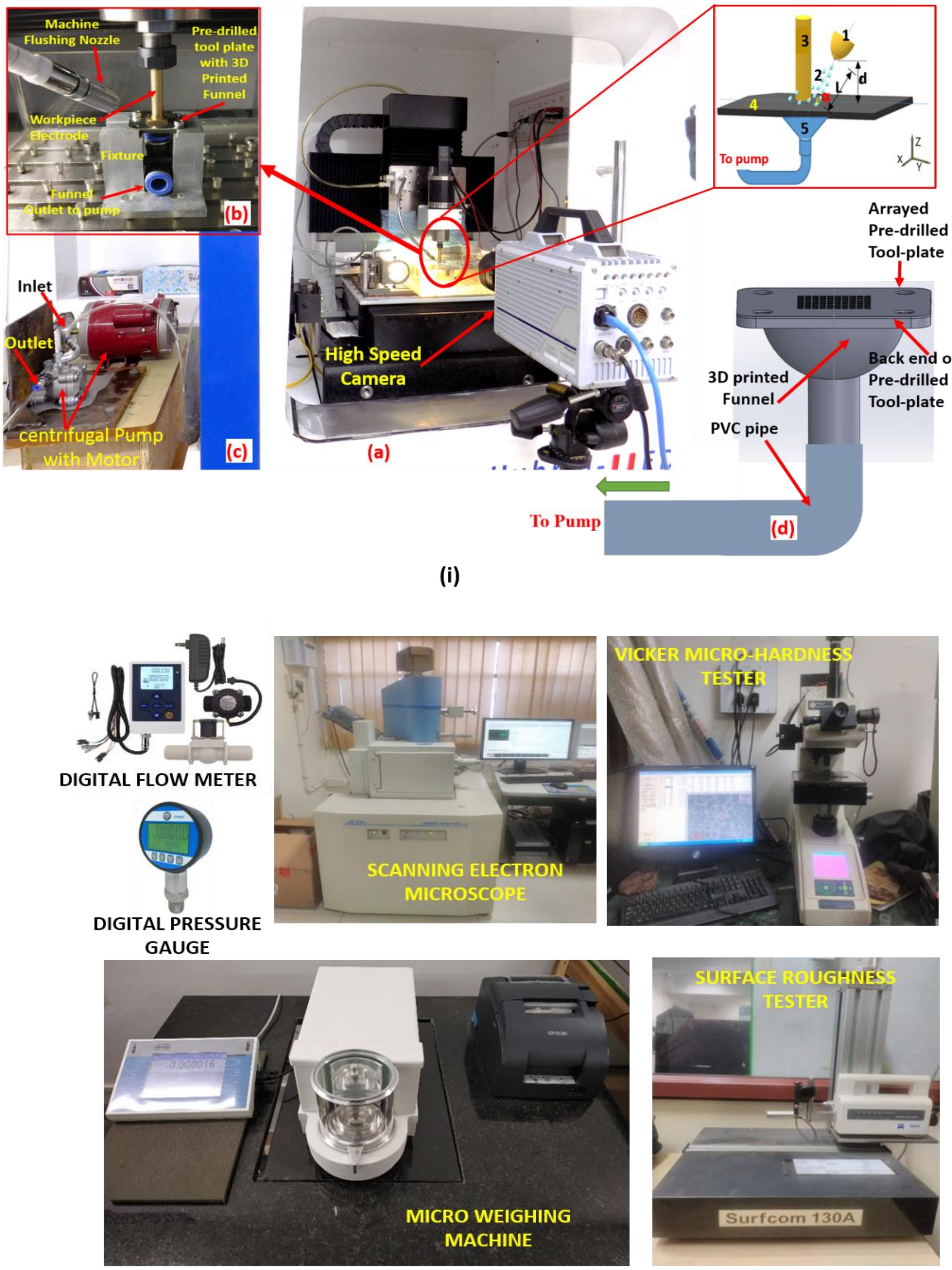
Machine Flushing Nozzle
Pre-drilled tool plate with 3D Printed Funnel
Workpiece Electrode
Fixture
Funnel
Outlet to pump
(b)
Inlet
Outlet
centrifugal Pump with Motor
(c)
High Speed Camera
(a)
1
2
3
4
5
d
L
To pump
Z
X
Y
Arrayed Pre-drilled Tool-plate
3D printed Funnel
Back end of Pre-drilled Tool-plate
PVC pipe
To Pump
(d)
DIGITAL FLOW METER
DIGITAL PRESSURE GAUGE
SCANNING ELECTRON MICROSCOPE
VICKER MICRO-HARDNESS TESTER
MICRO WEIGHING MACHINE
SURFACE ROUGHNESS TESTER
Surfcom 130A

(i)

(ii)

Fig. 5.10 (i) Overall suction flushing setup (a) machine setup, (b) RµEDM setup, (c) centrifugal pump with motor (d) suction cup/funnel, and (ii) measuring equipment used.

using the digital pressure gauge (Make: Nishka Instruments, Mumbai; Model: PG802C) attached to the pump's inlet. From the numerical simulation study, a pressure of 0.6 MPa is found suitable for the complete evacuation of debris from the machining gap. The ejected clusters of debris are collected first in the suction funnel of which a free hollow cylindrical end is attached to the pump's inlet through connecting pipes and connectors. Further, the dielectric mixed with ejected debris collected at the primary filtration chamber via a dielectric collection tank. Eventually, it reaches the secondary filtration chamber for final filtration of any debris that remains. The filtered dielectric entered into the main dielectric chamber/reservoir which is already filled with fresh dielectric. The fresh dielectric is supplied at the machining zone, maintaining the EDM tank level through the machining time, using an inbuilt flushing nozzle attached with the machine. This circulatory motion happens until the desired machining depth is achieved, say for the total arrayed protrusions length. The elaborated analysis has been performed at the optimal RµEDM parametric setting, of which a detailed study is performed and presented in chapter 3. Table 5.1 provides the wide workable ranges of the suction-based high-pressure flushing technology.

Table 5.1. Specification of the suction-based high-pressure flushing technology used in the present study.

Components	**Ranges**
Single phase AC motor	0.5 HP- 1 HP
Auto-transformer	0 V - 240 V
Suction pump	30 mbar - 90 mbar
Digital flow meter	3-10 ltr/min.
3D printed Suction Funnel height	30 mm – 40 mm
3D printed Suction Funnel material	Plastic, metal, composite
High-speed camera	3000-10000 fps
EDM Tank height	120 mm
EDM Tank length	100 mm - 150 mm
EDM Tank base	10 mm – 30 mm
Pressure Gauge	Below 100 mbar
PVC pipes	8 mm (outer diameter)
Filter cartridge	1 µm mesh size
Machine Nozzle flushing pressure	1-8 MPa
Tool plate with pre-drilled holes	Arrayed micro holes of any cross-section profile
Machine spindle rpm	100-3000

5.6. Outcomes of the new flushing technology

With this effective flushing technology, arrayed micro protrusions in the elliptical, Piranha cross-section profile and droplet have been fabricated at the optimal machining parametric settings. The optimal parametric setting of used microfabrication technology (integrated RμEDM and LBμM) are listed in Table 5.2 along with the measured machining responses.

Table 5.2. RμEDM and LBμM conditions for the fabrication of arrayed micro protrusions.

RμEDM parameters		**LBμM parameters**	
Setup	RC based	LASER type	Nd-YAG YLR-150/1500-QCW-MM-AC-Y11
Resolution (X,Y,Z)	0.1 μm	Wavelength	1070 nm
Tool plate	Titanium (Grade II)	Power	150 W
Workpiece	Cu_3Zn_2 (Yellow Brass)	Frequency	50 Hz
Gap voltage	110 V	Pulse width	0.5 ms
Capacitance	10 nF	Spot dia.	50 μm
Electrode Feed rate	10 μm/s	Current percentage	20%

Measured Responses

Machining conditions of LBμMed tool plate (elliptical profile)	**Approximately Time (hrs)**	***MRR*** **(mm^3/min.)**	**TWR (mm^3/min.)**	**Avg. Surface Roughness (μm)**	**Micro-hardness of tool plate (VHN)**	
					Before M/cing	**After M/cing**
(i) without suction flushing	19	0.14	0.08	1.78	210	215
(ii) with suction flushing	17	0.18	0.07	1.55	210	219
Machining conditions of LBμMed tool plate (droplet profile)						
(i) without suction flushing	24	0.13	0.07	2.13	210	217
(ii) with suction flushing	19	0.17	0.06	1.59	210	221
Machining conditions of LBμMed tool plate (Piranha profile)						
(i) without suction flushing	21	0.16	0.07	1.64	210	215
(ii) with suction flushing	16	0.20	0.06	1.28	210	218

The capabilities of new suction-based high-pressure flushing technology in the quality fabrication of arrayed elliptical profile micro protrusions compared to normal flushing are claimed through the SEM images shown in Figure 5.11. The SEM images shown in Figure 5.11(a,b,c) are captured at the central location in an array of micro protrusions, knowing that higher debris accumulation is particularly high in this particular zone. Noteworthy to say, the comparative studies in the fabrication of arrayed micro

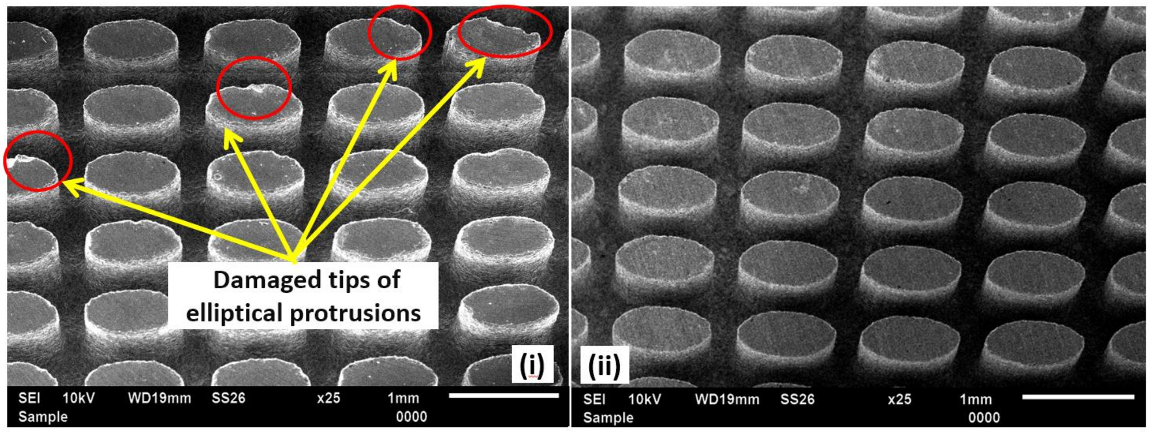
Damaged tips of elliptical protrusions
(i)
(ii)
SEI 10kV WD19mm SS26 x25 1mm
Sample 0000
SEI 10kV WD19mm SS26 x25 1mm
Sample 0000

(a) Arrayed elliptical protrusions

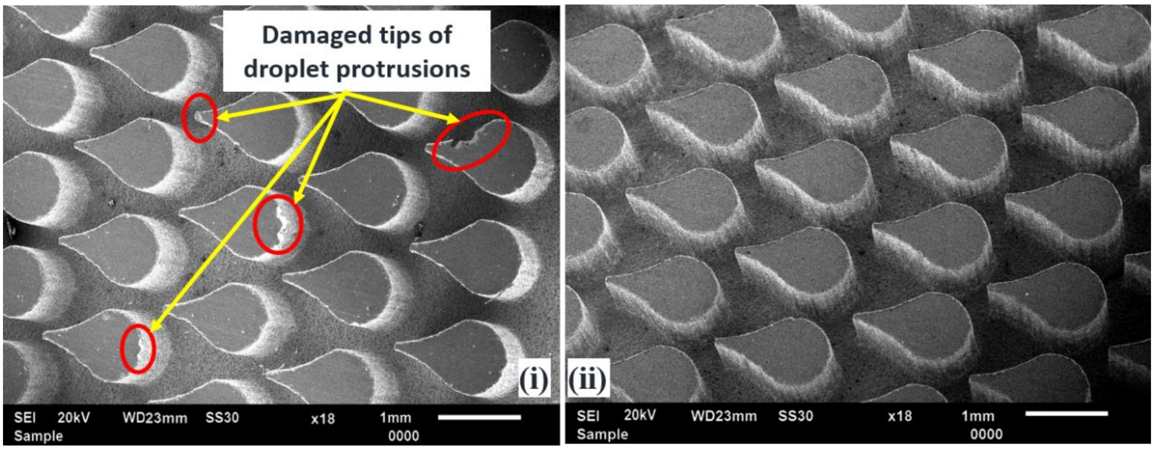
Damaged tips of droplet protrusions
(i)
(ii)
SEI 20kV WD23mm SS30 x18 1mm
Sample 0000
SEI 20kV WD23mm SS30 x18 1mm
Sample 0000

(b) Arrayed droplet protrusions

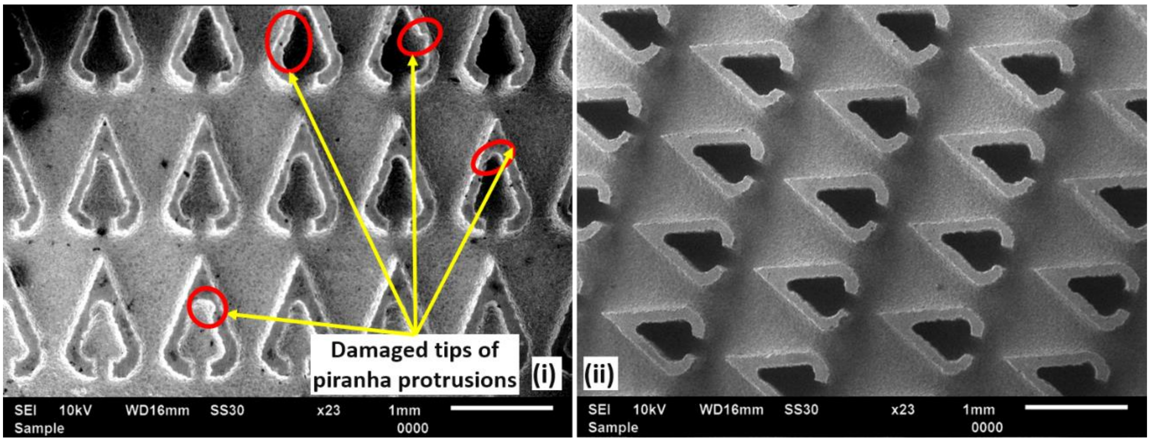
Damaged tips of piranha protrusions
(i)
(ii)
SEI 10kV WD16mm SS30 x23 1mm
Sample 0000
SEI 10kV WD16mm SS30 x23 1mm
Sample 0000

(c) Arrayed Piranha protrusions

Fig. 5. 11 SEM images of fabricated micro protrusions under (i) normal, and (ii) suction flushing conditions.

protrusions have been done at the same machining parametric settings with normal flushing and suction flushing conditions. Pilot experimental runs have been performed to validate the developed suction flushing model. Each fabricated array is programmed to have the micro protrusions height of 900 µm with an inter-electrode gap of 120 µm in inline and staggered arrangements. It is found that the tips of a few micro protrusions are damaged when the machining is performed without using suction flushing technology. It happened due to inadequate flushing at the central zone, resulting in higher-order discharges and arcing in the RμEDM process. Whereas, there is no such visible damage in the case of fabricated arrayed micro protrusions using suction-based flushing technology (shown in above Figure 5.11(a,b,c(ii)) Arrayed microstructures have not demonstrated any roundness or fillet at the microstructure's root. Also, the entire length of each protrusion is evidenced for hardly any taper in an array.

The machining responses such as machining time, Ra, MRR and TWR along with the micro-hardness of the tool plate are recorded as presented in Table 5.2. A significant improvement in all these responses has been found in the case of machining with suction flushing. A reduced TWR in machining with suction flushing evidences an effective debris flushing that prevents secondary or higher-order discharges which is the main cause of the tool wear in RμEDM. Moreover, the micro-hardness of the pre-drilled tool plate also plays a significant role in its wear. In this regard, the micro-hardness of the tool plate is measured before and after the RμEDM in both the machining conditions (with and without suction flushing). It is observed that the tool plate exhibits higher micro-hardness values post-machining in both conditions, relatively more while machining using the suction flushing. This is due to the effect of surface alloying of the ejected workpiece material on the tool plate through the inherent melting and vaporization. The ejected material in the form of debris having size ranges from a few nanometers to a few tens of micrometers, forms compounds with the released pyrolytic carbon from the liquid dielectric, Eventually, it gets re-solidified quickly and settled down on the tool plate surface due to high suction pressure causes work hardening. Hence, this phenomenon was found to be beneficial in the enhancement of tool plate micro-hardness and its reusability.

It is also evidenced that the surface quality of the fabricated protrusions plays an important role in determining their interactions with the application environment. In this regard, the Ra of each arrayed protrusions cross-sections when fabricated (i) without suction flushing, and (ii) with suction flushing have been evaluated. The Ra values of different cross-sections arrayed protrusions are in the range of 2.132 µm to 1.283 µm. The increased values of Ra when machined without suction flushing are due to frequent short-circuiting and arcing caused by debris accumulation at the tiny discharge gap that restricted the progressive machining. The second-order discharges resulted in the removal of the material non-linearly from the workpiece and produces larger craters, hence, higher Ra values in each case.

5.7. Chapter conclusion

The design and development of new suction-based high-pressure flushing technology has been benchmarked through a detailed investigation of different RμEDM responses and flushing parametric studies. With this, it can be summarized that the implementation of new flushing technology not only enhances the process stability of the RμEDM process but also the geometrical and surface characteristics of fabricated 3D arrayed protrusions greatly improved.

Chapter 6

Numerical Evaluation of Thermal Performance

6.1. Introduction

This chapter presents dimensional optimization, thermal modeling, and simulation of different unconventional cross-sections of MPFs in different arrangements (in-line and staggered). Multi-objective particle swarm optimization (PSO) code is developed for the numerical modeling. The optimal geometrical design consideration is taken for thermal simulation using ANSYS® for a comparative analysis of thermal performances under heat loading conditions and laminar flow regimes.

6.2. Mathematical model for thermal performance optimization

A systematic and detailed numerical analysis of arrayed MPFs cross-section particularly those with a streamline shape, would be complicated, expensive and time-consuming. A powerful numerical modeling using PSO offers an alternative approach for performing the task of design-based parametric optimization of arrayed MPFs, and hence elaborated in further sections.

6.2.1. Numerical modeling using PSO

The PSO algorithm is initialized with a population of random solutions searching for optimum value through updated new positions generated in the search space [223]. All potential solution members, called particles, fly through the problem search space (swarm) by following the best particle's performance and tracking their best positions. Each particle is assigned the desired position, (x), and velocity, (v), gets updated as the best fittest solution after each iteration. Noteworthy, in PSO, it is easy to get an optimal local value of any particle when the best particle is known. All other particles have slightly deviated during the performance in the population. In addition, a few parameters like acceleration factors with separate random numbers, and inertia weights should be adjustable with the new particle’s location being generated to accelerate particles towards achieving the global best positions in the swarm. The updated particle’s position and its corresponding velocities are calculated using the following Eqs. (6.1) and (6.2) [224]:

$$v(i,:) = wv(i,:) + C_1\, rand_1 \left(pbx(i,:) - px(i,:)\right) C_2 rand_2 \left(gbx\, px(i,:)\right) \tag{6.1}$$

$$px(i,:) = px(i,:) + \; v(i,:) \tag{6.2}$$

where $i = 1,2,3 \ldots i^{th}$ term is the particle index, pbx represents the best previous position that the particular particle has achieved, gbx represents the global best location. The $rand_1$ and $rand_2$ are the two independent random numbers associated with the acceleration weight factor within a range between 0-1. C_1 as a perceptional (cognitive) parameter and C_2 as a social parameter is the acceleration weight constants chosen optimally. These constants have been evaluated by utilizing the inertia weight factor using the given expression in Eq. (6.3):

$$C_1 = C_2 = \frac{(W+1)^2}{2} \tag{6.3}$$

The inertia weight factor is also assigned to improve the convergence performance in PSO which is calculated by linear decreasing weight (LDW) strategy, w, as given by Eq. (6.4) [223]. It allows the controllable exploration of the particles in the swarm [225] by protecting the limitations of bad pseudo-random generators, which results in the inadequate coverage of search locations in the random search space.

$$w = w_{max} - \frac{iteration(w_{max} - w_{min})}{iteration_{max}} \tag{6.4}$$

where, $iteration$ is the current iterations number and $iteration_{\ max}$ is the number of maximum iterations. In the developed PSO algorithm, the maximum and minimum inertia weight factors of w_{min} = 0.3 and w_{max} = 0.7.

In order to have a good balance between each particle, the limit of the velocity is changed after every iteration to avoid exploration and exploitation of the particle's velocities. To compute the current velocity limit as L_i, and the initial velocity limit as l_i are multiplied by a factor which is a function of the current iteration number t shown in Eq. (6.5) [226]:

$$L_i = f(t) l_i \tag{6.5}$$

$$where, \qquad l_i = \left(\frac{x_{i,max} - x_{i,min}}{2}\right) \tag{6.6}$$

$x_{i,max}$ *and* $x_{i,min}$ in Eq. (6.6) are the minimum and maximum values of a particle position, respectively. The initial velocity limit, l_i for the i^{th} variable dimension, has been initialized to half of the length of the search limits. The given function, $f(t)$ for total iterations, depends on the convergence criteria as the maximum number of iterations is limited to 1000 with an initial population of 50. The PSO algorithm is developed in commercial MATLAB® software. The flowchart consisting of the steps followed in the developed PSO algorithm is presented in Figure 6.1.

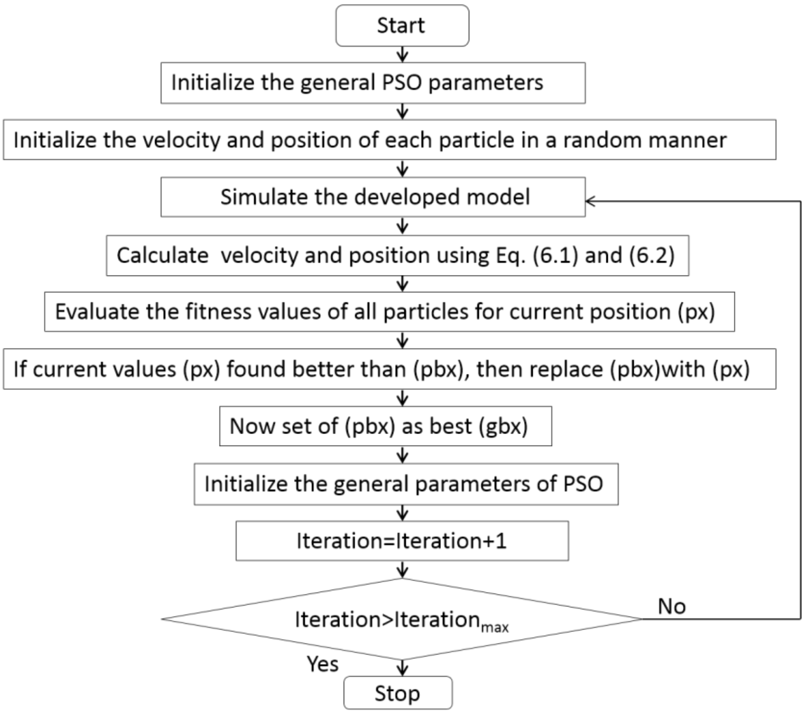
Start
Initialize the general PSO parameters
Initialize the velocity and position of each particle in a random manner
Simulate the developed model
Calculate velocity and position using Eq. (6.1) and (6.2)
Evaluate the fitness values of all particles for current position (px)
If current values (px) found better than (pbx), then replace (pbx)with (px)
Now set of (pbx) as best (gbx)
Initialize the general parameters of PSO
Iteration=Iteration+1
Iteration>Iteration_max
No
Yes
Stop

Fig. 6.1 Flowchart of a PSO algorithm.

6.2.2. Boundary Conditions

Typically, for thermodynamic optimization of MPFs heat sink design, appropriate thermal performance parameters need to be considered (Table 6.1) before solving the optimization problem. The developed algorithm aims to determine the optimal heat sink geometrical dimensions under given space restrictions. Therefore, a few assumptions that need to be taken for developing the PSO code are as follows:

6.2.3. Assumptions in the present study

1. The material of MPFs cross-section is considered homogeneous and isotropic.
2. No contact resistance between MPFs and the base plate.
3. The air, as Newtonian fluid, is considered for the present analysis
4. The fluid flow is assumed to be steady and laminar while passing through the different MPFs arrangements (inline and staggered).
4. The MPFs have no internal thermal energy sources within themselves.
5. The radiation and gravity effects from the MPFs body are not considered.

The developed numerical model and associated boundary conditions for solving the numerical model are depicted in Figure 6.2 and Table 6.3, respectively.

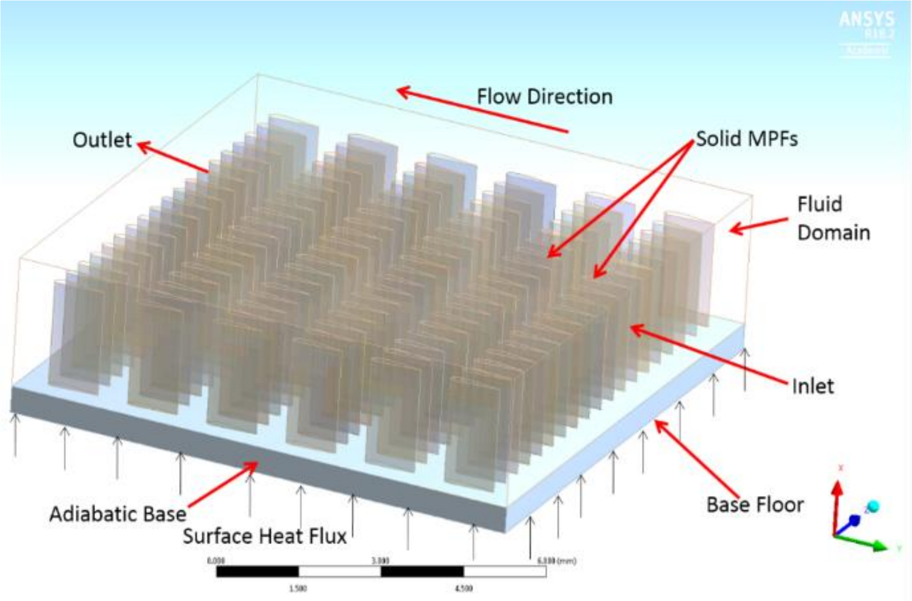
ANSYS
R18.2
Academic
Flow Direction
Outlet
Solid MPFs
Fluid Domain
Inlet
Adiabatic Base
Surface Heat Flux
Base Floor
0.000
3.000
6.000 (mm)
1.500
4.500

Fig. 6.2 Typical boundary conditions for the developed computational domain.

6.2.4. Mathematical formulation of main PSO algorithm

Certain modifications in the main PSO algorithm can meet the objective functions of 'Entropy Generation Minimization' (*EGM*) through arrayed MPFs. The objective function in the developed PSO depends upon the different linear and nonlinear inequality constraints. Sequentially, it includes characteristic chord length, cross-section area, perimeter, MPFs number, and height of a single MPF. Additionally, inter MPFs pitch distance in the transverse, longitudinal direction is considered for optimization given in Eq. (6.7):

$Minimize,$

$$EGM = f(L, H, A_c, P, N, D_T, D_L, D_D) = f(x_1, x_2, x_3, x_4, x_5, x_6, x_7, x_8) \quad (6.7)$$

The below equation shows the basic objective function without considering any constraint conditions given by Eq. (6.8):

$$fitness = \begin{cases} EGM \\ EGM + constant \end{cases} \quad (6.8)$$

where, $constant$ is set as penalty constant = 3000, for restricting the changes in the values of the constraints beyond the range. If the solution does not lie in the range, the objective function equals the sum of the entropy generation rate and the penalty constant.

A modified PSO algorithm given by Khan et al., [227] has been formulated by applying conservation of mass and energy laws and the entropy balance for a fluid flowing across the MPFs heat sink geometrical design. The equation for the entropy generation rate is given in Eq. (6.9):

$$EGM = (\frac{Q^2}{T_{amb}T_{base}})R_{hs} + \frac{\dot{m}\Delta P}{\rho T_{amb}} \tag{6.9}$$

where, R_{hs} is the total thermal resistance of the heat sink, ρ is the density of the MPFs material. The given expression of entropy generation rate also depends on the ΔP pressure drop across the heat sink provided the heat load, Q, and given mass flow rate, $\dot{m}$, at fixed ambient conditions. The heat load and the fluid properties at the ambient temperature are considered according to the typical microelectronic applications. The total thermal heat sink resistance is given by Eq. (6.10):

$$R_{hs} = R_m + R_{fins} \tag{6.10}$$

where R_m is the bulk heat sink material resistance and R_{fins} is the overall resistance of the MPFs heat sink, respectively given by Eqs. (6.11) and (6.12):

$$R_m = \frac{t_{bp}}{KL_bW} \tag{6.11}$$

where, W is the maximum width of the base plate along the transverse direction, t_{bp} is the thickness of the base plate, L_b is the longitudinal length of the base plate.
and,

$$R_{fins} = \frac{1}{\frac{N}{R_c + R_{fin}} + \frac{1}{R_{bp}}} \tag{6.12}$$

where, R_c is the contact resistance between MPFs and the base plate surface considered as zero. N is the total number of MPFs in the heat sink. R_{fin} and R_{bp} are the resistance of single MPF and the base plate, expressed by given Eqs. (6.13) and (6.14):

$$R_{singlefin} = \frac{1}{\sqrt{h_{fin}KA_cP}\ tanh\ tanh\ (mH)} \tag{6.13}$$

$$R_{bp} = \frac{1}{h_{bp}(L_b W - NA_c)} \tag{6.14}$$

The fin parameter, m, and the heat transfer coefficients, h_{fin}, for MPFs and h_{bp} for the square base plate surface are given in Eq. (6.15):

$$m = \sqrt{\frac{h_{fin}P}{KA_c}}, h_{fin} = \frac{Nu_L K_f}{L}, h_{bp} = \frac{Nu_{Lb} K_b}{L_b} \tag{6.15}$$

where, the Nusselt number correlations for the MPFs and the base plate are given in Eq. (6.16) and (6.17) [193],[227]:

$$Nu_L = \frac{h_{fin}L}{k} = 0.607 Re_L^{1/2} Pr^{1/3} \tag{6.16}$$

$$Nu_{L_b} = \frac{h_{bp}L}{k} = 0.75 Re_b^{1/2} Pr^{1/3} \tag{6.17}$$

where, k is the thermal conductivity of the fluid, $Re_L^{1/2}$ and $Re_b^{1/2}$ are the Reynolds Number for the maximum chord length L of single MPF and length of the base plate L_b in the flow direction given in Eq. (6.18):

$$Re_L = \frac{U_{app}L}{\nu} \; and \; Re_b = \frac{U_{app}L_b}{\nu} \tag{6.18}$$

where, ν is the Kinematic viscosity (m^2/s), and U_{app} is the approach velocity of the fluid flow (4-8 m/s). The mass flow rate of the fluid flowing through the MPFs is given by Eq. (6.19):

$$\dot{m} = \rho_f U_{app} N_T D_T H L \tag{6.19}$$

The pressure drop associated through MPFs heat sink in both inline and staggered arrangement is obtained by Eq. (6.20) [228]:

$$f = \frac{2(\Delta P)\rho_F}{N_{row}G^2} \tag{6.20}$$

where, ΔP is the change in fluid pressure at inlet and outlet of the fluid domain, and G is the mass flux calculated based on the minimum cross-sectional area available for the fluid to flow using an expression given in Eq. (6.21):

$$G = \frac{Q\rho_F}{A_{min}} \tag{6.21}$$

where, A_{min} is the minimum cross-sectional area for fluid flow calculated based on the MPF arrangements using the expressions given in Eqs. (6.22-6.24):

For inline arrangement:

$$A_{min} = \frac{D_T - D_f}{D_T} WH \tag{6.22}$$

For staggered arrangement:

$$A_{min} = \frac{D_T - D_f}{D_T} WH \, for \, \frac{D_T + D_f}{2} < D_D \tag{6.23}$$

$$A_{min} = \frac{2(D_D - D_f)}{D_T} WH \, for \, \frac{D_T + D_f}{2} > D_D \tag{6.24}$$

where, D_D is the diagonal distance between two MPFs in the staggered arrangement ($D_D = \sqrt{D_L^2 + \left(\frac{D_T}{2}\right)^2}$). Besides, the overall friction factor (f) correlation utilized by Tullius et al. [170] is a good representation for the geometric optimization of MPFs cross-section. Thus, the friction factor for optimal MPFs cross-section is calculated by Eq. (6.25):

$$f = C_f \left(\frac{D_L}{D_f}\right)^{0.2} \left(\frac{D_T}{D_f}\right)^{0.2} \left(\frac{H}{D_f}\right)^{0.18} \left(1 + \frac{dh}{D_f}\right)^{0.2} Re_L^{-0.435} \tag{6.25}$$

where, C_f is the frictional coefficient factor - 3.44, H is the height of the MPFs, D_L and D_T are the inter MPFs gaps in longitudinal and transverse direction for both arrangements. The dh is the clearance above the MPFs top for the fluid flow, and the hydraulic diameter of MPFs (D_f) is given by Eq. (6.26):

$$D_f = \frac{4A_c}{P} \tag{6.26}$$

Thus, the derived equation for the total thermal resistance of the MPFs heat sink is given by Eq. (6.27):

$$R_{hs} = \left[\frac{1}{\left(N\sqrt{h_f k A_c P} \, tanh \, tanh \, (mH)\right) + \, h_b(L_b W \, - \, N A_c)} + \, R_m\right] \tag{6.27}$$

The formulated PSO algorithm for EGM as an objective function and design constraints along with ranges are given in Eq. (6.28):

$$\left\{ minimize, EGM\ for\ MPFs \right.$$

$$= \frac{K_f v T_{amb}}{U_{app}} \left[\left[\frac{1}{\left(N\sqrt{h_{fin} k A_c P}\ tanh\ tanh\ (mH)\right) + h_{bp}(L_b W - NA_c)} + R_m \right] \left(\frac{1}{T_b}\right) + \frac{\dot{m}\Delta P}{\rho Q^2} \right] \left. \right\} \tag{6.28}$$

$subjected\ to\ contraints\ (mm);$

$g_1: 1 < L \le 1.6$	$g_6: 100 \le N \le 130$ (Staggered)
$g_2: 0.2 \le H \le 0.95$	$g_7: 0.7 \le D_T \le 1$
$g_3: 0.16 \le A_c \le 0.62$	$g_8: 1.15 \le D_L \le 1.3$
$g_4: 2.13 \le P \le 4.32$	$g_{10}: N * A_c - 0.0001440 \le 0$ (bounding factor (penalty approach))
$g_5: 115 \le N145$ (Inline)	$g_9: 1.3 \le D_D \le 1.35$ (for staggered arrangement)

Table 6.1. Operating parameters.

Parameters	**Values**	**Parameters**	**Values**
Footprint (mm^2)	12 X 12	Coefficient of thermal expansion (K^{-1})	22.9 X 10^{-6}
Base plate thickness (mm)	0.5	Acceleration due to gravity (m/s^2)	9.81
Kinematic viscosity of air (m^2/s)	1.58 X 10^{-5}	Specific heat of heat sink (J/Kg.K)	921
Thermal conductivity of air (W/mK)	0.0267	Heat Flux (W/m^2)	2 X 10^6
Thermal conductivity of heat sink (W/mK)	205 (Al)	Approach Velocity (m/s)	0.5
Density of air (kg/m^3)	1.225	Prandtl number (Air)	0.71
Density of solid heat sink (Kg/m^3)	2710		

6.2.5. Developed PSO mathematical model

In view of the essential concern of higher heat loads and smaller space availability, optimal MPFs heat sinks geometrical design is limited to smaller base plate dimensions and maximum MPFs height up to 950 μm. Therefore, the objective function is set to select the best possible heat sink geometrical design requirements in both the arrangements of densely arrayed MPFs. The developed PSO algorithm minimizes the objective function at variable PSO parameters such as inertia weight, number of particles, and acceleration parameters. The optimal EGM values based on optimal PSO parameters have been solved for both arrangements.

In the present analysis, the PSO algorithm runs three times with 1000 number iterations, each time with a maximum population size of 110. In each iteration, many solutions are found, but the algorithm chooses the constraint values that give the optimal solution. Then, these values have been compared with the previous optimal solution it has achieved so far (the global best value) and it found that the global best value moves towards an optimized solution. When all the solutions moved towards better solutions, it can be understood that the developed PSO algorithm has achieved convergence for the provided iteration numbers. Accordingly, the global best value of the objective function gets constant after certain iterations. It remains unchanged further for all iterations, showing the optimal results consistency for EGM through arrayed MPFs heat sinks. The optimization objectives, including EGM are performed using the developed PSO algorithm that accounted for the maximum thermal losses between the MPFs heat sink and the fluid. Figure 6.3(a,b) shows the comparative convergence plot of the global EGM per number of generations for both inline and staggered arrangements of MPFs heat sinks. It is found that the EGM value gives an acceptable thermal performance for the staggered MPFs arrangement than the inline of 0.007357 W/K and 0.497710 W/K, respectively. Thus, the staggered arrangement with higher MPFs density gives a minimum EGM value under the same thermal parametric conditions and for the same material. Hence, it can be inferred that the staggered arrangement of MPFs for the whole range of different constraints values will be considered a better alternative for excessive heat dissipation in a controlled volume.

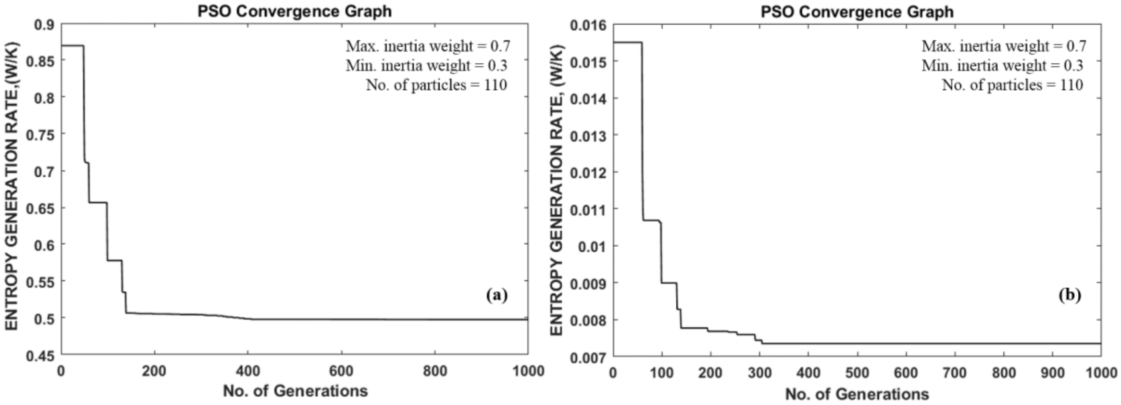

Fig. 6.3 EGM convergence plots for (a) inline and (b) staggered arrangements of arrayed MPFs heat sinks.

Based on the minimum rate of *EGM*, the obtained optimum geometrical design parameters for the inline and staggered arrangements of MPFs heat sinks are presented in Table 6.2. These parameters are further utilized to quantify the heat transfer performance through the complex cross-section MPFs profiles. For this, numerical simulations have been performed in ANSYS-FLUENT® using the generated MPFs heat sink design model.

Table 6.2. Optimal geometric design parameters of MPFs heat sinks.

MPFs arrangement	**Fins spacing, (μm)**			**Height of each MPF (μm)**	**Chord Length of each MPF (μm)**	**Cross-section area of single MPF (mm)**	**Perimeter of single MPF (mm)**	**Number of fins (N)**
	D_T	D_L	D_D					
Inline	980	1278		950	1265	0.59	4.02	131
Staggered	945	1280	1320	931	1118	0.61	4.18	115

6.3. Numerical simulation for thermal performance evaluation

The optimized geometric design parameters have been used to reproduce heat sink models using a coupled CAD geometrical profile and developed MATLAB® code. The cross-sections of the MPFs include elliptical, aerofoil (NACA 2412), droplet, and Piranha considered for numerical simulation are presented in Figure 6.4(i). It is noteworthy that the optimal geometric parameters for each MPFs profile are similarly assigned. Figure 6.4 shows the dimensional detail and shape of the MPF heat sinks model in an inline and staggered arrangement (elliptical profile) subjected to thermal simulation.

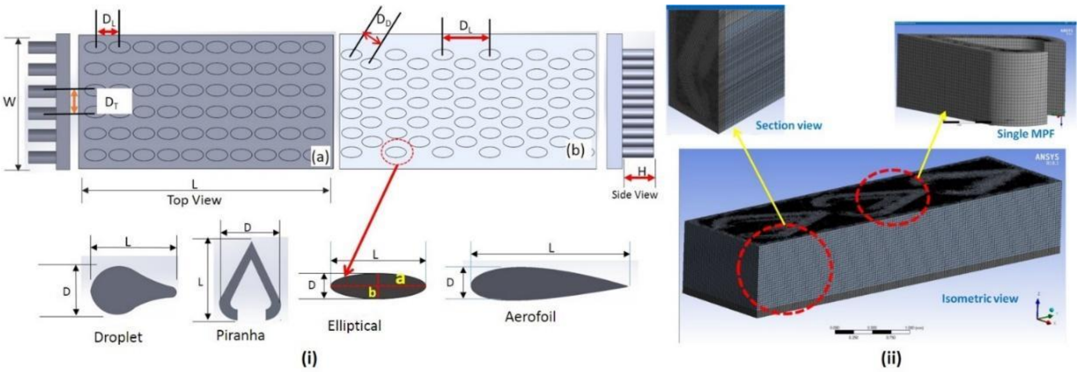

Fig. 6.4 (i) Arrayed MPFs heat sink arrangements (a) inline (b) staggered along with the geometrical representation of different MPFs profiles, and (ii) mesh model of the computational domain.

A unit cell approach for each MPFs heat sink profile is used to perform thermal analysis in both inline and staggered MPFs arrangements. The computational model consisting of solving identities is presented in Figure 6.2. The single-phase, steady-state, conjugate symmetrical boundary conditions on both sides of the unit cell are applied to reduce excessive simulation runs, longer computational time, and operation costs.

Air as the working fluid with a varying flow velocity at the inlet wall temperature of 27^0C is taken for convective heat transfer analysis. The constant heat flux (Q = 2 X 10^6 W/m^2) is applied at the bottom surface of the base plate. The thermal convection coefficient of fluid flowing (10 W/m^2.K) is set inside the domain. Also, a turbulence intensity of 1% and a length scale of 2% are considered for the initial height of the fluid domain next to the inlet. The non-slip condition is applied to every solid wall of the computational domain, including the MPFs body and the fluid domain's internal surface. The material for the MPFs heat sink is considered aluminium with constant thermal properties. A fine-structured grid system with a hexahedral mesh element is used to generate mesh for the whole computational domain. The highly refined mesh is applied in critical areas (near to MPFs body) to ensure parametric results convergence near the no-slip MPFs walls. It is supposed that the fluid velocity and temperature gradients are expected to be high enough in these areas.

An apparent test of grid independence study has been examined with different grid sizes to improve the convergence speed and computational accuracy. The subsequent trial runs refine the mesh by decreasing cell size for the whole computational domain. A temperature difference of approximately 0.69 °C is observed from the several simulation runs when the mesh size has been kept between 5500000 and 5800000 cells. Therefore, the computational domain with around 5500000 cells has been selected to perform simulations for faster computational time and minimum CPU power consumption with a trivial compromise of accuracy. An illustrative view of the optimally meshed computational domain is depicted in Figure 6.4(ii).

6.3.1. Governing equations

Here, the three-dimensional governing equations employed for continuity, momentum, and energy have been solved simultaneously for a higher convergence rate of the computational model. These governing differential equations also describe the fluid flow and heat transfer behavior through the computational domain. The basic governing equations are presented in Eqs. (6.29-6.31):

Continuity equation:

$$\nabla . \vec{v} = 0 \tag{6.29}$$

Conservation of momentum equation:

$$\rho \, (\vec{v} . \nabla \, \vec{v}) = - \nabla P + \mu . \nabla^2 \vec{v} \tag{6.30}$$

Conservation of energy equation:

$$\rho C_p (\vec{v} . \nabla T) = K \vec{\nabla}^2 T \tag{6.31}$$

where, $\vec{v}$ is the velocity of fluid flow, ρ density of the fluid, P is the fluid pressure, μ is the coefficient of fluid viscosity, C_p is the specific heat capacity of the fluid, K is the thermal conductivity of the fluid and T is the initial fluid temperature. The significant boundary conditions assigned to the different zones of the computational domain are also presented in Table 6.3.

Table 6.3. Boundary conditions.

Inlet	$u = const, v = w = 0, T = constant$
Outlet	$\frac{\partial u_i}{\partial x} = \frac{\partial T}{\partial x} = 0$
Other surfaces of the extended and fluid domain region	Slip and adiabatic wall
Interface between air and solid MPFs	No-slip, no thermal resistance
Top surface of the fluid domain	Adiabatic

The 3D numerical simulations of each MPFs profile with the optimal mesh have been performed based on the finite volume method. A three-dimensional conjugate MPFs heat sink model is used to evaluate the heat transfer between the MPFs heat sink material and the fluid flow. The governing differential equations of mass momentum and energy, and essential thermal parametric values are utilized in the simulation runs. The power-law scheme is used for discretizing the momentum and energy equations. A viscous-laminar model for the varying *Re* regime between ($100 \leq Re \leq 1000$) is adopted. The second-order upwind mode is selected for discretizing the governing equations and stability of solution convergence. The semi-Implicit Method for Pressure Linked Equations (SIMPLE) algorithm is used for faster convergence of pressure-velocity coupling. It is due to the change in the fluid flow state from the inlet to outlet wall within the computational domain. The normalized residuals falling between 10^{-5} and 10^{-7} are set to converge continuity, momentum, and energy equations. Other significant details for faster computation have been considered from ANSYS Fluent software user's guide. Furthermore, the results of the numerical simulations are utilized for evaluating thermal performance parameters associated with arrayed MPFs heat sinks, which mostly affect heat transfer efficiency.

6.3.2. Validation of the model

The computational domain utilized in this work has been verified for its authenticity by comparing the experimental results of Liu et al. [229]. The experimental results obtained for circular MPFs heat sinks, as depicted in Figure 6.5 are used to validate the developed numerical model. The heat sink dimensions and arrangement are considered actual to the experimental test specimen used and are listed in Table 6.4.

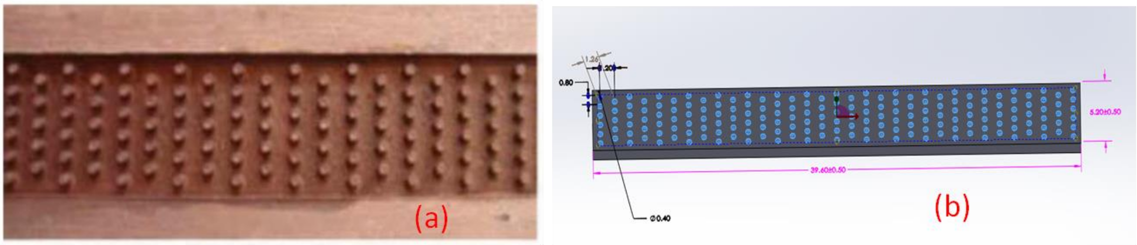

Fig. 6.5 Representation of circular MPFs (a) experimental test section, (b) similar CAD model [229].

The applied experimental conditions have been taken as it is for better comparison of results. Initially, several runs have been performed with different mesh configurations for the model validation. After getting the appropriate mesh configuration, the numerical thermal performance evaluation of the model has been performed. The results obtained have been compared with the experimental results and are presented in terms of f, Nu, and ΔP with varying Re. For the present study, Re is chosen for the basis of comparison because the varying Re shows the conductive as well as convective heat transfer behavior through the model.

Table 6.4. Detailed geometric dimensions of circular MPFs arrangement.

Details of test section	**Values (mm)**
Shape	Circular
Diameter	0.4
Height	0.5
Longitudinal Pitch	0.8
Transverse Pitch	1.2
Distance from the first fin to the next row fins	1.265

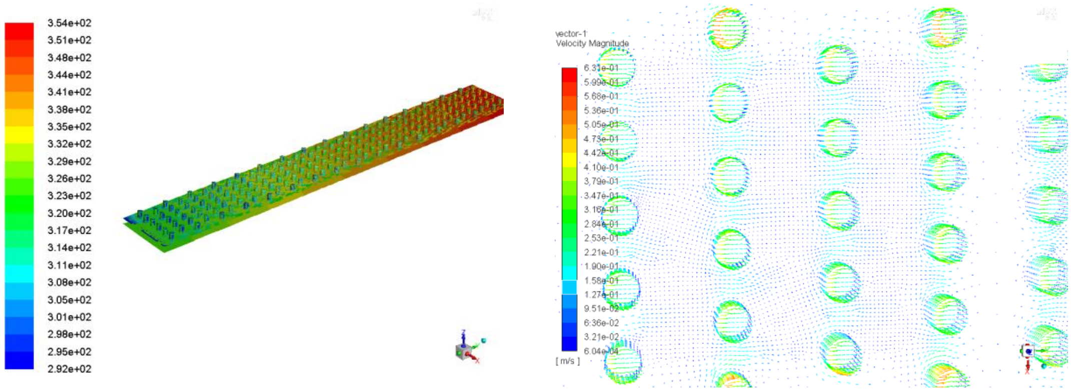

(a) (b)

Fig. 6.6 (a) Temperature contours of the validation model, and (b) velocity vectors in staggered arrangement of circular MPFs.

Figure 6.6 shows the validated numerical model of circular MPFs in a staggered arrangement. The comparative results of thermal parameters, *f*, *Nu*, and ΔP are shown in Figure 6.7(a-c). It is found that the simulation results obtained are very close with the experimental results. The maximum deviations in *f* and *Nu*, are found approximately of 2% and 3%, respectively. The maximum pressure drop is found to be 38.83 kPa by simulation compared to 38.26 kPa for experimental results at a mass flow rate of 180 ml/min with a maximum error of 2%. This deviation may be due to the surface integrity of MPFs and the complexity of the governing equations. From this validation run, the present computational domain can be further used with reasonable accuracy for successive calculations.

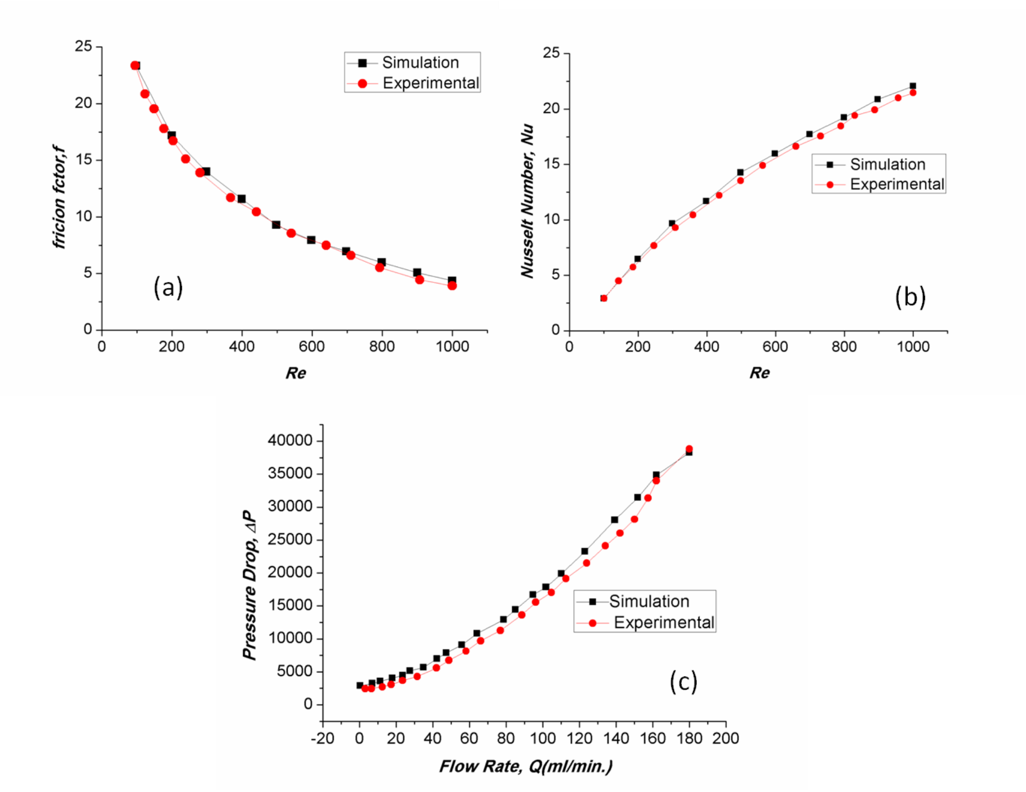

Fig. 6.7 Validation results of simulation and experimental runs (a) f, (b) Nu, and (c) ΔP through circular MPFs [229].

6.4. Thermal performance results

The Nu is one of the most critical and interesting thermal parameters associated with the convective heat transfer through MPFs heat sinks. Since it was not possible to directly examine the behavior of the Nu unless the local heat transfer coefficient is not known. The Nu is calculated using the following Eq. (6.32):

$$Nu = \frac{hd_h}{k_f} \tag{6.32}$$

where, d_h and k_f are the hydraulic diameter of the MPFs heat sink and thermal conductivity of the flowing fluid, respectively. Whereas, h is the average convective heat transfer coefficient determined by the energy balance between the heater input power and the sensible heat increase of the fluid during the single-phase heat transfer analysis. The h is calculated for each arrayed MPFs cross-sections using the following Eq. (6.33):

$$h = \frac{QA_h}{\left[\left(A_h - N_{tot}\frac{\pi L_f^2}{4}\right) + \left(\pi L_f H_f N_{tot} \eta_f\right)\right]\left(T_b - T_f\right)} \tag{6.33}$$

Here, L_f and H_f are the MPF characteristic length and height, respectively. N is the total number of MPFs, T_b is the average temperature at the heat sinks base, which is estimated using the one-dimensional heat conduction from the bottom surface of the computational domain (Figure 6.9). T_f is the bulk fluid temperature along the MPFs heat sink and η_f is the MPF efficiency, which can be determined by Eq. (6.34):

$$\eta_f = \frac{tanh\ (H_f)}{mH_f} \tag{6.34}$$

where, m is the MPF constant defined by relation given in Eq. (6.35):

$$m = \sqrt{\frac{hP_f}{k_a A_f}} \tag{6.35}$$

where, k_a is the thermal conductivity of the MPF material (aluminum), and P_f and A_f are the perimeter and cross-sectional area of the single MPF, respectively.

Figure 6.8(a,b) presents the variation of the *Nu* number as a function of *Re* for different MPFs profiles in both arrangements. Commonly, at higher *Re*, the *Nu* number is larger, resulting in the flow disturbance and enhanced convective heat transfer rate than at smaller *Re*. It has been observed, $Re > 100$, *Nu* significantly depends on the MPFs cross-sections as well as the operating conditions which have substantial effect on fluid interaction with the MPFs body.

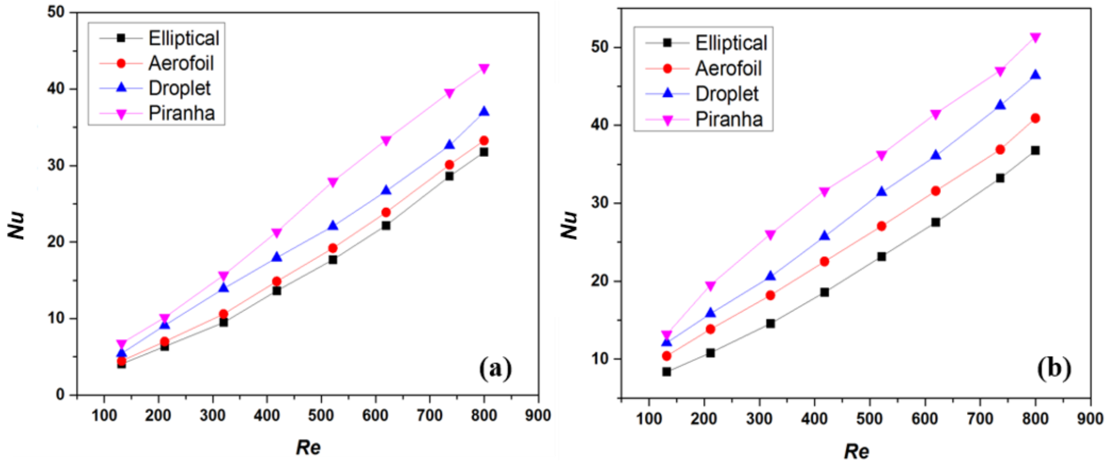

Fig. 6.8 *Nu* as a function of *Re* in (a) inline and (b) staggered arrangement of different MPFs cross-sections.

From Figure 6.8(a,b), it is observed that the Piranha MPFs profile has a higher *Nu* number followed by droplet, aerofoil, and elliptical profiles in both the arrangements. It is due to the larger surface area of Piranha MPFs in contact with the fluid flowing. This resulted in thin thermal boundary layer thickness and better fluid flow mixing in the arrayed heat sinks. Additionally, it may be due to the larger beneficiary recirculating region at the trailing edge of each MPFs, especially in the case of Piranha MPFs profile shown in Figure 6.10(a-d). Due to this, the better heat transfer efficiency has been observed in staggered arrangement than inline arrangement. It is because the fluid flowing through the arrayed heat sink has enough kinetic energy to dissipate heat in a staggered arrangement.

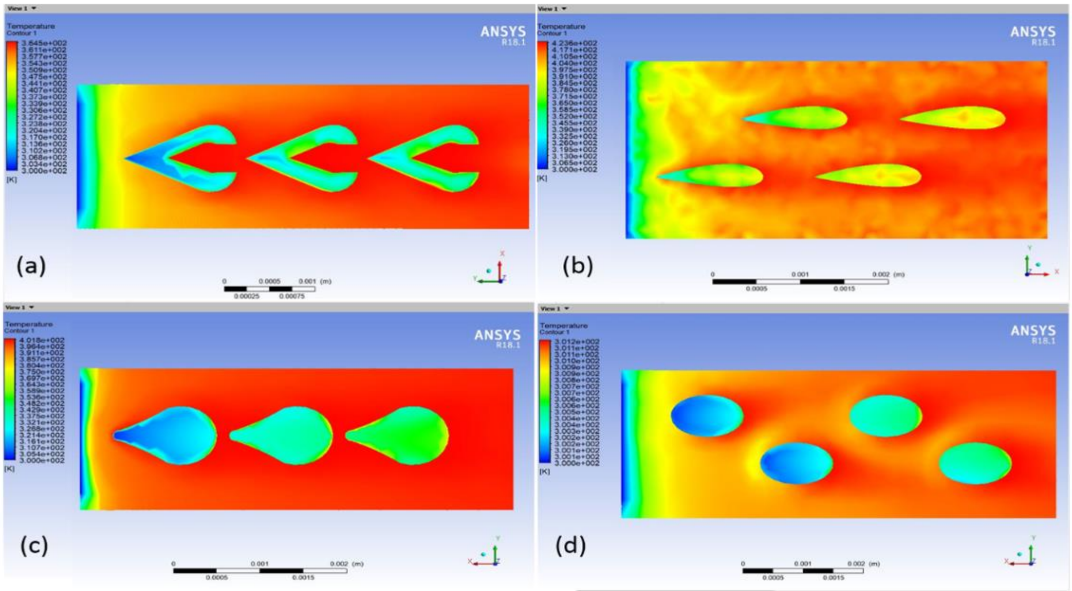

Fig. 6.9 (i) Temperature distribution (a,c) inline, and (b,d) staggered arrangement of different MPFs cross-sections at *Re* = 319.

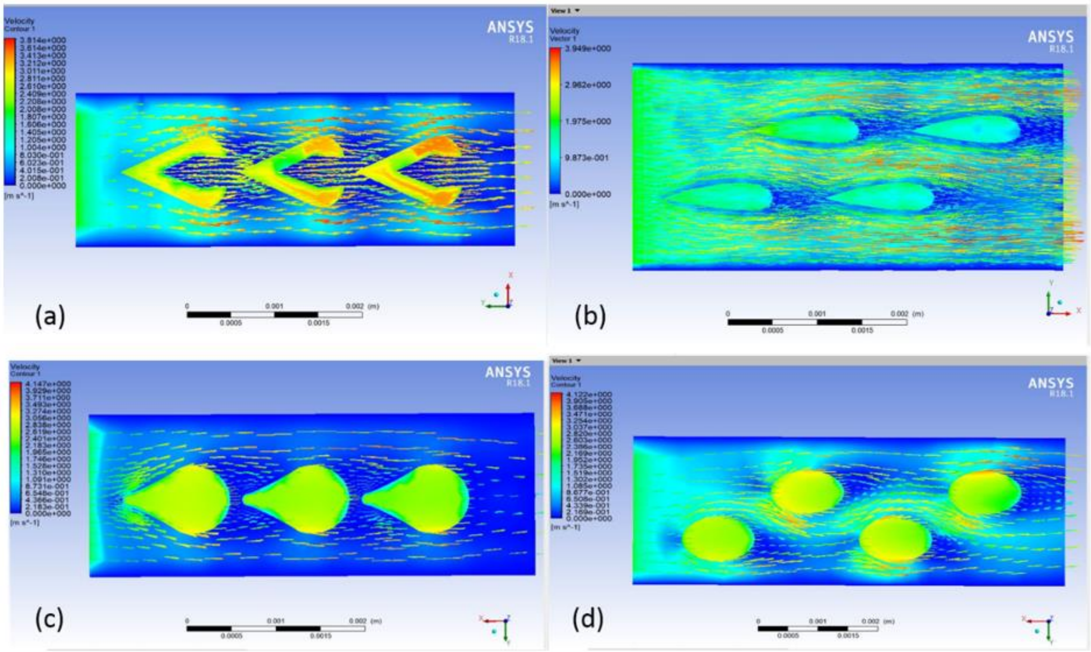

Fig. 6.10 Flow pathlines (a,c) inline, and (b,d) staggered arrangement of different MPFs cross-sections at Re = 319.

The augmented heat transfer efficiency is vital for cooling; however, the pumping power of the fluid flowing should be considered for the energy efficiency in terms of power consumption of the cooling system. The required energy for pumping power can be evaluated from the pressure drop along the arrayed MPFs heat sinks which is given by Eqs. (6.36) and (6.37):

$$\Lambda = \Delta P \times Q_{flow} \tag{6.36}$$

$$\Delta P = P_{in} - P_{out} \tag{6.37}$$

where, Λ is the pumping power, and Q is the desired flow rate of fluid flow. Figure 6.11(a,b) depicts the varying ΔP (kPa) with increasing Re for each MPFs profile in an inline and staggered arrangement. At lower Re, each arrayed MPFs heat sink shows lesser ΔP under the same fluid flow velocity. On the other hand, when a fluid flow velocity increases, the ΔP in each MPFs cross-section increases apparently in both the arrangements. Moreover, it is observed that the Piranha MPFs in both arrangements have the lowest pressure drop for the whole Re range, followed by aerofoil, elliptical, and droplet MPFs profiles. This is due to the geometrical cross-section profiles and arrangement of the MPFs resulting in lesser pressure drop. This fact is attributed that the Piranha MPFs profile has a smaller shear angle at the leading edge, facilitating the smooth fluid flow and reducing friction drag conditions. These conditions also prevail similarly for the aerofoil, elliptical, and droplet MPFs, but are larger than Piranha MPFs due to the more fillet at the leading edge. Hence, this resulted in an increase ΔP at higher Re in both arrangements.

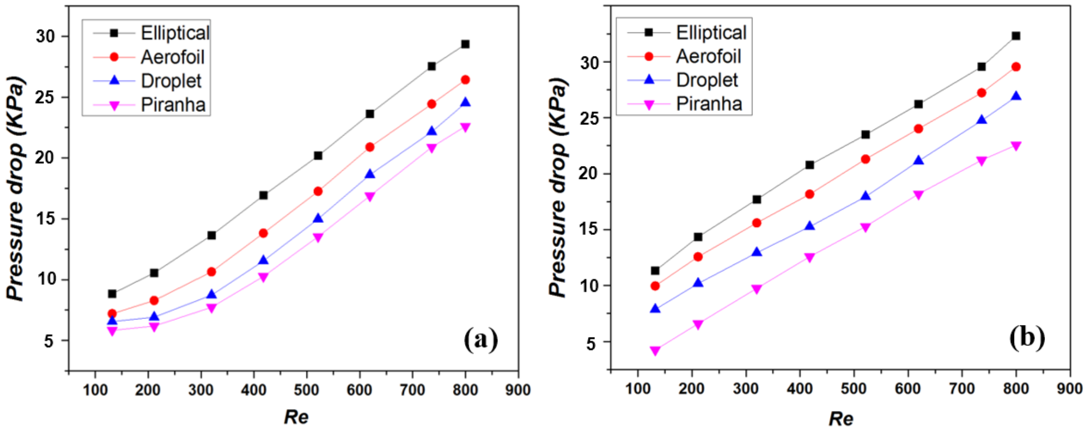

Fig. 6.11 ΔP as a function of Re in (a) inline and (b) staggered arrangement of different cross-sections.

A non-dimensional parameter termed as $TPI = \left(\frac{(Nu/Nu_0)}{(\Delta P/\Delta P_o)^{1/3}}\right)$ is evaluated for identifying the overall performance of the different MPFs profiles. Figure 6.12 shows TPI based on the finned and unfinned heat sinks as a function of Re. The Piranha MPFs heat sink has shown the highest TPI over the whole Re followed by droplet, aerofoil, and elliptical MPFs heat sinks in a staggered arrangement. It is due to higher heat carrying capacity and less flow separation of flowing fluid leading to the high heat transfer rate. The flow streamlines in the Piranha MPFs heat sink follows the surface movement, leading to a higher convective heat transfer rate and lower pressure drop than other MPFs profiles. Hence, it can be understood that the geometrical profiles of MPFs have a crucial influence on heat transfer performances in both conductive and convection heat transfer modes.

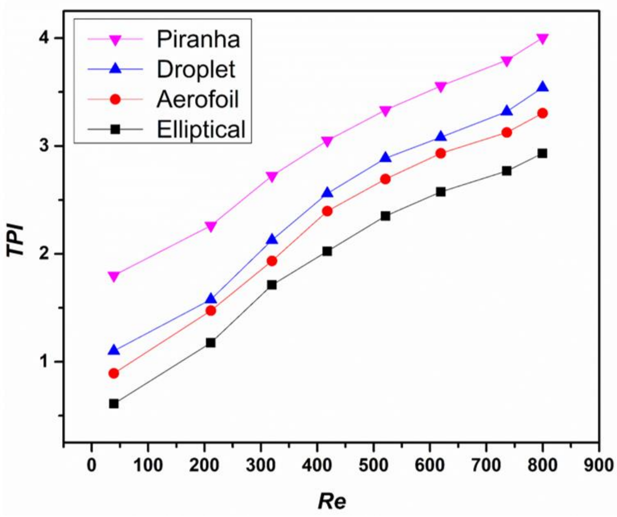

Fig. 6.12 TPI as a function of Re for different MPFs cross-sections in a staggered arrangement.

From this numerical study, it can be concluded that the cooling capacity through the unconventional cross-section arrayed MPFs has been enhanced for given heat loading conditions. Moreover, the geometrical parametric optimization and thermal performance analysis reached out in deciding the optimal design parameters and best-performing cross-section of the MPFs. The obtained numerical results showed that unconventional cross-section arrayed MPFs would be a better alternative in dissipating high heat flux compared to regular cross-sections MPFs. The obtained thermal performance needs to be verified using an experimental approach when the combined effect of Nu and ΔP would have been considered. A detailed experimental study regarding the evaluation of thermal performances has been performed in the next chapter.

6.5. Chapter conclusion

This chapter has demonstrated an in-depth evaluation of thermal losses based on the EGM approach to design arrayed MPFs heat sinks. This thermodynamic approach primarily evaluates the effect of different thermal parameters such as thermal resistance, pressure drop, Nusselt number, etc. EGM as an objective function is formulated in MATLAB® using the PSO algorithm to optimize the dimensional parameters of the MPFs. The axial length, height, inter MPFs gaps, cross-section area, perimeter and density of MPFs are considered the decisive design parameters for geometrical optimization. The design parameters are evaluated based on the EGM at the optimal

PSO parameters, in both, the inline and the staggered arrangements. The optimal design parameters are used further to model various cross-sectional profiles viz. elliptical, aerofoil, droplet and Piranha of MPFs for comparative numerical simulations. Piranha MPFs profile in the staggered arrangement with a maximum height of 931 μm and an array size of 115 MPFs is found to be providing the best TPI by dissipating heat flux up to $2x10^6$ W/m^2.

Chapter 7

Experimental Evaluation of Thermal Performance

7.1 Introduction

The present chapter demonstrates the experimental verification of the thermal performance through the optimized arrayed MPFs configurations. This chapter presents the fabrication of optimal arrayed MPFs heat sinks in different cross-section profiles by implementing optimal machining parameters and assisted facilities elaborated in chapters 3, 4, and 5. The development of an in-house closed-loop testing facility, for analyzing the thermal performance of the fabricated MPFs heat sinks, is presented in this chapter. The results obtained from the iterative experimentation are analyzed and presented in terms of overall thermal performance viz. *TPI*.

7.2. Test rig design

The test rig designing and fabrication, as shown in below Figure 7.1, is based on the optimal geometrical design parameters of arrayed MPFs heat sinks obtained from numerical modeling. The optimal geometrical design parameters of arrayed MPFs heat sinks in both inline and staggered arrangements (Figure 7.4) used for thermal performance analysis are presented in Table 7.1.

Table 7.1. Optimal geometric design parameters of MPFs.

MPFs arrangement	**Fins spacing, (μm)**			**Height of each MPF, (μm)**	**Chord Length of each MPF, (μm)**	**Cross-section area of single MPF, (mm)**	**Perimeter of single MPF, (mm)**	**Number of fins (N)**
	D_T	D_L	D_D					
Inline	980	1278		950	1265	0.59	4.02	131
Staggered	945	1280	1320	931	1118	0.61	4.18	115

The dimensional details of the fabricated test rig are given in Figure 7.1(a). The test rig is divided into (a) the upper part and (b) the lower part (Figure 7.1(b)). In the lower part, an inlet and outlet ports are machined at the test rig's right face for the continuous fluid flow to the reservoir. The outlet port opens to the atmosphere while the inlet is connected to the outlet of the blower for systematic fluid flow through the test rig. Two reservoirs have been made at either end of the test rig for a continuous supply of fluid at the desired flow velocity into the rectangular channel. The dimensions of machined reservoirs are provided with a diameter of 50 mm and a height of 35 mm ensuring the laminar flow in the channel.

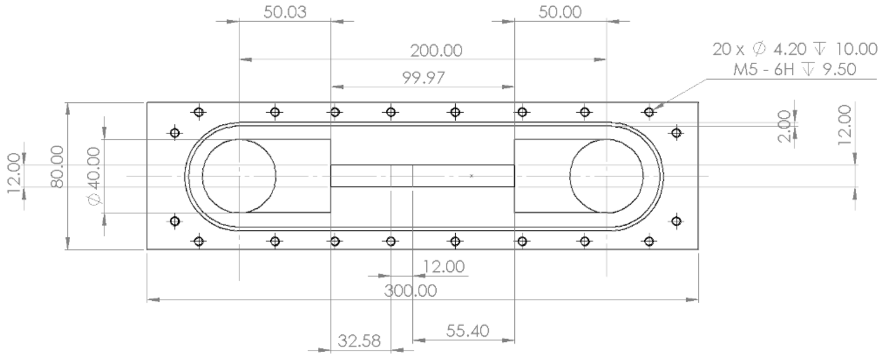
50.03
50.00
200.00
99.97
20 x ∅ 4.20 ↧ 10.00
M5 - 6H ↧ 9.50
2.00
12.00
12.00
80.00
∅ 40.00
12.00
300.00
32.58
55.40

(a) Dimensional details of the test rig design

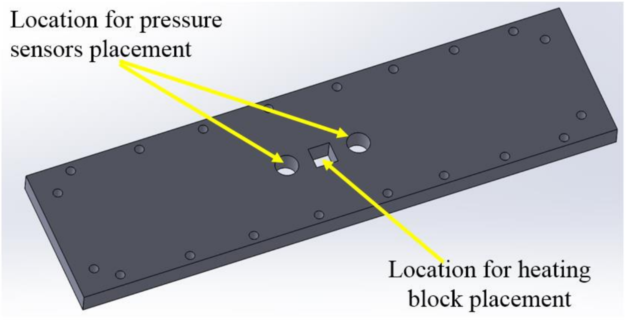
Location for pressure sensors placement
Location for heating block placement

(i) Upper part

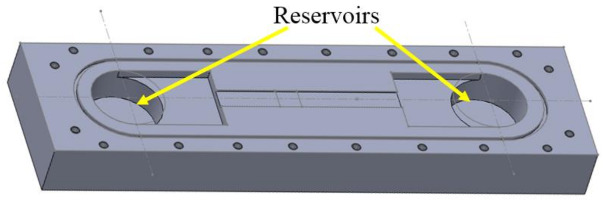
Reservoirs

(ii) Lower part

(b) 3D CAD model of the test rig

Fig. 7.1 In-house designed test rig used for experimental analysis.

The fluid flow velocity profile entering into the rectangular channel needs to be fully developed such that the velocity profile does not change along the direction of flow (axial direction, for effective heat transfer performance. Therefore, in the lower part of the test rig, a long rectangular channel of 1 mm x 12 mm is machined in the middle which guides the flowing fluid through the MPFs heat sinks of height 950 µm.

The rectangular channel has been provided with sufficient hydrodynamic development length in upstream (approximately 50 times the hydraulic diameter of a single MPF) and downstream (20 times the hydraulic diameter of a single MPF) from the MPFs heat sink placement to minimize entry and exit effects of fluid flow. Here, the hydrodynamic length means the distance travelled by the flowing fluid after entering into the rectangular channel to become a fully developed flow. This rectangular channel recesses allow the inner surfaces of the upper and lower part of the test rig to provide space to flush out generated heat flux within the arrayed MPFs heat sinks. The upper part of the test rig is a cover plate that consists of a recess for the heating block placement, and drilled holes for accurate positioning of the temperature and pressure sensors are shown in Figure 7.1(b). Two pressure ports have been machined at 12 mm upstream and downstream of the heat sink in the upper part of the test rig for installing pressure sensors.

Heat dissipation to the ambient air from the heating block apart from the base area should be minimal and need to be quantified before the thermal performance experiment. This has been achieved by the suitable geometry selection of the heating block and minimum insulation layer thickness and material. The thickness of the insulation layer has been decided based on the simulation results of the one-dimensional heat conduction result through the heating block. In this regard, a finite element model is developed with the desired geometry of the heating block, and the three-dimensional steady-state heat conduction equation is solved in ANSYS® 19.3. A fine-structured grid system of hexahedral mesh (Hex8 noded brick element) is adopted for the model development of heating block carefully built by using ANSYS® Meshing in ANSYS-19.3. The size of the element is taken of $9.291\text{x}10^{-4}$m. The maximal heat losses occur when the heating block is solved at the provided heat flux at the internal wall of the heating block. To minimize the heat loss, it is assumed that the thermal resistance between the heating block covered with the insulation layer and the environment reached its highest value. A similar heat flux boundary condition is applied to the heating block to achieve a maximum steady temperature of 70-degree Celsius at the outer surface. The simulation results show that the heating block undergoes heat losses to the surrounding from 4-6% when an insulation layer of 4 mm thick is collectively provided of glass wool and nitrile foam material. Figure 7.2 shows the temperature contour of the heating block under steady-state conditions.

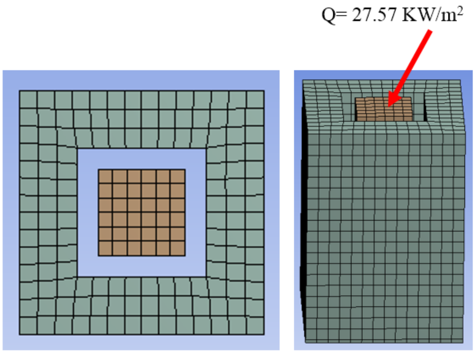

(a) Meshed model

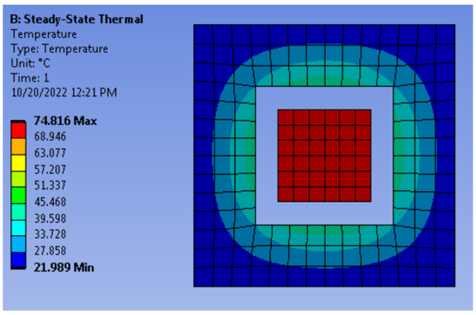

(b) Temperature contour plot

Fig.7.2 Numerical model of the heating block.

After designing the heating block and insulation layer thickness for minimum heat losses, leak-proof fluid flow is the most important aspect of the test rig design. Pressurized air is ensured not leaking through the contact area between the upper and lower part of the test rig and also from the heating block slot. A silicon rubber band is placed in the machined slot (Figure 7.1(b)) all around the top surface of the lower part of the test rig. A gasket all around is also placed at the edge of the lower part to prevent leakage. Both the rubber band and gasket are sandwiched between the upper and lower part of the test rig and tightened by bolts all through the test rig. The soap bubble test has been done to ensure that the test rig is free from any leakage at the mating surface and through the machined slots (for the heating block and sensors) in the upper part of the test rig. The schematic of the test rig consisting of all the necessary components is shown in Figure 7.3.

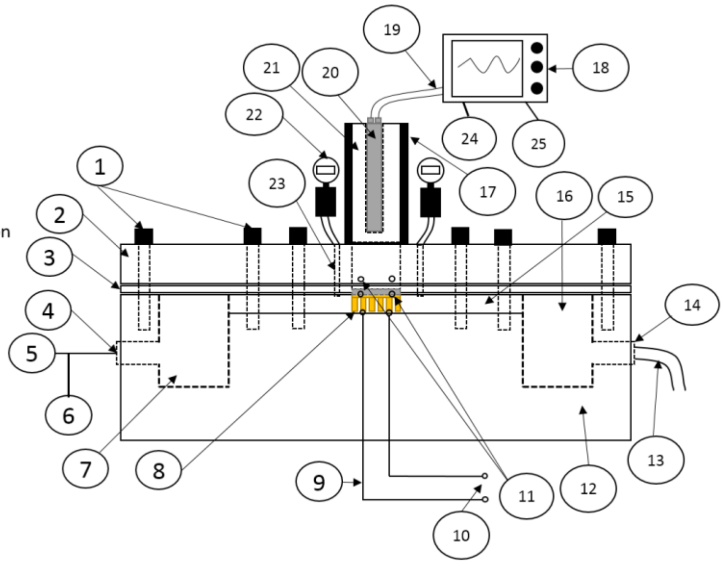

1. Lock nut
2. Cover plate (Upper part)
3. Leak proof (Top washer)
4. Inlet
5. Air blower with flow controller
6. Anemometer
7. Fluid supplying reservoir
8. MPFs heat sink
9. Thermocouple sensors (K-type)
10. Multi point temperature scanner
11. Machined slots for thermocouple insertion
12. Test section (Lower part)
13. Transparent PU pipe
14. Outlet
15. Rectangular channel for fluid flow
16. Collecting reservoir
17. Thermal insulation layer
18. Auto-transformer
19. Electrical connections
20. Cartridge heater
21. Heating block
22. Pressure transducers
23. Pressure taps
24. Multimeter for "V" measurement
25. Multimeter for "A" measurement

Fig. 7.3 Schematic illustration of the in-house developed test rig.

7.2.1. Thermal performance experimental design

The generated one-dimensional heat flux through the heating block is transferred to the bottom surface of arrayed MPFs heat sinks. The arrayed MPFs heat sink sample is pasted at the interface of the heating block by a thin layer of thermally conductive silicone paste (Gelid Solutions GC-Extreme 3.5 g) of thermal conductivity 8.5 W/mK to minimize the contact resistance. The heating block has a recess at the center for holding the 220 V/ 200 W cartridge heater (RS components & Controls (I) Ltd.) diameter of 13 mm. The cartridge heater is located in a heating block, such that one-dimensional heat flow towards the heat sink is ensured. A calibrated auto-transformer is used for providing a constant power supply (36.25 V/0.153 A) to the cartridge heaters. Two calibrated digital multimeters have been used to record the supplied voltage and current values (Fluke India, 87 V).

The arrayed MPFs heat sink is sandwiched between the lower and upper halves of the test rig, which are fixed together as depicted in Figure 7.3 (marked as the 8th number in the list). Pressurized air is supplied through the portable digital tire inflator (Agaro, 120 W, max. 150 psi) at a velocity between 4-7 m/s through the inlet port of the test rig. The velocity of fluid flowing into the test rig is measured using a digital anemometer (Testo® India, 416). Based on the calculated values and utilizing the continuity equation, the actual velocity of the fluid at the entrance of the rectangular channel has been estimated.

The inlet and exit temperatures of the fluid flowing are measured in the upstream and downstream heat sink using Teflon-insulated K-type thermocouples of diameter 0.25 mm (Unitech Instrumentation). All the thermocouples are connected to a multichannel temperature scanner (RS485 Modbus RTU serial port, Masibus) via a multi-point switch box, which allows four inputs at the same time. Two calibrated pressure transducers (Huba control, 5280260) have been used for measuring the pressure at the inlet and the outlet of the heat sink. A data acquisition unit (Keithley, 6510) with 12 plug-in switch modules up to 80-channel capacity is used to record the pressure data from both transducers.

7.2.2. Material selection

The test rig is fabricated using different components of different materials given in Table 7.2.

Table 7.2. Test rig components materials and its properties.

Components of test rig setup	Material used	Thermal conductivity
Heating block	Aluminium (6061)	198 W/mK
Insulation layer	Glass wool and Nitrile rubber	0.023 W/mK and 0.033 W/mK
Micro pin-fins	Brass	110 W/mK
Test rig (Lower part)	Teflon (polytetrafluoroethylene)	0.2 W/mK
Test rig (upper part)	Acrylic (polypropylene)	0.3 W/mK
Sealant and Gasket	Silicon rubber pad	148 W/mK at 300 K

Aluminum alloy (Al-6061) is selected to fabricate the heating block of the test rig. The temperature gradients within the heating block are observed to be low due to high thermal conductivity, which is preferred for such purposes. The heating block is covered with a glass wool layer of 4 mm followed by a nitrile rubber layer all-around of 2 mm thickness. These materials are used to insulate the heating block from the surrounding air. For the upper and lower part of the test rig, two different material blocks are used viz. acrylic (polypropylene) and Teflon (polytetrafluoroethylene) that exhibits good insulating properties and minimizes the heat leakage rate is machined to get desired geometrical shape. The chosen materials' strengths are fair enough and can withstand high temperatures of 250 ºC and 150 ºC, respectively. Both parts of the test rig are sealed with silicone rubber and a gasket due to their lower viscosity and high heat withstanding capability. The material of fabricated arrayed micro MPFs is taken as brass that adheres good thermal conductivity for dissipating high heat flux.

7.3. Thermal performance assessment of MPFs using the developed test rig

A modular test rig design allows the swapping of different MPFs heat sinks after each experiment. For the present study, three MPFs cross-section profiles including aerofoil, droplet, and Piranha, have been taken for thermal performance evaluation in an inline and staggered arrangement. After each successive experiment, the MPFs are changed with another MPFs cross-section in an iterative manner. Schematic diagrams of those MPFs heat sinks, shown in Figure 7.4(c), have been adopted for similar MPF spacing and height on a fixed base plate of cross-section 12 mm x 12 mm. All heat sinks as arrayed micro protrusions are fabricated on the base plate in inline and staggered arrangements (Figure 7.4(a,b)) to calculate a baseline for the comparative heat transfer performance.

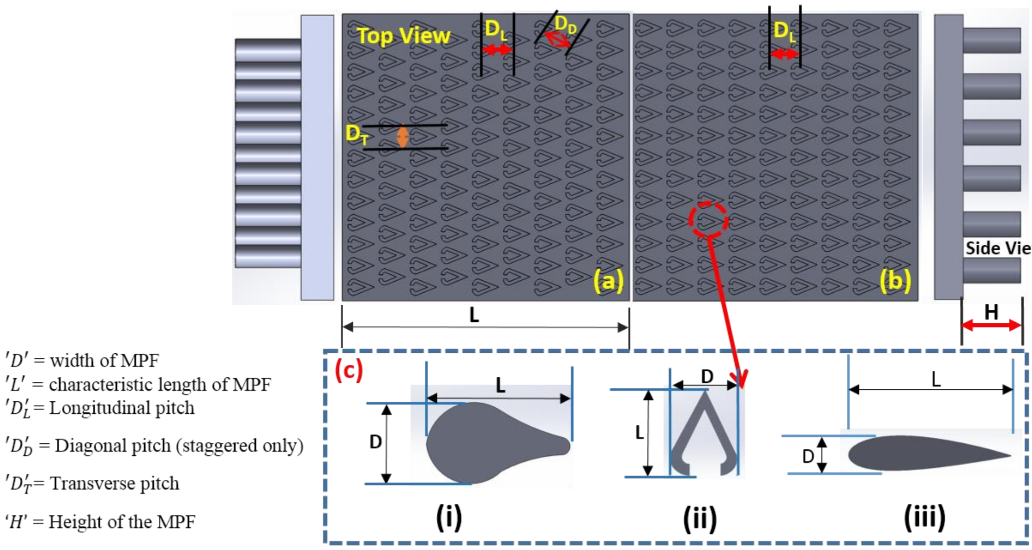
Top View
D_L
D_D
D_T
(a)
D_L
(b)
Side View
L
H
(c)
L
D
(i)
D
L
(ii)
L
D
(iii)
$'D'$ = width of MPF
$'L'$ = characteristic length of MPF
$'D_L'$ = Longitudinal pitch
$'D_D'$ = Diagonal pitch (staggered only)
$'D_T'$ = Transverse pitch
'H' = Height of the MPF

Fig. 7.4 Schematic diagrams of MPFs heat sink: (a) staggered, (b) inline arrangements; (c) cross-sections of the three different MPFs heat sink; (i) droplet, (ii) Piranha, and (iii) aerofoil.

The arrayed MPFs heat sinks in different configurations have been fabricated using the integrated microfabrication technology and assisted facilities which are discussed in the previous chapters 3, 4, and 5. The heat transfer analysis has been performed three times under the steady-state condition, and the average data have been recorded for the analysis. The fluid flow pressure and temperature results are recorded using the above-mentioned equipment at the desired locations. The fabricated test rig with all equipment used for thermal performance analysis has been shown in Figure 7.5(a). A closed view of the fabricated test rig for thermal performance evaluation is also shown in Figure 7.5(b).

Results are obtained as a function of volumetric flow corresponding to *Re* in the laminar flow regime (from 100 to 800). To analyze the thermal performance of fabricated MPFs heat sinks, air as a coolant is used for the whole experimentation. The compressed air is drawn from the blower which is supplied to fill the reservoir and then flows through the rectangular channel. Each fluid flow velocity was set and maintained to the desired value using the air blower. A constant heat flux boundary condition is produced through the heating block and is provided to the bottom surface of the arrayed MPFs heat sink. For different heat sinks configuration, fluid flow velocity, pressure, and temperature data acquisition have been recorded after steady-state conditions are attained (at steady state, the surface temperature at the center of the heating block becomes constant). The pressure data have been measured again after each experimental run with no heat flux applied to verify the previously obtained results.

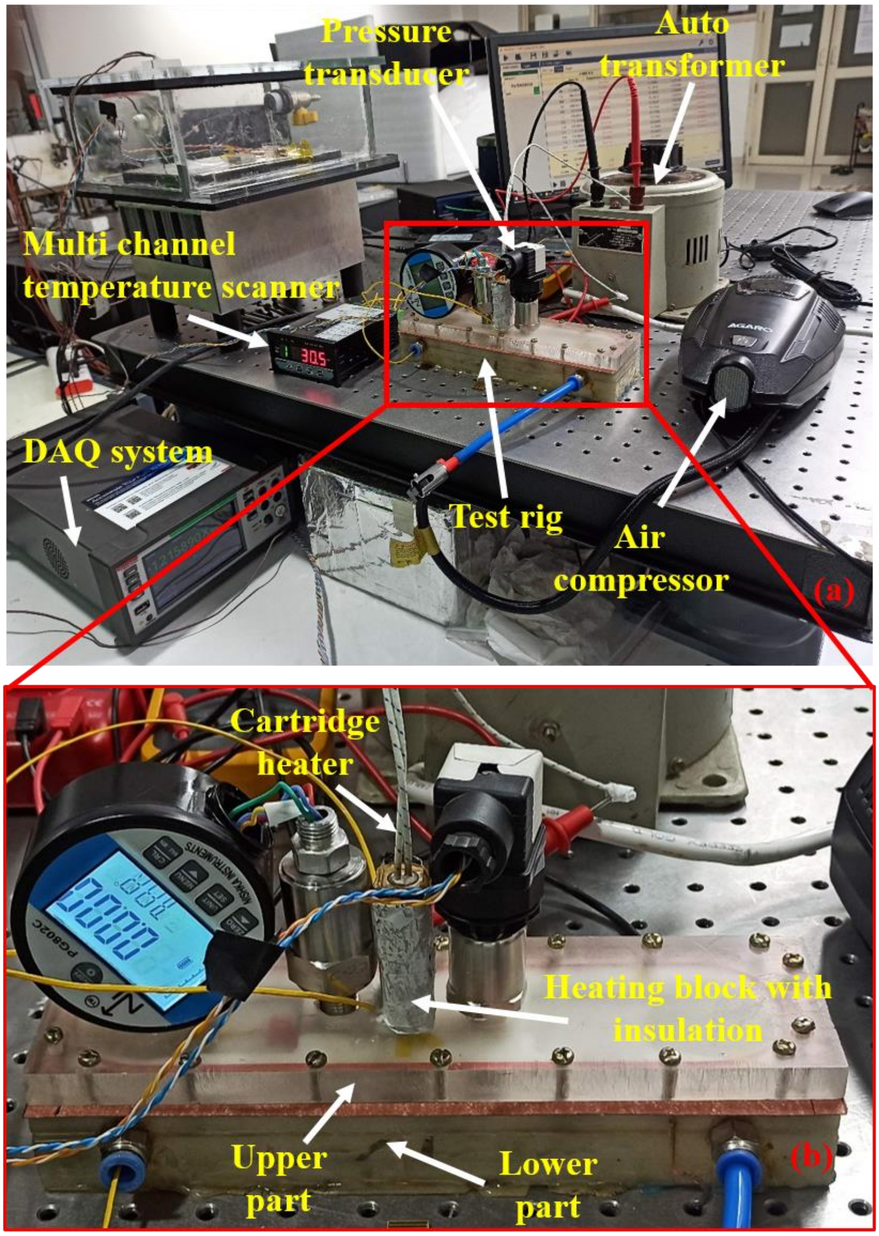
Pressure transducer
Auto transformer
Multi channel temperature scanner
DAQ system
Test rig
Air compressor
(a)
Cartridge heater
Heating block with insulation
Upper part
Lower part
(b)

Fig. 7.5 (a) Pictorial view of thermal performance testing facility setup, and (b) closed view of in-house developed test rig.

7.4. Thermal performance index, *TPI*

To find the thermal performance of different MPFs heat sinks, several experiments are carried out at different Reynolds numbers under balanced flow. The present analysis is done in steady state conditions using the following heat input and heat transfer through arrayed MPFs relation given in Eq. (7.1):

$$q_{electrical} = q_{conductive} + q_{radiative} + q_{convective} \tag{7.1}$$

The total electrical heat input power provided to the heating block is given by Eq. (7.2):

$$q_{electrical} = VI \tag{7.2}$$

where $q_{electrical}$ is the total input power, V and I are the input voltage and current readings obtained from the digital power meter. Radiation heat transfer from the heating block and MPFs heat sink is negligible compared to the convective heat transfer rate. Heat loss through conduction, $q_{conductive}$ from insulation is not contributing to actual heat transfer. The effective power supplied to the heat sink base $q_{effective}$ is evaluated by the heat loss due to convection to the atmosphere and is given by Eq. (7.3):

$$q_{effective} = q_{electrical} - q_{convective} \tag{7.3}$$

The effective heat flux at the base of the MPFs heat sink is given by Eq. (7.4):

$$Q_{heat\,flux} = \frac{q_{effective}}{A} \tag{7.4}$$

in which A is the bottom surface area of the heat sink substrate, which is a product of, W and L i.e. the width and length of the heat sink and surface area of the total number of MPFs in an array. Uniform heat flux is supplied for heating the MPFs heat sink base surface, which is properly amalgamated with a heating block ensuring no air gap between them.

The maximum thermal resistance is evaluated using the relation given in Eq. (7.5):

$$R_{max} = \frac{T_{tipmax} - T_{in}}{Q_{heat\,flux}} \tag{7.5}$$

T_{tipmax} is the maximum temperature of the bottom substrate (fin tip) and $Q_{heat\,flux}$ is the heat flux dissipated by the bottom substrate. In the arrayed MPFs heat sinks, heat flow is driven entirely by thermal gradients to control the heat flow in the system where it is installed. For the present study, the heater temperature reaches a steady temperature of 60. 2 ^{0}C without any further change in the provided one-dimensional heat flux value. Re at the inlet is calculated using Eq. (7.6):

$$Re = \frac{\rho u d_h}{\mu} \tag{7.6}$$

where ρ is the fluid density (1.164 kg/m^3), u is the inlet velocity, d_h is the hydraulic diameter of the rectangular channel $\left(D_h = \frac{2W_{ch}H_{ch}}{W_{ch} + H_{ch}}\right)$ and μ is the fluid dynamic viscosity (1.872 x 10^{-5} kg/ms). The average Nusselt number (*Nu*) is derived using a thermal resistance method and computed using the relation in Eq. (7.7):

$$Nu = \frac{h_{avg} D_h}{k} \tag{7.7}$$

where, h_{avg} is the heat transfer coefficient, and k is the thermal conductivity of the air

(0.025 W/mK). The h_{avg} of different MPFs heat sinks cross-sections and arrangement at different Reynolds numbers are calculated using the following relation given in Eq. (7.8):

$$h_{avg} = \frac{Q_{heatflux}}{(T_h - T_{bulk})} \tag{7.8}$$

where T_h is the heater temperature and the bulk heat sink temperature (T_{bulk}) is calculated using the Eq. (7.9):

$$T_{bulk} = \frac{1}{2}(T_{in} + T_{out}) \tag{7.9}$$

The pressure drop across the MPFs heat sink is calculated by the given Eq. (7.10):

$$\Delta P = P_{in} - P_{out} \tag{7.10}$$

where P_{in} denotes the inlet pressure, P_{out} is the outlet pressure (kPa). The obtained pressure drop ΔP is considered in the single-phase flow region. At higher Reynolds number (Re>60), the thermal-hydraulic performance of MPFs heat sink is quantified using a non-dimensional parameter, *TPI*, which is the ratio of heat transfer enhancement to rise in the pressure drop [230]. The ΔP and Nu of the unfinned heat sink are used for comparison purposes, respectively. For all *Re*, the Nu_0 lies in the range of 4.6-5.3 and for ΔP_o 0.25-2.8 kPa. Here the *TPI* of the heat sink is given by Eq. (7.11):

$$TPI = \frac{(\frac{Nu}{Nu_0})}{(\frac{\Delta P}{\Delta P_o})^{1/3}} \tag{7.11}$$

7.5. Experimental results and uncertainty analysis

In the heat exchanger, the properties of the fluid such as specific heat, density, thermal conductivity, and dynamic viscosity are evaluated at the bulk temperature (Eq. 7.9). This section presents the experimental results and the uncertainty analysis.

7.5.1. Experimental results

The experimental raw data recorded during the experiments are provided in Table 7.3 and 7.4 for different cross-section MPFs heat sinks. Repeatability of all the test runs is within 2%.

Table 7.3. Thermal data of experimental runs for different MPFs heat sinks.

Q = 27.578 KW/m^2	***Re***				
	485	**546**	**601**	**685**	**766**
MPFs profiles (inline)	T_{tip}	T_{tip}	T_{tip}	T_{tip}	T_{tip}
Piranha	52.1	48.4	46.2	43	39.7
Droplet	54.2	52.6	49.1	45.3	43.4
Aerofoil	55.7	53.4	51.2	48.1	46.6
MPFs profiles (Staggered)	T_{tip}	T_{tip}	T_{tip}	T_{tip}	T_{tip}
Piranha	50.3	47.2	44.9	40.6	37
Droplet	52.4	50.6	48.2	45.5	43.2
Aerofoil	53.4	51.2	50.3	47.8	44

Table 7.4. Bulk temperature data of experimental runs for different MPFs heat sinks.

Q = 27.578 KW/m^2	***Re***				
	485	**546**	**601**	**685**	**766**
MPFs profiles (inline)	T_{bulk}	T_{bulk}	T_{bulk}	T_{bulk}	T_{bulk}
Piranha	36.4	37.9	38.2	39.7	41.6
Droplet	34.8	36.2	37.5	38.8	42.7
Aerofoil	35.1	36.4	37.6	39.7	43.6
MPFs profiles (Staggered)	T_{bulk}	T_{bulk}	T_{bulk}	T_{bulk}	T_{bulk}
Piranha	33.8	35.7	36.5	36.8	38.5
Droplet	32.3	33.1	34.1	34.7	36.3
Aerofoil	32.1	32.8	33.5	34	35.8

7.5.2. Uncertainty Analysis

The uncertainty analysis is required to understand the maximum deviation of the measurement. The Air compressor shows an uncertainty of 3.1% to the fluid flow velocity. Uncertainties in the temperature measurement using K-type thermocouple and pressure measurements are ±0.2% and ±0.3%, respectively, provided by the manufacturer and verified. The maximum error in measuring electrical parameters such as voltage and current are ±1.2% and ±1.43%, respectively. Uncertainty in power supply ($q_{electrical}$) is predicted using the following Eq. (7.12) [231]:

$$\frac{\delta q_{electrical}}{q_{electrical}} = \pm\sqrt{\left(\frac{\delta V}{V}\right)^2 + \left(\frac{\delta I}{I}\right)^2} \tag{7.12}$$

In addition, the following physical quantities have not been considered for uncertainty calculation:

- The thermal conductivities of the metals assumed constant (even though these vary with temperature).
- The height of the arrayed MPFs is assumed to be identical.
- The locations at which temperature data are calculated (these locations are 1/16 inch diameter holes and not points)
- The layer thickness of the thermally conductive paste applied is not fixed.

Based on the literature data, intervals of confidence were specified for the quantities listed above as summarized in Table 7.5. Furthermore, it is assumed that fixed errors are negligible and there are no other sources of error.

Table 7.5. Interval of confidence for other quantities.

Quantity	K_{MPF}	K_{Al}	H (µm)	$l_{silcone}$	l_{Al}
Absolute (±)	1.0	2.0	5	20	465

7.6. Results and Discussion

The heat transfer efficiency of each MPFs heat sink has been evaluated through different thermal parameters at different Re. The range of Re is chosen in a way to show both the conductive and convective heat transfer behavior in the laminar flow regime. The thermal parameters characterized are synchronized for understanding the overall performance of protruded arrayed MPFs compared to unfinned heat sinks.

7.6.1. Thermal resistance evaluation

Similar pitches and constant characteristic length of each MPFs cross-section in an array resulted in an enhanced convective heat transfer rate. The plots in Figure 7.6 show the R_{max} variations depending on the increasing Re for inline and staggered MPFs arrangements. The R_{max} of each MPFs cross-section is found to be constantly lower with increasing Re. R_{max} for Piranha, droplet and aerofoil MPFs in staggered arrangement decrease by approximately 30% compared to the inline arrangement. This is due to the tip corners of MPFs triggering flow separation and higher fluid mixing downstream. The combined effect of phenomenal axial conduction and forced convection in fluid flow direction decreases thermal resistance. However, Piranha MPFs cross-section shows lower R_{max} than droplet and aerofoil by 48% and 60% in both

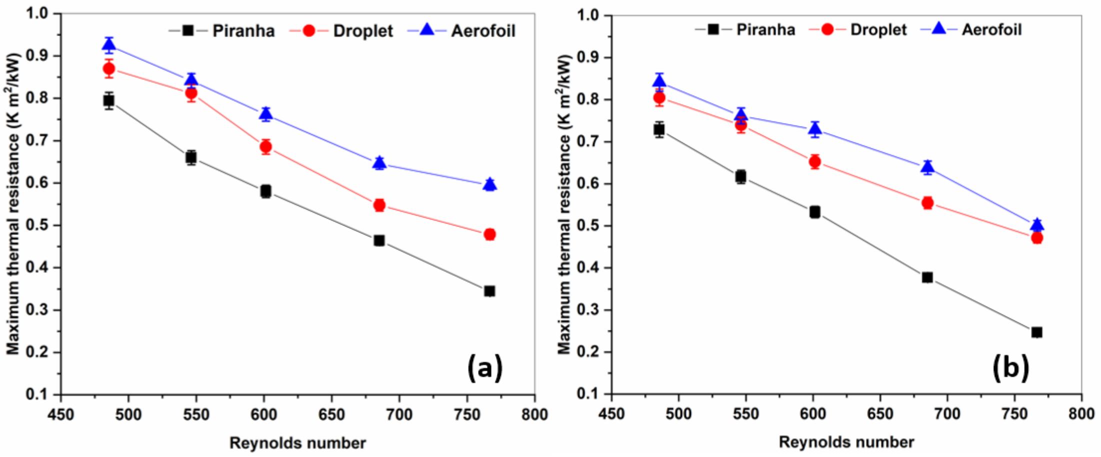

Fig. 7.6 Variation of R_{max} in (a) inline, (b) staggered arrangement of different MPFs heat sinks.

arrangements, respectively. This means that the Piranha MPFs can transfer a larger amount of heat under forced convection at the same heat input conditions compared to the others because the thermal boundary layer thickness diminishes with increasing *Re* due to more surface area contact with the fluid flowing. A recirculation zone in the middle accelerates the heat transfer rate and may cause significant wake formation behind the MPF cross-section.

7.6.2. Average heat transfer coefficient

Figure 7.7 shows single-phase h_{avg} for each MPFs cross-sections, in which the h_{avg} is plotted for increasing *Re*, respectively. The h_{avg} was found to be boosted gradually with increasing *Re* in both inline and staggered arrangements. It may be due to the small pitches between MPFs bodies, which played a significant role in fluid interaction and increased flow resistance of fluid flowing due to the surface integrity of MPFs. The difference in heat transfer performance of all three MPFs cross-sections can be linked to the different flow behaviors through the MPFs body in both arrangements. Besides, the h_{avg} of arrayed Piranha MPFs is higher than the droplet and aerofoil, respectively due to larger heat sink surface interaction with the fluid. As the growth of flow velocity, the temperature of fluid decreases under the same heat flux, and the proportion of the flow velocity and viscosity rises. Also, it could be concluded that the enhancement of Re is advantageous to the h_{avg}.

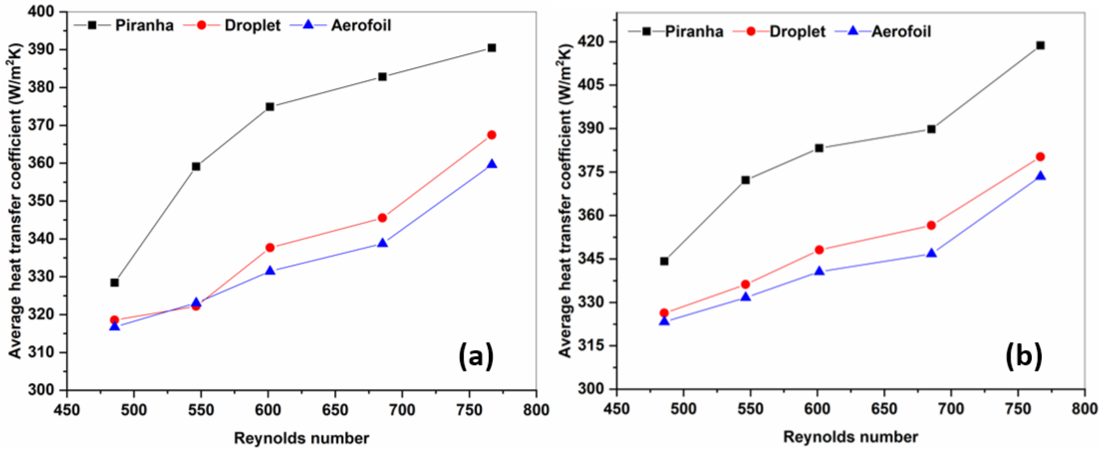

Fig. 7.7 Variation of h_{avg} in (a) inline, (b) staggered arrangement of different MPFs heat sinks.

7.6.3. Average Nusselt number

Figure 7.8 shows the comparative plots of Nu as a function of Re for different MPFs cross-sections. The results are as per the expectation, Nu increases with Re in both the MPFs arrangements. It is evidenced that the Nu for Piranha MPFs is high compared to droplet and aerofoil MPFs in both arrangements, which is mainly due to the presence of extended surfaces and triangular geometrical design with recirculation zone. However, at steady-state, the heat dissipation rate increases since flowing fluid near the MPFs body is heated adequately, lowering the MPFs body temperature. Hence, Nu increases at higher Re for all MPFs cross-sections. The Nu value obtained for Piranha MPFs is typically 24% higher compared to droplet and aerofoil obtained for all Re. The shrouded structures of MPFs lead to the development of a thermal boundary layer that strengthens flow separation and takes away maximum heat. The collective effect of the developed boundary layer and enhanced fluid flow interaction with the MPFs body is responsible for an increase in Nu with increasing Re.

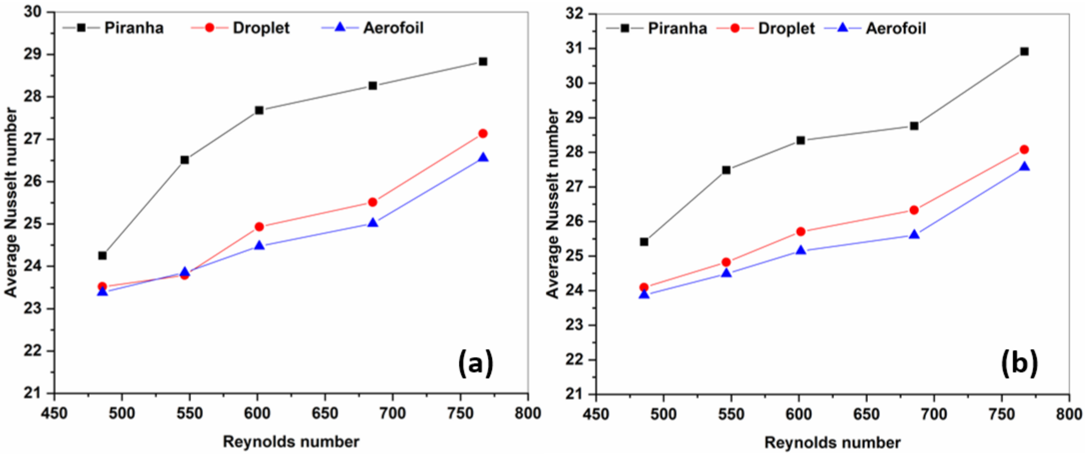

Fig. 7.8 Variation of Nu in (a) inline, (b) staggered arrangement of different MPFs heat sinks.

7.6.4. Pressure drop

Theoretically, the ΔP is directly proportional to the fluid flow velocity and inversely proportional to the MPFs spacing. Figure 7.9 illustrates the gradual increase in ΔP with increasing Re for different MPFs cross-sections in inline and staggered arrangements. As expected, the pressure drop in a staggered arrangement is lower than the inline arrangement by approximately 40%. The former arrangement imparts the viscous shear effect due to surface integrity; the number of rows of MPFs and spacing contributes to the total pressure drop. It can be observed that Piranha MPFs have lower pressure drop than droplet and aerofoil MPFs in both configurations. For Piranha MPFs, pressure drop decreased by 55% and 42% compared to droplet and aerofoil MPFs with increasing Re, respectively. It is due to its linear geometrical cross-section, which formed ‘form drag’ and ‘friction drag’ at different Re values. Also, the recirculation zone downstream of Piranha MPFs suppresses the vortex shedding at lower Re. With the increasing Re, large pressure drops have been observed for all MPFs, possibly due to the larger force applied by fluid flow. It leads to boundary layer separation from the MPFs wall leading to waking formation due to vortex shedding. On the other hand, streamlining separation at the tip of Piranha MPFs at lower Re is higher; therefore, the ΔP is smaller than others.

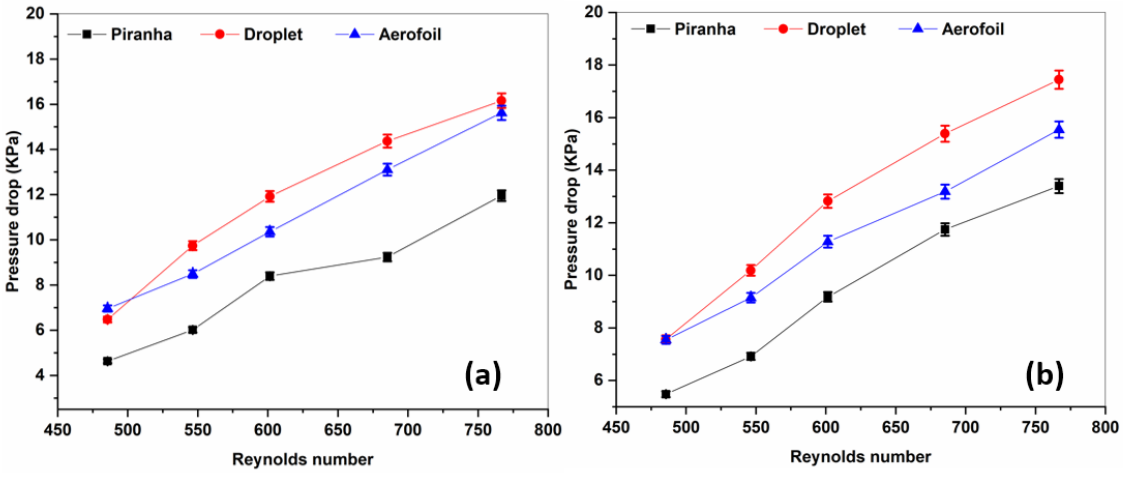

Fig. 7.9 Variation of ΔP in (a) inline, (b) staggered arrangement of different MPFs heat sinks.

7.6.5. Thermal performance index

The thermal performance index, TPI, describes the effectiveness of the MPFs heat sinks in achieving a certain heat dissipation rate over the applied pumping power. Figure 7.10 shows TPI based on the finned and unfinned heat sinks as a function of Re. The Piranha MPFs heat sink has shown the highest TPI over the whole Re followed by droplet, and aerofoil MPFs profiles in both arrangements. The result shows that an approximately 20% increase in TPI is observed more than others. It may be due to the non-apparent wake zone and lesser flow separation in Piranha MPFs. The flow streamlines in the Piranha MPFs heat sink follow the surface movement, leading to a higher convective heat transfer rate and lower pressure drop than other MPFs profiles. According to the plots, at any Re, TPI is found to be larger in the staggered arrangement of MPFs than the inline and is larger than 1.0. It means that thermal performance through MPFs heat sinks in the staggered arrangement has shown advantages over the inline arrayed MPFs counterpart. Conclusively, it can be understood that the geometrical cross-sectional profiles of MPFs have also a crucial influence on heat transfer performances.

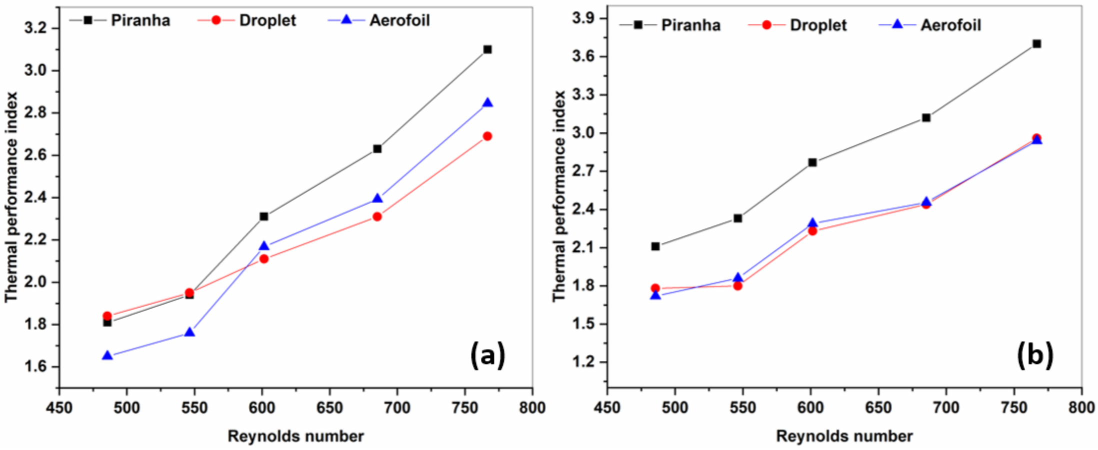

Fig. 7.10 Variation of TPI in (a) inline, (b) staggered arrangement of different MPFs heat sinks.

7.7. Validation study

The recorded experimental results of Piranha MPFs cross-sections have been validated through numerical simulation for authenticity. The developed numerical model results are compared for ΔP and R_{max} which provides the basis for the forced convective heat transfer rate.

Figure 7.11(a) shows the comparison of computed ΔP with experimental results for increasing Re. Simulation results of ΔP with Re are slightly higher than the experimental results. The variation in the experimental and simulation results is less deviated, with a maximum error of 4% for both MPFs arrangements. The deviation in results may be due to the pressure losses at the inlet and outlet geometry of the computational domain. This is attributed to the small gap at the tip of MPFs in the test rig, which may result in minor losses which are not considered in the numerical model. Additionally, it may be due to the difference in surface integrity of MPFs, working fluid flowing conditions, and the difference in modeling conditions due to the complexity of the governing equations. Figure 7.12 shows the computed velocity contours and vector plots around single Piranha MPFs, as Re increased from 400 to 800. As the Re increases, flow separation and wake interaction are found to be increased, which impacts both the pressure drop and heat transfer. It is understood that the increase in Re results in a more substantial flow recirculation downstream of each MPF.

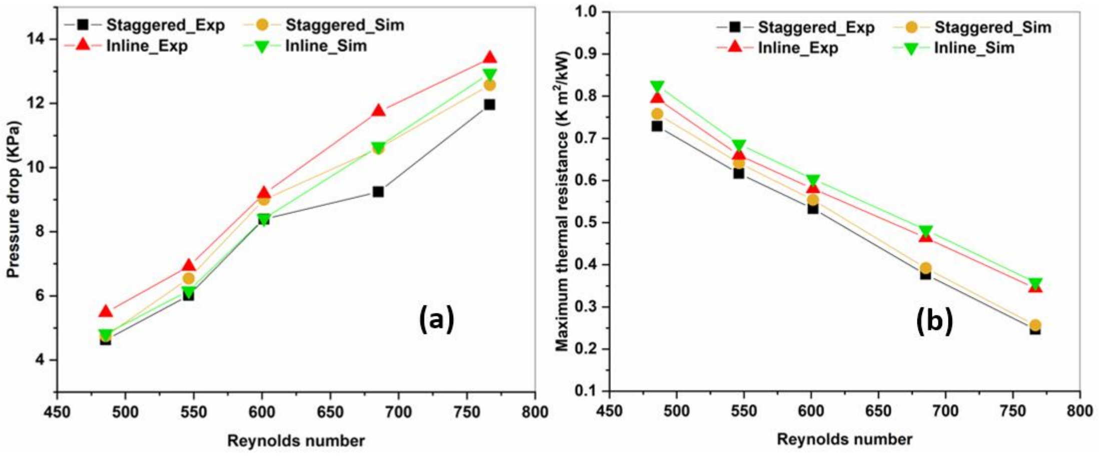

Fig. 7.11 Comparative experimental and simulation results for ΔP and R_{max} with increasing Re.

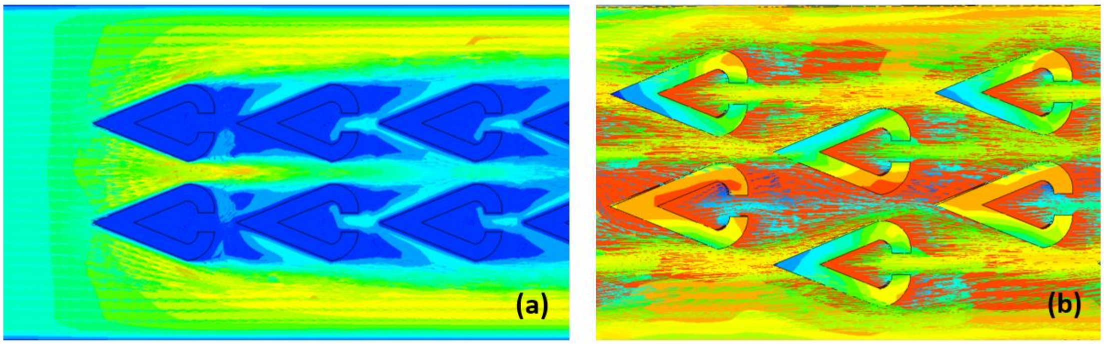

Fig. 7.12 Flow streamlines in arrayed Piranha MPFs: (a) inline (b) staggered arrangements (Re -766).

Figure 7.11(b) shows the comparative results of R_{max} with increasing Re. The numerically measured temperature data are in good agreement with the experimental results, with a maximum error of 2.9%. This indicates that the heat flux supplied at the base of the heat sink, is effectively dissipated by the fluid flow axially with negligible heat loss to the surrounding. The MPFs in the first few rows are colder than those in the last rows as shown in Figure 7.13(a,b). It is due to the first few rows MPFs facing the oncoming ambient fluid continuously. While the last rows of MPFs in the inline arrangement don’t interact well with the ambient fluid flowing. They are shadowed in a wake region which is overcome in a staggered arrangement, resulting in more efficient heat transfer due to more interaction of fluid flowing with the MPFs. From the above discussion, it can be concluded that the present computational domain can imply reasonable accuracy for successive thermal performance through arrayed Piranha MPFs.

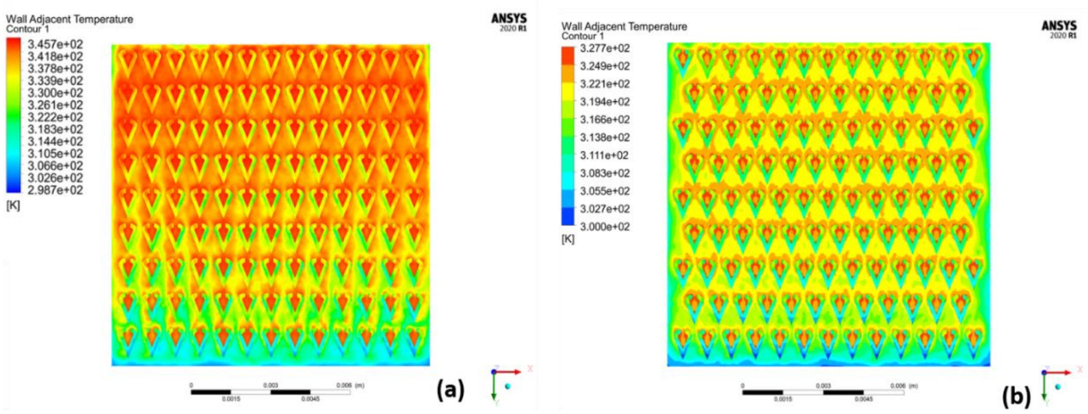

Fig. 7.13 Temperature distribution in arrayed Piranha MPFs: (a) inline (b) staggered arrangements (Re - 601).

7.8. Chapter conclusion

In this chapter, the thermal performance through the arrayed MPFs of unconventional cross-sections has been evaluated. An in-house testing facility has been designed and developed in order to quantify the thermal parameters through these arrayed MPFs. The arrayed MPFs in both inline and staggered arrangements have been analyzed for steady-state heat transfer analysis by evaluating TPI. Further, it could be suggested that unconventional cross-section arrayed MPFs heat sinks show significant improvement in effective heat dissipation. This could be beneficial where high heat transfer efficiency at the cost of the lesser pumping power is required, especially in semiconductor applications.

Chapter 8

Conclusions and Future Scope

8.1. Overview

The present work elaborated the fabrication feasibility study of high aspect ratio arrayed micro protrusions of various metallic materials. RμEDM was utilized as the main process for fabricating arrayed protrusions, while the LBμM was found a suitable technology for producing RμEDM tool plates consisting of precisely fabricated arrayed micro holes. The capability of both processes in quality fabrication has been demonstrated through detailed parametric studies to ensure minimum errors in their respective products. Multi-objective optimization approaches have been utilized to identify the optimal process' parametric combination for effective machining and good surface quality of fabricated tool plates and thereby micro protrusions. Additionally, the augmented RμEDM process stability, promoting primary discharges and effective flushing, was achieved by implementing a new suction-based high-pressure dielectric flushing technology. This new flushing technology was integrated with the existing RμEDM setup to remove debris from the machining gap while fabricating large-size arrayed micro protrusions.

The optimal geometry of the arrayed MPF heat exchangers was obtained by numerical modeling. The optimal geometry was then simulated to analyze the thermal performance. The obtained results were experimentally validated using an in-house developed test rig in terms of a non-dimensional thermal performance parameter called TPI.

The following can be considered as the key contributions:

1. Integration of RμEDM-LBμM to make promising microfabrication technology for fabrication of arrayed micro protrusions in unconventional cross-sections.
2. Exploring LBμM (fiber laser) for fabrication of dimensionally accurate tool plates for RμEDM.
3. Introduction of a new suction-based high-pressure flushing in RμEDM for effective debris removal and hence increasing MRR in RμEDM.
4. Development of an in-house testing facility for thermal performance analysis of arrayed MPFs heat sinks fabricated at optimal parameters.

8.2. Conclusions

The following conclusions are drawn from the thesis work:

- Arrayed micro protrusions in different unconventional cross-sections, such as Piranha, aerofoil, diamond, elliptical, square, and droplet, were fabricated using the proposed RμEDM-LBμM integrated technology. The array with a minimum cross-sectional dimension of 200 μm and inter-MPF gaps as low as 40 μm are fabricated on different metallic materials, including biomaterial.

- A parametric study based on the GA approach was performed to identify the optimal parametric combination to enhance the processing speed. A significant improvement in machining responses, such as higher MRR, lower tool wear rate, and deviation in cylindricity of fabricated micro protrusions was observed at optimal parametric combination.

- A GRA approach is used to find the optimal parametric combination for LBμM to achieve damage-free arrayed micro holes to act as RμEDM tool plate. Improved machining responses with negligible deviation in the dimensional accuracy and good surface quality characteristics of fabricated micro holes are found at the optimal parameters.

- Subsequently, RμEDM experiments are performed with optimally fabricated tool plate resulting in damage-free protrusions fabrication with an improved MRR_P, TWR, and Ra_P by 16%, 20% and 10%, respectively.

- A suction-based high-pressure dielectric flushing technology was designed and developed to enhance the responses that are beyond the scope of the optimization in RμEDM. A well-known 'Brachistochrone curve' of the fastest descent path was considered for optimal designing of one of the components of this flushing technology, viz., suction funnel/cup. A significant improvement in MRR by 25% and a reduced TWR by 8% was recorded.

- A numerical study was performed to analyze the debris flow behaviors during the machining of arrayed micro protrusions. The discrete phase modeling and fluid dynamics boundary conditions had been utilized to understand the debris evacuation phenomena in this new flushing technology.

- The optimal cross-sectional design of MPFs in an array was through a thermodynamic-based 'EGM' method which was formulated in a PSO multi-objective optimization algorithm. It was followed by numerical thermal simulations. The $'EGM'$ value is found to be lower for the staggered MPFs arrangement than the inline as 0.007357 W/K and 0.497710 W/K, respectively, at similar thermal parametric conditions.

- Thermal parameters were evaluated in a single-phase laminar flow regime. The recorded thermal performance was evaluated and a comparative assessment is reported for each MPFs profile in both inline and staggered arrangements. Arrayed Piranha MPFs in a staggered arrangement, height - 931 μm, number of MPFs in an array - 115, inter-electrode-gap - 945 μm proven as the best MPFs profile for effective heat transfer rate under constant heat loading conditions.

- An in-house testing facility was designed and developed to quantify the thermal parameters through the optimal fabricated arrayed MPFs. The arrayed MPFs in both inline and staggered arrangements have been analyzed for steady-state heat transfer analysis by evaluating various thermal performance parameters. Arrayed Piranha MPFs have shown an increasing trend of TPI ranging from 2.11-3.7, followed by droplets 1.78-2.96 and aerofoil 1.72-2.94 in a staggered arrangement.

8.3. Scope for future work

During the course of detailed experimental and numerical investigations carried out in the present research work, following scopes for future research work is found:

- Exploring a wide range of materials for the fabrication of arrayed micro protrusions for a wide range of applications.
- Analysis of plasma channel formation and material removal mechanism through molecular dynamics simulation can be attempted to understand the multi-physics involved in the RμEDM process.
- Consideration of flexible design of new flushing technology for the accommodation of large array size high aspect ratio micro protrusions for better debris evacuation.

- A real-time thermal simulation and experimental work related to maximum generated heat flux can be performed when arrayed MPFs are placed in the dense circuit of high-performance MEMS.
- A fluid flow visualization study through different arrayed MPFs cross-section profiles can be performed to better understand fluid dynamics phenomena.

APPENDIX-A

1. Formulation of Numerical model

The generated surface roughness in RμEDM and its variants are quietly different due to the workpiece-tool plate configuration, dielectric flushing and discharge energy settings. It may also due to process parameters like the discharge voltage, the current, the spark duration, the crater geometry etc. A simple numerical model of RμEDM process is developed using necessary boundary conditions for the determination of the surface roughness of fabricated protrusions. In RμEDM, series of repetitive discharge pulses occurred leads to material removal at different locations on the (workpiece) anode. Also, the amount of material removed during each spark will vary due to the nature of frequently occurring discharges (such as, primary, secondary and higher order discharges).

The sole requirement of healthier machining is to promote primary discharges occur at the minimum inter-electrode gap (IEG) between the walls of workpiece and micro holes in the tool plate (cathode) in Figure 1(a). Secondary discharges occur between walls of the either anode or cathode and debris that adheres to either wall of the cathode/anode respectively, thereby reducing local IEG at specific areas as shown in Figure 1(b). The higher order discharges occur between floating debris particles in the IEG or attached to walls of the cathode and anode as shown in Figure 1(b). It is evidenced that the primary discharge is the main phenomena for material removal in RμEDM, whereas, the amount of secondary and higher order discharges increases with increasing depth of micro protrusions. Moreover, secondary and higher order discharging phenomena results in higher surface roughness at the particular areas at which the accumulation of debris is severe [50].

The following assumptions have been considered in the formulation of the model which are as follows:

- Conduction heat transfer mode in considered for actual heat transfer at the discharge location.
- Energy transfer in the dielectric environment during discharge is considered to be constant to both the anode and cathode.
- The nature of the dielectric used is homogeneous, incompressible and isotropic.

- The shape of debris is taken as spherical.
- The removal of material takes place after the melting point of it.

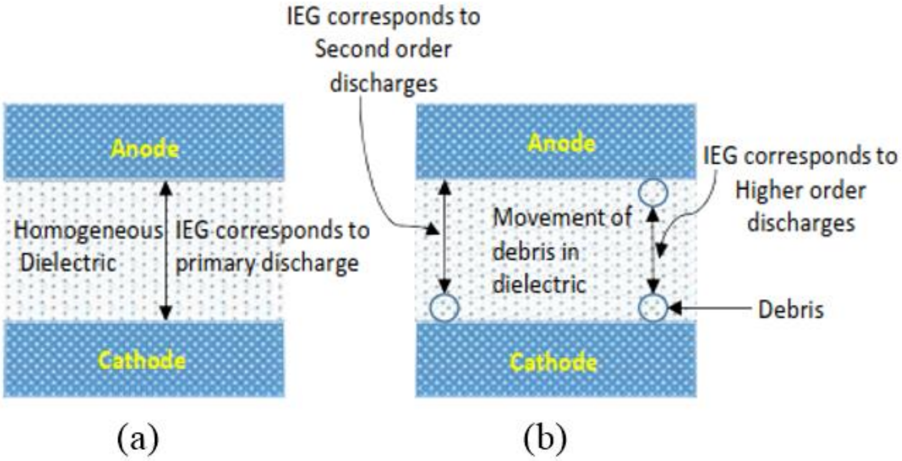
IEG corresponds to Second order discharges
Anode
Homogeneous Dielectric
IEG corresponds to primary discharge
Cathode
Anode
IEG corresponds to Higher order discharges
Movement of debris in dielectric
Debris
Cathode
(a)
(b)

Fig. 1(a) Primary discharge and (b) second and higher order discharges in RμEDM.

2. Governing equations and boundary conditions

The different governing equations that responds to determine the surface roughness profile includes electrostatics, heat transfer and fluid flow. Interaction boundary conditions have been provided between debris with anode and debris to debris which is responsible for higher order discharges. The electrostatics equation is solved for defining electric field distribution at anode/cathode surfaces. The electrical discharge takes place at the surfaces when the magnitude of electric field intensity is equal or higher than breakdown strength of dielectric. A well-known Gauss's law in differential form provides the correlation between changing electric field with the charge density. The below Eqs. (1) and (2) are solved simultaneously to determine the electric field intensity, respectively.

$$E = -\nabla V \tag{1}$$

$$\nabla . E = \frac{\rho V}{\varepsilon_0} \tag{2}$$

The conductive heat transfer takes place at the location where the electric field intensity exceeds the strength of breakdown force between metallic bond, which is given by Eq. (3):

$$\rho C_p \frac{\delta T}{\delta t} - k \nabla^2 T = q_0 \tag{3}$$

The material removal takes place when the localized temperature "T" at the point of discharging exceeds the melting point "T_{melt}" of the workpiece material. The deformation of material ("h") due to latent heat is specified by Eqs. (4) and (5). The ramp function "f" is used which depicts the temperature dependent heat transfer coefficient having very high slope for phase transition of material removal from the workpiece and is given by:

$$h = \frac{q_l}{\rho_l} \tag{4}$$

$$q_l = f(T - T_{melt}) \times (T - T_{melt}) \tag{5}$$

Asymmetrical geometry of the model is considered for this study and the different boundary conditions are shown in Figure 2. The shape of the crater generated by simulation has been discussed and the approach for surface roughness prediction are detailed in the next sub-section.

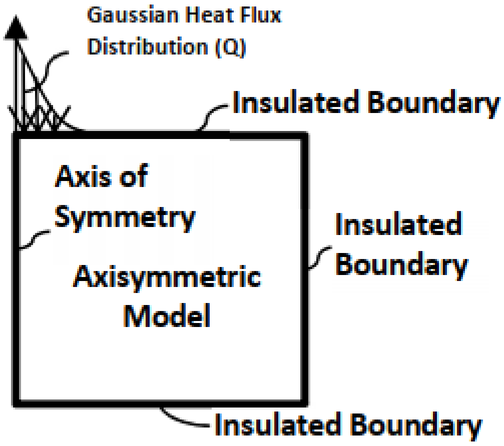

Fig. 2 Gaussian's heat model and boundary conditions.

A simplified model of RμEDM process has been developed in ANSYS® 18.2 (Mechanical APDL user-interface) including Multiphysics compilation (electrostatics, heat transfer).

2.1. Electrostatics

In RμEDM, RC circuit is used in which the discharge pulses are generating due to one to one charging and discharging of the capacitor. During discharging, the electric field intensity increases severely to those points where the IEG become less and sudden discharge happen when $E \geq E_{th}$. Due to which, the plasma channel is formed in which flow of electrons is high enough that increases the localized temperature on the workpiece surface which is beyond the melting point of it. This plasma channel can be approximated as Gaussian heat source with a heat flux radius, "r_{hf}" given by Eq. (6) [232].

$$r_{hf} = 0.0284.\, t_{on}^{0.9115} \qquad (6)$$

2.2. Heat transfer

Due to concentrated plasma channel, a heat source, Q, is applied at the workpiece at $E \geq E_{th}$. The segment of the total energy of plasma transferred to the workpiece electrode is p=0.39 [232]. Another heat source q_l (Eq. 5) is integrated with induced effect of latent heat that is responsible for ejection of melted material from the surface of workpiece and is given by Eq. (7):

$$Q = p.\frac{\frac{1}{2}.CV^2}{\pi.r_{hf}^2.t_{on}} \qquad (7)$$

The simulation is carried out using integrated Multiphysics compilation, ANSYS®-18. After the simulation, the cross-section generated due to the applied boundary conditions on the workpiece surface result in crater formation. This crater formation is eventually used in the prediction of surface roughness values. The different solver configuration used in the simulation has been presented in the Table 1.

Table 1. Simulation parameters.

Solver details	Parameters
Solver type	Mechanical APDL
No-linear method	Newton-Raphson method
Simulation type model	Temperature dependent
Type of mesh	Hex8 noded brick element
Shape function	Lagrange (Linear)
Material properties	All temperature dependent (In SI unit)

3. Crater size and surface roughness prediction

Based on the analysis of the simulation results in Figure 3.8 of chapter 3, a crater formed on the protrusion surface due to discharge pulse is assumed to have hemispherical shape as shown in Figure 3 which is described by Eq. (8):

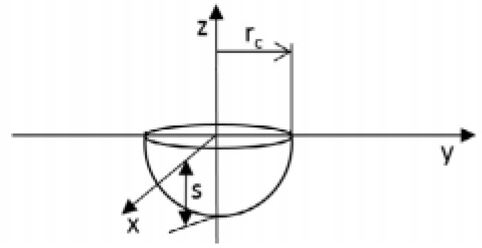

Fig. 3 Crater size.

$$\frac{x^2+y^2}{r_c^2} = \frac{(s-z)}{s} \tag{8}$$

where r_c and s represent crater's radius and depth, respectively.

Rebelo et al. [212] had derived a relation between the radius of crater, current and spark duration which is given by the following Eq. (9):

$$r_c = \frac{d_c}{2} = A \times (I.t_s)^B \tag{9}$$

Where d_c is the diameter of the formed crater (μm), I is the discharge current, t_s is the spark duration, and A and B are the material dependent constant. For the present work, copper alloys constant values have been considered (A = 1743 and B = 0.40) [212]. Therefore, the amount of material removed per spark is given by the Eq. (10):

$$V_c = \frac{1}{2}\pi s r_c^2 \tag{10}$$

where V_c represents the volume of material removed.

The depth of the crater has also been evaluated as the outcome of the simulation. Element birth and death technique is applied to analyze the crater volume, in which the elements subjected above the melting point get deactivated. The results of this developed numerical model are further utilized to determine the crater's volume to find the Ra values. The possible shape of crater is hemispherical and is obtained by primary erosion as well as higher order erosion as shown in Figure 3.8 of chapter 3.

The material removal due to higher order discharges and subsequent surface roughness could be summarized using Figure 3.8 of chapter 3. The maximum surface roughness is assumed to be equal to the depth of the crater formed during an individual spark discharge. The outcome of the experiment on the final finished workpiece surface represents a series of overlapping craters as shown in Figure 3.9(a) of chapter 3. The maximum non-conformity of the workpiece surface is equal to the depth a, which corresponds Ra.

The elementary assumption for estimating the average surface roughness Ra is that in addition to the formed crater C_1, and successive crater C_2 formed only due to subsequent discharging on the surface of the workpiece and not on the flank of the crater. Therefore, the axis of heat source radius on the crater C_2 will be in the distance equal to (r_c and r_s) from the axis of the crater C_1 in Figure 3.9(b). The craters dimensions can be derived from Eqs. (11) and (12):

$$C_1\colon \frac{y^2}{r_c^2} = \frac{(s-z)}{s} \tag{11}$$

$$C_2\colon \frac{(y-(r_c+r_s))^2}{r_c^2} = \frac{(s-z)}{s} \tag{12}$$

Using the parameters y and z, the linear system can be solved for estimating depth a using Eq. 13:

$$a = s - z_A = \frac{1}{4}\left[\frac{r_c + r_s}{r_s}\right]^2 s \tag{13}$$

Therefore, the maximum surface roughness and the Ra are given by Eqs. (14) and (15), respectively:

$$R_{max} = s \tag{14}$$

$$Ra = \frac{1}{4}\left[\frac{r_c + r_s}{r_c}\right]^2 s \tag{15}$$

The RµEDM experiments are performed to fabricate arrayed micro protrusions. Then, the crater size and Ra on the fabricated protrusion surface are evaluated. The recorded Ra value is of 2.50 µm on the machined surface. The obtained experimental results are compared with the simulation results and found to be in minimum percentage deviation of 6% given in Table 2.

Table 2. Validation results of Ra values.

Responses	Experimental	Simulation
Discharge energy, (KW/mm^2)	5.17	5.17
Average surface roughness, (Ra)	2.49	2.52

4. Formulation of the mathematical model in Brachistochrone curve

The analysis of the Brachistochrone curve involves utilization of calculus and the principle of least action. The principle of least action states that the path taken by a system between two points is the one that minimizes the action, which is the integral of the Lagrangian over time. From the principle of least action, the path taken by the particle between two points (x_1, y_1) and (x_2, y_2) is found. The Lagrangian is given by $L = T - U$, where T is the kinetic energy and U is the potential energy of the debris. By applying the Euler-Lagrange equation to this Lagrangian, the differential equation that the Brachistochrone curve must satisfy is obtained and is given by Eq. (1):

$$(1 + \left[\left(\frac{dy}{dx}\right)^2\right]^{3/2} = k \tag{1}$$

where, k is a constant determined by the initial conditions of the numerical simulation. This differential equation is solved to obtain the equation of the Brachistochrone curve.

$$y = a - a\cos\left(\frac{x}{a}\right) \tag{2}$$

where, a is a constant determined by the initial conditions of the debris position.

To derive the equation of the Brachistochrone curve, the potential energy of a particle of mass m in a gravitational field is considered. Moreover, for analyzing the motion of debris on the Brachistochrone curve, the principle of conservation of energy is used. By assuming that the particle has zero initial velocity and is released at the top of the curve, then its total energy is equal to its potential energy at the top of the curve, which is given by Eq. (3):

$$E = mgh \tag{3}$$

Where, m is the mass of the debris, g is the acceleration due to gravity, and h is the height of the top of the curve above the bottom. As the debris moves down the curve, its potential energy is converted into kinetic energy, which is given by:

$$K = \left(\frac{1}{2}\right)mv^2 \tag{4}$$

where, v is the velocity of the debris ejecting in the suction cup.

The total energy of the debris is conserved, such that the initial potential energy is now equal to the final kinetic energy:

$$mgh = K = \left(\frac{1}{2}\right)mv^2 \tag{5}$$

Rearranging the above equation to solve for the velocity of the debris at any point on the curve:

$$v = \sqrt{(2gh)} \tag{6}$$

This equation tells us that the velocity of the debris depends only on the height of the debris above the bottom of the curve and the acceleration due to gravity which is implemented in the numerical model to calculate the velocity of the particle at any point on the Brachistochrone curve and used in designing suction cup of the new high-pressure suction-assisted flushing technology.

5. Calibration chart Table for power supply through auto-transformer

(v)	***(I)***	***(δV)***	***(δI)***	***T (^{0}C)***
15	0.072	15.68	0.071	27.12
36	0.15	36.25	0.161	61.03
40	0.17	40.33	0.176	68.22
48	0.22	48.51	0.227	82.34

References

[1] Qingfeng Y., Xingqiao W., Ping W., Zhiqiang Q., Lin Z., Yongbin Z. "Fabrication of micro rod electrode by electrical discharge grinding using two block electrodes". Journal of Materials Processing Technology. 2016; 234: 143-149. https://doi.org/10.1016/j.jmatprotec.2016.03.023.

[2] Mastud S., Garg M., Singh R., Samuel J., Joshi S. "Experimental characterization of vibration-assisted reverse micro electrical discharge machining (EDM) for surface texturing". in Proc. ASME Int. Manuf. Sci. Eng. Conf. (MSEC), South Bend, IN, USA, 2012; 439–448. https://doi.org/10.1115/MSEC2012-7314.

[3] Woodcock C., Ng'oma C., Sweet M., Wang Y., Peles Y., Plawsky J. "Ultra-high heat flux dissipation with Piranha Pin Fins". Int J of Heat and Mass Transf. 2019; 128: 504-515. https://doi.org/10.1016/j.ijheatmasstransfer.2018.09.030.

[4] Claude S. Avionics, Cooling, KHIEPCOOL Project, Micro Heat Pipe, Thermal Management.[https://www.electronics-cooling.com/2001/11/thermal-management-of-highly-integrated-electronicpackages-in-avionics-applications/]

[5] https://www.istockphoto.com/photo/heatsink-gm480599612-68672183 [accessed on October 2022].

[6] Kim B. H., Park B. J., Chu C. N. "Fabrication of multiple electrodes by reverse EDM and their application in micro ECM". J. Micromechanics Microengineering. 2006; 16: 843–850. https://doi.org/10.1088/0960-1317/16/4/022.

[7] Romoli L., Moroni F., Khan M. M. A. "A study on the influence of surface laser texturing on the adhesive strength of bonded joints in aluminium alloys". J of CIRP Annals-Manufacturing Technology. 2017; 1: 237-240. http://dx.doi.org/10.1016/ j.cirp.2017.04.123.

[8] Zhang H., Hua M., Dong G.-N., Zhang D.-Y., Chin K.-S. "A mixed lubrication model for studying tribological behaviors of surface texturing". Tribology International. 2016; 93: 583-592. https://doi.org/10.1016/j.triboint.2015.03.027.

[9] Etsion I., Burstein L. "A model for mechanical seals with regular microsurface structure". Tribol. Trans. 1996; 39: 677–83. https://doi.org/10.1080/10402009608983582.

[10] Kim E.-S., Kim S.-M., Lee Y.-Z. “The effect of plateau honing on the friction and wear of cylinder liners”. Wear. 2018; 400: 207–12. http://dx.doi.org/10.1016/j.wear.2017.09.028.

[11] Imran M., Saragih A. S., Sahar M. S. U., Ko T. J. “Digital maskless lithography capabilities for surface texturing with biomachining”. Int. J. Adv. Manuf. Technol. 2017; 89: 3709–3719. http://dx.doi.org/10.1007/s00170-016-9317-6.

[12] Segu D. Z., Kim S. S. “Influence on friction behavior of micro-texturing under lubricated nonconformal contact”. Meccanica. 2014; 49: 483–492. https://doi.org/10.1007/s11012-013-9806-8.

[13] Yuan W., Li L.‑H., Lee W.‑B., Chan C.‑Y. “Fabrication of Microlens Array and Its Application: A Review”. Chin. J. Mech. Eng. 2018; 31: 1-16. https://doi.org/10.1186/s10033-018-0204-y.

[14] Hejazi V., Moghadam A. D., Rohatgi P., and Nosonovsky M. “Beyond Wenzel and Cassie−Baxter: Second-Order Effects on the Wetting of Rough Surfaces”. Langmuir. 2014; 30: 9423−9429. dx.doi.org/10.1021/la502143v.

[15] Wang Y., Houshmand F., Elcock D., Peles Y. “Convective heat transfer and mixing enhancement in a microchannel with a pillar”. Int. J. Heat Mass Transf. 2013; 62: 553–561. https://doi.org/10.1016/j.ijheatmasstransfer.2013.03.034.

[16] Yeo J., Choi M. J., Kim D. S. “Robust hydrophobic surfaces with various micropillar arrays”. J. Micromechanics Microengineering. 2010; 20: 025028. https://doi.org/10.1088/0960-1317/20/2/025028.

[17] Yadav S., Kaushal M., Varun, Siddhartha. “Nusselt number and friction factor correlations for solar air heater duct having protrusions as roughness elements on absorber plate”. Exp. Therm.Fluid Sci. 2013; 44: 34–41. https://doi.org/10.1016/j.expthermflusci.2012.05.011.

[18] Li J.S., Li Y.L , He D. Y., Yu H. Y., Yan X. B. “Design and mechanism of cost-effective and highly efficient ultrathin µm GaAs solar cells employing nano-hemisphere surface texturing”. AIP Adv. 2014; 3: 032145-1-032145-7. https://doi.org/10.1063/1.4799731.

[19] Markal B., Kul B., Avci M., Varol R. “Effect of gradually expanding flow passages on flow boiling of micro pin fin heat sinks”. International Journal of Heat and Mass Transfer. 2022; 197(15):123355. https://doi.org/10.1016/j.ijheatmasstransfer.2022.123355.

[20] Arumugaprabu V., Ko T., Kumaran T., Kurniawan R., Uthaykumar M. “A brief review on importance of surface texturing in materials to improve the tribological performance”. Rev.Adv. Mater. Sci. 2018; 53: 40-48. https://doi.org/10.1515/rams-2018-0003.

[21] Chern G. L., Lee H. J. “Using workpiece vibration cutting for micro-drilling”. Int. J. Adv. Manuf. Technol. 2006; 27: 688–692. https://doi.org/10.1007/s00170-004-2255-8.159.

[22] Cheong M. S., Cho D. W., Ehmann K. F. “Identification and control for micro-drilling productivity enhancement”. Int. J. Mach. Tools Manuf. 1999; 39: 1539–1561. https://doi.org/10.1016/S0890-6955(99)00019-X.

[23] Egashira K., Mizutani K. “Micro-drilling of monocrystalline silicon using a cutting tool”. Precis. Eng. 2002; 26: 263–268. https://doi.org/10.1016/S0141-6359(01)00113-1.

[24] Kumar R., Agrawal P.K., Singh I. “Fabrication of micro holes in CFRP laminates using EDM”. J. Manuf. Process. 2018; 31: 859–866. https://doi.org/10.1016/j.jmapro.2018.01.011.

[25] Yadav U. S., Yadava V. “Experimental investigation on electrical discharge diamond drilling of nickel-based superalloy aerospace material”. Proc. Inst. Mech. Eng. Part B J. Eng. Manuf. 2017; 231: 1160–1168. https://doi.org/10.1177/0954405415592124.

[26] Singh P., Yadava V., Narayan A., “Parametric study of ultrasonic-assisted hole sinking microEDM of titanium alloy” Int. J. Adv. Manuf. Technol. 2018; 94: 2551–2562. https://doi.org/10.1007/s00170-017-1051-1.

[27] Yu Z. Y., Rajurkar K. P., Shen H. “High Aspect Ratio and Complex Shaped Blind Micro Holes by Micro EDM”. CIRP Ann. - Manuf. Technol. 2002; 51: 359–362. https://doi.org/10.1016/S0007-8506(07)61536-4.

[28] Jahan M. P., Wong Y. S., Rahman M. “A study on the quality micro-hole machining of tungsten carbide by micro-EDM process using transistor and RC-type pulse generator”. J. Mater. Process. Technol. 2009. https://doi.org/10.1016/j.jmatprotec.2008.04.029.

[29] Yu Z. Y., Zhang Y., Li J., Luan J., Zhao F., Guo D. “High aspect ratio micro-hole drilling aided with ultrasonic vibration and planetary movement of electrode by micro-EDM”. CIRP Ann. Manuf. Technol. 2009; 58: 213–216. https://doi.org/10.1016/j.cirp.2009.03.111.

[30] Byun J. W., Shin H. S., Kwon M. H., Kim B. H., Chu C. N. “Surface texturing by micro ECM for friction reduction”. Int. J. Precis. Eng. Manuf. 2010; 11: 747–753. https://doi.org/10.1007/s12541-010-0088-y.

[31] Jo C. H., Kim B. H., Chu C. N. “Micro electrochemical machining for complex internal micro features”. CIRP Ann. - Manuf. Technol. 2009; 58: 181–184. https://doi.org/10.1016/j.cirp.2009.03.072.

[32] Liu G., Li Y., Kong Q., Yu L. “Impact Analysis of Electrolyte Pressure on Shape Accuracy of Micro Holes in ECM with Hollow Electrodes”. Procedia CIRP, 2018. https://doi.org/10.1016/j.procir.2017.12.089.

[33] Correa D., Almeida J., Almeida G., Cardoso M., De Boni L., Mendonça C. “Ultrafast Laser Pulses for Structuring Materials at Micro/Nano Scale: From Waveguides to Superhydrophobic Surfaces”. Photonics. 2017; 4(8): https://doi.org/10.3390/photonics4010008.

[34] Umer U., Mohammed M. K., Al-Ahmari A. “Multi-response optimization of machining parameters in micro milling of alumina ceramics using Nd:YAG laser”. Meas. J. Int. Meas. Confed. 2017; 95: 181–192. https://doi.org/10.1016/j.measurement.2016.10.004.

[35] Aguilar C. A., Lu Y., Mao S., Chen S. “Direct micro-patterning of biodegradable polymers using ultraviolet and femtosecond lasers”. Biomaterials. 2005; 26: 7642–7649. https://doi.org/10.1016/j.biomaterials.2005.04.053.

[36] Becker E.W., Ehrfeld W., Hagmann P., Maner A., Münchmeyer D. “Fabrication of microstructures with high aspect ratios and great structural heights by synchrotron radiation lithography, galvanoforming, and plastic moulding (LIGA process)”. Micro electron. Eng. 1986; 4: 35–56. https://doi.org/10.1016/0167-9317(86)90004-3.

[37] Malek C.K., Saile V. “Applications of LIGA technology to precision manufacturing of high aspect-ratio micro-components and -systems: A review”. Microelectronics J. 2004; 160: 131-143. https://doi.org/10.1016/j.mejo.2003.10.003.

[38] Revzin A., Russell R.J., Yadavalli V.K., Koh W., Deister C., Hile D.D., Mellott M.B., Pishko M. V. “Fabrication of Poly(ethylene glycol) Hydrogel Microstructures Using Photolithography”. Langmuir. 2001; 17: 5440–5447.

[39] Qin D., Xia Y., Whitesides G.M. “Soft lithography for micro- and nanoscale patterning”. Nat. Protoc. 2010; 5: 491–502. https://doi.org/10.1038/nprot.2009.234.

[40] Rühe J. “There Was Light: Prospects for the Creation of Micro- and Nanostructures through Maskless Photolithography”. ACS Nano. 11 (2017) 8537–8541. https://doi.org/10.1021/acsnano.7b05593.

[41] Li Y., Deng J., Chai Y., Fan W. “Surface textures on cemented carbide cutting tools by micro EDM assisted with high-frequency vibration.”. Int. J .Adv Manuf Technol. 2016; 82: 2157-2165. https://doi.org/10.1007/s00170-015-7544-x.

[42] Roy T., Datta D. Balasubramaniam R. “Numerical modelling and simulation of surface roughness of 3-D hemispherical convex micro-feature generated by reverse micro-EDM”. Int J Adv Manuf Technol 2018; 97: 979–992. https://doi.org/10.1007/s00170-018-1971-4.

[43] Nirala C. K.; Saha P. “Evaluation of μEDM-drilling and μEDMdressing Performances Based on Online Monitoring of Discharge Gap Conditions”. Int J. Adv. Manuf. Technol. 2016; 85: 1995–2012. https://doi.org/10.1007/s00170-015-7934-0.

[44] Yamazaki M., Suzuki T., Mori N., Kunieda M. “EDM of micro-rods by self-drilled holes”. Journal of Materials Processing Technology. 2004; 149: 134-138. https://doi.org/10.1016/j.jmatprotec.2004.03.006.

[45] Yi S. M., Jin S. H., Lee J. D. Chu C. N. “Fabrication of a high-aspect-ratio stainless steel shadow mask and its application to pentacene thin-film transistors”. J. Micromech. Microeng. 2005; 15(2): 263–269. https://doi.org/10.1088/0960-1317/15/2/003.

[46] Zeng W., Wang Z., Dong D. “New micro-EDM reverse copying technology for microelectrode array fabrication”. in: Int. Technol. Innov. Conf. (ITIC 2006), 2006; 1633–1636.

[47] Zeng W.L., Gong Y.P., Liu Y., Wang Z.L. “Experimental Study of Microelectrode Array and Micro-Hole Array Fabricated by Ultrasonic Enhanced Micro-EDM”. Key Eng. Mater. 2008; (364-366): 482-487. https://doi.org/10.4028/www.scientific.net/KEM.364-366.482.

[48] Hwang Y.L., Kuo C.L., Hwang S.F. “Fabrication of a micro-pin array with high density and high hardness by combining mechanical peck-drilling and reverse-EDM”. J. Mater. Process. Technol. 2010; 210(9): 1103-1130. https://doi.org/10.1016/j.jmatprotec.2010.02.022.

[49] Peng Z.L., Wang Z.L., Wang Y.K., Dong Y.H., Chen H. “Study on Micro Reversible Electrical Discharge Machining Method for the Fabrication of Micro

Structures". Material Science Forum. 2009; 626-627: 279–284. https://doi.org/10.4028/www.scientific.net/MSF.626-627.279.

[50] Mujumdar S.S., Mastud S.A., Singh R.K., Joshi S.S. "Experimental characterization of the reverse micro-electro discharge machining process for fabrication of high-aspect-ratio microrod arrays". Proc. Inst. Mech. Eng. Part B J. Eng. Manuf. 2010; 224: 777–794. https://doi.org/10.1243/09544054JEM1745.

[51] Mastud S., Singh R.K., Joshi S.S. "Analysis of fabrication of arrayed micro-rods on tungsten carbide using reverse micro-EDM". Int. J. Manuf. Technol. Manag. 2012; 26(1-4): 176-195. https://doi.org/10.1504/IJMTM.2012.051430.

[52] Mastud S.A., Kothari N.S., Singh R.K., Joshi S.S. "Modeling Debris Motion in Vibration Assisted Reverse Micro Electrical Discharge Machining Process (R-MEDM)". J. Microelectromechanical Syst. 2014; 24: 661–676. https://doi.org/10.1109/JMEMS.2014.2343227.

[53] Shah Md S., Saha P. "Assessment of vibration-assisted micro-EDM dressing process-stability by monitoring and analyzing debris evacuation during Ti-6Al-7Nb machining". Journal of Manufacturing Processes. 2021; 66: 250-268. https://doi.org/10.1016/j.jmapro.2021.04.011.

[54] Lim H.S., Wong Y.S., Rahman M., Lee M.K. E. "A study on the machining of high-aspect ratio micro-structures using micro-EDM". Journal of Materials Processing Technology. 2003; 140: 318–325. https://doi.org/10.1016/S0924-0136(03)00760-X.

[55] Fofonoff T.A., Martel S.M., Hatsopoulos G.N., Hunter I.W. "Microelectrode Array Fabrication by Electrical Discharge Machining and Chemical Etching". IEEE Transactions on Biomedical Engineering. 2004; 51(6): 890-895. https://doi.org/10.1109/TBME.2004.826679.

[56] Rakwal D., Heamawatanachai S., Tathireddy P., Solzbacher F., Bamberg E. "Fabrication of compliant high aspect ratio silicon microelectrode arrays using micro-wire electrical discharge machining". Microsyst. Technol. 2009; 15(5): 789–797. https://doi.org/10.1007/s00542-009-0792-7.

[57] Tathireddy P., Rakwal D., Bamberg E., Solzbacher F. "Fabrication of 3-dimensional silicon microelectrode arrays using micro electro discharge machining for neural applications". Proceeding of TRANSDUCERS 2009 - International Solid-State Sensors, Actuators and Microsystems Conference. 1206-1209.

[58] Jahan M.P. “Micro-Electrical Discharge Machining. J. P. Davim (ed.), Nontraditional Machining Processes”. Chapter 4. 111-151. https://doi.org/10.1007/978-1-4471-5179-1_4. Springer-Verlag London 2013.

[59] Singh A. K., Patowari P. K., Deshpande N. V. “Experimental Analysis of Reverse Micro-EDM for Machining Microtool”. Materials and Manufacturing Processes. 2016; 31(4): 530-540. https://doi.org/10.1080/10426914.2015.1070426.

[60] Nirala C. K., Saha P. “A New Approach of Tool Wear Monitoring and Compensationin RμEDM Process”. Materials and Manufacturing Processes. 2016; 31: 483–494. https://doi.org/10.1080/10426914.2015.1058950.

[61] Singh A.K., Patowari P.K., Deshpande N.V. “Analysis of micro-rods machined using reverse micro-EDM”. J Braz. Soc. Mech. Sci. Eng. 2019; 41(1): 1-12. https://doi.org/10.1007/s40430-018-1519-4.

[62] Roy T., Datta D., Balasubramaniam R. “Reverse Micro EDMed 3D Hemispherical protruded Micro Feature: Microstructural and Mechanical Characterization". Mater. Res. Express. 6(3): p.036513. https://doi.org/10.1088/2053-1591/aaf490.

[63] Zhang Y., Xie B., “Investigation on hole diameter non-uniformity of hole arrays by ultrasonic vibration-assisted EDM”. IJAMT, 2021; 112: 3083-3091. https://doi.org/10.1007/s00170-021-06597-3.

[64] Shah Md S., Saha P. “Investigation on performance characteristics of micro-EDM dressing for the fabrication of micro-rod(s) on Ti-6Al-7Nb biomedical material”. Journal of Machining Science and Technology. 2021; 25(3): 398-421. https://doi.org/10.1080/10910344.2020.1815050.

[65] Mahardika M., Mitsui K. “A new method for monitoring micro-electric discharge machining processes”. Int. J. Mach. Tools Manuf. 2008; 48: 446–458. https://doi.org/10.1016/j.ijmachtools.2007.08.023.

[66] Luo Y. F. “The dependence of interspace discharge transitivity upon the gap debris in precision electro discharge machining”. J. Mater. Process. Technol. 2007; 68(2): 121–131. https://doi.org/10.1016/S0924-0136(96)00019-2.

[67] Kiran M. P. K., Joshi S. S. “Modeling of surface roughness and role of debris in micro EDM”. J. Manuf. Sci. Eng. 2006; 129(2): 265–273. https://doi.org/10.1115/1.2540683.

[68] Masuzawa T., Cui X., Taniguchi N. "Improved Jet flushing for EDM". CIRP Ann. Manuf. Technol., 1992; 41(1): 239-242. https://doi.org/10.1016/S0007-8506(07)61194-9.

[69] Wang Y., Bai J.C., Guo Y.F., Huang H. "Investigation of the effects of dielectric inlet pressure in inner jetted dielectric EDM milling". J Adv Mat Res. 2011; 189–193: 125–128. https://doi.org/10.4028/www.scientific.net/AMR.189-193.125.

[70] Pattabhiraman A., Marla D., Kapoor S.G. "A Computational Model to Study Film Formation and Debris Flushing Phenomena in Spray-Electric Discharge Machining". J Micro Nano Manuf. 2016; 4(3): 031002(1-10). https://doi.org/10.1115/1.4033709.

[71] Tanjilul M., Ahmed A., Kumar A.S., Rahman M. “A study on EDM debris particle size and flushing mechanism for efficient debris removal in EDM-drilling of Inconel 718”. J. Mater. Process. Technol. 2018; 255: 263–274. https://doi:10.1016/j.jmatprotec.2017.12.01.

[72] Lin Y.-C., Lee H.-S. “Machining characteristics of magnetic force-assisted EDM”. Int. J. Mach. Tools Manuf. 2008; 48(11): 1179–1186. https://doi.org/10.1016/j.ijmachtools.2008.04.004.

[73] Liao Y.S., Wu P.S., Liang F.Y. “Study of debris exclusion effect in linear motor equipped diesinking EDM process”. Procedia CIRP. 2013; 6: 123–128. http://dx.doi.org/10.1016/j.procir.2013.03.058.

[74] Cetin S., Okada A., Uno Y. “Effect of Debris Distribution on Wall Concavity in Deep-Hole EDM”. JSME Int. J. Ser. C. 2004; 47: 553–559. http://dx.doi.org/10.1299/jsmec.47.553.

[75] Wang J., Wang Y.G., Zhao F.L. “Simulation of Debris Movement in Micro Electrical Discharge Machining of Deep Holes”. Mater. Sci. Forum. 2009; 626–627: 267–272. http://dx.doi.org/10.4028/www.scientific.net/MSF.626-627.267.

[76] Shabgard M. R., Sadizadeh B., Kakoulv H. “The effect of ultrasonic vibration of work-piece in electrical discharge machining of AISIH13 tool steel”. World Acad. Sci., Eng., Technol. 2009; 52: 392–396.

[77] Wong Y. S., Lim L. C., Lee L. C. “Effects of flushing on electrodischarge machined surfaces”. J. Mater. Process. Technol. 1995; 48(1–4): 299–305. https://doi.org/10.1016/0924-0136(94)01662-K.

[78] Li G., Natsu W., Yu Z. “Elucidation of the mechanism of the detoriating interelectrode environment in micro EDM drilling”. Int J of Machine Tools and Manufacture. 2021; 167: 103747. https://doi.org/10.1016/j.ijmachtools.2021.103747.

[79] Boban J., Ahmed A., Assam A. “Effect of recirculation zone on debris evacuation during EDM deep hole drilling”. Procedia CIRP. 2021; 102: 393-398. http://dx.doi.org/10.1016/j.procir.2021.09.067.

[80] Makenzi M.M. and Ikua B.W. “A review of flushing techniques used in electricaldischarge machining”. Proceedings of the 2012 Mechanical Engineering Conference on Sustainable Research and Innovation. 2012; 4. ISSN 2079-6226.

[81] Salonitis K., Stournaras A., Stavropoulos P., Chryssolouris G. “Thermal modeling of the material removal rate and surface roughness for die-sinking EDM”. Int. J. Adv. Manuf. Technol. 2009; 40: 316–323. http://dx.doi.org/10.1007/s00170-007-1327-y.

[82] Kurnia W., Tan P.C., Yeo S.H., Tan Q.P. “Surface roughness model for micro electrical discharge machining”. Proc. Inst. Mech. Eng. Part B J. Eng. Manuf. 2009; 223: 279–287. http://dx.doi.org/10.1243/09544054JEM1188.

[83] Tong H., Li Y., Zhang L. “Servo scanning 3D micro EDM for array micro cavities using on-machine fabricated tool electrodes”. J Micromech Microeng. 2018; 28(2): 25013. http://dx.doi.org/10.1088/1361-6439/aaa04b.

[84] Abbasi J.A., Jahanzaib M., Azam M., Hussain S., Wasim A., Abbas M. “Effects of wire-Cut EDM process parameters on surface roughness of HSLA steel”. Int. J. Adv. Manuf. Technol. 2017; 91: 1867–1878. http://dx.doi.org/10.1007/s00170-016-9881-9.

[85] Kiyak M., Aldemir B.E., Altan E. “Effects of discharge energy density on wear rate and surface roughness in EDM”. Int. J. Adv. Manuf. Technol. 2015; 79: 513–518. http://dx.doi.org/10.1007/s00170-015-6840-9.

[86] Singh A. K., Patowari P. K., Deshpande N. V. “Analysis of Micro-rods Machined Using Reverse micro-EDM”. J. Braz. Soc. Mech. Sci. Eng. 2019; 41(15). http://dx.doi.org/10.1007/s40430-018-1519-4.

[87] Talla G., Gangopadhyay S., Kona N.B. “Experimental investigation and optimization during the fabrication of arrayed structures using reverse EDM”. Mater Manuf Process. 2017; 32: 958–969. https://doi.org/10.1080/10426914.2016.1221085.

[88] Takahata K., Gianchandani Y.B. “Batch mode micro-electrodischarge machining”. J Microelectromech Syst. 2002; 11: 102–110. http://dx.doi.org/10.1109/84.993444.

[89] Yu Z., Rajurkar K.P., Shen H. “High Aspect Ratio and Complex Shaped Blind Micro Holes by Micro EDM”. Annals of the CIRP. 2002; 51(1): 359–362. https://doi.org/10.1016/S0007-8506(07)61536-4.

[90] Kunieda M., Lauwers B., Rajurkar K.P., Schumacher M. “Advancing EDM through Fundamental Insight into the Process”. CIRP Annals. 2005; 54(2): 64-87. https://doi.org/10.1016/S0007-8506(07)60020-1.

[91] Hung J.C., Lin J.K., Yan B.H., Liu H.S., Ho P.H. “Using a Helical Microtool in Micro-EDM Combined with Ultrasonic Vibration for Micro-hole Machining”. Journal of Micromechanics and Microengineering. 2006; 16: 2705–2713. https://doi.org/10.1088/0960-1317/16/12/025.

[92] Yu Z.Y., Zhang Y., Li J., Luan J., Zhao F., Guo D. “High aspect ratio micro-hole drilling aided with ultrasonic vibration and planetary movement of electrode by micro-EDM”. CIRP Annals - Manufacturing Technology. 2009; 58: 213–216. http://dx.doi.org/10.1016/j.cirp.2009.03.111.

[93] Ferraris E., Castiglioni V., Ceyssens F., Annoni M., Lauwers B., Reynaerts D. “EDM drilling of ultra-high aspect ratio micro holes with insulated tools”. CIRP Annals-Manufacturing Technology. 2013; 62: 191–194. http://dx.doi.org/10.1016/j.cirp.2013.03.115.

[94] Wang J., Han F. “Simulation model of debris and bubble movement in consecutive-pulse discharge of electrical discharge machining”. Int J Mach Tools Manuf. 2014; 77: 56–65. http://dx.doi.org/10.1016/j.ijmachtools.2013.10.007.

[95] Kliuev M., Maradia U., Wegener K. “EDM Drilling of Non-Conducting Materials in Deionised Water”. Procedia CIRP. 2018; 68: 11-16. https://doi.org/10.1016/j.procir.2017.12.014.

[96] Kumar R., Singh I. “A modified electrode design for improving process performance of electric discharge drilling”. Journal of Materials Processing Tech. 2019; 264: 211-219. https://doi.org/10.1016/j.jmatprotec.2018.09.014.

[97] Feng, Y., Guo, Y., Ling, Z. et al. “Micro-holes EDM of superalloy Inconel 718 based on a magnetic suspension spindle system”. Int J Adv Manuf Technol. 2019; 101: 2015–2026. https://doi.org/10.1007/s00170-018-3075-6.

[98] Amorim F.L., Weingaertner W.L. “The behavior of graphite and copper electrodes on the fnish die-sinking electrical discharge machining (EDM) of AISI P20 tool steel”. J Braz Soc Mech Sci Eng. 2007; 29: 366–371. https://doi.org/10.1590/S1678-58782007000400004.

[99] Jain V.K. Advanced machining processes. Allied Publishers, New Delhi. 2009.

[100] Zhengkai L., Jicheng B., Yan C., Wang Y., Zhu G. “Fabrication of microelectrode with large aspect ratio and precision machining of micro-hole array by micro-EDM”. Journal of Materials Processing Technology. 2019; 268: 70-79. https://doi.org/10.1016/j.jmatprotec.2019.01.009.

[101] Zilong P., Zhenlong W., Yinghuai D., Hui C. “Development of a reversible machining method for fabrication of microstructures by using micro-EDM”. Journal of Materials Processing Technology. 2010; 210(1): 129-136. https://doi.org/10.1016/j.jmatprotec.2009.08.002.

[102] Masaki K., Wada N. “Development of the repetitive transform processing of micro-EDM”. in: Proceedings of the Electrical-Machining Symposium. 2000; 47–48. (in Japanese).

[103] D’Urso G., Longo M., Maccarini G., Ravasio C. “Electrical discharge machining of micro holes on titanium sheets”. Proceedings of the ASME Design Engineering Technical Conference. 2011; 417-424G. http://dx.doi.org/10.1115/DETC2011-47298.

[104] Siva M., Parivallal M., Kumar M.P. “Investigation on the effect of process parameters in micro electrical discharge machining”. Proc. Mater. Sci.. 2014; 5: 1829-1836. https://doi.org/10.1016/j.mspro.2014.07.470.

[105] D’Urso G., Maccarini G., Quarto M., Ravasio C., Caldara M. “Micro-electro discharge machining drilling of stainless steel with copper electrode: the influence of process parameters and electrode size”. Adv. Mech. Eng. 2016; 8 (12): 1-16. https://doi.org/10.1177/1687814016676425.

[106] Natarajan N., Suresh P. “Experimental investigations on the microhole machining of 304 stainless steel by micro-EDM process using RC-type pulse generator”. Int. J. Adv. Manuf. Technol. 2015; 77(9-12): 1741-1750. https://doi.org/10.1007/s00170-014-6494-z.

[107] Klein-Wiele J.H., Bekesi J., Simon P. “Sub micron patterning of solid materials with ultraviolet femtosecond pulses”. Appl Phys A. 2004; 79: 775-778. https://doi.org/10.1007/s00339-004-2589-y.

[108] Hanon M.M., Akman E., Genc Oztoprak B., Gunes M., Taha Z.A., Hajim K.I., et al. "Experimental and theoretical investigation of the drilling of alumina ceramic using Nd:YAG pulsed laser". Opt Laser Technol. 2012; 44: 913–22. https://doi.org/10.1016/j.optlastec.2011.11.010.

[109] Wang X., Huang Y., Xing Y., Fu X., Zhang Z., Ma C. "Fabrication of micro-channels on Al2O3/TiC ceramics using picosecond laser induced plasma micromachining". Journal of Manufacturing Processes. 2019; 44: 102–12. https://doi:10.1016/j.jmapro.2019.05.048.

[110] Roth G.L., Haubner J., Kefer S., Esen C., Hellmann R. "Fs-laser based hybrid micromachining for polymer micro-opto electrical systems". Opt Lasers Eng 2021; 137. https://doi.org/10.1016/j.optlaseng.2020.106362.

[111] Pecholt B., Vendan M., Dong Y., Molian P. "Ultrafast laser micromachining of 3C-SiC thin films for MEMS device fabrication". Int J Adv Manuf Technol. 2008; 39: 239–50. https://doi.org/10.1007/s00170-007-1223-5.

[112] Weck A., Crawford T.H.R., Wilkinson D.S., Haugen H.K., Preston J.S. "Laser drilling of high aspect ratio holes in copper with femtosecond, picosecond and nanosecond pulses". Appl Phys A Mater Sci Process. 2008; 90: 537–43. https://doi.org/10.1007/s00339-007-4300-6.

[113] Neuenschwander B., Jaeggi B., Zimmermann M., Hennig G. "Influence of particle shielding and heat accumulation effects onto the removal rate for laser micromachining with ultra-short pulses at high repetition rates". 2014; 218: 218–26. https://doi.org/10.2351/1.5063063.

[114] Behera R.R., Sankar M.R., Swaminathan J., Kumar I., Sharma A.K., Khare A. "Experimental investigation of underwater laser beam micromachining (UW-LBμM) on 304 stainless steel". Int J Adv Manuf Technol. 2016; 85: 1969–82. https://doi.org/10.1007/s00170-016-8635-z.

[115] Singh S.S., Baruah P.K., Khare A., Joshi S.N. "Effect of laser beam conditioning on fabrication of clean micro-channel on stainless steel 316L using second harmonic of Q-switched Nd:YAG laser". Opt Laser Technol. 2018; 99: 107–17. https://doi.org/10.1016/j.optlastec.2017.08.020.

[116] Martan J., Prokešová L., Moskal D., Ferreira de Faria B.C., Honner M., Lang V. Heat accumulation temperature measurement in ultrashort pulse laser micromachining. Int J Heat Mass Transf 2021; 168: 120866. https://doi.org/10.1016/j.ijheatmasstransfer.2020.120866.

[117] Almeida I.A., De Rossi W., Lima M.S.F., Berretta J.R., Nogueira G.E.C., Wetter N.U., Viera N.D., "Optimization of titanium cutting by factorial analysis of the pulsed Nd:YAG laser parameters". J Mater Process Technol. 2006; 179: 105-110. https://doi.org/10.1016/j.jmatprotec.2006.03.107.

[118] Kudesia S.S., Solana P., Rodden W.S.O., Hand D.P., Jones J.D.C. "Appropriate regimes of laser drilling models containing melt eject mechanisms". J Laser Appl. 2002; 14: 159–164. https://doi.org/10.2351/1.1494081.

[119] Whitehead D.J., Crouse P.L., Schmidt M.J.J., Li L. "Turner M.W., Smith A.J.E. Monitoring laser cleaning of titanium alloys by probe beam reflection and emission spectroscopy". Appl Phys A. 2008; 93: 123–127. https://doi.org/10.1007/s00339-008-4643-7.

[120] Banks P.S., Feit M.D., Rubenchik A.M., Stuart B.C., Perry M.D. "Material effects in ultra-short pulse laser drilling of metals". Appl Phys A. 1999; 69: S377–S380. https://doi.org/10.1007/s003390051420.

[121] Nolte S., Momma C., Kamlage G., Ostendorf A., Fallnich C., Von Alvensleben F., Welling H. "Polarization effects in ultrashort-pulse laser drilling". Appl Phys A 1999; 68: 563–567. https://doi.org/10.1007/s003390050941.

[122] Wei Y., Zhang G., Huang C., Huang L., Wei M. "High power single wavelength 1338 nm Nd:YAG laser". Opt Laser Technol. 2006; 38: 173–6. https://doi.org/10.1016/j.optlastec.2004.11.015.

[123] Lee S.W., Shin H.S., Chu C.N. "Fabrication of micro-pin array with high aspect ratio on stainless steel using nanosecond laser beam machining". Appl Surf Sci. 2013; 264: 653–63. https://doi.org/10.1016/j.apsusc.2012.10.087.

[124] Singh S.S., Joshi S.N., Khare A. "Laser Induced Micromachining and Preliminary Experiments on Manufacturing of Micro-channel on Mild Steel". In: Joshi S., Dixit U. (eds) Lasers Based Manuf Topic in Min, Metall and Mater Eng. Springer, New Delhi. 2015; 179-20. https://doi.org/10.1007/978-81-322-2352-8_11.

[125] Lavisse L., Jouvard J.M., Gallien J.P., Berger P., Grevey D., Naudy P. "The influence of laser power and repetition rate on oxygen and nitrogen insertion into titanium using pulsed Nd:YAG laser irradiation". Appl Surf Sci. 2007; 254: 916–920. https://doi.org/10.1016/j.apsusc.2007.07.204.

[126] Leitz K.H., Redlingshöer B., Reg Y., Otto A., Schmidt M. "Metal ablation with short and ultrashort laser pulses". Phys Procedia. 2011; 12: 230–238. https://doi.org/10.1016/j.phpro.2011.03.128.

[127] Schille J., Schneider L., Loeschner U. “Process optimization in high-average-power ultrashort pulse laser microfabrication: how laser process parameters influence efficiency, throughput and quality”. Appl Phys A Mater Sci Process. 2015; 120: 847–55. https://doi.org/10.1007/s00339-015-9352-4.

[128] Badyopadhyay S., Gokhale H., Sundar J.K.S., Sundararajan S., Joshi S.V. “A statistical approach to determine process parameter impact in Nd:YAG laser drilling of IN718 and Ti-6Al-4V sheets”. Opt Lasers Eng. 2005; 43: 163–182. https://doi.org/10.1016/j.optlaseng.2004.06.013.

[129] Tunna L., O'Neill W., Khan A., Sutcliffe C. “Analysis of laser micro drilled holes through aluminium for micro-manufacturing applications”. Opt Lasers Eng 2005;43: 937–50. https://doi.org/10.1016/j.optlaseng.2004.11.001.

[130] Yilbas B.S. “Parametric study to improve laser drilling process”. Opt Lasers Eng 1997; 70: 264–273. https://doi.org/10.1016/S0924-0136(97)00076-9.

[131] Biffi C.A., Previtali B. “Spatter reduction during titanium microdrilling using pulsed fiber laser”. Proceedings of Icaleo, 27th International Congress on Applications of Lasers and Electro-Optics, Laser Microprocessing Conference, Temecula, California, USA, 2008; M106. 27–36.

[132] Schille J., Schneider L., Loeschner U. “Process optimization in high-average-power ultrashort pulse laser microfabrication: how laser process parameters influence efficiency, throughput and quality”. Appl Phys A Mater Sci Process. 2015; 120: 847–55. https://doi.org/10.1007/s00339-015-9352-4.

[133] Leitz K.H., Redlingshöer B., Reg Y., Otto A., Schmidt M. “Metal ablation with short and ultrashort laser pulses”. Phys Procedia. 2011; 12: 230–8. https://doi.org/10.1016/j.phpro.2011.03.128.

[134] Liu D.X., Sun Y.L., Dong W.F., Yang R.Z., Chen Q.D., Sun H.B. “Dynamic laser prototyping for biomimetic nanofabrication”. Laser Photonics Rev. 2014; 8: 882–888. https://doi.org/10.1002/lpor.201400043.

[135] Farasati R., Ebrahimzadeh P., Fathi J., Teimouri R. “Optimization of laser micromachining of Ti–6Al–4V”. Int J Light Mater Manuf. 2019; 2: 305–17. https://doi.org/10.1016/j.ijlmm.2019.08.002.

[136] Heinemann, R., Hinduja, S., Barrow, G., and Petuelli, G. "The Performance of Small Diameter Twist Drills in Deep-Hole Drilling." ASME. J. Manuf. Sci. Eng. 2006; 128(4): 884–892. https://doi.org/10.1115/1.2335859.

[137] Cicală E., Soveja A., Sallamand P., Grevey D., Jouvard J.M. “The application of the random balance method in laser machining of metals”. J Mater Process Technol. 2008;196: 393–401. https://doi.org/10.1016/j.jmatprotec.2007.05.049.

[138] Demir A.G., Pangovski K., O'Neill W., Previtali B. “Laser micromachining of TiN coatings with variable pulse durations and shapes in ns regime”. Surf Coatings Technol 2014; 258: 240–8. https://doi.org/10.1016/j.surfcoat.2014.09.021.

[139] Chatterjee S., Mahapatra S. S., Bhardwaj V., Choubey A., Upadhyay B. N., Bindra K. S. “Drilling of micro holes on titanium alloy using pulsed Nd:YAG laser: Parametric appraisal and prediction of performance characteristics”. Institution of Mechanical engineers Proc IMechE Part B: J Engineering Manufacture, 2018; 223(8): 1-18. https://doi.org/10.1177/0954405418805604.

[140] Dubey A.K., Yadava V. “Multi-objective optimization of laser beam cutting process”. Opt. Laser. Technol. 2008; 40: 562-570. http://dx.doi.org/10.1016/J.OPTLASTEC.2007.09.002.

[141] Dhupal D., Doloi B., Bhattacharayya B. “Modeling and optimization on Nd:YAG laser turned micro-grooving of cylindrical ceramic material”. Opt. Lasers Eng. 2009; 47: 917-925. https://doi.org/10.1016/j.optlaseng.2009.03.016.

[142] Rao R., Yadava V. “Multi-objective optimization of Nd:YAG laser cutting of thin superalloy sheet using grey relational analysis with entropy measurement”. Opt. Laser. Technol., 2009; 41: 922-930. https://doi.org/10.1016/j.optlastec.2009.03.008.

[143] Sharma A., Yadava V. “Modelling and optimization of cut quality during pulsed Nd:YAG laser cutting of thin Al-alloy sheet for straight profile”. Opt Laser Eng 2013; 51(1):77-88. https://doi.org/10.1016/j.optlastec.2011.06.012.

[144] Hallgren C., Reimers H., Chakarov D., Gold J., Wennerberg A. “An in vivo study of bone response to implants topographically modified by laser micromachining”. Biomater. 2003; 24: 701–710. http://dx.doi.org/10.1016/s0142-9612(02)00266-1.

[145] Rahman M., Lim H.S., Neo K.S., Kumar S. A., Wong Y.S., Li X.P. “Tool-based nanofinishing and micromachining”. Journal of Materials Processing Technology. 2007; 185: 2–16, https://doi.org/10.1016/j.jmatprotec.2006.03.121.

[146] Rahman M., Asad A.B.M.A., Masaki T., Saleh T., Wong Y.S., Kumar S. A. “A multiprocess machine tool for compound micromachining”. International Journal of Machine Tools & Manufacture. 2010; 50(4): 344-356. https://doi.org/10.1016/j.ijmachtools.2009.10.007.

[147] Rashid M.A., Rahman M., Kumar S. A. “A study on compound micromachining using laser and Electric Discharge Machining (EDM)”. Advances in Materials and Processing Technologies. 2016; Volume 2(2): 258-265 https://doi.org/10.1080/2374068X.2016.1164531.

[148] Liu Z., Wu B., Samanta A., Shen N., Ding H., Xu R., Zhao K. “Ultrasound-assisted water-confined laser micromachining (UWLM) of metals: Experimental study and time-resolved observation”. Journal of Materials Processing Technology. 2017; 245: 259-269, https://doi.org/10.1016/j.jmatprotec.2016.11.038.

[149] Sahu A. K., Malhotra J., Jha S. “Laser-based hybrid micromachining processes: A review”. Optics & Laser Technology. 2022; 146: 107554(1-30). https://doi.org/10.1016/j.optlastec.2021.107554.

[150] Koo J. M., Im S., Jiang L., Goodson K. E. “Integrated microchannel cooling for three-dimensional electronic circuit architectures”. J. Heat Transfer. 2005; 127(1): 49–58, https://doi.org/10.1115/1.1839582.

[151] Kleinstreuer C., Li J., and Koo J., “Microfluidics of nano-drug delivery”. Int. J. Heat Mass. Transfer. 2008; 51: 5590–5597, https://doi.org/10.1016/j.ijheatmasstransfer.2008.04.043.

[152] Sohel Murshed S.M., Nieto de Castro C.A. “A critical review of traditional and emerging techniques and fluids for electronics cooling”. Renewable and Sustainable Energy Reviews. 2017; 78: 821–833. https://doi.org/10.1016/j.rser.2017.04.112.

[153] Karayiannis T.G., Mahmoud M.M. “Flow boiling in microchannels: Fundamentals and applications”. Applied Thermal Engineering. 2017; 115: 1372–1397. https://doi.org/10.1016/j.applthermaleng.2016.08.063.

[154] Mudhafar M.A.H., Yu X. “Fluid flow and heat transfer characteristics on uncoated and micro porous straight and divergent heat exchangers for high - powered electronic devices”. Heat and Mass Transfer. 2022. https://doi.org/10.1007/s00231-022-03282-3.

[155] Ye M., Du J., Wang J., Chen L., Varbanov P. S., Klemeš J. J. “Investigation on thermal performance of nanofluids in a microchannel with fan-shaped cavities and oval pin fins”. Energy. 2022; 260: 125000(1-12). https://doi.org/10.1016/j.energy.2022.125000.

[156] Bar-Cohen A., Wang P. “Thermal management of on-chip hot spot”. Journal of Heat Transfer. 2012; 134: 1–11. https://doi.org/10.1115/1.4005708.

[157] Jalil M. J., Reja A. H., Hadi A.M. "Numerical Investigation of Thermal Performance of Micro-Pin Fin with Different Arrangements". IOP Conf. Series: Materials Science and Engineering, 2000; 765: 012037(1-11). https://doi.org/10.1088/1757-899X/765/1/012037.

[158] Tuckerman D.B., Pease R. F. W., “Ultrahigh Thermal Conductance Microstructures for Cooling Integrated Circuits,” "Proceedings 32nd Electronics Components Conference". San Diego, CA, IEEE, 1981; 145–149.

[159] Peng X.F., Peterson G.P., “Convective heat transfer and flow friction for water flow in microchannel structures”. Int. J. Heat Mass Transf. 1996; 39: 2599–2608. https://doi.org/10.1016/0017-9310(95)00327-4.

[160] Qu W., Mala G.M., Li D. “Heat transfer for water flow in trapezoidal silicon microchannels”. International Journal of Heat and Mass Transfer. 2000; 43: 3925–3936. https://doi.org/10.1016/S0017-9310(00)00045-4.

[161] Xia G., Chen Z., Cheng L., Ma D., Zhai Y., Yang Y. “Micro-PIV visualization and numerical simulation of flow and heat transfer in three micro pin-fin heat sinks”. International Journal of Thermal Sciences. 2017; 119: 9–23. https://doi.org/10.1016/j.ijthermalsci.2017.05.015.

[162] Wei J., Chen N., Li L., Liu J., Zhao J., Wang C., He N. “Effect of spoiler columns on heat transfer performance of aluminum nitride-based microchannel heat sink”. Ceramics International. 2022; 1–12. https://doi.org/10.1016/j.ceramint.2022.08.180.

[163] Jaseliūnaitė J., Šeporaitis M. “Performance optimisation of microchannel pin-fins using 2D CFD”. Applied Thermal Engineering. 2022; 206: 118040(1-10). https://doi.org/10.1016/j.applthermaleng.2022.118040.

[164] Yang D., Jin Z., Wang Y., Ding G., Wang G. “Heat removal capacity of laminar coolant flow in a micro channel heat sink with different pin fins”. International Journal of Heat and Mass Transfer. 2017; 113: 366–372. https://doi.org/10.1016/j.ijheatmasstransfer.2017.05.106.

[165] Colla L., Ercole D., Fedele L., Mancin S., Manca O., Bobbo S. “Nano-phase change materials for electronics cooling applications”. Journal of Heat Transfer. 2017; 139: 1–9. https://doi.org/10.1115/1.4036017.W.

[166] Gao X., Li R. “Spray Impingement Cooling: The State of the Art, Advanced Cooling Technologies and Applications”. (2019). https://doi.org/10.5772/intechopen.80256.

[167] Qiu Y., Hu W., Wu C., Chen W. “An experimental study of microchannel and micro- pin-fin based on-chip cooling systems with silicon-to-silicon direct bonding”. Sensors. 2020; 20: 1–14. https://doi.org/10.3390/s20195533.

[168] Chiu H.C., Hsieh R.H., Wang K., Jang J.H., Yu C.R. “The heat transfer characteristics of liquid cooling heat sink with micro pin fins”. International Communications in Heat and Mass Transfer. 2017; 86: 174–180. https://doi.org/10.1016/j.icheatmasstransfer.2017.05.027.

[169] Zhao J., Huang S., Gong L., Huang Z. “Numerical study and optimizing on micro square pin-fin heat sink for electronic cooling”. Applied Thermal Engineering. 2016; 93: 1347–1359. https://doi.org/10.1016/j.applthermaleng.2015.08.105.

[170] Tullius J.F., Tullius T.K., Bayazitoglu Y. “Optimization of short micro pin fins in minichannels”. International Journal of Heat and Mass Transfer. 2012; 55: 3921–3932. https://doi.org/10.1016/j.ijheatmasstransfer.2012.03.022.

[171] Niranjan R., Singh O., Ramkumar J. "Numerical study on thermal analysis of square micro pin fins under forced convection". Journal of Heat and Mass Transfer, 2022; 58(608): 263-281. https://doi.org/10.1007/s00231-021-03105-x.

[172] Micheli L., Reddy K.S., Mallick T.K. “Experimental comparison of micro-scaled plate-fins and pin-fins under natural convection”. International Communications in Heat and Mass Transfer. 2016; 75: 59–66. https://doi.org/10.1016/j.icheatmasstransfer.2016.03.023.

[173] Wan Z., Joshi Y. “Pressure drop and heat transfer characteristics of pin fin enhanced microgaps in single phase microfluidic cooling”. International Journal of Heat and Mass Transfer. 2017; 115: 115–126. https://doi.org/10.1016/j.ijheatmasstransfer.2017.06.117.

[174] Izci T., Koz M., Koşar A.. “The effect of micro pin-fin shape on thermal and hydraulic performance of micro pin-fin heat sinks”. Heat Transfer Engineering. 2015; 36: 1447–1457. https://doi.org/10.1080/01457632.2015.1010921.

[175] Qin L., Hua J., Zhao X., Zhu Y., Li D., Liu Z. “Micro-PIV and numerical study on influence of vortex on flow and heat transfer performance in micro arrays”. Applied Thermal Engineering. 2019; 161: 114186. https://doi.org/10.1016/j.applthermaleng.2019.114186.

[176] Gupta D., Saha P., Roy S. "Computational analysis of perforation effect on the thermo-hydraulic performance of micro pin-fin heat sink". International Journal of Thermal Sciences. 2021; 163: 106857. https://doi.org/10.1016/j.ijthermalsci.2021.106857.

[177] Khalil W., Azzawi I. D. J., Al-damook A., Alkasmoul F. S. "Hydrothermal Performance Maximisation and Entropy Generation Minimisation of Different Perforated Pinned Heat Sink Designs for Electronic Cooling". Journal of Heat Transfer. 2022; 144(11): 114502 (1-6). https://doi.org/10.1115/1.4055243.

[178] Ndao S., Peles Y., Jensen M.K. "Multi-objective thermal design optimization and comparative analysis of electronics cooling technologies". International Journal of Heat and Mass Transfer. 2009; 52: 4317–4326. https://doi.org/10.1016/j.ijheatmasstransfer.2009.03.069.

[179] Bello-Ochende T., Meyer J.P., Ighalo F.U. "Combined numerical optimization and constructal theory for the design of microchannel heat sinks". Numerical Heat Transfer; Part A: Applications. 2010; 58: 882–899. https://doi.org/10.1080/10407782.2010.529036.

[180] Normah G.M., Oh J.T., Nguyen B.C., Choi K. I., Robiah A. "Comparison of the optimized thermal performance of square and circular ammonia-cooled microchannel heat sink with genetic algorithm". Energy Conversion and Management. 2015; 102: 59–65. https://doi.org/10.1016/j.enconman.2015.02.008.

[181] Tan H., Wu L., Wang M., Yang Z., Du P. "Heat transfer improvement in microchannel heat sink by topology design and optimization for high heat flux chip cooling, International Journal of Heat and Mass Transfer. 2019; 129:681–689. https://doi.org/10.1016/j.ijheatmasstransfer.2018.09.092.

[182] Lorenzini-Gutierrez D., Kandlikar S.G. "Variable fin density flow channels for effective cooling and mitigation of temperature nonuniformity in three-dimensional integrated circuits". Journal of Electronic Packaging, Transactions of the ASME. 2014; 136: 1–11. https://doi.org/10.1115/1.4027091.

[183] Reddy S.R., Abdoli A., Dulikravich G.S., Pacheco C.C., Vasquez G., Jha R., Colaco M.J., Orlande H.R.B. "Multi-Objective Optimization of Micro Pin-Fin Arrays for Cooling of High Heat Flux Electronics with a Hot Spot". Heat Transfer Engineering. 2017; 38: 1235–1246. https://doi.org/10.1080/01457632.2016.1242953.

[184] Vilarrubí M., Riera S., Ibañez M., Omri M., Laguna G., Fréchette L., Barrau J. “Experimental and numerical study of micro-pin-fin heat sinks with variable density for increased temperature uniformity”. International Journal of Thermal Sciences. 2018; 132: 424–434. https://doi.org/10.1016/j.ijthermalsci.2018.06.019.

[185] Sakanova A., Tseng K.J. “Comparison of pin-fin and finned shape heat sink for power electronics in future aircraft” Applied Thermal Engineering. 2018; 136: 364–374. https://doi.org/10.1016/j.applthermaleng.2018.03.020.

[186] Ismayilov F., Wang Y., Peles Y. “Challenges in micro-channel heat transfer experiments: insight on conjugate heat transfer effects” in: 16th IEEE Intersoc.Conf. Therm. Thermomechanical Phenom. Electron. Syst, 2017; 263–275. https://doi.org/10.1109/ITHERM.2017.7992481.

[187] Bejan A., Tsarsaronis G., Moran M. “Thermal Design and Optimization” John Wiley, New York, 1996.

[188] Iyengar M., Bar-Cohen A. “Least-energy optimization of forced convection plate-fin heat sinks”. IEEE Transactions on Components and Packaging Technologies. 2003; 26: 62–70. https://doi.org/10.1109/TCAPT.2003.811484.

[189] Rao R. V., Patel V.K. “Thermodynamic optimization of cross flow plate-fin heat exchanger using a particle swarm optimization algorithm”. International Journal of Thermal Sciences. 2010; 49: 1712–1721. https://doi.org/10.1016/j.ijthermalsci.2010.04.001.

[190] Liang C.H., Zeng S., Li Z.X., Yang D.G., Sherif S.A. “Optimal Design of Plate-Fin Heat Sink under Natural Convection Using a Particle Swarm Optimization Algorithm”. International Journal of Heat and Technology. 2016; 34: 275–280. https://doi.org/10.18280/ijht.340217.

[191] Mishra M., Das P.K., Sarangi S. “Second law based optimisation of crossflow plate-fin heat exchanger design using genetic algorithm”. Applied Thermal Engineering. 2009; 29: 2983–2989. https://doi.org/10.1016/j.applthermaleng.2009.03.009.

[192] Kennedy J., Eberhart R. “Particle swarm optimization”. in: Proceedings of the IEEE International Conference on Neural Networks, Perth, Australia, 1995; 1942-1948.

[193] Hamadneh N., Khan W.A., Sathasivam S., Ong H.C. “Design Optimization of Pin Fin Geometry Using Particle Swarm Optimization Algorithm”. PLoS ONE. 2013; 8: 1–9. https://doi.org/10.1371/journal.pone.0066080.

[194] Azarkish H., Farahat S., Sarvari S.M.H. “Comparing the Performance of the Particle Swarm Optimization and the Genetic Algorithm on the Geometry Design of Longitudinal Fin”. Eps. 2012; 5: 836–839.

[195] Mohammadi N., Mirabedini S.J. “Comparison Of Particle Swarm Optimization And Backpropagation Algorithms For Training Feedforward Neural Network, Journal of Mathematics and Computer Science”. 2014; 12: 113–123. https://doi.org/10.22436/jmcs.012.02.03.

[196] Daewoong J., Leea H., Daeyoung K., Cho E., Jung K. W., Kharangate C. R. Iyengar M., Malone C., Asheghi M., Goodson K. E., Lee H. “Thermal design and management of micro-pin fin heat sinks for energy-efficient three-dimensional stacked integrated circuits”. Int J of Heat and Mass Transf, 2021; 175: 121192. https://doi.org/10.1016/j.ijheatmasstransfer.2021.121192.

[197] Yu X., Woodcock C., Plawsky J., Peles Y. “An investigation of convective heat transfer in microchannel with Piranha Pin Fin”. Int. J of Heat and Mass Transf. 2016; 103: 1125-1132. https://doi.org/10.1016/j.ijheatmasstransfer.2016.07.069.

[198] Zhou M. Z., Xia G. D., Chai L., Zhou L. J., Gao N., “Flow and Heat Transfer Characteristics of Drop-Shaped Micro Pin-Fin Heat Sinks With Cross Flow”. Chin. J. Aeronaut. 2012; 27(12): 2681–2686.

[199] Babar H., Ali H. M. “Airfoil shaped pin-fin heat sink: Potential evaluation of ferric oxide and titania nanofluids” J of Energy Conv. and Management. 2019; 202: 112194. https://doi.org/10.1016/j.enconman.2019.112194.

[200] Ismayilov F., Akturk A., Peles Y. “Systematic micro heat sink optimization based on hydrofoil shape pin fins, Case Studies in Thermal Engineering”. 2021; 26: 101028. https://doi.org/10.1016/j.csite.2021.101028.

[201] Koşar A., Peles Y. “Micro scale pin fin heat sinks - Parametric performance evaluation study”. IEEE Transactions on Components and Packaging Technologies. 2007; 30: 855–865. https://doi.org/10.1109/TCAPT.2007.906334.

[202] Zhang J., Manglik R. M., Muley A., Borghese, J. B. Three-Dimensional Numerical Simulation of LaminarAirFlows in Wavy Plate-Fin Channels, Proc.

13th International Symposium on Transport Phenomena (ISTP-13), Victoria, British Columbia, Canada. (2002).

[203] Chamoli S., Chauhan R., Thakur N.S. “Numerical Analysis of Heat Transfer and Thermal Performance Analysis of Surface with Circular Profile Fins”. International Journal of Energy Science. 2011; 1(1): 11-18 www.ijesci.org. World Academic Publishing.

[204] Abdel H. El-Hofy G. “Fundamentals of Machining Processes: Conventional and Nonconventional Processes”. Edition 2nd 2013.

[205] Dhanik S., and Joshi S. S. “Modeling of a Single Resistance Capacitance Pulse Discharge in Micro-Electro Discharge Machining”. ASME. J. Manuf. Sci. Eng. 2005; 127(4): 759–767. https://doi.org/10.1115/1.2034512.

[206] Ivanov A., Lahiri A., Baldzhiev V., Wildner A.-T. "Suggested Research Trends in the Area of Micro-EDM—Study of Some Parameters Affecting Micro-EDM". Micromachines. 2021; 12: 1184(1-13). https://doi.org/10.3390/mi12101184.

[207] Jahan M.P., Rahman, M., Wong Y.S. “A review on the conventional and micro-electro discharge machining of tungsten carbide”. Int. J. Mach. Tools & Manufacturer. 2011; 51: 837–858. https://doi.org/10.1016/j.ijmachtools.2011.08.016.

[208] Imai Y., Nagakawa T., Miyake H., Hidai H., Tokura H. “Local actuator for highly accurate micro-EDM”. *J. Mater. Processing Technol.*, 2004, 149(1-3): 328–333. https://doi.org/10.1016/j.jmatprotec.2004.01.060.

[209] Mehfuz R., Ali M.Y. “Investigation of machining parameters for the multiple-response optimization of micro electrodischarge milling”. Int J Adv Manuf Technol. 2009; 43: 264–275. https://doi.org/10.1007/s00170-008-1705-0.

[210] Somashekhar K.P., Ramachandran N. Mathew J. “Material removal characteristics of microslot (kerf) geometry in μ-WEDM on aluminum”. Int J Adv Manuf Technol. 2010; 51: 611–626. https://doi.org/10.1007/s00170-010-2645-z.

[211] Muammer K.O.C,; Ozel, T.G. “Micro-manufacturing – Design and Manufacturing of Micro-Products”. *John Wiley & Sons, Inc., Hoboken, New Jersey* 2011.

[212] Rebelo J. C., Dias A. M., Mesquita R., Vassalo P., Santos M. “An experimental study on electro-discharge machining and polishing of high strength copper-beryllium alloys”. *J Mater Process Technol.* 2000; 103:389-397. https://doi.org/10.1016/S0924-0136(99)00492-6.

[213] Yeo S.H., Kurnia W., Tan P.C. “Electro-thermal modeling of anode and cathode in micro-EDM”. J Phy D Appl Phy. 2017; 40: 2513-2521. 10.1088/0022-3727/40/8/015. https://doi.org/10.1088/0022-3727/40/8/015.

[214] Bahrami M., Yovanovich M. M., Culham R. J. “Role of random roughness on thermal performance of microfins”. J Thermophys Heat Transfer 2007; 21(1): 153-157. https://doi.org/10.2514/1.22353.

[215] Coronado P.D.U., Garcia J.M., Tinoco E.V., Orta-Castanon P. “Online monitoring of a micro-EDM machine: machining diagnosis on the cloud based on discharge currents and voltages”. Manuf Lett. 2018; 15:115–8. https://doi.org/10.1016/j.mfglet.2017.12.004.

[216] Raj A. J., Balasubramanian K., Palanisamy D., Emmanuel A. G. S. “Experimental Investigations on WEDM Process for Machining High Manganese Steel”. Mater. Manuf. Process. 2020; 35(14): 1612–1621. DOI: https://doi.org/10.1080/10426914.2020.1779941.

[217] Somashekhar K. P., Ramachandran N., Mathew J. “Optimization of Material Removal Rate in Micro-EDM UsingArtificial Neural Network and Genetic Algorithms”. Materials and Manufacturing Processes. 25: 467–475. https://doi.org/10.1080/10426910903365760.

[218] Alting L., Kimura F., Hansen H. N., Bissacco G. “Micro Engineering”. CIRP Annals. 2003; 52(2): 635–657. https://doi.org/10.1016/S0007-8506(07)60208-X.

[219] Giorleo L., Ceretti E., Giardini C. “Optimization of Laser Micromachining Process for Biomedical Device Fabrication”. Int. J. Adv. Manuf. Technol. 2016; 82: 901–907. https://doi.org/10.1007/s00170-015-7450-2.

[220] Benton M., Hossan M.R., Konari P.R., Gamagedara S. “Effect of Process Parameters and Material Properties on Laser Micromachining of Microchannels”. Micromachines. 2019; 10(2): 123. https://doi.org/10.3390/mi10020123.

[221] Karthikeyan G., Garg A.K., Ramkumar J., Dhamodaran S. "A microscopic investigation of machining behavior in μeD-milling process", J Manuf Process. 2012; 14(3): 297–306. https://doi.org/10.1016/j.jmapro.2012.01.003.

[222] Mullya S.A., Karthikeyan G., "Accretion behavior and debris flow along interelectrode gap in μED-milling process". Int. J of Adv Manuf Technol, 2018; 96(9–12): 4381–4392. https://doi.org/10.1007/s00170-018-1861-9.

[223] Eberhart R.C., Shi Y. “Particle swarm optimization: Developments, applications and resources”. Proceedings of the IEEE Conference on Evolutionary Computation, ICEC. (2001; 1: 81–86. https://doi.org/10.1109/cec.2001.934374.

[224] Liang C.H., Zeng S., Li Z.X., Yang D.G., Sherif S.A. “Optimal Design of Plate-Fin Heat Sink under Natural Convection Using a Particle Swarm Optimization Algorithm”. International Journal of Heat and Technology. 2016; 34: 275–280. https://doi.org/10.18280/ijht.340217.

[225] Van Den Bergh F., Engelbrecht A.P. “A study of particle swarm optimization particle trajectories”. Information Sciences. 2006; 176: 937–971. https://doi.org/10.1016/j.ins.2005.02.003.

[226] Barrera J., lvarez-Bajo O., Flores J.J., Coello C.A.C. “Limiting the velocity in the particle swarm optimization algorithm”. Computacion y Sistemas. 2016; 20: 635–645. https://doi.org/10.13053/CyS-20-4-2505.

[227] Khan W.A., Culham J.R., Yovanovich M.M. “Optimization of pin-fin heat sinks using entropy generation minimization, Thermomechanical Phenomena in Electronic Systems”. Proceedings of the Intersociety Conference. 2004; 1: 259–267. https://doi.org/10.1109/itherm.2004.1319183.

[228] Koşar A., Mishra C., Peles Y. “Laminar flow across a bank of low aspect ratio micro pin fins, Journal of Fluids Engineering”. Transactions of the ASME. 2005; 127: 419–430. https://doi.org/10.1115/1.1900139.

[229] Liu Z.G., Guan N., Zhang C.W., Jiang G.L., “The Flow Resistance and Heat Transfer Characteristics of Micro Pin-Fins with Different Cross-Sectional Shapes”. Nanoscale and Microscale Thermophysical Engineering. 2015; 19(3): 221-243. https://doi.org/10.1080/15567265.2015.1073820.

[230] Saravanan V., Umesh C.K. “Numerical comparison for thermo-hydraulic performance of pin fin heat sink with micro channel pin fin heat sink”. Sadhana -Academy Proceedings in Engineering Sciences. 2018; 43: 1–15. https://doi.org/10.1007/s12046-018-0875-1.

[231] Sreehari D., Sharma A.K. “On thermal performance of serpentine silicon microchannels”. International Journal of Thermal Sciences. 2019; 146: 106067. https://doi.org/10.1016/j.ijthermalsci.2019.106067.

[232] Shao B. Modeling and simulation of micro electrical discharge machining, Ph.D. thesis. The University of Nebraska-Lincoln. Accessed on 25th November, 2018.

Biodata

Name: Mr. Hreetabh Kishore

Address for correspondence: Room No.-302, 2nd Floor, Advanced Manufacturing Technology Lab, Satish Dhawan Block, Department of Mechanical Engineering, Main Campus, IIT Ropar, Rupnagar (Punjab-140001)

E-mail: 2017mez0007@iitrpr.ac.in, hreetabhkishore09@gmail.com
Contact number: +91-7814943526, 9569126311

Date of Birth: February 15th, 1994

Educational Qualifications (all national exam results from secondary school):

Sr. No	EXAMS PASSED / Previous Degree	UNIVERSITY / INSTITUTION / BOARD	YEAR OF PASSING	MAIN DOMAIN	SUBJECT OF SPECIALIZATION
1	Matriculation	CBSE	2008	All compulsory subjects	All compulsory subjects (English medium)
2	Certificate	SLIET	2010	Mechanical	Foundry and Forging
3	Diploma	SLIET	2012	Mechanical	Foundry Technology
4.	B.E.	SLIET	2015	Mechanical	Welding Technology
5.	MTech.	SLIET	2017	Mechanical	Welding & Fabrication

Research Interests:

- Microstructural in Additive Manufacturing
- Material processing engineering
- Modeling and simulation of modern manufacturing processes (Non-conventional micromachining)
- Reliability study and optimization of process parameters
- Heat transfer analysis, CFD, Fluid Dynamics
- Electronic packaging

Graduate Aptitude Test in Engineering-(GATE) Qualified (yes/no): Yes. HREETABH KISHORE, Registration Number: ME88039S3323, Gate Score- 484, Marks 45.42, (2015)

Professional Training:

Sr. No	Organization	Period	Details of Training/ Project undertaken
1	Bharat Wagon Engineering Limited (Muzaffarpur, Bihar)	June 2009 & June 2011	To study the overall manufacturing processes used in the production of different Wagons supplied to Indian Railways for carrying goods.
2	Bharat Heavy Electrical Limited (Haridwar,	June-July 2013	Effect of heat input on MS plate using cladding electrode E-316L and their testings (Impact testing, wear test, dilution Test, DPT, Hardness Test etc.)

	Uttarakhand)		
3	Birla Cellulosic (Kharach, Gujarat)-Aditya Birla Group	July-August 2013	Pipe welding and A-Z manufacturing of cotton balls for Grasim India using natural and artificial pulp.
4	IIT Ropar (Rupnagar, Punjab)	June-July 2016	Studies on Single Point Incremental forming process: Simulation study of GTAW welding using ABAQUS and Python Scripting.